Modélisation de la polydispersion des brouillards de gouttes sous l'effet des interactions two-way turbulentes pour l'injection directe à haute pression dans les moteurs

Oguz Emre

THÈSE

présentée par

Oğuz EMRE

pour l'obtention du

GRADE de DOCTEUR

Formation doctorale : Energétique, Mathématiques Appliquées

Laboratoire d'accueil : Laboratoire d'Energétique Moléculaire et Macroscopique, Combustion (EM2C) du CNRS et de l'ECP

Modeling of spray polydispersion with two-way turbulent interactions for high pressure direct injection in engines

Soutenue le 21 Mars 2014

Jury :	MM.	Daniel	E.	Rapporteur
		Demoulin	F.-X.	Rapporteur
		Desjardins	O.	Rapporteur
		Lance	M.	Examinateur
		Som	S.	Examinateur
		Murrone	A.	Examinateur
		Fox	R. O.	Examinateur
		Massot	M.	Directeur de thèse
	Mme.	Laurent	F.	Co-Directrice de thèse
	MM.	Jay	S.	Encadrant IFPEN
		de Chaisemartin	S.	Encadrant IFPEN

Ecole Centrale des Arts et Manufactures
Grand Établissement sous tutelle
du Ministère de l'Éducation Nationale
Grande Voie des Vignes
92295 Châtenay-Malabry Cedex
Tél : 33 (1) 41 13 10 00
Télex : 634 991 F EC PARIS

Laboratoire d'Énergétique Moléculaire et Macroscopique, Combustion (E.M2.C.)
UPR 288, CNRS et Ecole Centrale Paris
Tél : 33 (1) 41 13 10 31
Fax : 33 (1) 47 02 80 35

2014-2014ECAP0029

ABSTRACT

The ability to simulate two-phase flows is of crucial importance for the prediction of internal combustion engine (ICE) performance and pollutant emissions. The direct injection of the liquid fuel inside the combustion chamber generates a cloud of polydisperse droplets, called spray, far downstream of the injector. From the modeling point of view, the emergence of Eulerian techniques for the spray description is considered promising by the scientific community. Moreover, the bottleneck issue for Eulerian methods of capturing the droplet size distribution with a reasonable computational cost, has been successfully tackled through the development of Eulerian Multi Size Moment (EMSM) method. Towards realistic ICE applications, the present PhD work addresses the modeling of two-way turbulent interactions between the polydisperse spray and its surrounding gas-phase through EMSM method. Following to the moving mesh formalism Arbitrary Lagrangian Eulerian (ALE), the source terms arising in the two-phase model have been treated separately from other contributions. The equation system is closed through the maximum entropy (ME) reconstruction technique originally introduced for EMSM. A new resolution strategy is developed in order to guarantee the numerical stability under very fast time scales related to mass, momentum and energy transfers, while preserving the realizability condition associated to the set of high order moments. From the academic point of view, both the accuracy and the stability have been deeply investigated under both constant and time dependent evaporation laws. All these developments have been integrated in the industrial software IFP-C3D dedicated to compressible reactive flows. In the context of 2-D injection simulations, very encouraging quantitative and qualitative results have been obtained as compared to the reference Lagrangian simulation of droplets. Moreover, simulations conducted under a typical 3-D configuration of a combustion chamber and realistic injection conditions have given rise to fruitful achievements. Within the framework of industrial turbulence modeling, a Reynolds averaged (RA) extension of the two-way coupling equations is derived, providing appropriate closures for turbulent correlations. The correct energy partitions inside the spray and turbulent interactions between phases have been demonstrated through homogeneous test-cases. The latter cases gave also some significant insights on underlying physics in ICE. This new RA approach is now ready for ICE application simulations.

Keywords Evaporating spray, turbulent two-way coupling, polydispersity, Eulerian models, high order moment method, Reynolds averaging, ALE formalism

RÉSUMÉ

La simulation des écoulements diphasiques rencontrés dans les moteurs à combustion interne (MCI) est de grande importance pour la prédiction de la performance des moteurs et des émissions polluantes. L'injection directe du carburant liquide à l'intérieur de la chambre de combustion génère loin de l'injecteur un brouillard de gouttes polydisperses, communément appelé spray. Du point de vue de la modélisation, l'émergence des méthodes Eulériennes pour la description du spray est considerée prometteuse par la communauté scientifique. De plus, la prise en compte de la distribution en taille des gouttes par les approches Eulériennes, de manière peu coûteuse en temps de calcul, n'est plus considérée comme un verrou depuis le développement de la méthode Eulerian Multi Size Moment (EMSM). Afin d'envisager la simulation de configurations réalistes de MCI, ce travail de thèse propose de modéliser les interactions turbulentes two-way entre le spray polydisperse évaporant et la phase gazeuse environnante par la méthode EMSM. Dans le contexte du formalisme *Arbitrary Lagrangian Eulerian* (ALE) dédiée au traitement du maillage mobile, les termes sources présents dans le modèle diphasique sont traités séparément des autres contributions. Le système d'équations est fermé à l'aide d'une technique de reconstruction par maximisation d'entropie (ME), originellement introduite pour EMSM. Une nouvelle stratégie de résolution a été développée pour garantir la stabilité numérique aux échelles de temps très rapides introduites par les transferts de masse, quantité de mouvement et énergie, tout en réspectant la condition de réalisabilité associée à la préservation de l'éspace des moments d'ordre élevé. A l'aide des simulations académiques, la stabilité et la précision de la méthode ont été étudiées aussi bien pour des lois d'évaporation constantes que dépendantes du temps. Tous ces développements ont été intégrés dans le code industriel IFP-C3D dédié aux écoulements compressibles et réactifs. Dans le contexte de la simulation en 2-D de l'injection directe, les résultats se sont avérés très encourageants comme en témoignent les comparaisons qualitatives et quantitatives de la méthode Eulerienne à la simulation Lagrangienne de référence des gouttes. De plus, les simulations en 3-D effectuées dans une configuration typique de chambre de combustion et des conditions d'injection réalistes ont donné lieu à des résultats qualitativement très satisfaisants. Afin de prendre en compte la modélisation de la turbulence, une extension moyennée, au sens de Reynolds, des équations du modèle diphasique two-way est dérivée, un soin particulier étant apporté aux fermetures des corrélations turbulentes. La répartition de l'énergie dans le spray ainsi que les intéractions turbulentes entre les phases ont été étudiées dans des cas tests homogènes. Ces derniers donnent un aperçu intéressant sur la physique sous-jacente dans les MCI. Cette nouvelle approche RANS diphasique est maintenant prête à être employée pour les simulations d'application de MCI.

Mots Clés Spray évaporant, polydispersion, couplage two-way turbulent, modèles Eulériens, méthode de moments d'ordre élevé, moyenne de Reynolds, formalisme ALE

REMERCIEMENTS

Cette thèse est le produit d'une collaboration étroite entre IFP Energies nouvelles et le laboratoire EM2C de l'Ecole Centrale Paris. Je salue vivement tous ceux qui ont participé de près ou de loin à la réalisation de ce travail de longue haleine.

Mes premiers remerciements s'adressent évidemment à l'équipe de mes encadrants, Marc Massot, Frédérique Laurent, Stéphane Jay et Stéphane de Chaisemartin, qui m'ont permis de faire cette thèse dans une ambiance amicale et agréable, tout en m'assurant les meilleurs conditions pour réussir. Je salue mes directeurs de thèse, Marc et Fréderique, qui m'ont donné gôut au sujet. Leur implication dans l'ensemble de mes travaux de thèse, leur excellence scientifique ainsi que leur disponibilité m'ont permis d'apprendre beaucoup. Je retiens également nos discussions chaleureuses lors de mes passages à EM2C. Passons maintenant à mes encadrants du côté de IFP Energies nouvelles. Je salue Stéphane Jay pour les échanges amicaux que j'ai eu avec lui au cours de ces trois années et ses efforts précieux sur la valorisation de mes travaux dans un contexte industriel. Je salue Stéphane de Chaisemartin pour ses aides lors de mes timides débuts dans le sujet mais aussi pour son implication forte dans l'ensemble de mes travaux. Je le remercie également pour sa gentillesse et sa disponibilité.

Je remercie vivement Eric Daniel, François-Xavier Demoulin et Olivier Desjardins d'avoir accepté la lourde tâche d'être les rapporteurs de mon travail de recherche, leurs avis sur ce travail permettra d'apporter des idées nouvelles pour les études futures. Je remercie Michel Lance de m'avoir fait l'honneur de présider mon jury de thèse et pour l'intérêt qu'il a manifesté pour mon travail. Je remercie Rodney O. Fox, Sibendu Som et Angelo Murrone autant pour leurs remarques sur le manuscrit que les questions pertinentes posées lors de la soutenance.

Au delà de mon encadrement officiel, Il est important que j'évoque les personnes avec qui j'ai échangé de près. J'ai eu la chance de travailler avec Rodney O. Fox. Son expertise exceptionnelle sur l'aspect modélisation de la turbulence a énormement contribué à la valorisation de ma thèse. Il faudrait aussi que je remercie encore une fois Marc d'avoir organisé cette collaboration fructueuse avec Rodney. Je salue Huy Tran qui a consacré une partie non négligeable de son temps pour m'initier aux aspects numériques de ma thèse. Il est également intervenu de nombreuses fois lors des différentes étapes de mes travaux. Je retiens nos sessions agréables avec Huy. Et enfin, je salue Anthony Velghe qui m'a donné de l'appui plusieurs fois pour surmonter les difficultés liées au développement du code IFP-C3D.

J'adresse toute ma gratitude à IFP Energies nouvelles et au laboratoire EM2C qui, par les moyens humains, matériels et financiers m'ont apporté un environnement de travail de qualité. Je remercie Antonio Pires da Cruz, chef du département R102 (Modélisation et Simulation Système) pour m'avoir accueilli dans son équipe. Je remercie Estelle Iacona, directrice du laboratoire EM2C, ainsi qu'Olivier Gicquel qui lui a succédé et m'a permis de finir mon travail de thèse dans de bonnes conditions. Je remercie également l'ensemble des ingénieurs et des chercheurs à IFP Energies nouvelles et à EM2C pour leurs accueils

chaleureux. Je retiens les échanges avec Nicolas Gillet, Julien Bohbot et Rajesh Kumar que j'ai eu sur IFP-C3D. Je remercie également Damien Kah, Aymeric Vié et Adam Larat pour nos échanges sur les méthodes des moments et les méthodes numériques.

Je salue les thésardes et thésards avec qui j'ai partagé cette aventure. La liste est longue, j'en oublie certainement. Du côté de IFP Energies nouvelles, je remercie Damien et Sophie avec qui j'ai passé des moments agréables et amusants dans le même bureau. Il m'est également impossible d'oublier les moments de partage, notemment au tour de la machine à café, avec Stavros, Haifa, Betty, Benjamin, Nikola, Emre, Federico, Nicolas, Carlo, Anthony, Stéphane, Adam, Ayoub, Jan, Lama, Elias, Pablo, Karl. Je salue également les thésards et les postdoc avec qui j'ai eu de très bons souvenirs lors de mes passages au labortoire EM2C. Je pense en particulier François, Alaric, Macole, Gizem, Pedro, Wassim, Haoxue, Marien, Jose.

Pour finir, je remercie de tout mon coeur mes parents de m'avoir soutenus durant ces longues années d'études et en particulier ma compagne Marguerite pour son soutien sans faille et sa patience pour mes nombreux jours de travail. Elle a su me redonner de la force quand il m'en manquait.

Contents

List of Figures

Chapter 1

Introduction

1.1 General context

In recent years, the global demand for energy has significantly increased with the rising world population and emerging industrial sectors. Yet the fossil fuel energy supplies are increasingly scarce and require advanced engineering techniques for their exploitation, prompting economical challenges. Moreover, the high amount of greenhouse gases and pollutant emissions continuously released in the atmosphere require to be limited in order to avoid the global warming and the irremediable degradation of the air quality. In that context, the road vehicle sector represents one of the main targets to deal with since the conventional Internal Combustion Engine (ICE), highly consuming fossil fuels, is the leading responsible for both CO_2 emissions and pollutant formations. In the present decade where fossil fuels will remain to be major energy sources for vehicles, many researchers and engineers from both public and private institutions collaborate to create innovative solutions for cleaner and energy efficient engines.

The high pressure direct injection system is actually widely recognized as efficient. Its main role is to inject the liquid fuel under very high pressure, up to 2000 bars, and release the required quantity of the fuel in the combustion chamber thanks to the very fast opening-closing time of the injector valve. This system provides a great cycle efficiency, controlling the amount of fuel injected in the combustion chamber. However, a good control of the combustion regime is required in order not to generate high quantity of pollutant emissions among which soot particles are an important preoccupation. A deep understanding of flow physics underlying the combustion chamber is therefore of primary importance in order to develop new engine configurations. There are many possible methods to achieve this goal. Experimental setups are essential to test the final version of a new engine concept before its industrialization phase. They also provide reliable data for testing new physical models. However, they are not profitable since it becomes costly to conduct many realizations. Moreover, they can not give enough information when the characteristic time scales of interesting phenomena, such as the injection physics, are too fast to capture. Given this limited number of experimental test benches, the numerical simulation techniques are considered to be complementary tools. Yet the fact that there are several numerical techniques which are classified according to the level of accuracy they provide, a brief review is required to highlight their interesting points and limitations.

1.2 Numerical tools for ICE simulation

It is appropriate to classify these simulation techniques into two main categories: System simulation and 3D Computational Fluid Dynamics (CFD) simulation.

1.2.1 System simulation methods

Based on 0D/1D models, system simulation tools have experienced rapid improvements in the past ten years and today is used at all stages of the engine development from concept design to powertrain control development and calibration. Contrary to 3D CFD approaches, these tools provide only mean values of global variables such as temperature, pressure, injection velocity, etc. 0-dimensional models are essentially based on empirical or phenomenological approaches which are mainly developed to reach very low computational times (real-time) as a target. Nevertheless, such models are often characterized by very limited prediction levels. Although in recent years some fruitful developments of refined physical models, based on the reduction of 3D approaches over a given domain volume as for example the combustion chamber have been conducted in [15, 48, 90, 122], they do not provide the resolution of complex 3D flows in ICE.

1.2.2 CFD methods

CFD allows a better understanding of physical phenomena taking place in combustion chambers such as spray development, heat transfer, combustion, pollutant formation, etc. All these phenomena are highly influenced by the high unsteady turbulent flow motion. The turbulent flow field is defined by all characteristic length scales and kinetic energies of the eddies describing the flow. Kolmogorov (1941) proposed a continuous distribution of the energy of turbulent eddies as function of their wave number. In such a representation, the flow energies supposed to be transfered from largest eddies to smaller ones through division processes without dissipation. The range of scales lies between the integral length scale (associated to the domain geometry) and the Kolmogorov scale from which the turbulent energy is dissipated as heat through the influence of molecular viscosity. During the last few years, numerical description of turbulent processes has been the subject of several investigations in order to be able to solve a given problem considering available computational resources. In that context, there are three different approaches used to simulate flows inside ICE:

- *DNS (Direct Numerical Simulation)*: This method is based on the direct resolution of transport equations for the fluid flow without any complimentary models or approximations. Within the validation limit of Navier Stokes equations, it provides a detailed and high quality study of physical phenomena. This implies however to resolve all turbulent scales with the help of mesh sizes of the order of the Kolmogorov scale or smaller. The latter means that an important number of grid points is required. Moreover, DNS needs highly precise numerical discretization schemes to limit the necessary grid. All these constraints make DNS a very expensive tool, prohibited for industrial applications. Let us precise that the DNS is widely used despite its CPU costs since it is the most accurate CFD tool. It permits rigorous

physical analysis [138, 134, 69], difficult to conduct experimentally. Moreover it is widely used for the development of physical models aimed to be implemented in industrial CFD softwares.

- *LES (Large Eddy Simulation)*: In this case, not all the flow scales are resolved. The main idea is to model energy dissipating flow scales which are small and isotropic but resolve all bigger and energy containing scales which are highly anisotropic and depending on the 3D geometry. This simulation technique requires coarser mesh sizes than used in DNS and thus provides results using less CPU time. Yet, until recent years its computational time was considered to be a bottleneck problem for complex 3D studies. After recent advances on parallel computing and supercomputers, it is nowadays considered as an emerging tool for industrial applications, thanks to its ability to capture cycle to cycle variations, rotational motion of the flow and the anisotropy under reasonable computational time [188]. Within the context of ICE applications, some fruitful recent works have been conducted such as in [108, 178] and displayed in Figure 1.1.

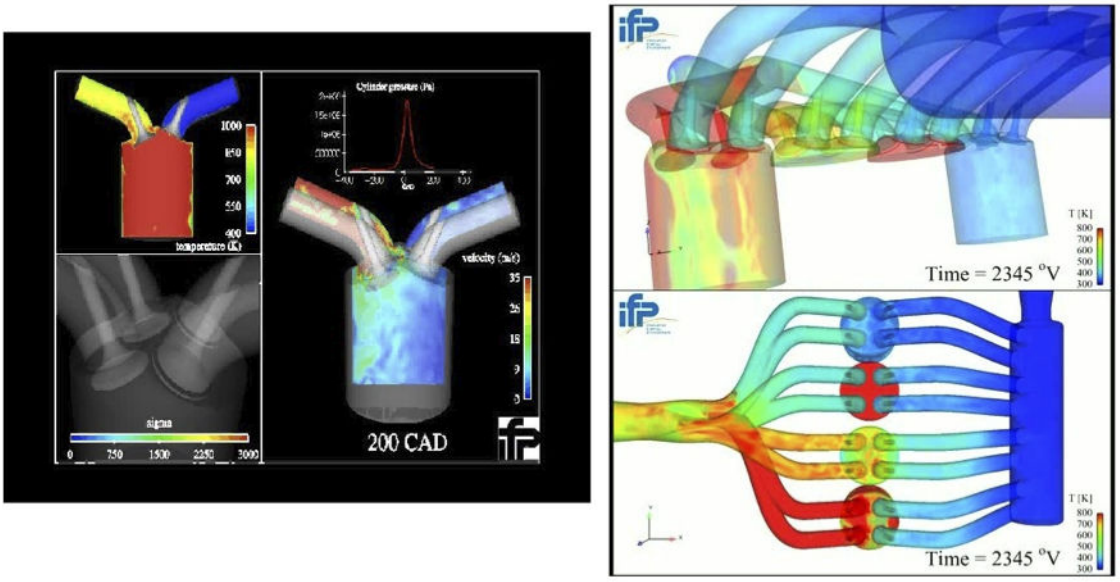

Figure 1.1: *LES simulations of a multi-cycle engine XU10-PSA (left, [185]) and of a multicylinder spark ignition engine (right, [91]*

- *RANS (Reynolds Averaged Navier Stokes equations)*: This approach is conceptually different than the last two numerical techniques. While only one realization of the flow is simulated through LES and DNS, RANS focuses on the ensemble average of the flow realizations. This accounts for dealing with Reynolds equations instead of Navier Stokes equations and ensemble averaged mean flow quantities. Within the well known k-ε approach, all turbulence scales are modeled through the concept of the mean turbulent kinetic energy and the turbulent energy dissipation rate [141]. Yet more accurate RANS models for complex flow simulations are also available for industrial simulation purposes [50]. The main drawback of RANS as compared to

DNS and LES is its inability to capture instantaneous flow variations and its lack of accuracy for highly anisotropic flows. Yet RANS is widely used and preferred to LES for industrial applications. Because its computational time is generally very low and does not require high order numerical algorithms for the treatment of the spatial discretization, which is also often difficult to implement in industrial CFD softwares.

Conscious of the necessity for high accuracy CFD tools for the future of car engine production, IFP Energies nouvelles has been leading a wide research and engineering activity on ICE modeling through its industrial codes, AVBP (LES) and IFP-C3D (RANS), [12] in order to provide innovative solutions for ICE and equipment producers.

Until now, a high maturity has been reached in the simulation of mono-phase gaseous combustion or turbulent gaseous flow fields. Yet taking into account two-phase flow effects has become a critical aspect for 3D ICE modeling. In fact, the two-phase flow coming from the high pressure direct injection of liquid fuel significantly influence flame structure and pollutant production.

Figure 1.2: *Experimental view of a direct liquid injection with various two-phase flow topologies [49].*

1.3 Injection physics

The injection flow is not straightforward to be described due to complex phenomena, which require a modeling effort to take into account coupled interactions inside the liquid phase and between the liquid and the gas phases. A broad range of two-phase flow structures are illustrated in Figure 1.2.

The phenomenon of cavitation is the main factor determining the two-phase flow regime encountered inside the injector. It occurs when the absolute liquid pressure drop down to the vapor saturation pressure which depends on the liquid temperature. Therefore, the formation of vapor bubbles and pockets is observed inside the carrier liquid phase [100]. The formation of cavitation inside the injector depends on the geometry of the spray tip and impacts the flow characteristics inside the nozzle. The cavitation is also

one of the underlying physics impacting the liquid desintegration at downstream of the injector.

The bulk fuel liquid jet coming out from the nozzle of the injector is disintegrated into small droplets by internal and external forces as a result of the interaction between the liquid and surrounding medium. The disintegration or breakup process starts right at the exit of the nozzle when the disruptive forces, caused by the presence of the gas phase in the combustion chamber and cavitating pockets already created inside the nozzle and mixed to the liquid, exceed the liquid surface tension and viscous forces. The competition between cohesive and disruptive forces will set up on the liquid surface, leading to oscillations and perturbations in the liquid. Under favorable conditions, the oscillations may be amplified to such an extent that the bulk liquid breaks up into ligaments, clusters and small drops. This initial breakup process is often referred to as *primary breakup* or *primary atomization*, happening right at the exit of the injector nozzle. Afterwards, the gas phase keeps interacting with the resulting discontinuous liquid phase. Momentum transfers occur through interactions between the spray and the gas turbulent eddies. These interactions may lead to *secondary break-up* or *secondary atomization* of the liquid ligaments and clusters into smaller spherical droplet of various in sizes, This cloud of droplets is dispersed in the combustion chamber while exchanging momentum and energy with the surrounding gas-phase. Due to ambiant thermodynamic conditions and two-way coupling interactions between phases, these droplets evaporate while transferring their mass to the gas-phase before disappearing completely. The remaining fuel species vapor pockets pilot the combustion temperature and the equivalence ratio, defining the combustion characteristics.

1.4 Injection flow description

In order to accurately describe injection physics, one can consider a resolution of the entire flow, using DNS techniques. But the cost of these methods is the main stumbling block for their use in industrial framework [100, 23, 22, 98] (Figure 1.3 illustrates a typical DNS two-phase flow simulation). Therefore, in order to still enable a resolution of the problem, reduced order models are derived despite the loose of information on the details of the flow. In that context, some works have been addressed to the complete injection modeling dealing with all types of two-phase flow structures. The technique so-called ELSA (Eulerian-Lagrangian Spray Atomization) [33] has been proven to be a promising option. Through the RANS formalism, some industrial simulations under the diesel engine conditions for ICEs have been conducted [101]. Moreover, ELSA has been extended to LES models, promising for the simulation of full injection process, although they are still under a development stage [24, 25].

On the other hand, some other studies focus on a particular zone in the injection flow. In that case, regarding physical phenomena driven by different characteristics of the flow, different types of modeling best suited for each zone are used. In the primary and secondary break-up zones, the liquid phase being either continuous or involves complex interfaces between phases, it is necessary to adopt a *separate-phase* flow description. On the other hand, far downstream of the injector, a *disperse-phase* flow description is more

appropriate. In the latter case, the liquid phase is assumed to be composed of spherical droplets, which are various in size. This leads to the notion of *polydispersity*.

The project of IFP Energies nouvelles involves the simulation of the fuel spray injection in the entire combustion chamber, from the flow in the nozzle injector to the area downstream of the injector. This simulation requires therefore the use of models correctly describing the topology of the two-phase flow in different zones of the injection. Recent works have adress the simulation of separate-phases at the dense zones of the injection [182, 186, 8, 104, 105].

Yet, the present work aims at contributing to the modeling of polydisperse flow regime. Therefore, it is interesting to briefly carry out modeling and resolution strategies for the disperse phase simulations.

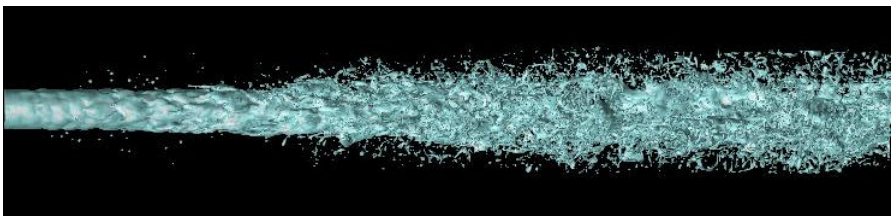

Figure 1.3: *DNS simulation of a liquid jet atomization through the hybrid VOF/Level Set sharp interface approach [126].*

1.5 Disperse phase simulation at a glance

In the literature, one can distinguish three different disperse-phase modeling categories: Microscale models, macroscale models derived from averaging of Navier Stokes equations and kinetic based models.

- *Microscale models*: There are basically three categories of microscale models, presented hereafter from the most to the least detailed one. The first one is the sharp interface methods (VOF, Level Set), which directly solve Navier Stokes equations [202, 70, 17, 76]. They allow to access all flow details in a two-phase flow, including detailed mass, energy and momentum exhanges through interfaces. Therefore, they are considered to be full DNS methods even if there are still stumbling blocks in resolving properly all scales in the vicinity of the interface. The second one is the DNS around solid bodies where, no detailed interface resolution is conducted. Yet the fluid flow around each particle is completely resolved [5, 197] through DNS. The third one is the Direct particle simulation (DPS) technique, which is less detailed than DNS around solid bodies in the sense that the effect of particle volume occupation on the surrounding fluid flow is not resolved [69, 135, 154, 203]. All these models are used to understand complex physics. But their use in industrial simulations face difficulties due to their excessive computational times required for their resolution. They are therefore used to improve and validate models and correlations for macroscopic and mesoscopic approaches.

- *Macroscale models derived from averaging of Navier Stokes equations of two-fluid type*: These are average models, which describe the two-phase flow topologies through volume or ensemble averaged quantities. Conceptually, they do not provide a detailed behavior of flows in the vicinity of interfaces. But they offer lower computational time, which is viewed as an attractive point for their development. These methods have been proven to be efficient for flows close to injector nozzle where the description of interface dynamics and thus interface conditions of equilibrium or non-equilibrium between the phases are of primary importance [6, 82, 32]. Through the same modeling philosophy, there has been also an attempt to describe the cloud of droplets at far down stream of the injector [186]. But in this case, since the fluid topology is accessed, only through a volume fraction and a surface area density variables, the polydispersity characteristic of these droplets could not be accounted for, and so some essential pieces of information are missed since recent works have shown that polydispersion has to be resolved in order to predict properly the physics of such two-phase flows.

- *Mesoscopic also called kinetic based models*: In order to take into account the polydispersity character of droplets under reasonable CPU time, the kinetic Williams-Boltzmann modeling of droplets developed in [193, 194] offers a good compromise. It allows tracking all particles and their associated velocities, sizes, temperatures and positions through the evolution of the number density function f.

In this thesis, we will therefore focus on kinetic based models for developing models capturing the polydisperse character of the disperse-phase flows. Yet there are two possible resolution approaches of the kinetic model, namely Lagrangian or Eulerian techniques.

- At present, Lagrangian methods are widely used for the disperse-phase simulation since they combine an efficient modeling of the polydisperse phase, not introducing any numerical diffusion, and an easiness of implementation. Nevertheless, they suffer from important drawbacks. First, they raise the question of the coupling with the Eulerian description of the gas phase. This question is still open since it involves two ways of description that are fundamentally different even if some recent contributions have pave the way to at least obtaining grid convergence of solutions. Sometimes a very high number of statistical particles is needed for convergence issues. Moreover, in the framework of domain decomposition for parallel computations it is needed to use complex and costly dynamic partitioning methods, to ensure a good load balancing between the different parallel processes. Let us recall also that some advances have been obtained in this field [71]. Finally, as previously mentioned, Lagrangian methods are restricted to disperse-phase flow only. In order to describe a full spray injection, Lagrangian methods, when they are used, have to be coupled with an Eulerian model for separate-phase flows [33].

- The Eulerian formalism consists in indirectly solving transport equations for the NDF by solving for selected moments of the kinetic equation, using a moment method. The use of moment methods results in the loss of some information but for the following two reasons the cost of such methods can potentially be much

lower than that of the Lagrangian alternative. The first is due to the fact that the equation is solved for a limited number of unknowns, the second is related to the high level of optimization one can reach, when both phases are solved within an Eulerian framework [30, 68, 66]. Besides, for comparison with data in practice, the principal quantities of interest are the moments of the NDF. Finally, it appears that this kind of method allows a priori a much easier coupling with a separate-phase two-fluid model than Lagrangian methods [83].

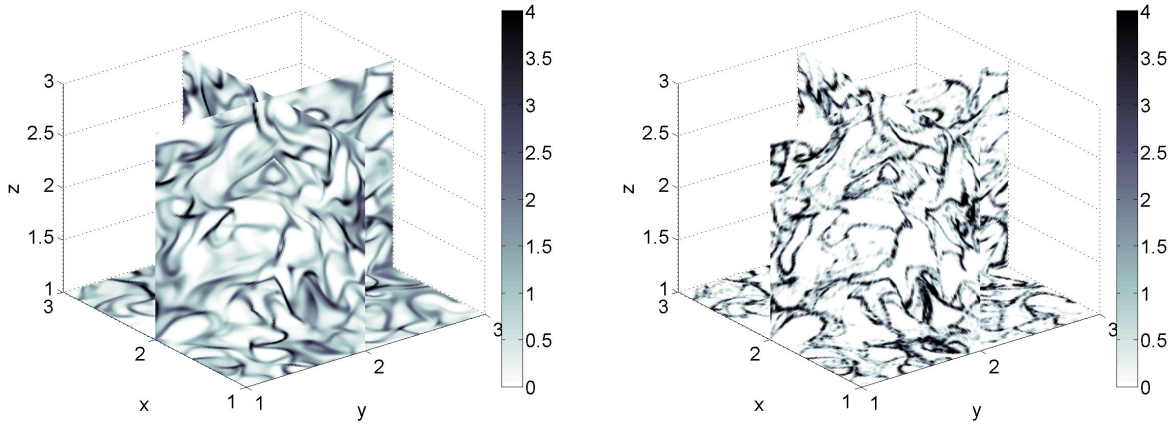

Figure 1.4: Mass density field comparison between the Eulerian Multi-Fluid approach (left) and Lagrangian (right) description of a polydisperse particle population in a 3-D simulation context [66].

1.6 Eulerian polydisperse modeling at a glance

In the literature, several types of Eulerian models for the description of spray polydispersity are provided.

- The first one is called the size sampling also called Multi-Class approach, which performs a discrete treatment of size so that the polydisperse solution is a superposition of monodisperse solutions evaluated at nodes or classes [94, 9, 131]. But it is intractable to tackle integral terms except at the cost of strong modal simplifications [184, 145].

- The second class consists in a discretization of the size phase space into size intervals called sections since the work of Tambour and coworkers [174, 163, 73]. There exists a large variety of applications and methods such as Multi-Fluid (MF) models for sprays (see [94, 92, 93, 95] extended from sectional models of Tambour, Greenberg et al. and [174, 163, 73]). The original MF approach relies on the derivation of a semi-kinetic model from the Williams-Boltzmann equation [193, 194] using a moment method for velocity and temperature conditioned by size, but keeping the size as a

variable [94]. This function is then discretized using a finite-volume approach that yields conservation equations for mass, momentum, energy of droplets in fixed size intervals called sections. It has led to very encouraging realizations [30] for DNS simulations. However, partitioning the particle phase into size sections leads to a high number of coupled *fluids*, and results in high computational cost. Yet, some numerical efforts have been carried out to decrease the number of size intervals while increasing the accuracy within each size [93, 45] depending on the physics involved [40, 41].

- The third approach is the quadrature based moment methods. In terms of computational cost, the possibility of high order moment method considering a single size section is attractive. To this end, either Quadrature Method of Moment (QMOM) where the dynamics of moments are evaluated after closing the source terms using quadrature methods [123, 196] or Direct Quadrature Method of Moment (DQMOM) wherein equations are directly written on the quadrature weights and abcissas which describe the reconstructed distribution function having the same moments [65]. Such methods have proved to be very efficient in a number of configurations. But, they are not able to accurately predict the evaporating flux at zero droplet size, which is a point-wise value to be reconstructed from the set of moments [65]. Some recent contributions have improved the ability of such approaches using Extended Quadrature Method of Moment (EQMOM) [199].

Within the context of typical ICE simulations, both the droplet evaporation and the polydispersity need to be correctly captured in order to evaluate the fuel vapor distribution inside the combustion chamber. The lack of accuracy of DQMOM approach in evaluating the polydisperse droplet evaporation and the high computational cost associated to Multi-Fluid method has encouraged recent fruitful works for the development of a new high order moment method [83]. Kah et al. [83, 120, 87] have proposed a new strategy, preserving the moment space, called Eulerian Multi-Size Moment model (EMSM). It consists of taking advantage of continuous description of the size distribution to determine, through an original kinetic scheme, the evaporation flux of disappearing droplets and to evaluate the shift in size induced by evaporation. The reconstruction of the NDF is done by Entropy Maximization through its moments [125]. Moreover, moments convection has been achieved through either first or second order kinetic scheme while respecting the moment conservation. The great potential of EMSM is demonstrated in [87], where it is shown that the computational time for equivalent accuracy is clearly an advantage over the Multi-fluid method. A first preliminary implementation of the EMSM in the industrial code IFP-C3D [12] has been also conducted. Let us also emphasize that the size velocity correlations, which was the missing aspect of EMSM have been also addressed through the work of Vie et al. [189]. Yet, these developments conducted by Kah [83] were in the context of one-way coupling, that is, a simple effect of the gas on droplets had been considered. But in order to take into account physical phenomena observed in a typical internal combustion engine, more numerical and modeling efforts need to be achieved with high order moment methods. Taking into account coupled interactions between the gas and the polydisperse spray under a Reynolds average or LES turbulence model are primary aspects towards a full engine simulations in industrial codes (i.e. IFP-C3D soft-

ware). Moreover, both quantitative and qualitative validations of the model compared to either experimental or widely used Lagrangian formulation are still missing and need to be conducted.

1.7 Objectives of this PhD

The are two main objectives for this PhD:

- Firstly, the two-way coupling modeling between the gas phase, described through compressible Navier Stokes equations, and polydisperse spray phase, modeled through EMSM method, has to be achieved. This involves to properly close source terms in both phases. Moreover, a significant effort has to be done for numerical aspects: in a combustion chamber mass, momentum and energy exchanges between the spray and the gas occur under rapid variations; a global simulation time step bigger than characteristic times related to different phenomena is expected to generate some stability problems, if not well treated. In the context of Arbitrary Lagrangian Eulerian (ALE) formalism [43, 78, 79, 57], which allows a splitted resolution of governing equations for treating moving geometries, the convection and acoustic physics are explicitly resolved in a separate manner. The stability is guaranteed thanks to Courant-Friedrichs-Lewy (CFL) condition, imposing a simulation time step small enough to capture the right physics. Yet two-way coupling interactions require a coupled resolution of the drag, evaporation, and the heat transfer between the gas and the spray, through source terms. The time characteristics associated to these phenomena impose to deal with multiple scales. Moreover, disappearing sizes of droplets due to the evaporation yield very small relaxation times which can not be captured by the simulation time step. Under these underlying complex physics, an accurate, unconditionally stable, while preserving the moment space two-way coupling resolution strategy should be developed. Moreover, the latter should respect the ALE formalism and preserve the robustness of the original method associated to the EMSM method. As far as the required developments are achieved, preliminary test cases and implementation under the IFP-C3D code first need to be conducted. Afterwards, the new development should be assess and validated through injection simulations under the IFP-C3D code.

- Secondly, the turbulence effects need to be taken into account in the two-way polydisperse interactions between the gas and the spray. In the context of kinetic based Eulerian models, Fevrier et al. [59] has shown, through DNS simulations, the necessity to model the fluctuating energy partition inside the spray phase. Fevrier et al. [59] showed that the instantaneous spray velocity contains two parts: spatially correlated and uncorrelated velocities. All these achievements have been done in the context of one-way coupling of mono-disperse spray with the gas. More recently, the fruitful work conducted by Rodney Fox gave rise to a new Reynolds-averaged two-phase k-ϵ model [64] for incompressible, non-evaporating, collisional two-way

coupled mono-disperse spray. The new model proposed in [64] for turbulent velocity correlations between phases agrees with the work of [59] and [175]. Offering a significant possibilities for industrial RANS simulations, it needs to be improved for ICE applications under IFP-C3D software. This requires to take into account the polydisperse character of the evaporating spray and the compressibility of the gas. For that aim, first of all, a significant effort on the derivation of complete gas-spray turbulence model has to be conducted. This should be followed by preliminary test-cases in the context of homogeneous turbulence to validate correct fluctuating energy exchanges between phases.

1.8 Organization of the manuscript

Answer to all these questions are organized in the manuscript as follows:

- The Eulerian evaporating polydisperse spray simulation requires to be well understood in order to appreciate the achievements of this PhD thesis detailed in this manuscript. It is therefore useful to dedicate Chapter 2 to a review on modeling aspects. Firstly, a review on the microscopic level of disperse-phase flow description will be discussed to point out the necessity of a kinetic modeling for industrial applications. Therefore the discussion conducted in section 1.5 will be further detailed. Afterwards, the basic kinetic Williams-Boltzmann equation along with its main assumptions will be presented. As far as resolution strategies are concerned, some discussions on widely used Stochastic Lagrangian methods, also adopted for injection simulations in Chapters 3 and 4, will be investigated while highlighting their limitations which make Eulerian moment methods relevant to be used. The polydisperse character of the spray along with its turbulent interactions are considered to be two major bottleneck issues towards to two-way coupling modeling. Therefore, an insightful review on disperse-phase turbulence modeling through Eulerian moment methods is first carried out. Afterwards, we extend the discussion conducted in section 1.6, making links between different Eulerian polydisperse methods. In the final section, the Eulerian Multi Size Moment (EMSM) method originally introduced during the PhD of Damien Kah [83] will be presented in details along with its main achievements. This chapter will be concluded with a discussion about applications towards industrial simulations through the use of EMSM method and will guide the reader for the remaining chapters of the manuscript.

The scientific novelties provided through this PhD thesis are introduced respectively in Chapters 3, 4 and 6 summarized in the following:

- Chapter 3 is dedicated to the first achievements of the present PhD, while includes also some of the works conducted in connection and collaboration with Damien Kah[1] [83]. The goal in this chapter is to develop a new numerical strategy for the full Eulerian two-way coupling modeling between the polydisperse evaporating spray and the compressible gas. The latter should respect the realizability condition of

[1] postdoctoral fellow at Center for Turbulence Research Stanford University

the high order moment method (EMSM). Moreover, since the characteristic time scales associated to evaporating droplets under strong mass and momentum coupling between phases can be inevitably lower than the global time step during an ICE simulation, the new method should also guarantee the numerical stability while providing accurate solutions. The final goal being a direct injection application under the IFP-C3D code, the method should also respect the Arbitrary Lagrangian Eulerian (ALE) formalism already derived previously for EMSM method in [83] and implemented in IFP-C3D code in the context of one-way coupling. Therefore, in this chapter a detailed insights will be given for the two-way coupling resolution strategy in the context of ALE formalism. Afterwards, some preliminary homogeneous test cases to assess the EMSM method and the stability and the accuracy of the two-way coupling have been discussed and shown. Then, more advanced studies on multi-dimensional framework should be carried out. The first test case consists in validating the ability to treat correctly the mesh motion effect on the spray dynamics through ALE formalism in IFPC3D. Afterwards, through 2D test cases and in the one-way context, comparisons between the academic code MUSES3D [30] and IFPC3D software [12] have been carried out, aiming at validating EMSM method under both structured and unstructured formalisms. Finally, the 2D injection simulation under the two-way coupling model has been pointed out. Rigorous comparisons between the Lagrangian and Eulerian simulations have been validated qualitatively and quantitatively.

- In Chapter 4, a detailed numerical analysis of the two-way coupling strategy will be conducted. Let us precise that the original method developed in Chapter 3 was in the context of a constant d-square evaporation law [167, 72]. Yet in a realistic context, the evaporation is in function of both gas-phase and spray-phase thermodynamic conditions [2]. Moreover, some convection-correction terms added to source terms can lead to even more complicated models. All these aspects require a deeper investigation in the numerical sense. Therefore the aim of Chapter 4 is to conduct a convergence and accuracy analysis of the numerical method. Through homogeneous context, some simulations under both constant and time dependent evaporation laws will be carried out. Afterwards the accuracy will be assessed through convergence studies, varying the simulation time. Afterwards, under a rather realistic temperature initial conditions, same injection configurations adopted in Chapter 3 will be done and compared to the solution of the Lagrangian in a qualitative and quantitative manner.

- Chapter 5 can be considered as the complimentary of Chapter 3 and 4 in the sense that, first, one presents the implementation effort of the the two-way coupled EMSM method in the code IFP-C3D. Then, a 3D injection configuration under realistic injection boundary conditions will be assessed and results will be analyzed qualitatively.

- Chapter 6 is dedicated to the turbulent two-way coupling modeling between the polydisperse spray and the compressible gas. Firstly, one discusses the derivation of an Eulerian-Eulerian model, within the framework of laminar two-phase flows

composed of an evaporating polydisperse spray and a compressible gas. The correct behavior of the energy partition in the spray phase for the turbulence modeling requires taking into account the granular temperature effect (also called uncorrelated motion), as highlighted first in [59]. This accounts for considering a polykinetic velocity distribution at the kinetic level. Based on this idea, first the original monokinetic EMSM model is extended to polykinetic in the context of laminar flow, through a transport equation for the granular temperature. Afterwards, a new Reynolds-averaged (RA) turbulence model is derived from the two-phase model presented in Chapter 3. This is based on the same philosophy introduced in [64] for two-way coupled monodisperse flows. However, one must deal with new terms and equations that arise due to size moment equations of the polydisperse evaporating spray and the gas-phase internal energy equation. To overcome this difficulty, new closure models are provided and discussed. The new turbulence model assessed through homogeneous test cases. First, the new model is qualitatively validated as compared to the test case of [59] for one-way coupling and then the extension to two-way coupling is studied for both evaporating and non-evaporating sprays. Next, the model is investigated under the conditions typical of high-pressure direct injection in ICE applications.

General conclusions of this PhD work along with perspective works will be discussed in Chapter 7

This present work was supported by a grant from IFP Energies nouvelles and S.A. Centrale Recherche, and benefited from a support from EM2C Laboratory of Ecole Centrale Paris. Furthermore, we wish to thank our collaborators Rodney O. Fox, Quang Huy Tran and Anthony Velghe for their scientific and technical contributions to this thesis.

- Contributions of this PhD thesis resulted in publications in international journals:
  - *D. Kah, O. Emre, Q. H. Tran, S. de Chaisemartin, S. Jay, F. Laurent, and M. Massot, High order moment method for polydisperse evaporating spray with mesh movement: application to internal combustion engines*, paper submitted in International Journal of Multiphase flows.
  - *O. Emre, R. O. Fox, M. Massot, S. de Chaisemartin, S. Jay, and F. Laurent, Eulerian modeling of a polydisperse evaporating spray under realistic internal-combustion-engine conditions*, paper published in Flow Turbulence and Combustion.
  - *O. Emre, D. Kah, S. Jay, Q.-H. Tran, A. Velghe, S. de Chaisemartin, R.O. Fox, F. Laurent, M. Massot, Eulerian Moment Methods for Automotive Sprays*, accepted for a publication in Atomization and Sprays.

  - *O. Emre, F. Laurent, S. de Chaisemartin, S. Jay, and M. Massot, Numerical analysis of a two-way coupled Eulerian high order moment method for the simulation of polydisperse evaporating sprays*, paper in preparation for a submission in Journal of Computational Physics.

- Presentations in the following international conferences have been done during the PhD period

  - *O. Emre, F. Laurent, S. de Chaisemartin, S. Jay, D. Kah and M. Massot, Two-way Coupling modeling through Eulerian moment method for spray injection in engine simulations*, European Congress on Computational Methods in Applied Sciences and Engineering (ECCOMAS), Vienna, Austria, 2012, pp. 1-18,
  - *O. Emre, F. Laurent, S. de Chaisemartin, S. Jay, D. Kah and M. Massot, Eulerian modeling of polydisperse evaporating spray under realistic internal combustion engine conditions*, International Conference on Multiphase Flow (ICMF), Jeju, Korea, 2013, pp. 1-15.

Chapter 2

Two-phase flow modeling of high pressure direct injection

2.1 Two-phase flow regimes in ICE

2.1.1 Physical mechanisms behind two-phase flow dynamics

As mentioned in the introduction, the liquid fuel injection yields a complex flow, involving the gas and the liquid phases, from the nozzle injector to the area downstream of the injector. Each phase is characterized by its proper thermodynamic state and exchanges mass, momentum and energy with the other phase through its spatial limiting border with the other phase called "interface". The topology of the interface is therefore a paramount aspect to take into account in two-phase flow modeling.

The shape of the interface, its curvature and wrinkles, in brief its complexity are driven by the competition between surface tension and strain, characterized through a Weber number. Weber numbers compare the dynamic forces to surface ones, as estimated by the surface tension $\sigma_{l,g}$. Such comparison can either resort to a liquid Weber if dynamic forces on the interface are mostly provoked by the motion of the liquid as in case during the primary atomization process:

$$\mathsf{We_l} = \frac{\rho_l L \mid \boldsymbol{u_l} - \boldsymbol{u_g} \mid^2}{\sigma_{l,g}} \tag{2.1}$$

or to an aerodynamic Weber number if the liquid topology is mainly driven by the impact of the gaseous flow, observed in the secondary atomization process

$$\mathsf{We_g} = \frac{\rho_g L \mid \boldsymbol{u_l} - \boldsymbol{u_g} \mid^2}{\sigma_{l,g}}, \tag{2.2}$$

with L is a characteristic length of the interface, ρ_l and ρ_g are densities for the liquid and gas phases respectively and $\boldsymbol{u_l} - \boldsymbol{u_g}$ represents the velocity difference between the phases [98, 51, 159]. These Weber numbers characterize the density of interface at equilibrium as regards surface tension and dynamic efforts. So they reflect the intensity of the atomization process and therefore its multi-scale character. $\mathsf{We_l}$ and $\mathsf{We_g}$ play a similar role

for atomization as the Reynolds number Re does for turbulence, indicating the number of relevant degrees of freedom of the system. Weber numbers are static criterions i.e accounting for the interface equilibrium; whereas the interface dynamics come down to the value of the Ohnsorge number Oh:

$$\mathsf{Oh}_l = \frac{\mu_l}{\sqrt{\sigma_{l,g}\rho_l L}}, \tag{2.3}$$

implying the dynamic viscosity μ_l of the liquid material and which relates the viscous forces to surface tension ones.

Yet the interface is not enough to determine the two-phase flow characteristics. The volume occupied by each phase as well as the mass partition are some other required parameters in qualifying the two-phase flow regimes. In fact, if the control volume $\mathcal{V}_c$ is the total volume occupied by both phases and $\mathcal{M}_c$ is the total mass associated to $\mathcal{V}_c$, the volume fraction α_i and the mass fraction $\Phi_{\mathsf{m}i}$ of the phase denoted through the index i are given as:

$$\alpha_i = \frac{\mathcal{V}_i}{\mathcal{V}_c}, \qquad \Phi_{\mathsf{m}i} = \frac{\mathcal{M}_i}{\mathcal{M}_c}, \tag{2.4}$$

with $\mathcal{V}_i$ and $\mathcal{M}_i$ are respectively the volume and the mass of the phase i.

As a conclusion of this brief introduction on mechanisms driving two-phase flows, let us mention the following definitions. When the interface is complex and none of the two phases has a remarkable geometry, the flow is said to be separate-phase. On the contrary, if the liquid-phase is diluted enough -i.e. with not too high a volume fraction α- to allow distinct packets to form and the flow is smooth enough for the packets to be spherical, this regime is referred to as disperse and the droplets phase is the disperse phase. Figure 2.1 illustrates separate and disperse flow zones in the injection proces.

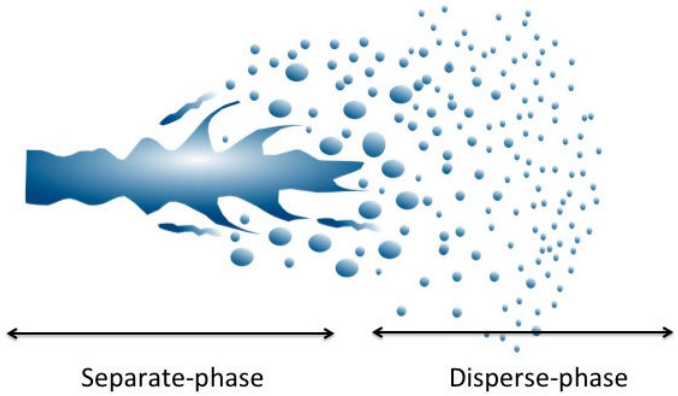

Figure 2.1: *Illustration of separate and disperse phases in the injection flow [51]*

2.1.2 Separate-phase

During the injected liquid core breakup processes in ICE, the interface between the liquid and the gas is complex and none of the two phases has a remarkable geometry. Therefore,

the flow is said to be separate-phase. The increase of the interface density under specific flow conditions, is referred to as atomization: Let us discuss for now only the main aspects of atomization, in the context of the present overview. The liquid Weber number $\mathsf{We_l}$ is the key parameter of primary atomization and the aerodynamic Weber number $\mathsf{We_g}$ rather describes secondary breakup.

The completion of the atomization process results the formation of a disperse phase flow. The modeling of pure disperse flows is eased by the fact that the interface topology is fixed, that is both aerodynamic Weber number $\mathsf{We_g}$ and Ohnsorge number Oh_l are very low. This accounts for dealing with the cloud of droplets inside the gas. Yet both inclusions and complex interfaces simultaneously appear, typically during the atomization process itself, it is remarkably difficult to account in detail for the separated phase domain and to account efficiently for the spray regime. The modeling of such transition is a key point in mastering many separate-phase flows [83], especially those where atomization is expected and where the resulting disperse phase is the desired final state, e.g. for combustion. Yet the aim of the present manuscript is limited only to the disperse phase modeling, which is essential to be correctly simulated to provide a future link with such transition zones. In the following, we therefore focus on pure disperse flows, that is after the secondary break-up process.

2.1.3 Disperse-phase

The pure disperse-phase flow regime corresponds, in the classification established in [133], to a liquid volume fraction α_l, going from $\alpha_l < 10^{-3}$ associated to a dilute regime to $\alpha_l = 10^{-2}$, limit where it begins to be moderately dense. Moreover, the aerodynamic Weber number $\mathsf{We_g}$ is small enough for droplets to remain spherical. This regime is referred to as disperse and the non continuous phase is the disperse phase. Although the liquid interface is not anymore a critical point determining the flow regime, there are other complicated physical mechanisms, which impact flow dynamics: because the material density of the liquid inside droplets is much bigger than the carrier gas density, the low droplets volume fraction is balanced by the liquid mass fraction $\mathsf{\Phi_m}$. This implies strong two-way interactions between phases in terms of mass, momentum and energy transfers. Moreover, collisions between droplets occur in moderately dense zones of the flow leading even to more complicated physics. The limit of these flow regimes are presented in [7].

2.1.3.1 Basic disperse-flow regimes

Within the dilute limit assumption made here, the dynamics of a gas-droplet flow is ruled by two major effects.

First, droplet-droplet collisions may occur in a two-phase flow, depending on the collision frequency. The flow can then be parameterized by the Knudsen number Kn

$$\mathrm{Kn} = \frac{\tau_c}{\tau_g}, \tag{2.5}$$

with τ_c is the collision time of droplets and τ_g is the gas-phase characteristic time. This number represents the importance of droplet-droplet collisions relative to free transport,

and is the equivalent of the Knudsen number defined from the gas kinetic theory [170]. Therefore, the flow behavior is characterized by Kn such as in the gas kinetic theory. The particle flow can be considered as a continuous flow as long as Kn ≤ 1. On the contrary, when Kn > 0.1, the rate of collisions is not significant enough to ensure that the flow is at equilibrium, i.e the velocity distribution function is Maxwellian, or at a state close to equilibrium.

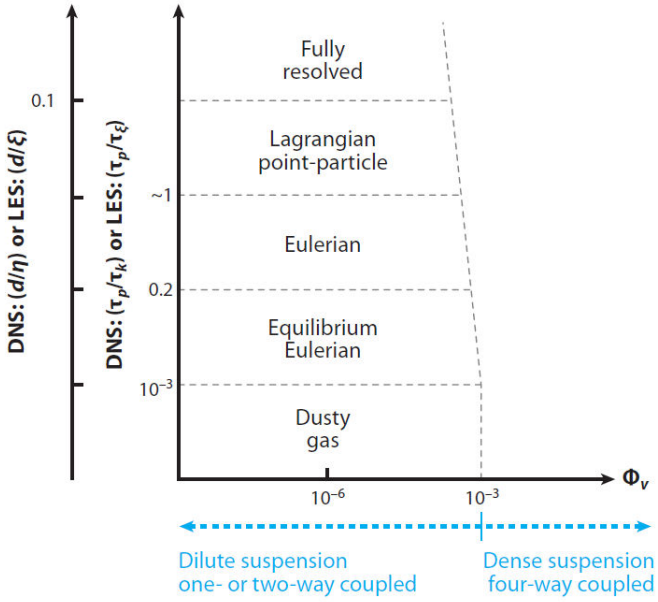

Figure 2.2: *Disperse-phase modeling hierarchy characterized through the volume fraction (horizontal axis) and the ratio of the droplet characteristic length or time scale over the gaseous characteristic turbulent length or time scale (vertical axis) [7].*

Secondly, the drag is the leading phenomenon intervening in disperse phase flow, which is the major actor allowing the distribution of droplets inside the combustion chamber. There are two main dimensionless numbers characterizing this behavior: the Stokes number St and the droplet Reynolds number Re_d.
The Stokes number expressed as:

$$\mathsf{St} = \frac{\tau_d}{\tau_g}, \tag{2.6}$$

with τ_d is the dynamic time scale associated to a droplet of size in surface S, represents the response of a droplet to a change inside a gas flow. If the Stokes number is small enough ($\mathsf{St} \leq 1$), the droplets will have nearly the same velocity as the gas. On the other hand, for large Stokes numbers, droplets barely feel the gas, so that their trajectory is hardly influenced by the gas. This issue will lead to the phenomenon called *particle trajectory crossing* PTC, which will be further discussed in 2.1.3.3. For an isolated droplet in a uniform gas, the droplet Reynolds number determines the net force of the gas on the droplet and expressed as:

$$\mathsf{Re}_d = \frac{\rho_g S^{1/2} \mid \boldsymbol{u_g} - \boldsymbol{u} \mid}{\sqrt{\pi}\mu_g}, \tag{2.7}$$

where $\boldsymbol{u}$ is the droplet velocity. Re_d is important to characterize the flow regime around a droplet. A finite particle with a diameter greater than the smallest length scale (Kolmogorov scale) of the continuous flow can modulate the turbulence of the fluid in the vicinity of its interface through a wake effect. Otherwise if the particle diameter is smaller than the Kolmogorov length scale, it is a point particle and the fluid flow around it will not be influenced by the motion of the particle. Let us also remind that even if a particle has a smaller diameter than the smallest fluid length scale, its high inertia can lead a Stokes number greater than 1. All these regimes of particles are important in choosing the right disperse-phase models, illustrated in Figure 2.2, but also discussed further in section 2.2.

2.1.3.2 Polydispersity

As far as the disperse-phase topology is concerned, various sizes of droplets determine the flow regime. In fact, both phases and droplet-droplet interactions are governed by the size. Characteristic time scales of physical phenomena occurring in the disperse-phase are therefore driven by the size. For instance, the Stokes number St, depending on size through dynamic time scale τ_d, previously given in Eq.(2.6) is one of the parameters influencing the velocity relaxation between the continuous phase and droplets. Yet one can also define other Stokes numbers in case where droplet evaporation and heating, determining the mass and heat exchanges between phases, are governing physics:

$$\mathsf{St}_v = \frac{\tau_v(S)}{\tau_g}, \qquad \mathsf{St}_\Theta = \frac{\tau_\Theta(S)}{\tau_g} \tag{2.8}$$

with τ_v the evaporation time scale and τ_Θ the thermal relaxation time scale, depending on size. The strength of polydispersity and the ways to quantify it depend on the application, but for internal combustion engine applications considered here, it has a crucial impact on the equivalence ratio, which conditions the combustions regime and the pollutant formation.

2.1.3.3 Particle Trajectory Crossings (PTC)

Particle trajectory crossings (PTC), are linked to the ability of droplets to have significantly different velocities in a same region of the flow. As the droplets tend to correlate their velocities at different rates according to their size in a given flow, it is natural to expect a major influence of size: while all the very small droplets have the gas velocity, small, medium and large droplets have a velocity depending on their size so that they do cross if their sizes are significantly different. This is referred to as *hetero-PTC* i.e. PTC at different sizes [39]. In addition, medium and large droplets may encounter crossings even for droplets of the same size, which is referred to as *homo-PTC*, PTC at same size [39]: this is due to the fact that medium and large droplets are defined to take a large time compared to that of the gas to correlate their velocities so these correlations weakly or never occur.

2.2 Modeling approaches for disperse-phases

Disperse two-phase flows can be modeled with different levels of detail, which we present from the most detailed, microscopic, to the coarsest, macroscopic ones. First, we briefly present the so-called DNS at the particle level methods that can be used for separate-phase flows as well: they prove to yield too much detail and to be costly for a full ICE computation. We then present the so-called Discrete Particle Simulation that provides a less detailed description but sometimes too costly for industrial computations. Afterwards, two-fluid models, that give a macroscopic, volume average description of disperse-phase but also widely used for interfacial two-phase flows will be discussed. The latter approach being considered not to be well adapted for the polydipersity modeling, we finally focus on kinetic modeling of the disperse-phase.

2.2.1 Direct numerical simulation at the particle level

2.2.1.1 Sharp interface tracking method

The starting point of the derivations to obtain microscopic models, which describe all scales within each phase and the two-phase flow topology in the vicinity of inter-phases, requires to write down the following single fluid conservation equations for each of two phases:

$$\partial_t \rho\phi + \nabla_{\boldsymbol{x}} \cdot (\rho\phi \mathbf{u}) = \nabla_{\boldsymbol{x}} \cdot \psi + S, \tag{2.9}$$

where the successive values of ϕ, ψ and S are given in the table 2.1: These equations are

Table 2.1: expressions for variables arose in Eq.(2.9)

ϕ	1	$\mathbf{u}$	$E = e + 1/2\mathbf{u}^2$
ψ	0	$\text{-}\mathbf{T} = -PI + \tau$	$\text{-}\mathbf{T}.\mathbf{u} + \mathbf{q}$
S	0	$\mathbf{F}$	$\mathbf{F}.\mathbf{u}$

valid in the interior of each phase. Here ρ denotes the density, $\boldsymbol{u}$ velocity, T the stress tensor, and $\mathbf{F}$ the body force density. One can directly solve the local instantaneous equations presented above in the context of DNS. Moreover, the position of the interface and associated discontinuities of properties across the interface must be solved accurately to impose satisfactory boundary conditions for both fluid domains [159]. In the literature, various sharp interface tracking or resolution methods have been designed to capture interfaces. These methods rely on techniques such as Volume of Fluid (VOF), Level Set, Ghost Fluid, or a combination of these techniques. Recent advances can be found in [202, 70, 17, 76]. At this level, since all the flow details are solved, there is no distinction between the disperse-phase and the separate-phase.

2.2.1.2 Fluid DNS around solid bodies

The principle of this second type of full DNS approach is to solve for a fluid around solid (not deformable) bodies: the method is sometimes referred to as Fully Resolved Simulation in the context of solid particles [5] but can also be used for a disperse liquid at low We_g.

The solid bodies can be fixed or may move depending on the forces from the surrounding flow. The treatment of the solid bodies is done with appropriate boundary conditions e.g. they are meshed or immersed boundary conditions are applied [197]. This approach can be used to solve the settling of a group of particles/droplets, as the interaction of particles through their wakes generates a long range interaction and modifies the physical properties of the system (settling velocities). This approach is costly, its cost increasing linearly with the number of particles. A less detailed approach should be considered except when the modeling effort is important.

2.2.1.3 Concluding remarks on DNS methods for the disperse-phase

Full DNS approaches are used to capture complex physics: they notably allow to render group effects [34], for instance, in group combustion which arises in specific conditions and where the flame structure and the overall dynamics is strongly linked to the organization of the cloud and its evolution at large scale [165]. The issue of group effects is also present in other domains such as in sedimentation modeling [181] and crowd modeling [121]. For all these group effects, the resolution of the flow at the level of each particle is required as it strongly differs from that of a single particle and it has an influence on macroscopic dynamics. Besides, the exact numerical resolution of interfaces is still a research topic, especially for the purpose of DNS computations to improve and validate models and correlations, mesoscopic approaches. Yet it is unfortunately very difficult to solve for a macroscopic system with a full DNS approach, regarding the high cost of the methods, so these methods are not considered for our problem.

2.2.2 Discrete Particle Simulation (DPS)

This method looks like the *DNS around solid bodies* except that the effect of particle volume occupation on the surrounding fluid flow is not resolved [135, 154, 203] and the fluid particle interactions are modeled under the form of a point particle assumption global exchange. This means that each particle is tracked separately through ordinary differential equations (ODE) on its internal variables which can contain the effects coming from the surrounding continuous fluid phase (i.e. mass, momentum, heat transfer) and other particles (i.e. collision, coalescence), the effect of return of particles can be taken into account at this level through specific collision detection algorithms [177, 42]. In case of the two-way coupling, the mass, momentum and heat-transfer effects of the particles on the fluid phase are taken into account through source terms in conservation equations Eq.(2.9). Most of the first numerical studies were dedicated to solid particle dispersion [168, 52]. The extension to evaporating droplets in turbulent flows has been provided in [111, 148, 127], and has been used in combustion applications in [110, 151, 128].

In the context of simulations through industrial tools where a very high number of particles is involved, tracking each particle through DPS approach can be costly. Yet let us precise that, one of widely used Stochastic Lagrangian method, further discussed in section 2.3, provides a coarser resolution of DPS approach [46]. The latter is widely adapted for the coupling with the continuous phase modeled through RANS or LES.

2.2.3 Two-fluid reduced models

So far in this section, we have focused on detailed resolution techniques of disperse-phase flows. As conclusion, we have clarified that, details on the disperse-phase flow are not required and not adapted for computations through industrial codes. In that case, the use of volume averaged models can be considered as a promising option. The averaging process is performed on a volume large enough to contain both phases, and small enough compared to the length scales desired to be solved [132]. A number of macroscopic quantities are then accounted for with distinct Eulerian conservation equations. So the two phases are described as fluids that virtually coexist, for all the quantities are defined at every location in space. Averaging approach generates closure problems as transfer terms within the averaging volume have macroscopic effects that should be taken into account, so that models are required for closure. Let us recall that some authors provided closures through preliminary detailed studies on a single particle level [2, 160] which make easier closures for disperse phase flow modeling through averaged methods [186].

There are mainly two different approaches employed to obtain averaged equations. A first approach involves applying an averaging operator directly to the local conservation system defined through (2.9). In the averaging process, the various terms appearing in the macroscopic equations are shown to arise from appropriate microscopic considerations. This method is used for example by authors such as Ishii [82] or Delhaye [32]. However, this technique bypasses the discrete nature of the two-phase flow since it does not provide a complementary equation on the volume fraction α which is crucial in determining the probable volume occupied by each phase. In the other approach, the notion of phase function is introduced. It follows the instantaneous interface between the two phases and is thus convected by the instantaneous interface velocity. Conservation laws are determined for each phase and they account for the exchanges of mass, momentum and energy between phase. Closures are provided through a thermodynamic analysis of the resulting system. This approach is used for example in [6]or in [107] and is taken up by authors such as in [157, 158].

In the context of ICE simulations at IFP Energies nouvelles, the latter technique based on the volume fraction equation along with the surface density approach has been used to describe liquid atomization [104, 105] and disperse-phase modeling [186] dedicated to the modeling for the dense zone of the injection. Yet it has been shown that the polydispersity character of droplets is poorly captured since at a given time and position, one could only access the mean size of the distribution [186]. Taking into account the size distribution at sub-grid scale is mandatory to describe the right two-phase flow regimes. Therefore, this technique is not adapted for our problem.

2.2.4 Kinetic spray modeling

The dispersed-phase assumption for the liquid, applicable for dilute sprays with volume fraction $\alpha < 10^{-2}$, allows the use of the so-called kinetic spray model. This model is based on the Williams equation [193, 194]. Although this represents a mesoscopic level of description, it is called kinetic by analogy with the mesoscopic kinetic theory of gases. Indeed, the assumptions made for the spray droplets [62], are similar to the ones made

for the gas molecules when deriving the kinetic model. These assumptions are recalled here. The model describes the transport of the NDF and its evolution, due to the physical phenomena like evaporation, heat transfer or particle interactions applied to the spray, as external forces. The source terms responsible for this phase space evolution of the NDF are analyzed here. Due to the above disperse-phase assumption, the liquid influence on the gas is obtained through source terms in the gas phase equations, as it was the case for DPS approach. The expressions for such source terms are provided in the framework of kinetic spray description. We present herein the framework which allows the derivation of the Williams-Boltzmann Equation (WBE) for spray, see for example [193, 194].

2.2.4.1 Fundamental assumption

Statistical modeling relies on ensemble (or statistical) averages. The goal is to reduce the information carried by the numerous particles to the only relevant one of ensemble behaviors. Each particle, denoted by the subscript i, is described by few degrees of freedom (DoF) that evolve in time, e.g. a minima its position $\boldsymbol{x}_i(t)$ and velocity $\boldsymbol{u}_i(t)$. So the particle system has $6N$ DoFs in total and its state is exactly described by a point in a $6N$ -dimensional space called the Γ phase space with $\Gamma = \mathbb{R}^{6N}$. For classic particles encountering an external force $\boldsymbol{F}^{ext}$ per unit mass and a particle-particle interaction force $\boldsymbol{F}_{i,j}$ per unit mass that differs on the relative distance $\mid \boldsymbol{x}_i - \boldsymbol{x}_j \mid$, the equations of motion at the microscopic level read:

$$\mathrm{d}_t \boldsymbol{x}_i(t) = \boldsymbol{u}_i(t), \tag{2.10a}$$

$$\mathrm{d}_t \boldsymbol{u}_i(t) = \boldsymbol{F}^{ext}(t) + \sum_{\substack{j=1 \\ j \neq i}}^{N} \boldsymbol{F}_{i,j}(t). \tag{2.10b}$$

We want to avoid describing all the details of the system and, instead, to follow some of the quantities that emerge at the macroscopic scale. These quantities define a state at the macroscopic level and they are not as numerous as the micro-DoFs. So a macroscopic state can be reached thanks to many different underlying microscopic configurations [143]. We now focus only on these macroscopic variables: we compute them as ensemble averages, i.e. an average over many copies of the initial system, possibly evolving differently at the microscopic scale, but similarly at the macroscopic scale: this idea, due to Gibbs, allows to smooth out the undesired fluctuations from the temporal behavior of the macroscopic quantities. The number of ensembles to consider is large enough for the microscopic state points to be dense in Γ. We thus adopt a statistical point of view, introducing a multiple-particle joint distribution function $f^N\left(t, x_1, x_2, \cdots, x_N, u_1, u_2, \cdots, u_N\right)$. The evolution of an N -particle system is then given by the Liouville equation for the NDF in $6N$ phase space:

$$\partial_t f^N + \sum_{i}^{N} \boldsymbol{u}_i \cdot \partial_x f^N + \sum_{i=1}^{N} \left(\boldsymbol{F}_i^{ext} + \sum_{\substack{j=1 \\ j \neq i}}^{N} \boldsymbol{F}_{i,j} \right) \cdot \partial_{\boldsymbol{u}_i} f^N = 0 \tag{2.11}$$

which originates from the conservation of the number of points in Γ and renders all the microscopic evolution equations of System (2.10). In practice the dimension of f^N is huge (it might be infinite) and one has to come up with a reduced (or contracted) description. Varying the number of particles retained in the state vector Γ, a reduced description is given by the classical BBGKY hierarchy (the initials are those of the authors who derived it independently: Bogoliubov, Born, Green, Kirkwood and Yvon) [21, 103]. It consists of transforming the Liouville equation into a chain of equations in which the first equation connects the evolution of one-particle PDF f^1 to the two-particle PDF f^2 , the second equation connects f^2 to f^3 and so on. The system is an exact approach to the Liouville equation. It is therefore redundant but it is practical to build approximations by truncation of the chain when some particle correlations are neglected. The most celebrated example of the utility of the BBGKY hierarchy consists in closing the first equation of the hierarchy by assuming:

$$f^2\left(t, \boldsymbol{x}_1, \boldsymbol{x}_2, \boldsymbol{u}_1, \boldsymbol{u}_2\right) = f^1\left(t, \boldsymbol{x}_1, \boldsymbol{u}_1\right) f^1\left(t, \boldsymbol{x}_2, \boldsymbol{u}_2\right) \tag{2.12}$$

which means that the particles are totally uncorrelated. The BBGKY hierarchy is then entirely defined by the knowledge of a one-particle Probability Density Function (PDF) f^1 evolving in a 6-dimensional space called -phase space according to the equation:

$$\partial_t f^1 + \boldsymbol{u}_1 \cdot \partial_x f^1 + \boldsymbol{F}_1^{ext} \cdot \partial_{\boldsymbol{u}_1} f^1 = -\int \boldsymbol{F}_{1,2} \cdot \partial_{\boldsymbol{u}_1} f^1\left(t, \boldsymbol{x}_1, \boldsymbol{u}_1\right) f^1\left(t, \boldsymbol{x}_2, \boldsymbol{u}_2\right) \mathrm{d}\boldsymbol{u}_2 \mathrm{d}\boldsymbol{x}_2 \tag{2.13}$$

The number density function (NDF) f, obtained by summing the one-particle PDF in order to describe N indiscernible particles [192]: $f = \sum_i^N f^i$. Its phase space variables are $\boldsymbol{x}$ et $\boldsymbol{u}$. Similarly to Eq.(2.13) for the evolution of f^1, the Williams-Boltzmann equation is classically used to describe the transport of NDF function.

2.2.4.2 Williams-Boltzmann Equation (WBE)

According to the kinetic spray modeling through Williams-Boltzmann equation (WBE), each droplet is assumed to be spherical, and is characterized by the unique size and temperature variables. Moreover, its velocity is defined at its mass center. The entire information of the disperse phase is included in the number density function (NDF) $f\left(t, \boldsymbol{x}, S, \boldsymbol{u}, T\right)$ so that:

$$\partial_t f + \nabla_{\boldsymbol{x}} \cdot (\boldsymbol{u} f) - \partial_S\left(R_S f\right) + \nabla_{\boldsymbol{u}} \cdot (\boldsymbol{F} f) + \partial_T\left(Q f\right) = \mathfrak{B} + \mathfrak{C} \tag{2.14}$$

is at time t the probable number of droplets at a location $\boldsymbol{x}$ in a d$\boldsymbol{x}$-neighborhood of $\boldsymbol{x}$, with a velocity $\boldsymbol{u}$ in a d$\boldsymbol{u}$-neighborhood of $\boldsymbol{u}$, with a temperature T in a dT-neighborhood of T, and with a size parameter in surface S in a dS-neighborhood of S. The velocity $\boldsymbol{u}$ is sometimes decomposed in Cartesian components $\boldsymbol{u} = (u_1, u_2, u_3)^T$. If d$\boldsymbol{x}$ is an elementary volume of the physical space, the infinitesimal volume d$\boldsymbol{u}$dTdS is an elementary volume of the phase space. The kinetic equation or Williams-Boltzmann equation or sometimes called Generalized Population Balance Equation simply expresses that the total derivative of the NDF is due to integral source terms [193]: that are break-up $\mathfrak{B}$, usually depending linearly on f, and collisions $\mathfrak{C}$, usually depending quadratically on f. The modeling effort also consists in closing the different rates of change:

- $\boldsymbol{F} = \mathrm{d}_t \boldsymbol{u}$ is the acceleration applied on droplets per unit mass,
- $Q = \mathrm{d}_t T$ is the rate of change of droplet temperature due to heat transfer,
- $R_S = -\mathrm{d}_t S$ is the rate of change of the size S of droplets, or evaporation term,
- $\mathfrak{C}$ is the rate of change of distribution function f due to collisions,
- $\mathfrak{B}$ is the rate of change of f through particle formation by secondary break-up process.

2.2.4.3 Source term closure models

Drag model

Among all the terms contained in the term of force applied by unit mass $\boldsymbol{F}$ (gravity and buoyancy effects, drag force, virtual mass effect, Basset force, lift force) described in [30], we will focus on the drag term. Indeed, as shown in [45], in a gas-liquid flow, where the ratio of the gas-phase mass density over the liquid-phase mass density inside droplets is of the order of 10^{-2} down to 10^{-3} , the only external forces that need to be accounted for are drag force and gravity. Furthermore, in order to work in a simple modeling framework, we neglect gravity in the studies presented in this work. Through the basic Stokes law assumption [169], the drag force is commonly expressed in function of the droplet dynamic time scale and the velocity difference between the surrounding gas-phase and droplet

$$\boldsymbol{F}\left(t, \boldsymbol{x}, \boldsymbol{u}, S, T\right) = \frac{1}{\tau_d}\left(\boldsymbol{u_g}\left(t, \boldsymbol{x}\right) - \boldsymbol{u}\right), \qquad \tau_d = \frac{\rho_l S}{18\pi\mu_g}. \tag{2.15}$$

with $\boldsymbol{u_g}$ is the gas-phase velocity, ρ_l the liquid mass density and μ_g is the gas-phase dynamic viscosity. Stokes law is correct as far as $\mathsf{Re}_d < 1$. Otherwise, the flow around the droplet renders the convection effects dominants, that is some correction models such as [160] are required for an accurate drag dynamics.

Evaporation and heating model

Theoritical derivation of the evaporation and the heat transfer coefficients are detailed in [30]. These coefficients are modeled, based on the film theory around an isolated droplet [165]. Let us now present their common expressions as:

$$R_S\left(t, \boldsymbol{x}, \boldsymbol{u}, S, T\right) = 4\pi\frac{\rho_g}{\rho_d}\mathrm{Sh_c} D_{Y_F} \ln\left(1 + \mathrm{B_M}\right) \tag{2.16}$$

and

$$Q\left(t, \boldsymbol{x}, \boldsymbol{u}, S, T\right) = 6\pi\frac{\rho_g}{\rho_d S C_{p,l}}\mathrm{Sh_c} D_{Y_F} \ln\left(1 + \mathrm{B_M}\right)\left(\frac{C_{p,g}\left(T_g(\infty) - \left[T\right]_s\right)}{\mathrm{B_T}} - \mathrm{L}_v\right) \tag{2.17}$$

with ρ_g the gas density, $T_g(\infty)$ the gas temperature beyond the diffusive thermal boundary layer, $\left[T\right]_s$ the temperature at the droplet surface, $C_{p,g}$ the gaseous specific heat capacity at constant pressure, ρ_d the liquid density, $C_{p,l}$ the liquid specific heat at constant pressure, D_{Y_F} Fick's law binary diffusion coefficient, L_v the latent heat of vaporization, $\mathrm{Sh_c}$

the convective modified Sherwood number, $\mathrm{B_M}$ the spalding dimensionless mass transfer number and $\mathrm{B_T}$ the spalding dimensionless heat transfer number. Let us give expressions for spalding dimensionless transfer numbers and the relation between them,

$$\mathrm{B_M} = \frac{[Y_F]_s - [Y_F]_\infty}{1 - [Y_F]_s}, \qquad \mathrm{B_T} = \frac{\rho_g u_s C_{p,g}}{h_c}, \qquad \mathrm{B_T} = (\mathrm{B_M} + 1)^{\frac{\mathrm{Sh_c}}{\mathrm{Nu_c}} \frac{\mathrm{Sc}}{\mathrm{Pr}}} \tag{2.18}$$

with $[Y_F]_s$ the fuel mass fraction at the droplet surface, $[Y_F]_\infty$ the fuel mass fraction beyond the diffusive mass boundary layer, h_c the convective modified heat transfer coefficient, $\mathrm{Nu_c}$ the convective modified Nusselt number, Sc the Schmitt number, Pr the Prandtl number. According to the film theory, the convection prompted by the relative velocity between the gas and the droplet reduces boundary layers around the droplets. Therefore some correction models on Sherwood and Nusselt numbers have been proposed in the literature [2, 165, 56, 26] and reviewed in [30].

2.3 Resolution strategies for the kinetic disperse phase modeling

Let us, in this section, discuss on the choice of the resolution method for the disperse-phase among two available approaches. The first and widely adopted choice for spray resolution method is a Stochastic Lagrangian method where we track particles in the flow. Lagrangian methods consist in tracking statistical particles in connection either with kinetic equation (2.14) or physical droplets modeled through DPS approach. On the other hand, Eulerian approach provides an alternative and promising solution to Lagrangian techniques for the resolution of the kinetic equation (2.14).

In the reminder of this section, let us first present stochastic-Lagrangian and then Eulerian methods before concluding on our choice for the present thesis.

2.3.1 Stochastic-Lagrangian resolution

The stochastic-Lagrangian description has been introduced in two different contexts.

- On the one hand it has been developed to supply DPS in configurations where the high number of physical droplets prevents to use one numerical particle for each droplet, given the high computational cost associated. In this framework, each numerical particle, also called parcel, represents several physical droplets. This approach has been first described in [28] and introduced for fuel spray and referred to as Stochastic Parcel (SP) in [133], extending the work of [46]. This method is referred in [29] as the discrete element method, and as a multi-continua method in [165], where the parcels are defined as classes of droplets. The computational cost of this method is obviously linked to the chosen number of tracked parcels: the SP method aims at coarsening the DPS description and the number of statistical parcels is thus set by the computational cost limitation, without drawing any links with kinetic level of description. The cost of the method is thus well controlled, and

it is therefore broadly used to compute industrial configurations but its rigorous meaning is doubtful.

- On the other hand, the stochastic-Lagrangian method can be seen as a resolution method of the Williams-Boltzmann kinetic Eq. (2.14) as stated by [172]. This approach is called Direct Simulation Monte Carlo (DSMC) method and is also introduced for rarefied gas in [11]. This approach aims at describing the evolution of the spray NDF moments, and thus a high number of statistical particles [171] are needed to obtain a converged solution. The numerical particle has a weight associated, adapted to the needed refinement: this weight is a real number so a numerical parcel may represent a fraction of physical droplet. This method provides directly the ensemble average, in terms of initial condition, and then the reconstructed Eulerian fields correspond to the same level of information than the one provided by a Eulerian method.

In cases without collision, the difference between the two methods, is only the level of refinements provided. Indeed, the convergence expected in the DSMC method demands a high number of statistical particles, leading to a higher refinement level than in DPS. On the contrary, the SP method aims at coarsening the DPS description. The number of statistical parcels is thus set by the computational cost limitation, without drawing any links with kinetic level of description. Stochastic-Lagrangian methods are implemented for instance in the KIVA II code [4] and in the IFP-C3D code [12] and are used in many industrial computational codes at present [81, 156, 36, 35].

2.3.2 Shortcomings of Lagrangian methods

To solve a disperse two-phase flow, the stochastic-Lagrangian approach is often coupled to a Eulerian approach for the carrier gas phase: we refer to this strategy as Euler-Lagrange. At present, SP methods are widely used for the disperse-phase simulation since they combine an easy modeling of the phase polydispersity and particle trajectory crossings (PTC), a high numerical efficiency, not introducing numerical diffusion, and an easiness of implementation. Nevertheless, they suffer from some shortcomings, in terms of modeling and computing. These shortcomings can be listed as follows:

- In some cases, the solution is impacted by the number of Lagrangian parcels used for the computations. In case where this number is not enough to obtain a converged solution, a statistical noise is observed. Convergence can be evaluated by performing several realizations with the same initial and boundary conditions and comparing the deviation of the solution according to the number of parcels used. However, convergence studies are rarely performed for industrial computations due to the limitations on resources.

- Accounting for two-way coupling with an Euler-Lagrange raises two issues.

  - First, the ODEs for the parcels are no longer independent but coupled through the gas equations. The quantities must ideally be relaxed simultaneously for all

the particles at a given location and for the underlying gas, the latter transmitting information at the velocity of its fastest eigenvalue to the surrounding gas and parcels. Numerical procedures rarely achieve such strong coupling, since it is interesting to keep the ODEs as decoupled so that splitting-like techniques are employed. This can compromise the accuracy of two-way coupling which is achieved with dedicated methods at the cost of additional efforts [16].

– Second, in a high performance computing context, possibilities of vectorization/parallelization or implicitation are limited for Euler-Lagrange simulations. The particle load balance is particularly difficult to achieve [71]. The parcels must indeed often communicate with the underlying fluid but they move in the domain in a way that is difficult to predict (at least for the load balance algorithm). As a result parcels that are computed by a given CPU must be dispatched to other ones according to a complex process, which does not comply with efficiency requirements of parallel architecture.

2.3.3 Eulerian resolution

Instead of discretizing all the kinetic degrees of freedom (DoFs) with parcels as in the stochastic-Lagrangian approach, we can resolve spray Eulerian conservative quantities, as number or mass density, momentum. These Eulerian methods can be seen as moment methods derived from the kinetic equation Eq.(2.14).

2.3.3.1 Derivation of the Eulerian model

The full resolution with finite volume of the kinetic equation, Eq.(2.14) can difficultly be used given its cost related to the high number of phase space dimensions. Indeed in a 3-D case, the phase space is of dimension eight (3 for space, 3 for velocity, 1 for size, 1 for temperature). Nevertheless, in many cases the knowledge of the full kinetic description of the spray is not needed, and it is sufficient to know the evolution of global quantities, the NDF moments. For an arbitrary function $\psi(y)$, the k th order moment m_k is defined by

$$m_k = \int y^k \psi(y) \mathrm{d}y. \tag{2.19}$$

Therefore, for the NDF we introduce the moment $\mathcal{M}$

$$\mathcal{M}_{l,n,i,j,k} = \int_S \int_T \int_{\boldsymbol{u}} S^l T^n u_x^i u_y^j u_z^k \; f\left(t, \boldsymbol{x}, \boldsymbol{u}, S, T\right) \; \mathrm{d}S \; \mathrm{d}T \; \mathrm{d}\boldsymbol{u}, \tag{2.20}$$

of order l in size, n in temperature, (i, j, k) for each component of the velocity, respectively. The evolution of these spray global quantities can therefore be derived from the Williams kinetic equation Eq.(2.14), in the following way:

$$\int_S \int_T \int_{\boldsymbol{u}} S^l T^n u_x^i u_y^j u_z^k \; \text{Eq. (2.14)} \; \mathrm{d}S \; \mathrm{d}T \; \mathrm{d}\boldsymbol{u}. \tag{2.21}$$

2.3.3.2 Bottleneck issue for Kinetic based Eulerian methods

One has to notice that the moment equation derivation leads to a loss of information and that, without any peculiar assumption, the system of equations for moments is not closed, even if the kinetic model was. Indeed, some quantities can not be expressed in function of the set of moments resolved; for example with regard to velocity moments, the equation for the pth order moment (with $p = i + j + k$) introduces the moments of order $p + 1$. Therefore taking one first order moment $\mathcal{M}_{0,0,1,0,0}$ introduces the second order moments $\mathcal{M}_{0,0,2,0,0}$, $\mathcal{M}_{0,0,1,1,0}$, $\mathcal{M}_{0,0,1,0,1}$. Assumptions have then to be done on the form of the NDF to close the moment evolution system. Therefore, there are two major strategies in the literature.

- For some of the spray Eulerian methods, the derivation of the moment system, along with its associated closures can be divided into two steps. First a form for the NDF in velocity and in temperature is presumed for each fixed size as follows:

$$f\left(t, \boldsymbol{x}, T, S\right) = n\left(t, \boldsymbol{x}, S\right) \phi_{\boldsymbol{u}}\left(t, \boldsymbol{x}, \boldsymbol{u}, S\right) \phi_T\left(t, \boldsymbol{x}, T, S\right) \tag{2.22}$$

  where $\phi_{\boldsymbol{u}}$ and ϕ_T are the presumed PDF in velocity and temperature, that are assumed independent of temperature and velocity, respectively. The variable n is the number density of the spray. This leads to the derivation of an intermediate closed system of conservation laws, the semi-kinetic system. The second step is devoted to the size-phase space treatment, there exist several methods introducing different types of system of conservation laws and closures.

- However, we can also find methods using quadrature-based approximations for the NDF, obtaining the unclosed moments by quadrature formula.

2.3.4 Conclusion about the resolution technique adopted for ICE applications

As discussed before, for reliable combustion applications, the project of IFP Energies nouvelles is to resolve the direct injection of the fuel, from upstream to far downstream of the injector. Yet this requires to resolve both the dense and dilute zones of the injection. So far, the discussion on resolution strategies has been conducted for the disperse-phase zone, which is treated either through Lagrangian or Eulerian approaches. Let us also remind that due to complex interfaces between phases, the resolution for the separate-phase zone is achieved through Eulerian description.

For a complete resolution of the injection, there are basically two main strategies. Either one resolves the disperse-phase zone through Lagrangian Stochasic method and couple it to a Eulerian model dedicated to separate-phase zone description, or the complete injection is fully described through Eulerian methods. In both cases, the transition zone, where both complex interfaces and droplets are simultaneously present, is required to be well treated. Through the development of the technique called Eulerian-Lagrangian Spray Atomization (ELSA) conducted in [33], involving a Stochastic Lagrangian method for the disperse-phase and a Eulerian interfacial flow model based on the work [183], an

interesting development of a transition zone has been achieved. Yet we believe that a full Eulerian description of the injection will help us to be more consistent for the development of such transitions. In the present PhD thesis, we hereafter focus on Eulerian methods for disperse-phase resolution.

But if Eulerian models appear to be a potential answer to the shortages of Lagrangian methods, they nevertheless face difficulties in treating the polydispersity. As mentioned previously, this issue along with the spray evaporation are the two most paramount aspects required to be accurately described for combustion applications. Treating the droplets trajectories crossings (PTC) in case of inertial droplets with high Stokes numbers is an other difficulty for Eulerian kinetic based methods. Moreover, taking into account correct turbulent interactions driving the spray-gas mixture is not straightforward issue and requires an important modeling effort.

Among existing models, there are only several Eulerian polydisperse models for evaporating droplets. Yet the issue of accurately capturing the evaporation characteristics under a reasonable CPU time remain a bottleneck problem. When it comes to turbulence disperse-phase modeling for industrial applications through Eulerian methods, most of them make use of monodisperse droplet distribution and uses different approach for modeling the particle-gas interactions. In the following of this chapter, we first discuss about Eulerian concepts which are able to predict particle trajectory crossing events. Then one moves on the Eulerian modeling strategies dedicated to predicting disperse-phase turbulence interactions. Afterwards, we will go into details on Eulerian polydisperse models for evaporating sprays.

2.4 Eulerian polykinetic modeling through kinetic based models

The common aspect of Eulerian polykinetic models is the fundamental modeling of the velocity distribution function $\phi_{\boldsymbol{u}}$ in Eq.(2.22). The basic mono-kinetic assumption for the velocity distribution that is a unique spray velocity for all droplets at a given time and position, leading a dirac δ-function $\phi_{\boldsymbol{u}} = \delta_{\boldsymbol{u}}$, has been the starting point for some Eulerian polydisperse models, discussed in section (2.6). Yet the latter approximation is not true for two-phase flows with inertial droplets in a gaseous carrier phase. In such flows the motion of droplets strongly depends on their inertia characterized by their Stokes number, based on the smallest time scale of the carrier flow which is, in case of a turbulent flow, the Kolmogorov scale or can be related to a strain rate as demonstrated by S. de Chaisemartin in his PhD [30]. For low Stokes numbers, the spray phase velocity is strongly correlated to the gas phase velocity and mono-kinetic velocity distribution is well adapted. Therefore, one can work with only velocity moments of zero and first order. Yet regimes with higher Stokes numbers St, droplets velocity are not well correlated locally with the gas velocity. This leads to an uncorrelated droplet motion either called the Random Uncorrelated Motion (RUM) [59] or the granular temperature [64]. The latter aspect drives the homo-PTC phenomenon (see part 2.1.3.3). It is important that the velocity distribution $\phi_{\boldsymbol{u}}$ locally reproduces polykinetic distribution, that is locally various velocities for same sized droplets at time t and location $\boldsymbol{x}$.

2.4.1 Modeling categories and hierarchies

The complete hierarchy of Eulerian methods, aiming at capturing homo-PTC is discussed in detail in [97]. We can divide up the Eulerian polykinetic approaches of the literature into two categories:

- Algebraic-Closure-Based Moment Methods (ACBMM): A limited set of moments, usually up to second order moments, are chosen and transported. Since their transport involves higher order moments, these missing moments are computed from the knowledge of the lower order moments through *equilibrium assumptions* inspired from RANS turbulence modeling using explicit algebraic closures [166]. One example of this class of methods introduced in [113, 115] considers and transports a unique, scalar second order moment. Other second or third order moments are then computed from the knowledge of the transported moments to get the most accurate closure at a reduced cost. This type of approach has already reached the real application level [189, 109, 152]. However it has to face local realizability problems [162], i.e. the occurrence of moments not linked to a non-negative NDF, and the design of adapted numerics is not straightforward and has never been conducted since the mathematical structure of the underlying system of Eulerian equations is not clearly identified.

- Kinetic-Based Moment Methods (KBMM): The main idea of this type of approach is to consider a set of moments for which we can associate in a one-to-one correspondence a unique kinetic velocity distribution with a sufficient number of parameters to control the given set of moments. This presumed NDF must be non negative and allows to evaluate high order moments needed in the system of moments for transport. Closures have been proposed to control moments up to second order [118, 187], up to the third order (CQMOM [198]), and up to the fourth order (Multi Gaussian [97]). Among the KBMM two categories emerge; the first is based on hydrodynamic equilibrium usually related to a given notional collision operator and the second is based on quadrature methods. The first category allows a well-defined mathematical structure and entropy inequality, whereas most of the time the second leads to weakly hyperbolic systems [20]. The main advantage with KBMM is the existence of dedicated numerical methods, which will guarantee the realizability and the stable behavior of the numerical schemes, either classical hyperbolic solvers [102, 179] or kinetic schemes [30, 198, 14].

In the following, let us be interested in KBMM rather than ACBMM methods since the former presents advantages over the latter in terms of realizability, mathematical structure and numerical scheme design. Although MG and CQMOM methods can capture a broad range of homo-PTC scales, these methods are costly due to the high number of velocity moments required to be transported. Towards the industrial applications framework, the compromise between the PTC accuracy and CPU cost can be achieve thanks to the transport of velocity moments up to second order. Let us precise that this implies that the NDF function is presumed such that third or higher order moments, naturally arising in the system derived form Eq.(2.14), are closed thanks to the lower order moments. In

that context the Eulerian polykinetic models based on the anisotropic Gaussian (AG) or the isotropic Gaussion (IG) function for $\phi_{\boldsymbol{u}}$ in Eq.(2.14) are promising.

2.4.2 Isotropic and Anisotropic Gaussian velocity closure for homo-PTC

For the sake of clarity on the methods discussed in this part, we consider a monodisperse droplet population under a constant and uniform temperature which undergoes the Stokes drag force through its one-way coupling interaction with the carrier gaseous flow. Moreover, the spatial dimension of our problem is in 2-D. Therefore, the NDF distribution presented in Eq.(2.22) reduces to the following form

$$f\left(t,\boldsymbol{x},\boldsymbol{u}\right)=\phi\left(\boldsymbol{u}-\boldsymbol{u_d}\left(t,\boldsymbol{x}\right)\right)n\left(t,\boldsymbol{x}\right) \tag{2.23}$$

where $\boldsymbol{u}=(u,v)^t$, while the kinetic equation becomes

$$\partial_t f+\nabla_{\boldsymbol{x}}\cdot\left(\boldsymbol{u}f\right)+\nabla_{\boldsymbol{u}}\cdot\left(\frac{1}{\tau_d}\left(\boldsymbol{u_g}\left(t,\boldsymbol{x}\right)-\boldsymbol{u}\right)f\right)=0. \tag{2.24}$$

The velocity distribution function is presumed through the Anisotropic Gaussian function by the following expression

$$\phi\left(\boldsymbol{u}\right)=\frac{1}{\left(2\pi\right)^{3/2}\mid\boldsymbol{\Sigma}\mid^{1/2}}\exp\left(-\frac{1}{2}\left(\boldsymbol{u}\right)^t\boldsymbol{\Sigma}^{-1}\left(\boldsymbol{u}\right)\right) \tag{2.25}$$

where $\boldsymbol{\Sigma}=\dfrac{1}{n}\displaystyle\int\left(\boldsymbol{u}-\boldsymbol{u_d}\right)\otimes\left(\boldsymbol{u}-\boldsymbol{u_d}\right)f\mathrm{d}\boldsymbol{u}$. Let us recall that, for an Isotropic Gaussian (IG) distribution, $\boldsymbol{\Sigma}$ is isotropic $\Sigma=\sigma\mathbf{I}$.

Integrating Eq.(2.24) over the velocity phase space leads to the following system of conservation laws with source terms related to the drag acceleration:

$$\partial_t\boldsymbol{\mathcal{M}}+\nabla_{\boldsymbol{x}}\cdot\boldsymbol{\mathcal{F}}\left(\boldsymbol{\mathcal{M}}\right)=\boldsymbol{\mathcal{S}}\left(\boldsymbol{\mathcal{M}}\right) \tag{2.26}$$

where the moment $\boldsymbol{\mathcal{M}}$ and fluxes $\boldsymbol{\mathcal{F}}=\left(\boldsymbol{\mathcal{F}}_1,\boldsymbol{\mathcal{F}}_2\right)^t$ take the expression:

$$\boldsymbol{\mathcal{M}}=n\begin{pmatrix}1\\u\\v\\u^2+\sigma_{11}\\uv+\sigma_{12}\\v^2+\sigma_{22}\end{pmatrix},\boldsymbol{\mathcal{F}}_1=n\begin{pmatrix}u\\u+\sigma_{11}\\uv+\sigma_{12}\\u^3+3u\sigma_{11}\\u^2v+2u\sigma_{12}+v\sigma_{11}\\v^2u+u\sigma_{22}+2v\sigma_{12}\end{pmatrix},\boldsymbol{\mathcal{S}}=\frac{n}{\tau_d}\begin{pmatrix}0\\u_g-u\\v_g-v\\2\left(uu_g-u^2-\sigma_{11}\right)\\uv_g+vu_g-2\left(uv-\sigma_{12}\right)\\2\left(vv_g-v^2-\sigma_{22}\right)\end{pmatrix} \tag{2.27}$$

and $\boldsymbol{\mathcal{F}}_2$ is deduced by obvious substitutions. Let us recall that only four equations will appear in 2.26 and be resolved if one works with an IG distribution instead of AG.

The system (2.26) has been shown to be hyperbolic and admit entropies [10]. These properties allow to treat the shocks that can naturally appear in Eulerian moment models

and also to rely on the large literature devoted to Godunov-like scheme. Yet the spray behavior under such models are complicated since one can observe both vacuum zones and stiff accumulations of droplets. Therefore some high order, realizability preserving, numerical schemes are developed to deal with such singularities [187].

In [187], it has been concluded, through comparisons with Lagrangian simulations, that the Anisotropic Gaussion (AG) distribution reproduces well homo-PTC for disperse-flow regimes characterized through small to moderate Stokes numbers. Moreover, its accuracy is higher than Isotropic Gaussian (IG) distribution since the PTC is an anisotropic phenomenon [187]. Yet IG requires less second order moments to be transported than AG, while still capturing the uncorrelated motion (granular temperature). Within the context of turbulence RANS or LES modeling, the last issue is necessary for modeling the correct energy partition inside the spray, as discussed in part 2.5. Computational costs being a bottleneck problem for industrial simulations, IG is a good candidate for deriving such turbulence models from moment system of equations, while providing lower costs compared to AG. IG will be also used for formulating a hybrid poydisperse-polykinetic model in the present thesis through Chapter 6 within the framework of Reynolds average modeling discussed in the next section.

2.5 Turbulent disperse flow modeling through Eulerian kinetic based models

The NDF appearing in WBE is deterministic in a laminar flow but fluctuates in a turbulent flow. These fluctuations generally arise in one of three ways: (i) the Reynolds number in the continuous-phase model is large enough for the gas-phase velocity $\boldsymbol{u_g}$ to be turbulent, (ii) the Reynolds number associated to a single droplet Re_d in the continuous-phase is large enough for the droplet velocity $\boldsymbol{u}$ to be turbulent, or (iii) the coupling terms between the phases lead to flow instabilities and turbulence [63].

Given the very small length and time scales encountered in disperse two-phase flows, the direct numerical simulation (DNS) of Eulerian models based on Eq.(2.14) is not affordable for industrial computations. In recent years, significant effort on disperse-phase turbulence modeling through Large Eddy Simulation (LES) or Reynolds-averaged (RA) techniques have been carried out to resolve the latter difficulty. The former technique consists in spatially filtering governing equations such that only energy containing large scales of the turbulence are resolved and smaller scales modeled. It has been discussed in [141, 63, 60, 142] that filtering-based LES formulations are not consistent with the underlying concepts used in turbulence modeling since they do not provide any statistical information on unresolved scales. The modeling concept of unresolved scales for disperse flow is very important since it conditions the flow regime: in LES, the characteristic fluid timescale used to define the Stokes number St is that of the smallest resolved scales. Because the resolved timescales in LES are much larger than the Kolmogorov timescales, the effective Stokes number in LES will be much smaller than in DNS. For this reason the correct statistical information on unresolved scales is of great importance. The required statistical consistence is rather obtained through the use of self-conditioned LES formulation recently presented in [142]. On the other hand, RA techniques consist on averaging

an infinite realization of the same flow. Conceptually, this accounts for resolving only the averaged fields while modeling all fluctuations around them. The small scale interactions between particles and continuous-phase are modeled through these fluctuations. Moreover, Stokes number is based on integral time scale much bigger then Kolmogorov time scale and the time associated to the smallest resolved scale in LES. Therefore, both the modeling of fluctuations and the energy partitioning should be carefully and accurately achieved [64]. In case of either LES or RA turbulence modeling through Eulerian kinetic based methods, there are basically two ideas in the literature:

- (i) *turbulence modeling at the kinetic level:* it consists of directly applying the adequate turbulence averaging (i.e. LES self-conditioned or RA) on Eq.(2.14), providing appropriate closures at kinetic level. The second step is then to take moments of turbulent kinetic equation to obtain an Eulerian system.
- (ii) *turbulence modeling at macroscopic level:* This method is to first derive moment equations through phase space integration of Eq.(2.14) then apply the turbulence averaging on the moment system and provide correct closures.

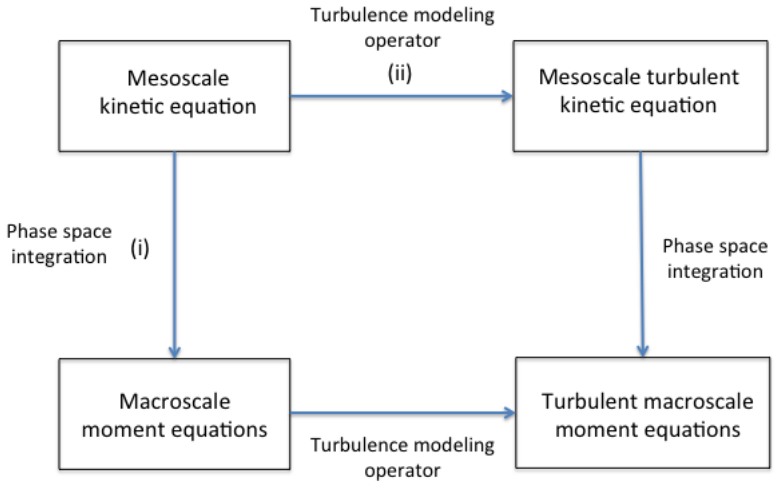

Figure 2.3: *Eulerian turbulence modeling through Reynolds-averaging or LES methods starting from the kinetic level of description. (i) denotes the turbulence modeling at the kinetic level, whereas (ii) represents turbulence modeling at macroscopic level*

In this part, let us give further details on both philosophies. For the sake of clarity, we take a simplified form of Eq.(2.14) through following assumption: (a) as the unique source term, the drag force under the Stokes law with constant τ_d is taken, (b) NDF function is simplified to $f = f(t, \boldsymbol{x}, \boldsymbol{u})$ (c) only one spatial dimension is considered for our problem. Eq.(2.14) is thus reduced to:

$$\partial_t f + \partial_x (uf) + \partial_u \left[\frac{1}{\tau_d} (u_g - u) f \right] = 0. \tag{2.28}$$

2.5.1 Turbulence modeling at the kinetic level

Taking the average of Eq.(2.28) gives rise to the following equation

$$\partial_t \langle f \rangle + \partial_x \left(u \langle f \rangle \right) + \partial_u \left[\frac{1}{\tau_d} \left(\langle u_g \rangle - u \right) \langle f \rangle \right] = -\frac{1}{\tau_d} \partial_u \left\langle u_g' f' \right\rangle \tag{2.29}$$

with the operator $\langle \cdot \rangle$ denotes either self-conditioned or spatially filtered or RA averaging. Therefore $\langle f \rangle$ is a probability density function (PDF) The final term in Eq.(2.29) is well known in the literature on very dilute gas-particle flows, fluid seen by the particle, and often modeled by the sum of a spatial flux and diffusion in velocity phase space [146, 200, 201]

$$\frac{1}{\tau_d} \left\langle u_g' f' \right\rangle = -\mu \partial_x \langle f \rangle - \lambda \partial_u \langle f \rangle , \tag{2.30}$$

for which details on the derivation of the diffusion coefficients μ and λ can be found in the literature [146, 200, 201, 80, 136]. In theory, these coefficients can be functions of the phase space variables or fluid-phase random variables. Yet let us point out that, in the context of isotropic turbulence modeling, these coefficients have been most of the time taken as constants either in LES or RA contexts [200, 201]. The turbulent kinetic equation closure through Eq.(2.30) allows us to conduct the second step towards the Eulerian moment system derivation. We therefore integrate Eq.(2.29) up to the second order in velocity, yielding the following moment system

$$\partial_t \langle \mathcal{M}_0 \rangle + \partial_x \langle \mathcal{M}_1 \rangle = 0, \tag{2.31a}$$

$$\partial_t \langle \mathcal{M}_1 \rangle + \partial_x \left(\langle \mathcal{M}_2 \rangle + \mu \langle \mathcal{M}_0 \rangle \right) = \frac{1}{\tau_d} \left(\langle \mathcal{M}_0 \rangle \langle u_g \rangle - \langle \mathcal{M}_1 \rangle \right), \tag{2.31b}$$

$$\partial_t \langle \mathcal{M}_2 \rangle + \partial_x \left(\langle \mathcal{M}_3 \rangle + 2\mu \langle \mathcal{M}_1 \rangle \right) = \frac{2}{\tau_d} \left(\langle \mathcal{M}_1 \rangle \langle u_g \rangle - \langle \mathcal{M}_2 \rangle \right) + 2\lambda \langle \mathcal{M}_0 \rangle , \tag{2.31c}$$

with

$$\langle \mathcal{M}_k \rangle = \int u^k \langle f \rangle \, \mathrm{d}u. \tag{2.32}$$

Let us recall that the unknown moment $\mathcal{M}_3$ is classically calculated through rigorous mathematical approximations, from the reconstruction of $\langle f \rangle$ through its lower order moments [62]. It is straightforward to observe that the system (2.31) is completely closed, since the physical modeling problem for the term $\left\langle u_g' f' \right\rangle$ in Eq.(2.29) has been already resolved through Eq.(2.30) at the kinetic level.

2.5.2 Turbulence modeling at macroscopic level

The second strategy consists of taking either self-conditioned or spatially filtered or RA averaging of moment system of equation, see references [188, 114, 129, 153, 161] for LES and [64] for RA modelings. The first step is therefore to take the velocity moments of

Eq.(2.28) yielding the system

$$\partial_t \mathcal{M}_0 + \partial_x \mathcal{M}_1 = 0, \tag{2.33a}$$

$$\partial_t \mathcal{M}_1 + \partial_x \mathcal{M}_2 = \frac{1}{\tau_d} \left(\mathcal{M}_0 u_g - \mathcal{M}_1 \right), \tag{2.33b}$$

$$\partial_t \mathcal{M}_2 + \partial_x \mathcal{M}_3 = \frac{2}{\tau_d} \left(\mathcal{M}_1 u_g - \mathcal{M}_2 \right), \tag{2.33c}$$

with

$$\mathcal{M}_k = \int u^k f \mathrm{d}u. \tag{2.34}$$

For turbulence modeling, one applies the RA or self-conditioning or spatially filtering operator directly to the closed moment equation set (2.33) which gives rise to the following moment system

$$\partial_t \langle \mathcal{M}_0 \rangle + \partial_x \langle \mathcal{M}_1 \rangle = 0, \tag{2.35a}$$

$$\partial_t \langle \mathcal{M}_1 \rangle + \partial_x \langle \mathcal{M}_2 \rangle = \frac{1}{\tau_d} \left(\langle \mathcal{M}_0 \rangle \langle u_g \rangle - \langle \mathcal{M}_1 \rangle + \left\langle \mathcal{M}_0' u_g' \right\rangle \right), \tag{2.35b}$$

$$\partial_t \langle \mathcal{M}_2 \rangle + \partial_x \langle \mathcal{M}_3 \rangle = \frac{2}{\tau_d} \left(\langle \mathcal{M}_1 \rangle \langle u_g \rangle - \langle \mathcal{M}_2 \rangle + \left\langle \mathcal{M}_1' u_g' \right\rangle \right), \tag{2.35c}$$

where unknown terms $\left\langle \mathcal{M}_0' u_g' \right\rangle$ $\left\langle \mathcal{M}_1' u_g' \right\rangle$ should be properly closed.

2.5.3 Concluding remarks

One can appreciate that unknown terms in system (2.35) should be consistent with the system (2.31) closed through the correlations given by Eq.(2.30). Yet the latter issue is not straightforward since it is not clear how to make the link between macroscopic variables in (2.35) and the internal variables of the PDF $\langle f \rangle$ at the kinetic level [64]. From that point of view, it is sometimes argued that finding a closure at the kinetic level would provide more accuracy [63]. Yet In the context of RA models, the necessity of describing the correct energy partitioning inside the spray requires separate models for the spray-phase turbulent kinetic energy (TKE), (the spatially correlated large-scale motion), and the granular-temperature (the spatially uncorrelated small-scale motion) [59, 175]. This implies that the kinetic closure Eq.(2.30) should involve the TKE which is actually a Eulerian quantity. Recalling that coefficients μ and λ in Eq.(2.30) are most of the time considered as constants, such a closure is not obvious for the RA modeling at the kinetic level.

As contrast to the lack of RA modeling at the kinetic level, the fruitful work done in [64] has recently shown the potential of RA modeling at the macroscopic level. Through the Full Eulerian Reynolds averaging of the two-way coupled monodisperse collisional particles with the gas-phase, some consistent closures has been given in [64]. The correct energy partition inside the spray has been taking into account thanks to equations on the spray TKE, the temperature granular and adequate closures validated as compared to the theory [59, 175]. This method is therefore promising for industrial disperse-phase turbulence modeling.

2.6 Kinetic based Eulerian simulation of polydisperse droplets

We now focus on kinetic based Eulerian models able to describe both the polydispersity and the droplets evaporation. The idea is to briefly discuss about each of the several existing methods along their potential towards ICE applications.

The derivation of some of the Eulerian polydisperse models are done in two steps. The first step consists of obtaining the semi-kinetic equation system through the integration in velocity and temperature of WBE and the second step is the derivation of Eulerian equations through the integration in size of the semi-kinetic system. Yet for the sake of simplicity, these methods are originally derived, assuming a monokinetic assumption for the NDF function but higher velocity moments could be considered. This implies that there are locally unique velocity and temperature for all droplets. It is therefore useful to first introduce the semi-kinetic modeling concept based on this strong assumption before discussing about each of relevant polydisperse models.

2.6.1 Semi-kinetic modeling under a monokinetic assumption

We highlight here the main assumptions on the NDF and give its form under an equilibrium assumption with no dispersion for the velocity and the temperature distribution:

- [H1] For a given droplet size, at a given point $(t, \boldsymbol{x})$, there is only one characteristic averaged velocity $\boldsymbol{u_d}(t, \boldsymbol{x}, S)$ and one characteristic temperature $T_d(t, \boldsymbol{x}, S)$.
- [H2] The dispersion in the distribution function around the mean velocity is zero in each direction, whatever the point $(t, \boldsymbol{x}, S)$.
- [H3] The dispersion in the distribution function around the mean temperature is zero in each direction, whatever the point $(t, \boldsymbol{x}, S)$.

It is equivalent to presume the following NDF conditioned by droplet size:

$$f(t, \boldsymbol{x}, T, S) = n(t, \boldsymbol{x}, S)\, \delta(\boldsymbol{u} - \boldsymbol{u_d}(t, \boldsymbol{x}, S))\, \delta(T - T_d(t, \boldsymbol{x}, S)). \tag{2.36}$$

From this approximation, we can derive a system of moment equations for the spray taking the moments in velocity of order 0 and 1 and in internal energy $e(T)$ of Equation (2.14). This gives rise to the semi-kinetic system of equations:

$$\partial_t n + \nabla_{\boldsymbol{x}} \cdot (n \boldsymbol{u_d}) = \partial_S (R_d n), \tag{2.37a}$$
$$\partial_t (n \boldsymbol{u_d}) + \nabla_{\boldsymbol{x}} \cdot (n \boldsymbol{u_d} \otimes \boldsymbol{u_d}) = \partial_S (R_d \boldsymbol{u_d} n) + \boldsymbol{F}_d\, n, \tag{2.37b}$$
$$\partial_t (n e_d) + \nabla_{\boldsymbol{x}} \cdot (n \boldsymbol{u_d} e_d) = \partial_S (R_d e_d n) + Q_d C_{v,l}(T_d)\, n, \tag{2.37c}$$

with

$$R_d = R_S(t, \boldsymbol{x}, \boldsymbol{u_d}, S, T_d), \qquad Q_d = Q(t, \boldsymbol{x}, \boldsymbol{u_d}, S, T_d), \qquad e_d = e(T_d). \tag{2.38}$$

Let us recall that the semi-kinetic system, derived from the monokinetic assumption on the NDF, is weakly hyperbolic since no pressure like dispersion term arises in Eq.(2.37b)

and Eq.(2.37c). Therefore, Eulerian methods which will be derived through system (2.37) will follow this pressure-less formalism. This remark is particularly important since the pressure-less system is known to generate delta-shocks and do not capture the homo-PTC [30]. To overcome this difficulties, these polydisperse methods can be coupled to Eulerian polykinetic approaches [39] which are already presented in part 2.4.

2.6.2 Eulerian polydisperse approach with size sampling

Let us start with the size sampling approach. The size sampling approach [94, 9] also referred to as Multi-Class method, or Lagrangian-in-size method [131], considers the NDF as sampled regarding the size variable, yielding I classes of particles of same size, illustrated in Figure 2.4. The sampling approach is based on the following approximate NDF:

$$f\left(t,\boldsymbol{x},T,S\right)=\sum_{i}^{I}N_i\left(t,\boldsymbol{x}\right)\delta\left(\boldsymbol{u}-\boldsymbol{u}_i\left(t,\boldsymbol{x}\right)\right)\delta\left(S-S_i\left(t,\boldsymbol{x}\right)\right)\delta\left(T-T_i\left(t,\boldsymbol{x}\right)\right) \tag{2.39}$$

where N_i, S_i, T_i and $\boldsymbol{u}_i$ are respectively the droplet number density, size, temperature and velocity at the location $(t,\boldsymbol{x})$. With this form, droplets with the same size are gathered into classes where i is the index of a class: the classes perform a sampling of the NDF over the whole phase space. The mass, momentum and energy conservation equation for each

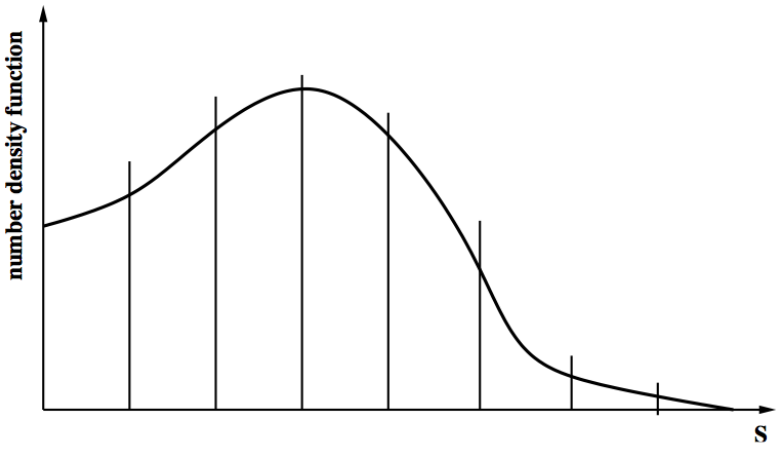

Figure 2.4: *Size distribution with size sampling approach*

class i of the spray is obtained through the integration of Eq.(2.14) in size S, temperature T and the velocity $\boldsymbol{u}$. The mass, momentum and heat source terms are evaluated as they depend on the sampled droplet variables.

The Multi-Class approach can yield a satisfactory representation of the disperse phase size distribution, prevented that enough classes are considered and that they correspond to relevant points. Choosing a satisfactory sampling of a given distribution is a classical problem but here, it is coupled to the question of predicting the correct evolution of the

spray, given such a distribution, which is a tough non-linear and implicit problem. So size samples are often chosen empirically. Moreover, as the approach is discretized regarding size with Dirac functions, the non-local transport cannot be accounted for properly: the size evolution due to sources (coalescence, break-up) is poorly rendered due to the fact that the samples have no particular reasons to match the new sizes. Conversely this technique is avoided when it comes to modeling discrete size-changing phenomena. Looking for the accurate evaporation, this method is not adapted for our problem.

2.6.3 Eulerian Multi-fluid model

The Eulerian Multi-Fluid model (MF), also referred to as sectional method, was developed in [94] to account for the droplet size in a continuous and affordable manner. It is inspired from the seminal work in [174], furthered in [163, 73]. But the origin and assumptions of the Multi-Fluid model have been precisely presented in [94]. Based on the mono-kinetic assumption, the original MF method is at first order in size for the evaporation [93]. Yet it has been extended to a second order in size for the evaporation through the work of [93, 40]. Moreover, recent advances in [39] took into account size-velocity correlations for a rather precise description of hetero-PTC through two size moments. In this part, we will first focus on the derivation of the original MF, then providing some information on recent achievements and finally give a brief conclusion about the method.

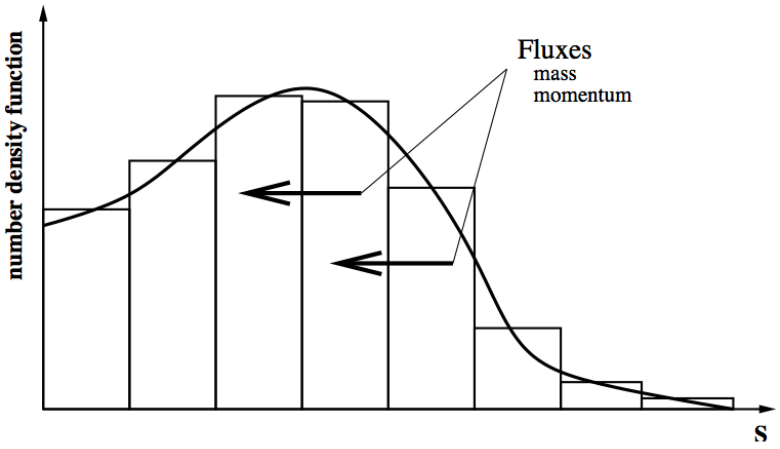

Figure 2.5: *Size distribution with MF method*

2.6.3.1 Original MF assumptions and the model derivation

The original MF method is derived, adopting a mono-kinetic velocity and temperature distribution. Therefore this accounts of working with the same system given through Eq.(2.37). Yet, Eq.(2.37) has still a size phase-space S dependence.

The Multi-Fluid model relies indeed on the choice of a discretization for the droplet

size phase space:

$$0 = S_0 < S_1 < \cdots < S_{N_{sec}} = \infty \tag{2.40}$$

where N_{sec} is the number of sections. The system of conservation laws is then averaged over each fixed size interval $[S_{k-1}, S_k[$, called section. The set of droplets in one section can be seen as a "fluid" for which conservation equation are written, the sections exchanging mass, momentum and energy. The principle of sectional discretization is shown in Figure 2.5 and can be seen as a finite volume method on the size dimension, continuous size-variation source terms (e.g. evaporation) resulting in fluxes at the edges of the size cells. In the following, let us recall the strategy to obtain a closed conservation equation system for each section through the integration in size of the semi-kinetic system (2.37).

The velocity and the temperature are supposed to be independent of size variable within each section. Therefore the notation $\boldsymbol{u}(t, \boldsymbol{x}, S) = \boldsymbol{u}^{(k)}(t, \boldsymbol{x})$ is chosen to designate the constant velocity distribution in section k. Similarly, one introduces presumed constant distribution within a section as $T(t, \boldsymbol{x}, S) = T^{(k)}(t, \boldsymbol{x})$ which allows to define the sectional specific heat capacity $c_d^{(k)} = c_{d,l}\left(T^{(k)}\right)$. The validity of these assumptions is linked to the strength of polydispersity in each section, which is quantified in a section by comparing the smallest to the biggest Stokes numbers. If the dynamic Stokes number spectrum is too wide, the discretization must then be refined [30, 41, 39] or or size-velocity coupled high order moments should be used within each section to improve the accuracy [39, 189].

For the polydispersity treatment, in each section, the form of n as a function of S is presumed which allows to reduce the size distribution information in each section at $(t, \boldsymbol{x})$ to a set of moments of S.

In the original MF method [94], the One-size Moment (OSM) method which consists of decoupling the contribution in size S from space-time $(t, \boldsymbol{x})$ dependence by the following way:

$$n(t, \boldsymbol{x}, S) = \kappa^{(k)}(S)\, m_{3/2}^{(k)}(t, \boldsymbol{x}) \tag{2.41}$$

where $\kappa^{(k)}$ is a function of size S and $m_{3/2}^{(k)}$ is the size moment corresponding to the spray mass density within the k th section which is expressed as:

$$m_{3/2}^{(k)}(t, \boldsymbol{x}) = \int_{S_{k-1}}^{S_k} \frac{\rho_l}{6\sqrt{\pi}} S^{3/2} n(t, \boldsymbol{x}, S)\, \mathrm{d}S = 1 \tag{2.42}$$

which gives us, for the form $\kappa^{(k)}$ in one section:

$$\int_{S_k - 1}^{S_k} \kappa^{(k)}(S)\, \frac{\rho_l}{6\sqrt{\pi}} S^{3/2} \mathrm{d}S = 1 \tag{2.43}$$

As mentioned in [94], $\kappa^{(k)}(S)$ is taken as constant in size distribution .

Let us know derive macroscopic MF equations. For the sake of simplicity, the spray temperature is assumed to be constant and uniform. From where, taking the integration in $\frac{\rho_l}{6\sqrt{\pi}} S^{3/2}$ of the semi-kinetic system (2.37) within a section $[S_{k+1}, S_k[$ leads to the

following system of conservation equations:

$$\partial_t m_{3/2}^{(k)} + \nabla_{\boldsymbol{x}} \cdot \left(m_{3/2}^{(k)} \boldsymbol{u_d}^{(k)} \right) = - \left(E_1^{(k)} + E_2^{(k)} \right) m_{3/2}^{(k)} + E_1^{(k+1)} m_{3/2}^{(k+1)}, \tag{2.44a}$$

$$\partial_t \left(m_{3/2}^{(k)} \boldsymbol{u_d}^{(k)} \right) + \nabla_{\boldsymbol{x}} \cdot \left(m_{3/2}^{(k)} \boldsymbol{u_d}^{(k)} \otimes \boldsymbol{u_d}^{(k)} \right) = - \left(E_1^{(k)} + E_2^{(k)} \right) m_{3/2}^{(k)} \boldsymbol{u_d}^{(k)} + E_1^{(k+1)} m_{3/2}^{(k+1)} \boldsymbol{u_d}^{(k+1)} + m_{3/2}^{(k)} \boldsymbol{F}_d^{(k)}, \tag{2.44b}$$

where we define, in the kth section, the averaged velocity

$$\boldsymbol{u_d}^{(k)} = \frac{1}{m_{3/2}^{(k)}} \int_{S_{k-1}}^{S_k} \frac{\rho_l}{6\sqrt{\pi}} S^{3/2} \boldsymbol{u_d}\left(t, \boldsymbol{x}, S\right) n\left(t, \boldsymbol{x}, S\right) \mathrm{d}S, \tag{2.45}$$

and the averaged drag term

$$\boldsymbol{F}_d^{(k)} = \frac{1}{m_{3/2}^{(k)}} \int_{S_{k-1}}^{S_k} \frac{\rho_l}{6\sqrt{\pi}} S^{3/2} \boldsymbol{F}_d\left(t, \boldsymbol{x}, S\right) n\left(t, \boldsymbol{x}, S\right) \mathrm{d}S. \tag{2.46}$$

Expressions for the evaporation terms $E_1^{(k)}$ and $E_2^{(k)}$ are given as

$$E_1^{(k)} = \frac{5 S_{(k-1)}^{3/2}}{2\left[S_{(k)}^{5/2} - S_{(k-1)}^{5/2}\right]} R_d\left(S_{(k-1)}\right), \tag{2.47}$$

and

$$E_2^{(k)} = \frac{5}{2\left[S_{(k)}^{5/2} - S_{(k-1)}^{5/2}\right]} \int_{S_{(k-1)}}^{S_{(k)}} \frac{3}{2} S^{1/2} R_d\left(S\right) \mathrm{d}S, \tag{2.48}$$

2.6.3.2 MF with two size moments per section

Yet the OSM yields a lack of accuracy in terms of the size distribution and requires a great number of sections to counterbalance its drawback. An accurate method is therefore needed to capture polydispersity at the compromise of computational cost, but also ease of implementation and flexibility. Instead of increasing the number of sections, increasing the number of moments per section is a promising option. The works done in [93, 40] rely on solving two size moments in each section and the method is referred to as Two Size Moment (TSM) method. It consists in transporting moments corresponding to both the number $m_0^{(k)}$ and the mass $m_{3/2}^{(k)}$ instead of one unique moment per section. These moments are expressed as:

$$\begin{pmatrix} m_0^{(k)} \\ m_{3/2}^{(k)} \end{pmatrix} = \int_{S_k - 1}^{S_k} \begin{pmatrix} 1 \\ \dfrac{\rho_l}{6\sqrt{\pi}} S^{3/2} \end{pmatrix} n\left(t, \boldsymbol{x}, S\right) \mathrm{d}S \tag{2.49}$$

The only realizability condition for a couple of size moments $\left(m_0^{(k)}, m_{3/2}^{(k)}\right)$ in a section is to be positive and to correspond to an average diameter that is in the size interval:

$$\left(m_0^{(k)} > 0 \text{ and } m_{3/2}^{(k)} > 0\right) \quad \text{or} \quad \left(m_0^{(k)} = m_{3/2}^{(k)} = 0\right) \tag{2.50a}$$

$$\frac{\rho_l \left(S^{k-1}\right)^{3/2}}{6\sqrt{\pi}} \leq \frac{m_{3/2}^{(k)}}{m_0^{(k)}} \leq \frac{\rho_l \left(S^{k}\right)^{3/2}}{6\sqrt{\pi}}$$

Respecting this realizability condition, there are several strategies in presuming an appropriate n. An exponential reconstruction called the exponential TSM (Exp-TSM) MF method, suggested in [45], was a first method, respecting the realizability condition. It has been proven to be well suited for evaporation, which requires mass flux information at the section boundary. The affine TSM (Aff-TSM) MF method is also based on a two-parameter approximation of the size distribution, through a positive affine function reconstruction, in each section. An early version was suggested in [93] and its more efficient extension has been recently proposed in [96].

2.6.3.3 PTC with MF method

As discussed before, droplets of different sizes can have different velocities due to the correlations between their sizes and velocities which yield to the hetero-PTC. Moreover, inertial droplets with the same size can have still different velocities, leading to the homo-PTC. Yet TSM method which captures the polydispersity resolution at a second order accuracy under a lower number of sections than OSM method, is not well adapted for the modeling of PTC. This is due to the fact that all droplets within a section share the same velocity and temperature. In [39], this lack of PTC accuracy has been addressed and MF method has been extended to capture the PTC.

- *Hetero-PTC:* Inspired from the work of Vié et al. [189] originally developed for high order moment methods (further detailed in section 2.7.6), the approach called Correlated Size-Velocity Two Size Moment (CSVTSM) method is designed to account efficiently for size-conditioned dynamics [39]. CSVTSM method, expected to be second order in size and velocity has been proven to suit well for coalescing cases. Yet additional to the two size moments transported in the original TSM MF method, two in 1D, four in 2D and six in 3D velocity moments per section are transported, having a significant impact on the CPU time.

- *Homo-PTC:* Inspired from the Kinetic Based Moment Methods (KBMM) [97, 190], MF extended and applied to moderate-inertia particle-laden flows in order to capture small scale PTC [187]. The velocity distribution in the NDF function is no longer taken as a Dirac function but based on an anisotropic Gaussian (AG) distribution given. MF method under AG distribution is shown to be well-suited to account for homo-PTC [39, 42]. The method is promising for moderately dense polydisperse two-phase flows, to treat the portion of coalescing droplets that has a significant enough inertia.

2.6.3.4 Conclusion on MF method

So far in this part, one has discussed the capability of the MF model to capture the physics of polydisperse evaporating sprays. However, even though this approach has been extended to be more accurate by Laurent et al. [96] and [40] for evaporating sprays, the necessity to discretize the size phase space can be a stumbling block. In that context, the Eulerian Multi-Size Moment (EMSM) method developed in [83, 120, 87] provides to increase the polydispersity accuracy within each section while diminishing the number of sections. Yet it has been proven in [87], a very good accuracy under a shorter CPU time then MF method is obtained even with the use of only one section. More detail on EMSM method will be given in section 2.7.

2.6.4 High order moment methods through quadrature approaches

An other way of describing the polydispersity is to track moments of WBE and to use a quadrature formula to compute the unknown high order size moments as a function of low order moments of the NDF.

2.6.4.1 Quadrature Method Of Moments (QMOM)

The original QMOM approach consists in transporting and conserving a set of $2N_p$ size moments $\boldsymbol{M} = \left(M_0, \ldots, M_{2N_p-1}\right)$ with $M_k\left(t,\boldsymbol{x}\right) = \int_{\mathbb{R}^+} \xi^k f\left(t,\boldsymbol{x},\xi\right) \mathrm{d}\xi$ [196, 124, 106]. The NDF function is presumed by the following expression:

$$f\left(t,\boldsymbol{x},\xi\right) = \sum_{i=1}^{N_p} w_i\left(t,\boldsymbol{x}\right) \delta\left(\xi - \xi_i\left(t,\boldsymbol{x}\right)\right) \tag{2.51}$$

with N_p is the number of peaks, w_i the weights, and ξ_i the abscissas. Thanks to the moment-inversion algorithm provided in [123], weights and abscissas are found from the relation

$$M_k = \sum_{i=1}^{N_p} w_i \xi_i^k, \qquad k \in 0, 1, \ldots, 2N_p - 1. \tag{2.52}$$

To illustrate the QMOM method, let us work with a rather simplified WBE for the aerosols transported through the gas velocity $\boldsymbol{u_g}$

$$\partial_t f + \nabla_{\boldsymbol{x}} \cdot \left(\boldsymbol{u_g} f\right) = \Lambda\left(t,\boldsymbol{x},\xi\right) f\left(t,\boldsymbol{x},\xi\right). \tag{2.53}$$

After the size integrations of Eq.(2.53), the evolution of the kth order size moment is given by:

$$\partial_t M_k + \nabla_{\boldsymbol{x}} \cdot \left(M_k \boldsymbol{u_g}\right) = \int_{\xi} \xi^k \Lambda\left(t,\boldsymbol{x},\xi\right) f\left(t,\boldsymbol{x},\xi\right) \mathrm{d}\xi \tag{2.54}$$

The evolution of the NDF is therefore described by $2N_p$ equations. Yet, The form of the function Λ can be complex and yields unclosed moments at the right hand side of system

(2.54). The strategy adopted in QMOM method is to first reconstruct quadrature points through Eq.(2.52) and then compute unclosed integral terms as:

$$\int_{\xi} \xi^k \Lambda\left(t, \boldsymbol{x}, \xi\right) f\left(t, \boldsymbol{x}, \xi\right) \mathrm{d}\xi = \sum_{i}^{N_p} \xi_i^k w_i\left(t, \boldsymbol{x}\right) \Lambda\left(t, \boldsymbol{x}, \xi_i\left(t, \boldsymbol{x}\right)\right) \tag{2.55}$$

In particular, from the quadrature formula, the non-conserved moments can be computed simply:

$$M_\alpha = \sum_{i=0}^{N_p} w_i \xi_i^\alpha \tag{2.56}$$

Yet the QMOM has a limitation for practical applications under the spray evaporation since the continous form of the distribution is required to be well described for an accurate evaluation of the disappearing flux of droplets at zero size. This is not possible such an expression given through Eq.(2.52). When using more quadrature nodes, QMOM is expected to be more and more accurate, the counterpart being a higher cost and a more difficult moment-inversion.

2.6.4.2 Direct Quadrature Moment of Methods (DQMOM)

This quadrature method has been originally developed for cases where a multi-variate NDF function is required for WBE [106]. For example, the description of particle trajectory crossings within the multi-dimensional context requires to consider a velocity component for each spatial dimension. In order to evaluate its effectiveness in the context of evaporating polydisperse spray modeling, it has been also compared to the MF method in [65]. Let us now write down the form of the NDF for the DQMOM derivation as

$$f\left(t, \boldsymbol{x}, \boldsymbol{u}, \xi\right) = \sum_{i}^{N_p} w_i\left(t, \boldsymbol{x}\right) \delta\left(\boldsymbol{u} - \boldsymbol{u}_i\left(t, \boldsymbol{x}, \xi_i\right)\right) \delta\left(\xi - \xi_i\left(t, \boldsymbol{x}\right)\right). \tag{2.57}$$

In this case, instead of transporting moments of the distribution, one transports all abscissas and weights of quadratures. This implies also transporting N_p diracs. The following Eulerian equation system is given as:

$$\partial_t w_i + \nabla_{\boldsymbol{x}} \cdot \left(w_i \boldsymbol{u}_i\right) = a_i, \tag{2.58a}$$

$$\partial_t \left(w_i \xi_i\right) + \nabla_{\boldsymbol{x}} \cdot \left(w_i \xi_i \boldsymbol{u}_i\right) = b_i, \tag{2.58b}$$

$$\partial_t \left(w_i \xi_i \boldsymbol{u}_i\right) + \nabla_{\boldsymbol{x}} \cdot \left(w_i \xi_i \boldsymbol{u}_i \otimes \boldsymbol{u}_i\right) = c_i, \tag{2.58c}$$

where source terms (a_i , b_i , c_i) are obtained from WBE, writing conservation equations on a set of chosen moments. Yet, in [65], it has been demonstrated that the DQMOM approach shows inaccuracies when it comes to predict droplet evaporations since as QMOM, it can not capture the pointwise value related to the number of disappearing droplets. Therefore, it does not provide a solution to our ambition to accurately simulate polydisperse evaporating droplets. Moreover, it has been proven to be inaccurate for PTC events for which the CQMOM approach is rather preferred [198].

2.6.5 High order moment methods based on the Maximum entropy NDF reconstruction

A promising alternative to QMOM is to reconstruct, among the infinity of solutions in the moment space, the unique NDF function, which maximizes the Shannon Entropy (ME) through its low order moments [125, 173], see Figure 2.6. Yet there are also other NDF reconstruction choices, like used in the description of aerosol Extended QMOM (EQMOM): a sum of beta PDF or gamma PDF, with the possibility to degenerate on quadratures, but sometimes with a loose of the highest moment in the reconstruction [199].

ME reconstruction technique and its associated numerical strategy for the accurate evaluation of evaporation dynamics has been proved to be very promising for applications in relations with polydisperse sprays [120]. Therefore, inspired from the basic assumptions of MF method [94], the Eulerian Multi Size Moment (EMSM) method has been developed in [83, 120, 87]. The ability of spray simulations under the unstructured mesh motion through EMSM has been successfully assessed in [86]. It has been shown in [87] that EMSM can reach comparable levels of accuracy, with a reasonable space discretization, with reference to a Lagrangian simulation, while leading to a much lower level of computational cost compared to the standard MF approach. Let us also mention that a more recent work called Coupled Size-Velocity Moment (CSVM) method has been developed, in [190], as an extension model of the EMSM, taking into account size-velocity correlations in the spray. In [190], a tabulation technique has been also developed to decrease significantly the CPU time associated to size moment reconstruction.

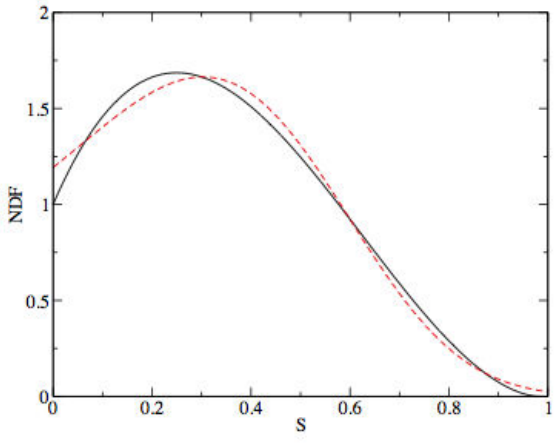

Figure 2.6: *Reconstruction of the size distribution through entropy maximisation (red dashed line), the real size distribution (black solid line).*

2.7 Eulerian Multi-Size Moment (EMSM) method

It has been previously shown that, although the MF method offers an accurate resolution for the evaporating polydisperse spray, the necessity to discretize the size phase space, making use of several sections, requires to transport a system of governing equations for each section, thus increasing the CPU time. Let us recall that the computational time can be decreased through the use of a two-size moment MF method, while maintaining a good accuracy on the size distribution. Yet still more than one section is required. In [120], a four-size moment MF method has been developed, leading a very good accuracy both in case of only two and even one size section. Since one section is enough to capture accurately the polydisperse evaporating spray, this one-section technique has been adopted in developing the high order moment method, called Eulerian Multi-Size Moment (EMSM) method as already presented to be accurate in part 2.6.5, while providing lower CPU time. In the reminder of this section, let us go into details of the EMSM method with four-size moments[1]. Firstly, its derivation strategy will be given. Then the bottleneck points in working with several size moments along with the associated realizability condition will be point out. Afterwards, we will discuss about dedicated numerical schemes developed in the literature and recent fruitful realizations. Then, one will briefly discuss about the recent work initiated from the basis of EMSM to capture the hetero-PTC. Finally, its implementation in the industrial code IFP-C3D as well as required developments towards ICE applications will be discussed. The latter aspect will guide the reader for the remaining chapters of the present manuscript.

2.7.1 Derivation of EMSM

As was the case for MF method, the EMSM method is also based on a mono-kinetic assumption for both the temperature and the velocity distribution. Yet deriving a size moment system at macroscopic (Eulerian) level is rather different in EMSM compared to MF since the size distribution function n is kept smooth and following assumptions are done:

$$\boldsymbol{u_d}\left(t,\boldsymbol{x},S\right)=\boldsymbol{u_d}\left(t,\boldsymbol{x}\right),\qquad T_d\left(t,\boldsymbol{x},S\right)=T_d\left(t,\boldsymbol{x}\right). \tag{2.59}$$

For the sake of simplicity, let us now take R_S in Equation (2.14) as a constant, so that $R_S = R_d$, and neglect the heat transfer term $Q = 0$. One first takes the moments of Eq.(2.37a) in size of order 0 up to 3. Then one takes the size moment of order one of Eq.(2.37b). Then the governing equations are given as:

$$\partial_t m_0+\nabla_{\boldsymbol{x}}\left(m_0\boldsymbol{u_d}\right)=-R_d n\left(S=0\right), \tag{2.60a}$$
$$\partial_t m_1+\nabla_{\boldsymbol{x}}\left(m_1\boldsymbol{u_d}\right)=-m_0R_d, \tag{2.60b}$$
$$\partial_t m_2+\nabla_{\boldsymbol{x}}\left(m_2\boldsymbol{u_d}\right)=-2m_1R_d, \tag{2.60c}$$
$$\partial_t m_3+\nabla_{\boldsymbol{x}}\left(m_3\boldsymbol{u_d}\right)=-3m_2R_d, \tag{2.60d}$$
$$\partial_t\left(m_1\boldsymbol{u_d}\right)+\nabla_{\boldsymbol{x}}\left(m_1\boldsymbol{u_d}^2\right)=-R_dm_0\boldsymbol{u_d}+\tfrac{18\pi}{\rho}\,\mu_g m_0(\boldsymbol{u_g}-\boldsymbol{u_d}). \tag{2.60e}$$

[1]EMSM can also be used in the context of a size discretization in each section as a hybrid approach making the link between Multi-Fluid and high order moment method [189]

with

$$m_k = \int_0^{S_{max}} S^k n\left(t, \boldsymbol{x}, S\right) \mathrm{d}S, \tag{2.61}$$

and the unclosed term $n\left(S=0\right)$ represents the number of disappearing droplets due to evaporation. S_{max} is the maximum size of the distribution. The system (2.60) has been investigated in [83, 120, 87] from both modeling and numerical point of view. The realizability issue is raised as the moment space in which the moment vector lives is a convex subspace of $(\mathbb{R}_+)^4$ but with a quite complex shape, as explained in part 2.7.2. Numerical methods (e.g. transport schemes) must be carefully developed to avoid approximations of the moment vector that would be out of the moment space, resulting in failure of the simulation.

Phenomena involved in (2.60) (i.e, evaporation and convection) can be decoupled through an operator splitting approach [102]. Therefore, the subsystem that represents the evolution due to the evaporation and Stokes drag is given as:

$$\partial_t m_0 = -R_d n\left(S=0\right), \tag{2.62a}$$
$$\partial_t m_1 = -m_0 R_d, \tag{2.62b}$$
$$\partial_t m_2 = -2 m_1 R_d, \tag{2.62c}$$
$$\partial_t m_3 = -3 m_2 R_d, \tag{2.62d}$$
$$\partial_t \left(m_1 \boldsymbol{u_d}\right) = -R_d m_0 \boldsymbol{u_d} + \tfrac{18\pi}{\rho}\, \mu_g m_0 (\boldsymbol{u_g} - \boldsymbol{u_d}), \tag{2.62e}$$

whereas the one for the convection is expressed as:

$$\partial_t m_0 + \nabla_{\boldsymbol{x}} \left(m_0 \boldsymbol{u_d}\right) = 0, \tag{2.63a}$$
$$\partial_t m_1 + \nabla_{\boldsymbol{x}} \left(m_1 \boldsymbol{u_d}\right) = 0, \tag{2.63b}$$
$$\partial_t m_2 + \nabla_{\boldsymbol{x}} \left(m_2 \boldsymbol{u_d}\right) = 0, \tag{2.63c}$$
$$\partial_t m_3 + \nabla_{\boldsymbol{x}} \left(m_3 \boldsymbol{u_d}\right) = 0, \tag{2.63d}$$
$$\partial_t \left(m_1 \boldsymbol{u_d}\right) + \nabla_{\boldsymbol{x}} \left(m_1 \boldsymbol{u_d}^2\right) = 0. \tag{2.63e}$$

For the numerical resolution of both (2.62) and (2.63), the main issue is to keep the integrity of moment set at anytime of the computation. An appropriate closure for the term $n\left(S=0\right)$ in Eq.(2.62a) and an accurate evolution of moments m_k through (2.62a)-(2.62d) due to evaporation require particular numerical strategy which will be detailed in part 2.7.4.1. The resolution of the pressure-less system (2.63) will be explained in section 2.7.4.2.

2.7.2 Moment space issue

The major challenge for numerical methods designed for evaporation and transport is to keep the integrity of the moment vector $\boldsymbol{m}$, i.e to ensure that $\boldsymbol{m} = (m_0, m_1, \ldots, m_3)^t$ belongs to the moment space at any time of the resolution process. Yet, even if the moment space $\mathbb{M}^3\left(0, S_{max}\right)$ where lies the size moment vector $\boldsymbol{m}$ is convex, it has a complex geometry in the semi-open space $(\mathbb{R}^+)^3$ [120]. A simpler space can be determined by using the canonical moments [38]. The geometry of the space of the canonical moments

vectors is much more simpler than the one of the moments since it is then the cube $[0,1]^3$. It is therefore interesting to know their expressions. Let us right down the first four canonical moments:

$$p_0 = 1, \tag{2.64a}$$
$$p_1 = \frac{m_1}{S_{max} m_0}, \tag{2.64b}$$
$$p_2 = \frac{m_0 m_2 - m_1^2}{m_1 \left(S_{max} m_0 - m_1\right)}, \tag{2.64c}$$
$$p_3 = \frac{\left(S_{max} m_0 - m_1\right)\left(m_1 m_3 - m_2^2\right)}{S_{max}\left(m_0 m_2 - m_1^2\right)\left(S_{max} m_1 - m_2\right)}. \tag{2.64d}$$

So the actual moments read:

$$m_1 = m_0 p_1 S_{max}, \tag{2.65a}$$
$$m_2 = m_0 p_1 S_{max}^2 \left[\left(1 - p_1\right) p_2 + p_1\right], \tag{2.65b}$$
$$m_3 = m_0 p_1 S_{max}^3 \left[\left(1 - p_1\right)\left(1 - p_2\right) p_2 p_3 + \left[\left(1 - p_1\right) p_2 + p_1\right]^2\right]. \tag{2.65c}$$

The canonical moments are then very useful in order to check the belonging to the moment space and design numerical schemes for system (2.62) and (2.63). The Hausdorff finite moment problem for the moments $\boldsymbol{m}$ is : finding a positive real valued function $\tilde{n}$ defined on $[0, S_{max}]$ such that:

$$\boldsymbol{m} = \int_0^{S_{max}} \begin{pmatrix} 1 \\ S \\ \vdots \\ S^N \end{pmatrix} \tilde{n}\left(\boldsymbol{m}, S\right) \mathrm{d}S \tag{2.66}$$

Yet if $\boldsymbol{m}$ belongs to the interior of $\mathbb{M}^3\left(0, S_{max}\right)$, there is an infinity of solutions. Let us recall that similar problems were tackled in different ways in the context of MF methods, previously introduced in section 2.6.3. In the case of MF-OSM [94], the positivity of only one size moment is enough to stay in the moment space, whereas for the case of MF-TSM [93, 45], the preservation of the moment space is conditioned through a more restrictive law given through (2.50).

In the following, some reconstructions are introduced for an arbitrary number of moments in relation with the structure of the moment space.

2.7.3 NDF Reconstruction through an arbitrary number of moments

In this part, one will discuss about available techniques for NDF reconstruction through its moments.

2.7.3.1 Lower principal representation

For any point in the interior of the Nth-moment space $\mathbb{M}^N(0, S_{max})$, with $N = 2s - 1$, it can be shown that there exists a unique lower principal representation (i.e. for which the moment m_{N+1} is minimal; $(m_0, \ldots, m_{N+1})$ then belongs to the boundary of $\mathbb{M}^{N+1}(0, S_{max})$ under the form of a sum of s weighted Dirac delta function, the support or roots of which are in $(0, S_{max})$. This support can be shown to be the root of some orthogonal polynomials associated to Hankel determinants [38]. It is this lower principal representation that is used in quadrature method of moments (QMOM) introduced in [123] and further used in the DQMOM [106].

Then for any $\boldsymbol{m} \in \mathbb{M}^N(0, S_{max})$, there exists one unique representation of the vector of moments by using weights (w_i) and abscissas (S_i), with $i \in [1, n]$, such that

$$\boldsymbol{m} = \begin{pmatrix} m_0 \\ \vdots \\ m_N \end{pmatrix} = \begin{pmatrix} \sum_{i=1}^{s} w_i \\ \sum_{i=1}^{s} w_i S_i \\ \vdots \\ \sum_{i=1}^{s} w_i S_i^N \end{pmatrix}, \tag{2.67}$$

The corresponding number density function is then :

$$\tilde{n}^-(S) = \sum_{i=1}^{s} w_i \delta(S - S_i). \tag{2.68}$$

Abscissas S_i are the roots of the polynomial $P = X^n + \sum_{k=0}^{n-1} \sigma_k X^k$, with:

$$\begin{bmatrix} m_0 & m_1 & \ldots & m_{s-1} \\ m_1 & & & \vdots \\ \vdots & & & \vdots \\ m_{s-1} & \ldots & \ldots & m_{2s-2} \end{bmatrix} \begin{pmatrix} \sigma_0 \\ \sigma_1 \\ \vdots \\ \sigma_{n-1} \end{pmatrix} = - \begin{pmatrix} m_s \\ m_{s+1} \\ \vdots \\ m_{2s-1} \end{pmatrix}. \tag{2.69}$$

The weights are then solutions of a linear system. A Product Difference (PD) (or Wheeler algorithm) can be used to compute these weights and abscissas [123].

The drawback of the Lower principal representation technique is that a point-wise value of the distribution at zero size of droplets is not available. Therefore, it does not provide any solution to close Eq.(2.62a).

2.7.3.2 NDF reconstruction through the Maximum Entropy formalism

A smooth approximated size distribution $\tilde{n}$ can be obtained by the Maximum Entropy (ME) reconstruction [125]. The ME method yields a smooth distribution that maximizes the following Shannon entropy from information theory :

$$\mathcal{H}[f] = \int_0^{S_{max}} f(x) \ln f(x) \, \mathrm{d}x \tag{2.70}$$

The existence of such ME distribution is shown in [173] as soon as the vector of moments $\boldsymbol{m}$ belongs to the interior of the moment space $\mathbb{M}^N(0, S_{max})$. This is a standard constrained optimization problem, leading to the following explicit representation of the ME approximate :

$$\tilde{n}(\boldsymbol{m}, x) = \exp\left(-\sum_{j=0}^{N} \xi_j x^j\right), \tag{2.71}$$

to be supplemented by the condition (2.66). It can be seen as a generalization of the reconstruction used in [45] except that the considered moments were moments of order 0 and 3/2 instead of integer moments here. The coefficients $\xi_0, \dots \xi_N$ are the Lagranges multipliers. We then just need to minimize the following convex potential :

$$\Delta = \int_0^{S_{max}} \left[\exp\left(-\sum_{j=0}^{N} \xi_j x^j\right) - 1\right] \mathrm{d}x + \sum_{j=0}^{N} \xi_j m_j \tag{2.72}$$

Indeed, its stationary points are given by

$$\frac{\partial \Delta}{\partial \xi_i} = 0 \qquad \Rightarrow \qquad \int_0^{S_{max}} x^i \exp\left(-\sum_{j=0}^{N} \xi_j x^j\right) \mathrm{d}x = m_i. \tag{2.73}$$

Numerically, a Newton method is used, as in [125] : starting from initial choices $\xi = (\xi_0, \dots, \xi_N)^t$, updated ξ's are defined from

$$\xi^+ = \xi - H^{-1}\left(\boldsymbol{m}^0 - \langle X \rangle_\xi\right), \tag{2.74}$$

where $\langle X \rangle_\xi = \left(\langle X^0 \rangle_\xi, \dots, \langle X^N \rangle_\xi\right)^t$ is the vector of approximated moments, with

$$\left\langle X^k \right\rangle_\xi = \int_0^{S_{max}} x^i \exp\left(-\sum_{j=0}^{N} \xi_j x^j\right) \mathrm{d}x \tag{2.75}$$

and H is the Hessian matrix defined by $H_{i,j} = \dfrac{\partial \Delta}{\partial \xi_i \partial \xi_j} = \left\langle X^{i+j} \right\rangle_\xi$ for $i = j = 0, \dots, N$.

In [125], they found that a double-precision 24-point Gaussian quadrature method very efficiently produces the demanded accuracy for $\left\langle X^k \right\rangle_\xi$. The quadrature points are computed once for the interval $[0, 1]$ and a change of variable is used for all the integrals in order to come back to this interval. Because H is symmetric positive definite, a classical Choleski decomposition is used in order to solve the linear system [144]. A number of iterations from 4 to 15 is needed for the Newton method to converge, with an accuracy of 10^{-6} on the normalized moments, from the initial value $= (-\ln(m_0)/(S_{max}), 0, \dots, 0)'$ corresponding to a constant reconstruction preserving the moment of order 0. This number of iterations depends on the distance to the boundary of the moment space : the closest the moment vector is to this boundary, the largest this number of iterations is.

The issue of the boundary of the moment space is not treated in [125], yet it has been highlighted in [120] that such an algorithm can lead to numerical difficulties due to ill-conditioned H matrices appearing in two cases:

- Such a bad condition number is encountered for moment vectors too close to the boundary of the moment space and results in highly oscillating ξ coefficients in the ME approximation for a reasonable number of moments.
- It can also appear in the case of a large vector of moments as a consequence of the peculiar high-dimensional geometry of the moment space.

Yet recent fruitful advances has been addressed the first issue through the work in [189].

2.7.3.3 Discussion on the EMSM closure

In [120], Maximum entropy (ME) reconstruction has been shown to provide an accurate closure for problem (2.62a) in terms of the moment vector. Despite numerical difficulties in the vicinity of the moment space boundaries, ME method has proven to be well accurate for the reconstruction of regular size distributions, preserving the moment space as far as a low-dimensional space, typically considering up to 6 moments, is adopted [120].

Yet using only four size moments has been shown to be a very good compromise to obtain a good accuracy under a reasonable CPU time [120]. Therefore major achievements with EMSM method has been conducted with four moments in [83, 87, 86].

2.7.4 Numerical resolution issue

In the context of high order moment methods, numerical schemes are required to respect the realizability condition at any time of the simulation. Kinetic based schemes for the transport of the moment vector $\boldsymbol{m}$ during the evaporation and the convection processes have been shown to accurately tackle the latter issue. Given the backgrounds on NDF reconstruction techniques, detailed in part 2.7.3 and the importance of working with canonical moments, presented in part 2.7.2, let us discuss first the kinetic based evaporation scheme [120] and then the convection scheme [87].

2.7.4.1 Evaporation scheme

In [120], it has been shown that the numerical solution of the equation system (2.62a)-(2.62d) within a time step Δt can be given as:

$$\exp\left(\Delta t R_d \boldsymbol{A}\right) \boldsymbol{m}\left(\Delta t\right) = \boldsymbol{m}\left(0\right) - \Phi^{-}\left(\Delta t\right) \tag{2.76}$$

where the flux at zero size Φ^{-} is expressed as:,

$$\Phi^{-}\left(\Delta t\right) = \int_{0}^{\Delta t R_d} \tilde{n}\left(\boldsymbol{m}, \beta\right) \begin{bmatrix} 1 \\ \beta \\ \vdots \\ \beta^{N} \end{bmatrix} \mathrm{d}\beta \tag{2.77}$$

and the translation nilpotent matrix $\boldsymbol{A}$ is given as follows:

$$\boldsymbol{A} = \begin{bmatrix} 0 & & & & 0 \\ 1 & 0 & & & \\ & 2 & \ddots & & \\ & & \ddots & \ddots & \\ 0 & & & N & 0 \end{bmatrix} \tag{2.78}$$

and has the following property

$$\forall t, \beta \qquad \exp\left(\boldsymbol{A}t\right) \begin{pmatrix} 1 \\ \beta \\ \vdots \\ \beta^N \end{pmatrix} = \begin{pmatrix} 1 \\ \beta + t \\ \vdots \\ (\beta + t)^N \end{pmatrix} \tag{2.79}$$

Starting from the Maximum entropy reconstruction of the size distribution $\tilde{n}$ (the technique introduced in 2.7.3.2), the evaluation of the evaporation process through Eq.(2.76) is made in two steps.

First, the disappearance flux Φ^- at zero size is evaluated, and corresponds to the part of the moment that will disappear during a time step Δt. The moments are then corrected as:

$$\hat{\boldsymbol{m}} = \boldsymbol{m}\left(0\right) - \Phi^-\left(\Delta t\right) \tag{2.80}$$

where $\hat{\boldsymbol{m}} \in \mathbb{M}^N\left(\Delta t R_d, S_{max}\right)$). Then, as far as $\hat{\boldsymbol{m}}$ is computed, one needs to compute the remaining contribution

$$\exp\left(\Delta t R_d \boldsymbol{A}\right) \boldsymbol{m}\left(\Delta t\right) = \hat{\boldsymbol{m}}. \tag{2.81}$$

This accounts for evolving the size distribution by means of the translation of its moments in size phase space [120]. Recalling that for any $\hat{\boldsymbol{m}}$, there exists one unique lower principal representation technique of the vector of moments by using weights $(w_i)_{i\in[1,n]}$ and abscissas $\left(\hat{S}_i\right)_{i\in[1,n]} \in \left]\Delta t R_d, S_{max}\right[$, as introduced in 2.7.3.1. therefore the corrected moments are then expressed, thanks to the quadrature points i, as

$$\hat{\boldsymbol{m}} = \sum_{i=1}^{n} w_i \begin{pmatrix} 1 \\ \hat{S}_i \\ \hat{S}_i^2 \\ \vdots \\ \hat{S}_i^N \end{pmatrix} \tag{2.82}$$

where weights (w_i) and abscissas $\hat{S}_i^k$ are computed through the Product Difference (PD) algorithm, for $n = 2$, given in [123]. Thanks to the structure of matrix $\boldsymbol{A}$ given in

Eq.(2.78), $\boldsymbol{m}$ is computed through quadrature points associated to $\hat{\boldsymbol{m}}$ as

$$\boldsymbol{m}\left(\Delta t\right) = \sum_{i=1}^{n} w_i \begin{pmatrix} 1 \\ \hat{S}_i - R_d \Delta t \\ \left(\hat{S}_i - R_d \Delta t\right)^2 \\ \vdots \\ \left(\hat{S}_i - R_d \Delta t\right)^N \end{pmatrix}. \tag{2.83}$$

A detailed explication as well as the order of accuracy study of this evaporation scheme are found in Chapter 4.

2.7.4.2 Convection scheme

In this part, we briefly discuss about the numerical scheme used to discretize the equations of system (2.63). Because of the conservative form of system (2.63), the finite-volume method [102] is a natural candidate for its discretization.

Usually, high order finite volume methods use some non-constant reconstructions of the variables to evaluate the fluxes between the cells. But, the properties of the scheme are conditioned by the expression of the fluxes. Two difficulties arise here. The first one concerns the way to do the reconstruction of the moments in order to keep the integrity of moment set. It has been seen that for a high order in space scheme, an independent reconstruction of each moment does not insure that the moment space is preserved [124, 195]. A second difficulty concerns the computation of the fluxes from the reconstructed quantities. If an approximate time solver is used (Explicit Euler, Runge-Kutta), the fluxes computation will introduce errors for non constant reconstructions, and the preservation of the moment space would not be guaranteed any more.

In [87], a second order scheme through piecewise linear reconstructions of conserved quantities within cells are considered. This scheme is given in Chapter 3. In order to render realizable the scheme, the canonical moments, which are proven to be transported quantities by system (2.63) and to satisfy a maximum principle are used for the reconstruction. For the time integration, a kinetic-based numerical scheme, using the ideas developed by Bouchut [14], has been developed [87]. For the latter, the fluxes are accurately evaluated, thanks to the exact resolution of the kinetic equation.

2.7.5 Academic realizations through EMSM method

Through academic test-cases, the robustness, the accuracy and computational efficiency of the EMSM method along with its numerical schemes and algorithms have been tested within 2D test-cases [83, 87]. Firstly, its is implemented in a Eulerian solver dedicated to spray simulations called MUSES3D [30, 117], developed at EM2C Laboratory carried out considering a stationary gas-phase through Taylor Green Vortices. Then, the free jet simulations are conducted with an academic solver, coupling the ASPHODELE solver, developed at CORIA by Julien Reveillon and collaborators [149, 147], with MUSES3D. For the latter case, the gas is therefore not frozen.

The evaporating polydisperse spray described through EMSM method has been successfully validated from both qualitative and quantitative point of view, comparing it to MF method (see figure 2.7) for each simulation.

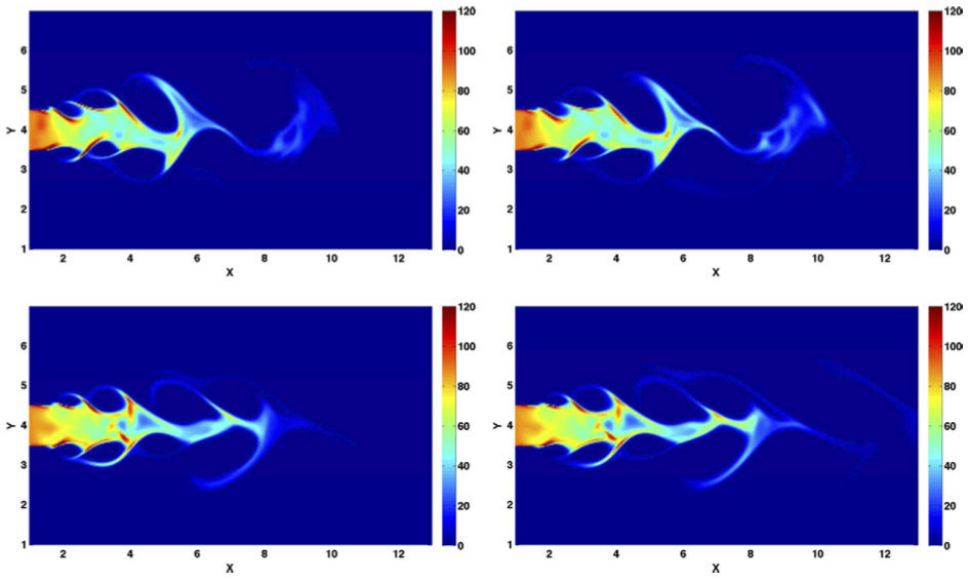

Figure 2.7: *Total mass density of the polydsiperse evaporating spray. (Top) Results at time $t = 15$. (Bottom) Results at time $t = 20$. (Left) EMSM model. (Right) Multi-fluid model with ten sections.)*

2.7.6 Recent extension of EMSM method to capture hetero-PTC: CSVM method

Despite its ability to accurately capture the size evolution of polydisperse evaporating droplets, the EMSM method lacks of accuracy to capture size-velocity correlations of droplets. This is due to the assumption of unique velocity for all droplets sharing the same location at a given time. Yet the work conducted in [189] has recently addressed this issue and a new method called Coupled Size-Velocity Moment (CSVM) method has been developed. In that case the NDF function is taken as the one given through Eq.(2.36). The profile for the velocity $\boldsymbol{u_d}$ has been presumed in terms of the size such that droplets with a zero size share the velocity with the gas-phase. Therefore, the numerical scheme originally developed for EMSM method has been extended since one needs to transport one more moment per spatial dimension due to the new size-velociy correlation assumption done at the kinetic level. Moreover, some further numerical efforts are required since the size-velocity correlation issue can yield distributions very close to the boundary of moment space. In such case, in order to make converge Maximum entropy algorithm with a reasonable CPU time and increase the accuracy of the method, the following numerical development has been achieved in [189]:

- To reduce the number of iterations needed for the Newton solver to converge, a tabulation method to calculate the NDF from its moments and associated interpolation methods have been investigated. It has been shown that the tabulation of the initial guess lowers significantly the number of Newton iterations needed, the fastest interpolation method being the more accurate third order polynomial reconstruction for the initial guess.

- To increase the accuracy of the reconstruction, an adaptive support for the Gauss-Legendre method has been implemented, that is, quadrature points are used only where the distribution is not too close to zero.

- At moment space boundaries, the distribution function represents the sum of diracs which involves a lower number of parameters less than the number of moments N. So the idea is that there is a transition zone in which one goes from a situation where N parameters (N moments) are needed (the interior of the moment space), to a situation where less parameters are needed (the frontier). This implies the use of less than N moments at borders of moment space. In this case, the number of moments used is defined such that one has the same level of accuracy as the interior of moment space obtained through N moments.

Through academic studies, the CSVM method along with its numerical tools have been proved to be more efficient than the original EMSM method in capturing the segregation inside the polydisperse spray with inertial droplets characterized by large Stokes number [189]. This is the direct consequence of capturing the hetero-PTC through CSVM method.

2.7.7 EMSM towards ICE applications

So far, all modeling and numerical efforts conducted for the EMSM method has been developed in the context of one-way coupling, that is the simple effect of the spray on the gas-phase. Moreover, its extension to Arbitrary Lagrangian Eulerian (ALE) formalism to treat moving geometries has gone through a preliminary step in [83, 86]. Following these achievements, the EMSM method has been partially implemented in the industrial code called IFP-C3D [12] dedicated to compressible, reactive flows [83, 86]. In the context of 2D and structured mesh configurations, the feasibility of injection computations through EMSM method has been demonstrated under IFP-C3D: both evaporating and non evaporating polydisperse droplets have been investigated. Some qualitative validations according to the widely used Lagrangian particles in IFP-C3D [46] have been done (i.e the figure 2.8).

Yet, within the framework of internal combustion engine (ICE) simulations, further improvement on EMSM need to be adressed in order to capture some relevant physical phenomena such as the two-way interaction of the polydisperse spray with its surrounding gas phase, the turbulence due to high Reynolds number two-phase flows and the compressible character of the spray prompted by important pressure changes during the normal engine operating conditions. Moreover, the ability of EMSM method to deal with complex 3-D geometries under realistic injection boundary conditions is required to be assessed.

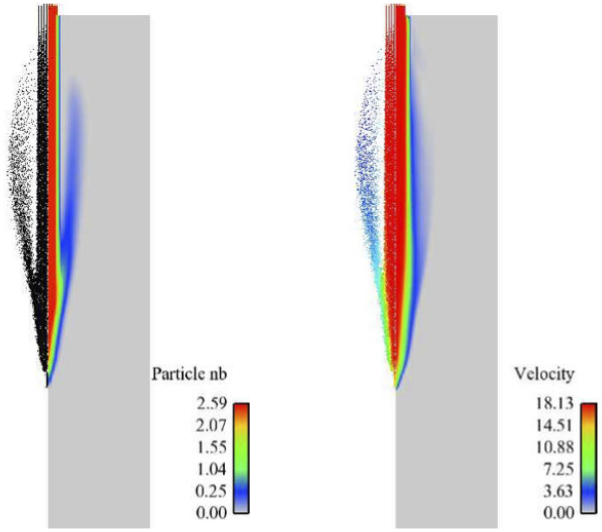

Figure 2.8: *Comparison of Lagrangian and Eulerian results for a polydisperse flow made of droplets of sauter mean radius* $20\mu m$ *within the context of one-way coupling through EMSM. In each figure, the Lagrangian particles are displayed on the left side on the domain, and the Eulerian field on the right side. Left: droplet number* m_0*; Right: particle velocity. (PhD of Damien Kah [83]).*

In the present thesis, the turbulent two-way polydisperse coupling modeling between the evaporating spray and the compressible gas is adressed. From the numerical point of view, the two-way coupling requires to cope with fast characteristic time scales associated to complex physics during the injection process such as mass, momentum and energy exchanges between the spray and the gas. Moreover, evaporating droplets will lead very small dynamic time scales in the computation domain. All these two-phase flow conditions make urgent the design of a numerical strategy which remains both accurate and stable eventhough the global simulation time step remains bigger then the smallest time scales associated to physics in ICE. Moreover, it should respect the realizability condition of the EMSM model. In that context, Chapter 3 is dedicated to a new two-way coupling strategy respecting all these constraints, while being implemented in IFP-C3D software under the ALE formalism. In Chapter 4, a numerical analysis of the two-way coupling strategy, first discussed in Chapter 3, is conducted. The influence of the time dependency of the evaporation law on the two-way coupling resolution is also discussed. In both Chapter 3 and 4, the two-way coupling numerical strategy will be assessed under injection test cases with IFP-C3D software. Moreover, the feasibility under complex 3D geometry with realistic injection conditions will be qualitatively investigated at the end of Chapter 4.
Based on the discussion conducted in sections 2.4 and 2.5 of the present Chapter, the RA turbulence modeling originally developed in [64] for two-way coupled monopdisperse disperse-flows will be extended to the two-way polydisperse coupling modeling between the evaporating spray and the compressible gas. The new turbulence model will be assessed

through homogeneous simulations based on data extracted from ICE studies under IFP-C3D with Lagrangian particles [12].

Chapter 3

Two-way coupling modeling between the polydisperse evaporation spray and the compressible gas

This chapter is from the text of the article submitted in the scientific journal [84]:

- D. Kah, O. Emre, Q. H. Tran, S. de Chaisemartin, S. Jay, F. Laurent, and M. Massot, High order moment method for polydisperse evaporating spray with mesh movement: application to internal combustion engines, Submitted, (2014).

3.1 Introduction

Fully integrated reactive simulations with spray in internal combustion engines have become a critical target in the automotive industry, where CFD has an increasing impact in the decision process for the design of new prototypes. If a substantial level of maturity has been reached for the simulation of gases, it is not exaggerated to claim that the description of the fuel liquid jet in the chamber still requires major improvements.

There is, however, an imperious need to model the fuel liquid jet from the very moment it is injected until it eventually becomes a cloud of polydisperse droplets after secondary atomization. For instance, in reactive cases, the gaseous fuel mass fraction is a key parameter that monitors the final temperature and species concentration issued from the combustion process. Several key properties of the engines, such as its energetic and environmental efficiencies depend on these elements. Models relying on a DNS framework can capture the whole jet dynamics in the chamber for a limited range of Weber and Reynolds numbers. But both the computational resources required as well as the modeling and physics of topology changes at small scales, make it unaffordable in terms of the range of scales to be resolved for realistic conditions of industrial interest. Reduced order models are then a powerful alternative as it allows computations to be done at a reasonable cost, regardless of the chosen framework, such as LES or RANS.

Two families of reduced models can be found, based on different ground physical assumptions pertaining to the area under study. The first one, the class of two-fluid models, provides an Eulerian description of the dense fuel region close to the injector,

referred to as separate phase flow [23, 22, 105, 6, 82, 158, 3, 89, 99]. It provides some level of description of the interface geometry depending on the modeling assumptions for potential equilibrium (see [83] for a general classification). The second modeling family relies on a statistical description of the particles/droplets far from injection when the atomization process has been fully completed. The particle properties are monitored by a number density function (NDF) that is solution of a kinetic equation [61, 116, 119]. Since the direct resolution of the kinetic equation is often intractable due to the large number of independent variables, stochastic Lagrangian methods "discretize" the NDF into "parcels", the dynamics of which is integrated using standard ODE solvers. This approach has been widely used and has shown to be efficient in numerous situations [133, 4, 147, 204, 74, 180]. While quite accurate, its main drawback is the coupling of a Eulerian description for the gaseous phase to a Lagrangian description of the disperse phase, thus offering limited possibilities of vectorization/parallelization. Besides, as in any statistical approach, Lagrangian methods require a relatively large number of parcels to control statistical noise, especially in the unsteady and polydisperse configurations we target, and thus can be computationally expensive, even if some recent contributions have allowed some progress [16].

An alternative to the Lagrangian approach is an Eulerian moment method. Potentially, Eulerian methods can be a breakthrough in the aspects aforementioned, but the Eulerian description of some spray features seems less natural and calls for some endeavor. Polydispersity is one of these features. The closure of the velocity moments conditioned on size is classical and conducted through a hydrodynamic limit leading to an equilibrium velocity distribution, i.e., Maxwell-Boltzmann distribution up to zero temperature in the framework of direct numerical simulation [30, 94, 85]. Such an approach is known to be valid for Stokes number up to approximatively one, when droplet trajectory crossing is very limited [7]; beyond such a limit another closure has to be chosen (see [188, 187, 20, 190, 19, 18, 112] and references therein) in order to describe statistical and deterministic trajectory crossing. Once a closure has been chosen in terms of velocity moments conditioned on droplet size, there are two options available for capturing the dynamics in the size phase space. One can either rely on size phase space discretization, with low order size moments in each section, as done in the multi-fluid approach developed in [188, 30, 94, 31] from [73]. The multi-fluid model considers only one size moment which accounts for the liquid mass density on small intervals of the size phase space called sections. Formally, the disperse phase is composed of several fluids exchanging mass, momentum and heat with each other and with the gas through evaporation, drag and heat exchange. This model has shown to yield simple transport algorithms for transport in physical space in [30, 31] implemented on parallel architectures [68, 66]. Another path to the description of polydispersity is to increase the amount of information in each section such as in [40, 41] when a very accurate description of the size distribution is required. Potentially a hybrid method can be conceived such as in [87, 189], but the ultimate choice is to use a single section for evaporating sprays with a high order moment method in order to describe polydispersity, an alternative solution which represents a very interesting tool for automotive engine simulations.

At present, several moment methods have been designed in order to treat size polydispersity. The first one consists in solving the evolution of moments of a prescribed NDF,

e.g., a log-normal law [130]. Presumably, this is very interesting since knowing the a priori profile of the NDF makes its reconstruction from the moments much easier. However, this assumption is restrictive in terms of the coverage of the physical processes. Moreover, this approach leads to serious numerical instabilities thus preventing its use for the treatment of an evaporating spray, since during the computation, a log-normal distribution function might not be reconstructed from the moment set dynamics. Another solution is high order moment methods, either quadrature method of moment (QMOM) where the dynamics of moments are evaluated after closing the source terms using quadrature methods (see [124] for example and references therein), or Direct Quadrature Method of Moment (DQMOM) [106] wherein equations are directly written on the quadrature weights and abscissas which describe the reconstructed distribution function having the same moments. Such methods have proved to be very efficient in a number of configurations, such as agglomeration, sintering, coagulation-fragmentation. But when it comes to accurately predicting the evaporating flux at zero size, which is a pointwise value to be reconstructed from the set of moments, these methods have shown their limits [65], even if some new developments have appeared [199], where some of the issues have been solved. The second problem is related to the transport in physical space. There exists a stumbling block for the usual approaches using high order moment method resolved with at least second-order finite volume methods. The transport algorithm does not systematically preserve the moment space, which means that slope reconstruction of moments by piecewise polynomials are likely to create vectors whose components fail to be the moments of a size distribution. One way to resolve this is to impose a posteriori to the moment vector to stay inside the realizable moment space, but this degrades the computational efficiency as well as the accuracy. We thus want to rely on a robust and built-in realizable numerical methods and algorithms.

Further studies have been undertaken and both issues have been successfully addressed. First, for the treatment of the evaporation term, the high order moment method together with the associated numerical scheme presented in [120] proposes a solution with a high level of accuracy. It can be effectively used for quantitative predictions of an evaporating spray. Second, a high order transport scheme preserving the integrity of the moment set is provided in [87]. It makes use of two ingredients: the reconstruction of the independent canonical moments [38], as well as the use of an exact time integration scheme, thus guaranteeing that no truncation error is introduced. These modeling and algorithmic tools are referred to as the EMSM (Eulerian Multi-Size Moment) model. Its potential has been demonstrated through test cases using an academic solver. Such an approach has also been compared to the methods introduced in [191]. As explained in [87], both classes of aerosols and sprays can be described by this model[1]. However, these preliminary studies have been restricted to one-way coupling, where the preservation of the realizability condition and high order numerical methods are achieved through operator splitting and developed in the framework of fixed meshes, be it structured or unstructured. For the purpose of dealing with internal combustion engines and proving that these methods are a good candidate for such configurations, these restrictions have

[1]What distinguishes these classes is their Stokes number based on some typical gas flow time. It is very small for aerosol, thus particles are transported at the carrier phase velocity. But for spray particles the Stokes number reaches higher values, accounting for the fact that they have their own dynamics.

to be alleviated and overcome.

In this paper, we focus on the spray class, even if most of what is investigated in the paper can be extended to aerosols. The purpose of the present contribution is three-fold. It aims firstly at extending the EMSM model to a two-way coupling framework, where the influence of the particles on the gas phase is taken into account, while maintaining the properties of the numerical strategy adopted so far, a robust and accurate resolution with built-in realizability preserving algorithms, as well as the ability of coping with very stiff source terms through implicit resolution. The second objective is to extend the numerical methods to moving computational domains required in the field of ICE. The latter objective is naturally motivated by the observation that the combustion chamber, where fuel injection takes place, is bounded by a moving piston. The appropriate tool to help us take up this challenge is the Arbitrary Lagrangian-Eulerian (ALE) formalism [43, 78, 79, 57], which lies at the heart of the RANS software IFP-C3D [12]. Considering the amount of material needed in order to reach the proposed objectives, we have decided to restrict ourselves to simplified models (Stokes drag, no heat exchange except through evaporation, simple evaporation laws) in order to prove the efficiency and potential of the proposed method, while the extension to complex models used in realistic configurations, as well as the detailed analysis of the convergence rate of the proposed methods, are postponed to a companion paper [55]. The third objective is to implement the method in the industrial code IFP-C3D and to adapt the new numerical methods to comply with the code structure, in order to propose a series of simulations in realistic injection configurations, where we can assess the achievements of the method in comparison with Lagrangian simulations classically available in the code. This should prove the potential of Eulerian high order moment models and related resolution strategy for ICE simulations.

The paper is then organized as follows. We first derive the two-way coupled EMSM model from the kinetic level of description. Section 3.3 is devoted to an overview of the numerical method, where we introduce the splitting strategy, the new numerical strategy in order to cope with stiff source terms implicitly while preserving the robustness of the original method and finally the ALE formalism. Specific details at the fully discrete level are provided in an Appendix in order to allow the possibility of reproducing the proposed simulations conducted in the paper. The theoretical and numerical issues associated with each phase are discussed, with a particular emphasis laid on the realizability of moments. In §3.4, we focus on the two novel features of the proposed method, namely the two-way coupling and the transport of moments, and provide a set of verifications configurations. For each feature, we present numerical results in simplified situations to illustrate the capability of the numerical algorithms. The implementation of the method in the industrial software IFP-C3D as well as the related validation simulations by comparison with the structured mesh DNS code MUSES3D [30, 67] are conducted in §3.5. The stability through mesh movement is assessed, evaporation and transport implemented algorithms are validated by a comparison with a DNS computation using a completely different numerical algorithm. Finally, the feasibility of the simulation of the injection of a spray in a chamber with two-way coupling using IFP-C3D is demonstrated in §3.6, paving the way for computations in real injection conditions.

3.2 Derivation of the EMSM model

The purpose of the present section is to derive the macroscopic Eulerian model for the spray. As done in [87], the derivation starts from a kinetic equation describing the spray at the mesoscopic scale. A closure assumption in velocity phase space conditioned in droplet size is first introduced, leading to an intermediate semi-kinetic system of conservation equations. A high order moment method in size is used to come up with the final macroscopic conservation laws. In the present paper, we will restrict ourselves to simple models, for the sake of legibility. The proposed approach can be extended easily to more complex models, as shown in a companion paper [55]. The underlying assumptions and physical validity of the proposed approach are highlighted in this section. We introduce a non-dimensional form of the equations and show some key properties satisfied at the continuous level by the obtained systems of conservation equations. We will take benefit of these properties to build a dedicated numerical method described in part 3.3.

3.2.1 From the kinetic equation to a semi-kinetic system

We take the general point of view of a dilute droplet spray described by a number density function (NDF) f such that

$$f(t, \boldsymbol{x}, S, \boldsymbol{u}, T)\, \mathrm{d}\boldsymbol{x}\, \mathrm{d}S\, \mathrm{d}\boldsymbol{u}\, \mathrm{d}T$$

represents, for each time t, the number of particles lying at position $\boldsymbol{x} = (x_1, x_2, x_3)$ within a volume element $\mathrm{d}\boldsymbol{x}$, moving at velocity $\boldsymbol{u} = (v_1, v_2, v_3)$ within a velocity element $\mathrm{d}\boldsymbol{u}$, having size S and temperature T within the corresponding phase element $\mathrm{d}S\,\mathrm{d}T$. In the applications under consideration, particles undergo evaporation and drag. In such a context, the NDF f is governed by the kinetic equation

$$\partial_t f + \nabla_{\boldsymbol{x}} \cdot (\boldsymbol{u} f) - \partial_S(K f) + \partial_T(Q f) + \nabla_{\boldsymbol{v}} \cdot (\boldsymbol{F} f) = 0, \tag{3.1}$$

which is also referred to as the Williams-Boltzmann equation [193]. In the left side of equation (3.1), the second term expresses the transport in the physical space, the third term reflects the droplet evaporation, the fourth term accounts for the heat exchange with the surrounding gas, and the fifth term stands for the drag exerted by the gas. The scalars K and Q are, respectively, the evaporation rate (at which the droplet surface decreases) and the droplet energy change rate. As for the vector $\boldsymbol{F}$, it is the droplet acceleration. It is taken for granted that K, Q and $\boldsymbol{F}$ are given functions of $(t, \boldsymbol{x}, S, \boldsymbol{u}, T)$. In fact, since $\boldsymbol{F}$ is the drag force due to the gas, it also depends on some extra variables associated with the gas phase.

What we do exactly mean by the "size" S of each droplet particle is its surface. As the particles are assumed to be spherical, we could also have decided to work with their radius r or their volume V. With a slight abuse of notation, we would of course have had

$$f(t, \boldsymbol{x}, r, \boldsymbol{u}, T)\, \mathrm{d}r = f(t, \boldsymbol{x}, S, \boldsymbol{u}, T)\, \mathrm{d}S = f(t, \boldsymbol{x}, V, \boldsymbol{u}, T)\, \mathrm{d}V$$

upon the change of variables

$$V = \frac{4}{3}\pi r^3 \qquad \text{and} \qquad S = 4\pi r^2. \tag{3.2}$$

As mentioned in the litterature describing kinetic-based spray model derivations ([30] and [83] for instance), the use of spray models based on a Williams-Boltzmann kinetic equation is associated with various assumptions :

- droplets are considered as point particles, thus no finite size effect is taken into account and no volume fraction appears in gas phase equations;
- long distance interactions are not accounted for.

In the present contribution, the computation configurations involve a relatively low spray volume fraction ($2.5 \cdot 10^{-4}$) and mass loading (around 0.2). In these conditions, the previous assumptions stand. These conditions will also justify the way we consider 2-way coupling, through source terms due to the spray in the gas equations, see for example [94] and [92].

To close the model derived in the following, we choose to limit ourselves to simple spray physical models : say d-square law evaporation model and Stokes drag force. As previously said this restriction is not a limit of the approach, used with complex models in [55], but it allows to focus on the difficulties of the derivation itself. No additional difficulties are to be found when coupling with more realistic models.

Starting from the microscopic model (3.1), our purpose is to work out a closed system of equations involving the total number density

$$n(t,\boldsymbol{x},S) = \iint_{\mathbb{R}^3\times\mathbb{R}^+} f(t,\boldsymbol{x},S,\boldsymbol{u},T)\,\mathrm{d}\boldsymbol{u}\,\mathrm{d}T, \tag{3.3a}$$

the mean particle velocity

$$\boldsymbol{u_d}(t,\boldsymbol{x},S) = \frac{1}{n(t,\boldsymbol{x},S)} \iint_{\mathbb{R}^3\times\mathbb{R}^+} f(t,\boldsymbol{x},S,\boldsymbol{u},T)\boldsymbol{u}\,\mathrm{d}\boldsymbol{u}\,\mathrm{d}T, \tag{3.3b}$$

and the mean particle temperature

$$T_d(t,\boldsymbol{x},S) = h_d^{-1}\left(\frac{1}{n(t,\boldsymbol{x},S)} \iint_{\mathbb{R}^3\times\mathbb{R}^+} f(t,\boldsymbol{x},S,\boldsymbol{u},T)h_d(T)\,\mathrm{d}\boldsymbol{u}\,\mathrm{d}T\right), \tag{3.3c}$$

for some enthalpy density h_d, required to be increasing (therefore invertible) function of the temperature. This system is said to be *semi-kinetic*. To this end, and in view of the closure assumption made in the Multi-Fluid model [30], we assume f to be of the form

$$f(t,\boldsymbol{x},S,\boldsymbol{u},T) = n(t,\boldsymbol{x},S)\,\delta(T - T_d(t,\boldsymbol{x},S))\,\delta(\boldsymbol{u} - \boldsymbol{u_d}(t,\boldsymbol{x},S)). \tag{3.4}$$

In other words, f is a distribution with a single velocity and a single temperature conditioned by the size. This corresponds to a regime when the particle Stokes number —that is particle inertia with respect to a typical gaseous flow time scale, which will be defined in §3.2.3— is small enough in order to neglect the velocity dispersion among particles, yet large enough so that the particles have their own velocity, different from the gas one[2].

[2]Let us underline that if this property is satisfied at time $t = 0$ and under some reasonable assumption on the gaseous velocity phase, which were mathematically characterized in [30, 116], this property is preserved as long as the Stokes number of the particles is below a critical Stokes number and there is a one-to-one correspondence between the kinetic or mesoscopic level of description and the macroscopic one, as for the normal solutions of the Botlzmann equation in the limit of hydrodynamic limit.

According to the classification established by Balachandar and Eaton in [7], this assumption is applicable for a range of Stokes between 0.2 and 1. For more inertial particles, Lagrangian methods can be thought of, as well as more refined Eulerian approaches, see for example [187, 190, 19, 18, 112].

The semi-kinetic equations are obtained by integrating (3.1) with respect to $(\boldsymbol{u}, T)$ after multiplying it by 1, $\boldsymbol{u}$, and $h_d(T)$. Thanks to the mono-kinetic assumption (3.4), this operation yields

$$\begin{aligned}
&\partial_t(n) &&+\nabla_{\boldsymbol{x}}\cdot(n\boldsymbol{u_d}) &&-\partial_S(Kn) &&=0, &(3.5a)\\
&\partial_t(n\boldsymbol{u_d}) &&+\nabla_{\boldsymbol{x}}\cdot(n\boldsymbol{u_d}\otimes\boldsymbol{u_d}) &&-\partial_S(Kn\boldsymbol{u_d}) &&-n\boldsymbol{F}_d=0, &(3.5b)\\
&\partial_t(nh_d) &&+\nabla_{\boldsymbol{x}}\cdot(nh_d\boldsymbol{u_d}) &&-\partial_S(Knh_d) &&-nC_{p,l}Q=0, &(3.5c)
\end{aligned}$$

where H, K, $\boldsymbol{F}_d$ are now evaluated at $(t, \boldsymbol{x}, S, \boldsymbol{u_d}, T_d)$, and $C_{p,l}(T_d) = h_d'(T_d)$ is the average heat capacity of the liquid. The actual value of $\boldsymbol{F}_d$, given by the Stokes law

$$\boldsymbol{F}_d(S, \boldsymbol{u_d}) = \frac{18\pi\mu_g}{\rho S}(\boldsymbol{u_g} - \boldsymbol{u_d}), \tag{3.6}$$

involves two quantities coming from the surrounding gas, namely, its dynamic viscosity μ_g and its local velocity $\boldsymbol{u_g}$. We are thus led to momentarily leave aside the spray system and to elaborate on the equations for the gas phase.

The gas is modeled by the compressible Navier-Stokes system, augmented with sources terms describing the interaction with the particles, i.e.,

$$\begin{aligned}
&\partial_t(\rho_g) &&+\nabla_{\boldsymbol{x}}\cdot(\rho_g\boldsymbol{u_g}) &&=\mathfrak{S}^{\rho}, &(3.7a)\\
&\partial_t(\rho_g\boldsymbol{u_g}) &&+\nabla_{\boldsymbol{x}}\cdot(\rho_g\boldsymbol{u_g}\otimes\boldsymbol{u_g}+P_g\boldsymbol{I}) &&=\mathfrak{S}^{\rho\boldsymbol{u}}+\nabla_{\boldsymbol{x}}\cdot(\boldsymbol{\Sigma}_g), &(3.7b)\\
&\partial_t(\rho_g E_g) &&+\nabla_{\boldsymbol{x}}\cdot(\rho_g E_g\boldsymbol{u_g}+P_g\boldsymbol{u_g}) &&=\mathfrak{S}^{\rho e}+\nabla_{\boldsymbol{x}}\cdot(\boldsymbol{\Sigma}_g\cdot\boldsymbol{u_g}), &(3.7c)
\end{aligned}$$

where $\boldsymbol{I}$ is the identity tensor, $\boldsymbol{\Sigma}_g = \mu_g(T_g)(\nabla_{\boldsymbol{x}}\boldsymbol{u_g} + \nabla_{\boldsymbol{x}}\boldsymbol{u_g}^T) - \frac{2}{3}\mu_g(T_g)(\nabla_{\boldsymbol{x}}\cdot\boldsymbol{u_g})\boldsymbol{I}$ is the classical Newtonian viscous stress tensor, and (see [83, p. 41])

$$\begin{aligned}
\mathfrak{S}^{\rho} &= \int\rho_d V' Kn\,\mathrm{d}S, &(3.8a)\\
\mathfrak{S}^{\rho\boldsymbol{u}} &= \int\rho_d V' Kn\boldsymbol{u_d}\,\mathrm{d}S - \int\rho_d Vn\boldsymbol{F}_d\,\mathrm{d}S, &(3.8b)\\
\mathfrak{S}^{\rho e} &= \int\rho_d V' Knh_d\,\mathrm{d}S - \int\rho_d VnC_{p,l}H\,\mathrm{d}S. &(3.8c)
\end{aligned}$$

In formulae (3.8), as well as in equation (3.6), the symbol ρ denotes the density of the liquid droplets. This density is assumed to be a given data. We recall that V is the volume of a droplet. Its value was given in equation (3.2) as a function of the radius r, but here must be thought of as a function of the surface S. More explicitly, we have

$$V(S) = \frac{S^{3/2}}{6\pi^{1/2}}, \qquad \text{with} \qquad V'(S) = \frac{S^{1/2}}{4\pi^{1/2}}. \tag{3.9}$$

For simplicity, we shall restrict ourselves to an ideal gas governed the law of state

$$P_g = (\gamma_g - 1)\rho_g(E_g - \tfrac{1}{2}\|\boldsymbol{u_g}\|^2) \qquad \text{and} \qquad T_g = \frac{P_g}{R_g\rho_g} \tag{3.10}$$

for some $\gamma_g > 1$ and $R_g > 0$. Note that, while the gas unknown functions ρ_g (density), $\boldsymbol{u_g}$ (velocity), E_g (total energy) depend merely on $(t, \boldsymbol{x})$, the spray unknown functions n, $\boldsymbol{u_d}$, h_d depend on $(t, \boldsymbol{x}, S)$.

3.2.2 From the semi-kinetic system to the multi-size moment system

The semi-kinetic system (3.5) for droplets is already a significant step forward but still has a continuous size phase space of dimension one. Our ultimate goal, however, is to simplify it further into a macroscopic model under the form of a system of conservation equations, the unknowns of which are moment in size, that is functions of only $(t, \boldsymbol{x})$. In the transformation process, it is naturally desirable that the new system could somehow "remember" the effect of the size S. For the sake of legibility of the paper, we will introduce a set of stronger hypotheses. In addition to the ansatz (3.4), we now prescribe that

$$\boldsymbol{u_d}(t, \boldsymbol{x}, S) = \boldsymbol{u_d}(t, \boldsymbol{x}) \qquad \text{and} \qquad K(t, \boldsymbol{x}, S, \boldsymbol{u_d}, T_d) = K(t, \boldsymbol{x}, \boldsymbol{u_d}, T_d). \tag{3.11}$$

To put it another way, neither the particle velocity nor the evaporation rate depend on the size variable. More advanced modeling is available with Eulerian moment method approaches, and size-velocity correlation could have been taken into account enriching the present model as done in [188]. We choose not to introduce this further modeling, requiring more complex algebraic computations, and to present the concepts on simplified test cases. Such a extension will be thought of later on.

This enables us to easily derive conservation laws for the moments, defined as

$$m_k(t, \boldsymbol{x}) = \int S^k n(t, \boldsymbol{x}, S)\, \mathrm{d}S, \qquad k \in \mathbb{N}. \tag{3.12}$$

A straightforward calculation shows that

$$\partial_t(m_0) + \nabla_{\boldsymbol{x}} \cdot (m_0 \boldsymbol{u_d}) = -Kn(t, \boldsymbol{x}, S = 0) \tag{3.13a}$$

for $k = 0$, with $Kn(t, \boldsymbol{x}, S = 0)$ being the disappearance rate of droplets through evaporation, and

$$\partial_t(m_k) + \nabla_{\boldsymbol{x}} \cdot (m_k \boldsymbol{u_d}) = -kKm_{k-1} \tag{3.13b}$$

for $k \geq 1$.

In practice, we will work with a sequence of $N+1$ size moments, $\boldsymbol{m} = (m_0, m_1, \ldots, m_N)$, the number of moments used being chosen for a good compromise between precision and computational cost related to involved algebraic computations. We need to derive a self-consistent system of conservation equation with source terms, which does not involve any more the relation to the kinetic level of description. This gives rise to the problem of designing a suitable approximation of n from the knowledge of the moment sequence, the value at $S = 0$ appearing in the right-hand side of equation (3.13a). A solution to this problem was proposed by Massot et al. [120]. By performing an entropy maximization [125] in the sense of information theory, it is possible to reconstruct a unique distribution function $\tilde{n}(\boldsymbol{m}, S)$, the $N + 1$ first moments of which coincide with $(m_0, m_1, \ldots, m_N)$ [125, 189]. At this level, we should rewrite a whole set of equations on the related approximation of the size moments we are working with. However, with a slight abuse of notation for the sake of legibility, we will keep the original notations and replace equation

(3.13a) by its approximated counterpart, which is autonomous from the original kinetic level of description :

$$\partial_t(m_0) + \nabla_{\boldsymbol{x}} \cdot (m_0 \boldsymbol{u_d}) = -K\tilde{n}(\boldsymbol{m}, 0). \tag{3.14}$$

Another straightforward calculation shows that

$$\partial_t(m_0 \boldsymbol{u_d}) + \nabla_{\boldsymbol{x}} \cdot (m_0 \boldsymbol{u_d} \otimes \boldsymbol{u_d}) = \int \boldsymbol{F}_d n \, \mathrm{d}S \tag{3.15a}$$

for $k = 0$, and

$$\partial_t(m_k \boldsymbol{u_d}) + \nabla_{\boldsymbol{x}} \cdot (m_k \boldsymbol{u_d} \otimes \boldsymbol{u_d}) = \int S^k \boldsymbol{F}_d n \, \mathrm{d}S - kKm_{k-1}\boldsymbol{u_d} \tag{3.15b}$$

for $k \geq 1$. Of these equations, we keep only that corresponding to $k = 1$.

The rationale for such a choice comes from several reasons. First we work with integer surface moments for both physical reasons related to evaporation, drag and heat transfer, coupled to computational efficiency and accuracy reasons (see [120, 87]). Besides, we want to involve only conservative variables for the accurate and stable treatment of the convective terms. Finally, out of the conserved size moments, the form (3.6) of the drag $\boldsymbol{F}_d$ acceleration is in favor of $k = 1$. Thus the natural form of the momentum evolution equation reads :

$$\partial_t(m_1 \boldsymbol{u_d}) + \nabla_{\boldsymbol{x}} \cdot (m_1 \boldsymbol{u_d} \otimes \boldsymbol{u_d}) = \tfrac{18\pi}{\rho} \mu_g m_0 (\boldsymbol{u_g} - \boldsymbol{u_d}) - kKm_0 \boldsymbol{u_d}. \tag{3.16}$$

Nonetheless, in order to ensure total mass and momentum conservation, half-integral moments will be involved. Indeed the mass of the spray is obtained by the 3/2-order size moment ; spray mass and momentum conservations read :

$$\partial_t(m_{3/2}) + \nabla_{\boldsymbol{x}} \cdot (m_{3/2} \boldsymbol{u_d}) = -\tfrac{3}{2} K m_{1/2}, \tag{3.17a}$$

$$\partial_t(m_{3/2} \boldsymbol{u_d}) + \nabla_{\boldsymbol{x}} \cdot (m_{3/2} \boldsymbol{u_d} \otimes \boldsymbol{u_d}) = -\tfrac{3}{2} K m_{1/2} \boldsymbol{u_d} + (18\pi/\rho_d) \mu_g m_{1/2} (\boldsymbol{u_g} - \boldsymbol{u_d}). \tag{3.17b}$$

Combining (3.17) with equations (3.7a)–(3.7b) of the gas, which spell out as

$$\partial_t(\rho_g) + \nabla_{\boldsymbol{x}} \cdot (\rho_g \boldsymbol{u_g}) = \tfrac{1}{4\pi^{1/2}} \rho_d K m_{1/2}, \tag{3.18a}$$

$$\partial_t(\rho_g \boldsymbol{u_g}) + \nabla_{\boldsymbol{x}} \cdot (\rho_g \boldsymbol{u_g} \otimes \boldsymbol{u_g} + P_g \boldsymbol{I}) = \tfrac{1}{4\pi^{1/2}} \rho_d K m_{1/2} \boldsymbol{u_d} - \tfrac{18\pi}{6\pi^{1/2}} \mu_g m_{1/2} (\boldsymbol{u_g} - \boldsymbol{u_d}) + \nabla_{\boldsymbol{x}} \cdot (\boldsymbol{\Sigma}_g), \tag{3.18b}$$

the zeroth-order source terms cancel out and we end up with the conservation laws

$$\partial_t(\rho_g + \tfrac{1}{6\pi^{1/2}} \rho_d m_{3/2}) + \nabla_{\boldsymbol{x}} \cdot (\rho_g \boldsymbol{u_g} + \tfrac{1}{6\pi^{1/2}} \rho_d m_{3/2} \boldsymbol{u_d}) = 0, \tag{3.19a}$$

$$\partial_t(\rho_g \boldsymbol{u_g} + \tfrac{1}{6\pi^{1/2}} \rho_d m_{3/2} \boldsymbol{u_d}) + \nabla_{\boldsymbol{x}} \cdot (\rho_g \boldsymbol{u_g} \otimes \boldsymbol{u_g} + P_g \boldsymbol{I} + \tfrac{1}{6\pi^{1/2}} \rho_d m_{3/2} \boldsymbol{u_d} \otimes \boldsymbol{u_d}) = \nabla_{\boldsymbol{x}} \cdot (\boldsymbol{\Sigma}_g), \tag{3.19b}$$

for the total mass and total momentum. Let us underline that these half-integral moments are functions of the vector of conserved integer moments $\boldsymbol{m}$ through $\tilde{n}(\boldsymbol{m}, t)$ and will thus be used in the method and system (3.19) and will be satisfied in the numerical method.

Returning to the multi-moment model, we now make a new assumption by asserting that

$$T_d(t,\boldsymbol{x},S) = T_{d0} \qquad \text{and} \qquad H(t,\boldsymbol{x},S,\boldsymbol{u_d},T_d) = 0. \tag{3.20}$$

The spray flow is assumed isothermal and the heat transfer term can be neglected [167, 72]. Contrary to (3.4) and (3.11), the last assumption (3.20) is in no way essential. It is meant to help us obtaining a simplest possible macroscopic model. More complex models can be envisaged [120]. As a matter of fact, even assumption (3.11) can be relaxed and models with size-dependent velocity can be considered, as exemplified in the recent work of Vié et al. [189]. But let us go back to assumption (3.20) and see what it implies. From $T_d = T_{d0}$, we infer that $h_d = h_d(T_{d0})$ is a also constant. Combining this with $H = 0$, it clearly appears that the enthalpy equation (3.5c) is no more than a scalar multiple of the number density equation (3.5a). Being redundant, the enthalpy equation can be left out.

Let us recapitulate the EMSM model. It consists of two coupled sets of PDEs, the unknowns of which are functions of $(t,\boldsymbol{x})$.

- For the spray, find $(\boldsymbol{m},\boldsymbol{u_d}) = (m_0, m_1, \ldots, m_N, \boldsymbol{u_d})$ such that

$$\begin{aligned}
&\partial_t(m_0) &&+\nabla_{\boldsymbol{x}}\cdot(m_0\boldsymbol{u_d}) &&= -\ K\tilde{n}(\boldsymbol{m}, S=0), && (3.21a)\\
&\partial_t(m_1) &&+\nabla_{\boldsymbol{x}}\cdot(m_1\boldsymbol{u_d}) &&= -\ Km_0, && (3.21b)\\
&\partial_t(m_2) &&+\nabla_{\boldsymbol{x}}\cdot(m_2\boldsymbol{u_d}) &&= -\ 2Km_1, && (3.21c)\\
&\ \vdots &&\ \vdots &&\ \vdots &&\\
&\partial_t(m_N) &&+\nabla_{\boldsymbol{x}}\cdot(m_N\boldsymbol{u_d}) &&= -NKm_{N-1}, && (3.21d)\\
&\partial_t(m_1\boldsymbol{u_d}) &&+\nabla_{\boldsymbol{x}}\cdot(m_1\boldsymbol{u_d}\otimes\boldsymbol{u_d}) &&= -\ Km_0\boldsymbol{u_d} + \tfrac{18\pi}{\rho}\,\mu_g m_0(\boldsymbol{u_g}-\boldsymbol{u_d}), && (3.21e)
\end{aligned}$$

  where $\tilde{n}(\boldsymbol{m}, S)$ is the entropy-maximizing reconstructed distribution [120]. In this paper, we set $N = 3$. This choice was shown [87] to be a good compromise between accuracy and efficiency.

- For the gas, find $(\rho_g, \boldsymbol{u_g}, E_g)$ such that

$$\begin{aligned}
&\partial_t(\rho_g) &&+\nabla_{\boldsymbol{x}}\cdot(\rho_g\boldsymbol{u_g}) &&= \tilde{\mathfrak{S}}^{\rho}, && (3.22a)\\
&\partial_t(\rho_g\boldsymbol{u_g}) &&+\nabla_{\boldsymbol{x}}\cdot(\rho_g\boldsymbol{u_g}\otimes\boldsymbol{u_g}+P_g\boldsymbol{I}) &&= \tilde{\mathfrak{S}}^{\rho\boldsymbol{u}}+\nabla_{\boldsymbol{x}}\cdot(\boldsymbol{\Sigma}_g), && (3.22b)\\
&\partial_t(\rho_g E_g) &&+\nabla_{\boldsymbol{x}}\cdot(\rho_g E_g\boldsymbol{u_g}+P_g\boldsymbol{u_g}) &&= \tilde{\mathfrak{S}}^{\rho e}+\nabla_{\boldsymbol{x}}\cdot(\boldsymbol{\Sigma}_g\cdot\boldsymbol{u_g}), && (3.22c)
\end{aligned}$$

  where

$$\begin{aligned}
\tilde{\mathfrak{S}}^{\rho} &= \textstyle\int \rho_d V' K\tilde{n}\,\mathrm{d}S, && = \tfrac{\rho_d}{4\pi^{1/2}}\,K\tilde{m}_{1/2} && (3.23a)\\
\tilde{\mathfrak{S}}^{\rho\boldsymbol{u}} &= \textstyle\int \rho_d V' K\tilde{n}\boldsymbol{u_d}\,\mathrm{d}S - \int \rho_d V\tilde{n}\boldsymbol{F}_d\,\mathrm{d}S && = \tfrac{\rho_d}{4\pi^{1/2}}\,K\tilde{m}_{1/2}\boldsymbol{u_d} - \tfrac{18\pi}{6\pi^{1/2}}\,\mu_g\tilde{m}_{1/2}(\boldsymbol{u_g}-\boldsymbol{u_d}), && (3.23b)\\
\tilde{\mathfrak{S}}^{\rho e} &= \textstyle\int \rho_d V' K\tilde{n}h_d\,\mathrm{d}S && = \tfrac{\rho_d}{4\pi^{1/2}}\,K\tilde{m}_{1/2}h_d && (3.23c)
\end{aligned}$$

  are the reconstructed counterparts of the original source terms (3.8) under the constraint $H = 0$. The ideal law of state (3.10) holds and the viscous stress tensor $\boldsymbol{\Sigma}_g$ is defined as before.

The full model (3.21)–(3.23) is called *two-way coupling* model. A simplified version, called *one-way coupling* model, is obtained by setting $\tilde{\mathfrak{S}}^{\rho} = \tilde{\mathfrak{S}}^{\rho \boldsymbol{u}} = \tilde{\mathfrak{S}}^{\rho e} = 0$. The one-way coupling model was investigated by Kah et al. [87] in order to demonstrate the potential of the EMSM approach regarding the dynamics of size moments.

3.2.3 Nondimensional formulation

To gain some insight, we formulate the above system with non-dimensional variables. Let L_0 be a reference length, U_0 be a reference velocity, and S_0 be a reference droplet size. We remark that S_0, usually taken to be the maximum size of droplets, can be very different from L_0^2 (or $4\pi L_0^2$), taken for example as an injector diameter in the applications considered in the paper. We introduce the dimensionless quantities

$$t^* = \frac{U_0}{L_0} t, \qquad \boldsymbol{x}^* = \frac{1}{L_0}\boldsymbol{x}, \qquad \boldsymbol{u}_{\boldsymbol{d}}^* = \frac{1}{U_0}\boldsymbol{u}_{\boldsymbol{d}}, \qquad S^* = \frac{1}{S_0} S, \qquad h^* = \frac{1}{U_0^2} h, \tag{3.24a}$$

$$n^* = L_0^3 S_0 n, \qquad \tilde{n}^* = L_0^3 S_0 \tilde{n}, \qquad m_k^* = \frac{L_0^3}{S_0^k} m_k, \qquad K^* = \frac{L_0}{S_0 U_0} K, \qquad \boldsymbol{F}_{\boldsymbol{d}}^* = \frac{L_0}{U_0^2} \boldsymbol{F}_d. \tag{3.24b}$$

Next, we take $\rho_0 = \rho_d$ (the constant density of each droplet particle) to be the reference density, T_0 (the constant temperature of the spray) to be the reference temperature. Then, $\mu_{g,0} = \mu_g(T_0)$ is the reference dynamic viscosity. Consider a second set of dimensionless quantities

$$\rho_g^* = \frac{1}{\rho_0}\rho_g, \qquad P_g^* = \frac{1}{\rho_0 u_0^2} P_g, \qquad \boldsymbol{u}_{\boldsymbol{g}}^* = \frac{1}{U_0}\boldsymbol{u}_{\boldsymbol{g}}, \qquad E_g^* = \frac{1}{U_0^2} E_g, \tag{3.25a}$$

$$T_g^* = \frac{1}{T_0} T_g, , \qquad R_g^* = \frac{T_0}{U_0^2} R_g \qquad \mu_g^* = \frac{1}{\mu_{g,0}}\mu_g, \qquad \boldsymbol{\Sigma}_{\boldsymbol{g}}^* = \frac{L_0^2}{\mu_{g,0} U_0} \boldsymbol{\Sigma}_g. \tag{3.25b}$$

Inserting (3.24) and (3.25) into (3.21)–(3.23) results in a non-dimensional version the EMSM model. This non-dimensional version consists of two parts.

- For the spray,

$$\begin{aligned}
\partial_{t^*}(m_0^*) \quad &+ \nabla_{\boldsymbol{x}^*} \cdot (m_0^* \boldsymbol{u}_{\boldsymbol{d}}^*) && = - \quad K^* \tilde{n}^*(\boldsymbol{m}^*, S^* = 0), && (3.26a)\\
\partial_{t^*}(m_1^*) \quad &+ \nabla_{\boldsymbol{x}^*} \cdot (m_1^* \boldsymbol{u}_{\boldsymbol{d}}^*) && = - \quad K^* m_0^*, && (3.26b)\\
\partial_{t^*}(m_2^*) \quad &+ \nabla_{\boldsymbol{x}^*} \cdot (m_2^* \boldsymbol{u}_{\boldsymbol{d}}^*) && = - \; 2K^* m_1^*, && (3.26c)\\
\quad \vdots \quad &\quad \vdots && \quad \vdots && \\
\partial_{t^*}(m_N^*) \quad &+ \nabla_{\boldsymbol{x}^*} \cdot (m_N^* \boldsymbol{u}_{\boldsymbol{d}}^*) && = -NK^* m_{N-1}^*, && (3.26d)\\
\partial_{t^*}(m_1^* \boldsymbol{u}_{\boldsymbol{d}}^*) &+ \nabla_{\boldsymbol{x}^*} \cdot (m_1^* \boldsymbol{u}_{\boldsymbol{d}}^* \otimes \boldsymbol{u}_{\boldsymbol{d}}^*) && = - \quad K^* m_0^* \boldsymbol{u}_{\boldsymbol{d}}^* + \mathsf{St}^{-1} \, \mu_g^* m_0^* (\boldsymbol{u}_{\boldsymbol{g}}^* - \boldsymbol{u}_{\boldsymbol{d}}^*), && (3.26e)
\end{aligned}$$

  where

$$\mathsf{St} = \frac{\rho_0 S_0 U_0}{18\pi \mu_{g,0} L_0} \tag{3.27}$$

is the Stokes number. The last term in the right-hand side of (3.26e) can be expressed as $\int S^* \boldsymbol{F}_{\boldsymbol{d}}^* \tilde{n}^* \, \mathrm{d}S^*$, which is consistent with the primary form (3.13b). We have to be cautious, though, as to the value of the dimensionless drag force, viz.

$$\boldsymbol{F}_d^* = \mathsf{St}^{-1} \, \frac{\mu_g^*(\boldsymbol{u}_{\boldsymbol{g}}^* - \boldsymbol{u}_{\boldsymbol{d}}^*)}{S^*}, \tag{3.28}$$

which could not be directly guessed from the Stokes law (3.6).

- For the gas,

$$\partial_{t^*}(\rho_g^*) \quad + \nabla_{\boldsymbol{x}^*} \cdot (\rho_g^* \boldsymbol{u}_{\boldsymbol{g}}^*) \qquad\qquad = \mathsf{R}_{\mathsf{drop-gas}}{}^{3/2} \, \tilde{\mathfrak{S}}^{\rho *}, \tag{3.29a}$$

$$\partial_{t^*}(\rho_g^* \boldsymbol{u}_{\boldsymbol{g}}^*) + \nabla_{\boldsymbol{x}^*} \cdot (\rho_g^* \boldsymbol{u}_{\boldsymbol{g}}^* \otimes \boldsymbol{u}_{\boldsymbol{g}}^* + P_g^* \boldsymbol{I}) = \mathsf{R}_{\mathsf{drop-gas}}{}^{3/2} \, \tilde{\mathfrak{S}}^{\rho \boldsymbol{u} *} + \mathsf{Re}^{-1} \, \nabla_{\boldsymbol{x}^*} \cdot (\boldsymbol{\Sigma}_{\boldsymbol{g}}^*), \tag{3.29b}$$

$$\partial_{t^*}(\rho_g^* E_g^*) + \nabla_{\boldsymbol{x}^*} \cdot (\rho_g^* E_g^* \boldsymbol{u}_{\boldsymbol{g}}^* + P_g^* \boldsymbol{u}_{\boldsymbol{g}}^*) \; = \mathsf{R}_{\mathsf{drop-gas}}{}^{3/2} \, \tilde{\mathfrak{S}}^{\rho e *} + \mathsf{Re}^{-1} \, \nabla_{\boldsymbol{x}^*} \cdot (\boldsymbol{\Sigma}_{\boldsymbol{g}}^* \cdot \boldsymbol{u}_{\boldsymbol{g}}^*), \tag{3.29c}$$

where

$$\mathsf{Re} = \frac{\rho_0 U_0 L_0}{\mu_{g,0}} \qquad \text{and} \qquad \mathsf{R}_{\mathsf{drop-gas}} = \frac{S_0}{L_0^2} = \frac{18\pi \mathsf{St}}{\mathsf{Re}} \tag{3.30}$$

are, respectively, the Reynolds number and a non-dimensional number arising due to the presence of two distinct reference surfaces for the spray and the gas. This number can be expressed as a combination between the Reynolds and Stokes numbers. The dimensionless source terms are

$$\tilde{\mathfrak{S}}^{\rho *} \; = \; \tfrac{1}{4\pi^{1/2}} \, K^* \tilde{m}_{1/2}^*, \tag{3.31a}$$

$$\tilde{\mathfrak{S}}^{\rho \boldsymbol{u} *} \; = \; \tfrac{1}{4\pi^{1/2}} \, K^* \tilde{m}_{1/2}^* \boldsymbol{u}_{\boldsymbol{d}}^* - \tfrac{1}{6\pi^{1/2}} \, \mathsf{St}^{-1} \, \mu_g^* \tilde{m}_{1/2}^* (\boldsymbol{u}_{\boldsymbol{g}}^* - \boldsymbol{u}_{\boldsymbol{d}}^*), \tag{3.31b}$$

$$\tilde{\mathfrak{S}}^{\rho e *} \; = \; \tfrac{1}{4\pi^{1/2}} \, K^* \tilde{m}_{1/2}^* h_d^*. \tag{3.31c}$$

Again, the last term in the right-hand side of (3.31b) can be expressed as $-\int V(S^*) \tilde{n}^* \boldsymbol{F}_{\boldsymbol{d}}^* \, \mathrm{d}S^*$, which is consistent with the primary form (3.8b).

It appears from the previous calculations that the EMSM model is governed essentially by two parameters: the Reynolds number and the Stokes number. For later use, we observe that the Stokes number (3.27) is the ratio of two characteristic times, that is,

$$\mathsf{St} = \frac{\tau_d}{\tau_{g,0}}, \qquad \text{with} \quad \tau_d = \frac{\rho_0 S_0}{18\pi \mu_{g,0}} \quad \text{and} \quad \tau_{g,0} = \frac{L_0}{U_0}. \tag{3.32}$$

3.2.4 Realizability of moments

The EMSM model belongs to the class of high order moment methods, to the extent that it predicts the evolution of size moments of orders from 0 to N. In such a refined picture, our biggest concern is to keep the $(N+1)$-tuple $\boldsymbol{m}$ *feasible* in the following sense.

Given a domain $\mathfrak{D} \subset \mathbb{R}^+$, let $\mathfrak{M}_{N+1}$ be the set of those $\boldsymbol{m} = (m_0, m_1, \ldots, m_N)$ that coincide with the first $N+1$ moments of some positive-valued function n defined on $\mathfrak{D}$, namely,

$$m_k = \int_{\mathfrak{D}} S^k n(S)\,\mathrm{d}S, \qquad \text{for all } \; k \in \{0, 1, \ldots, N\}. \tag{3.33}$$

Although $\mathfrak{M}_{N+1}$ is plainly a convex set, its geometrical shape is quite convoluted [38]. Characterizing $\mathfrak{M}_{N+1}$ by a set of necessary and sufficient algebraic conditions is called the *Stieljes* moment problem when $\mathfrak{D} = \mathbb{R}^+$, the *Hausdorff* moment problem[3] when $\mathfrak{D} = [0, S_0]$. For a finite N, uniqueness of n is no longer guaranteed. This is not a real issue, since as seen earlier, we have the unique entropy maximization reconstruction [120] at our disposal. The real issues arise when evolution equations on $\boldsymbol{m}$ are imposed and solved by some approximation method.

- At the continuous level, the evolution operator applied to $\boldsymbol{m}$ need to be consistent with what we call the realizability condition. This means that if $\boldsymbol{m}(t=0) \in \mathfrak{M}_{N+1}$, then $\boldsymbol{m}(t) \in \mathfrak{M}_{N+1}$ for all $t > 0$. The evolution operator on the size-moments in the present case is constituted of the sum of an evaporation operator, represented by the right-hand side of (3.21), and of a convection operator, represented by the divergence $\nabla_{\boldsymbol{x}}\cdot$ in the left-hand side of (3.21).

- At the discrete level, the numerical scheme used to update $\boldsymbol{m}$ need be consistent with the realizability condition. That is, if $\tilde{\boldsymbol{m}}(t) \in \mathfrak{M}_{N+1}$, then $\tilde{\boldsymbol{m}}(t+\Delta t) \in \mathfrak{M}_{N+1}$, where Δt is the time-step. Note that the realizability condition may fail at the discrete level while fulfilled at the continuous level. In such a situation, the sequence $\tilde{\boldsymbol{m}}$ is said to be corrupted and this leads the immediate crash of the simulation or requires clipping and thus loss of computational efficiency as well as accuracy.

The challenge when using such moment methods is thus to come up with a numerical method satisfying the realizability condition. One can found in the literature tools to handle evaporation and convection of polydisperse spray using moment method EMSM, see [120] and [87], with high order time-space accuracy and consistency with $\mathfrak{M}_{N+1}$. We shall of course make use of these tools. In this context, we shall, in order to come up with a high-order convection scheme, work with quantities derived from the moments rather than with the moments themselves. To illustrate this point, let us consider a moment advection equation

$$\partial_t m_k + \boldsymbol{w} \cdot \nabla_{\boldsymbol{x}} m_k = 0, \qquad k \in \{0, 1, \ldots, N\}, \tag{3.34}$$

where $\boldsymbol{w}$ stands for an imposed velocity field. In this pure transport of the moments, $\boldsymbol{m}^{n+1}$ is simply a shifted version of $\boldsymbol{m}^n$. Hence, $\boldsymbol{m}^{n+1} \in \mathfrak{M}_{N+1}$ if $\boldsymbol{m}^n \in \mathfrak{M}_{N+1}$, which is consistent with the realizability of moments at the continuous level. At the discrete level, however, things are more delicate. Indeed, if first-order standard finite volume schemes automatically preserve the moment space, increasing the order while preserving

[3] As a matter of fact, the Stieltjes and Hausdorff problems were originally stated for an infinite sequence ($N = \infty$), for which it is also possible to recover uniqueness of the function n under mild additional assumptions.

realizability is not straightforward. For second-order finite volume schemes using limited slope reconstructions, $\mathfrak{M}_{N+1}$ must be preserved in both the reconstruction step and fluxes computation. Wright [195] showed that, due to the complex shape of $\mathfrak{M}_{N+1}$, independent linear reconstruction of the moments may violate this requirement. To overcome the difficulty, Kah et al. [87] suggested to reconstruct not the moments but some derived quantities called *canonical moments*. To define these, let

$$c_0 = 1 \qquad \text{and} \qquad c_k = \frac{m_k}{m_0}, \qquad k \in \{1, 2, \dots, N\}, \tag{3.35}$$

be the normalized moments. From (3.34), it is straightforward to show that

$$\partial_t c_k + \boldsymbol{w} \cdot \nabla_{\boldsymbol{x}} c_k = 0. \tag{3.36}$$

Using the notation $\boldsymbol{c}_{k-1} = (c_0, c_1, \dots, c_{k-1})$ for $k \geq 1$, we define

$$\wp(\boldsymbol{c}_{k-1}) = \{(c_0, c_1, \dots, c_{k-1}, \gamma) \in \mathfrak{M}_{k+1} \text{ for all possible } \gamma\}. \tag{3.37}$$

Dette and Studden [38] introduced the canonical moments of order k as the ratio

$$p_k = \frac{c_k - c_k^-(\boldsymbol{c}_{k-1})}{c_k^+(\boldsymbol{c}_{k-1}) - c_k^-(\boldsymbol{c}_{k-1})}, \tag{3.38a}$$

where

$$c_k^+(\boldsymbol{c}_{k-1}) = \max_{\boldsymbol{\gamma} \in \wp(\boldsymbol{c}_{k-1})} c_k(\boldsymbol{\gamma}) \qquad \text{and} \qquad c_k^-(\boldsymbol{c}_{k-1}) = \min_{\boldsymbol{\gamma} \in \wp(\boldsymbol{c}_{k-1})} c_k(\boldsymbol{\gamma}) \tag{3.38b}$$

are respectively the upper and lower bounds of the admissible interval for the last component, for the vector $\boldsymbol{c}_k = (c_0, c_1, \dots, \gamma)$ to belong to $\mathfrak{M}_{k+1}$. From (3.36), it follows [87] that the canonical moments are advected too in the convection step, i.e.,

$$\partial_t p_k + \boldsymbol{w} \cdot \nabla_{\boldsymbol{x}} p_k = 0. \tag{3.39}$$

The decisive advantage of canonical moments is that the realizability condition amounts to

$$p_k \in [0, 1], \qquad \text{for all } k \in \{1, 2, \dots, N\}. \tag{3.40}$$

The geometry of this condition is very simple. As a result, it becomes possible to design [30] a slope limited reconstruction for the p_k's based on standard techniques. Details at the discrete level are given in §A.1.3. A numerical study is conducted in §3.4.2 to demonstrate the capabilities of the proposed scheme.

The present paper extends these techniques to simulate an injection occurring in internal combustion engines, using the industrial CFD code IFP-C3D, developed at IFPEN for automotive engine simulations. In this context, we will introduce two salient features: a two-way coupling and handle it by an original implicit method ensuring moment space conservation. We will come up with a discretization scheme that takes into account mesh movement and thus proposes a first ALE algorithm ensuring the realizability condition.

3.3 Overview of the numerical method

The EMSM model (3.21)–(3.23) is solved using a splitting strategy, where each stage corresponds to a class of physical phenomena. Instead of the standard Strang splitting, we rely on a splitting based on the Arbitrary Lagrange Euler (ALE) formalism [43, 78, 79, 57], which is more suitable to moving meshes. In both splitting approaches, the first stage — which we refer to as *phase A*— is the same, since it is concerned with drag and evaporation source terms (as well as heat source in the gaseous phase equations due to evaporation). The discretization of these source terms for both carrier gas and spray gives rise to a local coupled system. A splitting strategy using explicit methods has been used in Doisneau et al. [40, 41] for lower order size-moments, whereas we propose an implicit method here for high order moments, which can be extended to arbitrary droplet models, see Emre et al. [55]. This local system remains to be solved in a computationally efficient way.

We are going to describe this first stage with an emphasis on the two-way coupling, which is our novel contribution. Then, we will take a step back and look at the overall ALE formalism, which requires some work to be adapted to our two-velocity model.

3.3.1 Two-way coupling source terms

The system to be solved in phase A is obtained from (3.21)–(3.22) by dropping all divergence terms $\nabla_{\boldsymbol{x}} \cdot (\cdot)$. We thus have

$$\partial_t(m_0) = - K\tilde{n}(\boldsymbol{m}, 0), \tag{3.41a}$$
$$\partial_t(m_1) = - Km_0, \tag{3.41b}$$
$$\vdots \qquad \vdots$$
$$\partial_t(m_N) = -NKm_{N-1}, \tag{3.41c}$$
$$\partial_t(m_1\boldsymbol{u_d}) = - Km_0\boldsymbol{u_d} + \frac{18\pi}{\rho_d}\mu_g m_0(\boldsymbol{u_g} - \boldsymbol{u_d}), \tag{3.41d}$$

for the spray, and

$$\partial_t(\rho_g) = \tilde{\mathfrak{S}}^{\rho}, \tag{3.42a}$$
$$\partial_t(\rho_g\boldsymbol{u_g}) = \tilde{\mathfrak{S}}^{\rho\boldsymbol{u}}, \tag{3.42b}$$
$$\partial_t(\rho_g E_g) = \tilde{\mathfrak{S}}^{\rho e}, \tag{3.42c}$$

for the gas. In (3.41), we see that the first $N+1$ equations suffice to update $\boldsymbol{m}$, independently of the remaining equations.

The difficulty when attempting to solve system (3.41), is to preserve the realizability condition. At the discrete level, Massot et al. [120] have designed an evaporation solver that preserves the moment space. It relies on a kinetic scheme [139] coupled to a CQMOM approach [198]. The kinetic scheme allows to compute the source terms while ensuring realizability.

In fact, we use system (3.41)–(3.42) only for the one-way coupling model, i.e., when $\tilde{\mathfrak{S}}^{\rho} = \tilde{\mathfrak{S}}^{\rho\boldsymbol{u}} = \tilde{\mathfrak{S}}^{\rho e} = 0$. The fully-discrete details for the one-way coupling are recalled in

A.1.1. For the two-way coupling model, we recommend two slight modifications of the system (3.41)–(3.42) in phase A. The purpose of these modifications is to make phase A more meaningful physically and easier to solve numerically.

1. On the grounds of (3.17b) and (3.19b), we replace (3.41d) by

$$\partial_t(\tilde{m}_{3/2}\boldsymbol{u_d}) = -\frac{3}{2}K\tilde{m}_{1/2}\boldsymbol{u_d} + \frac{18\pi}{\rho_d}\,\mu_g\tilde{m}_{1/2}(\boldsymbol{u_g}-\boldsymbol{u_d}), \tag{3.43}$$

   where $\tilde{m}_{k+1/2} = \int S^{k+1/2}\tilde{n}(\boldsymbol{m},S)\,\mathrm{d}S$. This choice is driven by total momentum preservation $\partial_t(\rho_g\boldsymbol{u_g} + \frac{1}{6\pi^{1/2}}\rho_d\tilde{m}_{3/2}\boldsymbol{u_d}) = 0$.

2. In order to better separate the velocity $\boldsymbol{u}_g$ from other thermodynamical variables, we substitute to the total energy equation (3.42c) the internal energy equation

$$\partial_t(\rho_g e_g) = \frac{\rho_d}{4\pi^{1/2}}K\tilde{m}_{1/2}e_d, \tag{3.44}$$

   where $e_d(T_d) = \int_0^{T_d} C_{v,d}(T)\,\mathrm{d}T$ is the spray internal energy. Within assumption (3.20), it is a constant and equal to $e_d(T_{d0})$. The gas internal energy is defined as $e_g = E_g - \frac{1}{2}\|\boldsymbol{u}_g\|^2$.

The phase A two-way coupling system now reads

$$\begin{aligned}
\partial_t(m_0) &= -\ K\tilde{n}(\boldsymbol{m},0), && (3.45a)\\
\partial_t(m_1) &= -\ Km_0, && (3.45b)\\
&\ \vdots \quad \vdots && \\
\partial_t(m_N) &= -NKm_{N-1}, && (3.45c)\\
\partial_t(\tilde{m}_{3/2}\boldsymbol{u_d}) &= \underbrace{-\tfrac{3}{2}K\tilde{m}_{1/2}\boldsymbol{u_d}}_{\text{evap.}} + \underbrace{\tfrac{18\pi}{\rho_d}\,\mu_g\tilde{m}_{1/2}(\boldsymbol{u_g}-\boldsymbol{u_d})}_{\text{drag}}, && (3.45d)
\end{aligned}$$

for the spray, and

$$\begin{aligned}
\partial_t(\rho_g) &= \tfrac{1}{4\pi^{1/2}}\rho_d K\tilde{m}_{1/2}, && (3.46a)\\
\partial_t(\rho_g\boldsymbol{u_g}) &= \tfrac{1}{4\pi^{1/2}}\rho_d K\tilde{m}_{1/2}\boldsymbol{u_d} - \tfrac{18\pi}{6\pi^{1/2}}\mu_g\tilde{m}_{1/2}(\boldsymbol{u_g}-\boldsymbol{u_d}), && (3.46b)\\
\partial_t(\rho_g e_g) &= \underbrace{\tfrac{1}{4\pi^{1/2}}\rho_d K\tilde{m}_{1/2}e_d}_{\text{evap.}}, \quad \underbrace{\qquad\qquad}_{\text{drag}} && (3.46c)
\end{aligned}$$

for the gas. Let us assume, in addition to hypotheses (3.11), that K does not depend on $\boldsymbol{u_d}$—but may depend on t, as considered by Duarte et al. [44]. This holds true within the d^2 type evaporation law in the present work. Then, the first $N+1$ equations of (3.45) are decoupled from the remaining equations. As mentioned earlier and after Massot et al. [120], this subsystem (3.45a)–(3.45c) can be solved for $\boldsymbol{m}(t)$, from which we deduce

$\tilde{m}_{1/2}(t)$ and $\tilde{m}_{3/2}(t)$. Plugging the latter into (3.46) yields ρ_g and $\rho_g E_g$ as an explicit function of time, that is,

$$(\rho_g)(t) = (\rho_g)^n + \tfrac{1}{4\pi^{1/2}}\rho_d \int_{t^n}^t K(\tau)\tilde{m}_{1/2}(\tau)\,\mathrm{d}\tau, \tag{3.47a}$$

$$(\rho_g e_g)(t) = (\rho_g e_g)^n + \tfrac{1}{4\pi^{1/2}}\rho_d \int_{t^n}^t K(\tau)\tilde{m}_{1/2}(\tau) e_d\,\mathrm{d}\tau. \tag{3.47b}$$

The two remaining equations of (3.45)–(3.46), i.e.,

$$\partial_t(\tilde{m}_{3/2}\boldsymbol{u_d}) = -\tfrac{3}{2}K\tilde{m}_{1/2}\boldsymbol{u_d} + \tfrac{18\pi}{\rho_d}\mu_g\tilde{m}_{1/2}(\boldsymbol{u_g}-\boldsymbol{u_d}), \tag{3.48a}$$

$$\partial_t(\rho_g\boldsymbol{u_g}) = \tfrac{\rho_d}{4\pi^{1/2}}K\tilde{m}_{1/2}\boldsymbol{u_d} - \tfrac{18\pi}{6\pi^{1/2}}\mu_g\tilde{m}_{1/2}(\boldsymbol{u_g}-\boldsymbol{u_d}), \tag{3.48b}$$

are strongly coupled. Setting $\boldsymbol{y} = (\boldsymbol{u_d}, \boldsymbol{u_g})$, the above system can be put under the abstract form

$$\mathrm{d}_t\boldsymbol{y} = \boldsymbol{g}(\boldsymbol{y}, t), \tag{3.49}$$

where the explicit dependency of $\boldsymbol{g}$ in t reflects our knowledge of $\tilde{m}_{1/2}(t)$, $\tilde{m}_{3/2}(t)$ and $\rho_g(t)$, $e_g(t)$. As for $\mu_g = \mu_g(T_g)$, it can also be viewed as a function t via $T_g = e_g/C_{v,g} = (\gamma_g - 1)e_g/R_g$.

Taking into account the space discretization over a staggered grid requires some attention. For the sake of clarity, let us write down the details for the 1-D case. Generalization to the 3-D case is straightforward. Throughout phase A, since no mesh movement occurs, the spray $\boldsymbol{x}$-domain is divided into *static* disjoint cells

$$[x_{i-1/2}(t), x_{i+1/2}(t)[= [x^n_{i-1/2}, x^n_{i+1/2}[$$

of length

$$\Delta x_i(t) := x_{i+1/2}(t) - x_{i-1/2}(t) = x^n_{i+1/2} - x^n_{i-1/2} = \Delta x^n_i.$$

At the centers $x_i = \frac{1}{2}(x_{i-1/2} + x_{i+1/2})$ of these *primal* cells, we seek approximate values for the moments $\boldsymbol{m}_i$, the gas density $\rho_{g,i}$ and the total energy $E_{g,i}$. Solving the ODE subsytems (3.45a)–(3.45c) and (3.46a), (3.46c) on each primal cell, we have $\boldsymbol{m}_i(t)$, $\rho_{g,i}(t)$ and $(\rho_g e_g)_i(t)$ by formulae (3.47).

The *dual* cells are defined as $[x^n_i, x^n_{i+1}[$ and are assigned the velocities $\boldsymbol{u_d}_{i+1/2}$ and $\boldsymbol{u_g}_{i+1/2}$. In conformity with the finite-volume spirit, we first integrate (3.48) over the dual cell $[x_i, x_{i+1}[$ to get

$$\mathrm{d}_t\int_{x_i}^{x_{i+1}} \tilde{m}_{3/2}\boldsymbol{u_d}\,\mathrm{d}x = -\tfrac{3}{2}\int_{x_i}^{x_{i+1}} K\tilde{m}_{1/2}\boldsymbol{u_d}\,\mathrm{d}x + \tfrac{18\pi}{\rho_d}\int_{x_i}^{x_{i+1}} \mu_g\tilde{m}_{1/2}(\boldsymbol{u_g}-\boldsymbol{u_d})\,\mathrm{d}x, \tag{3.50a}$$

$$\mathrm{d}_t\int_{x_i}^{x_{i+1}} \rho_g\boldsymbol{u_g}\,\mathrm{d}x = \tfrac{\rho_d}{4\pi^{1/2}}\int_{x_i}^{x_{i+1}} K\tilde{m}_{1/2}\boldsymbol{u_d}\,\mathrm{d}x - \tfrac{18\pi}{6\pi^{1/2}}\int_{x_i}^{x_{i+1}} \mu_g\tilde{m}_{1/2}(\boldsymbol{u_g}-\boldsymbol{u_d})\,\mathrm{d}x. \tag{3.50b}$$

The next step is to invoke the approximations

$$\int_{x_i}^{x_{i+1}} \tilde{m}_{3/2}\boldsymbol{u_d}\,\mathrm{d}x \approx \tfrac{1}{2}(\Delta x_i\tilde{m}_{3/2,i} + \Delta x_{i+1}\tilde{m}_{3/2,i+1})\boldsymbol{u_d}_{i+1/2}, \tag{3.51a}$$

$$\int_{x_i}^{x_{i+1}} \rho_g\boldsymbol{u_g}\,\mathrm{d}x \approx \tfrac{1}{2}(\Delta x_i\rho_{g,i} + \Delta x_{i+1}\rho_{g,i+1})\boldsymbol{u_g}_{i+1/2}, \tag{3.51b}$$

$$\int_{x_i}^{x_{i+1}} K\tilde{m}_{1/2}\boldsymbol{u_d}\,\mathrm{d}x \approx \tfrac{1}{2}(\Delta x_i K_i\tilde{m}_{1/2,i} + \Delta x_{i+1}K_{i+1}\tilde{m}_{1/2,i+1})\boldsymbol{u_d}_{i+1/2}, \tag{3.51c}$$

$$\int_{x_i}^{x_{i+1}} \mu_g\tilde{m}_{1/2}(\boldsymbol{u_g}-\boldsymbol{u_d})\,\mathrm{d}x \approx \tfrac{1}{2}(\Delta x_i\mu_{g,i}\tilde{m}_{1/2,i} + \Delta x_{i+1}\mu_{g,i+1}\tilde{m}_{1/2,i+1})(\boldsymbol{u_g}-\boldsymbol{u_d})_{i+1/2}, \tag{3.51d}$$

in order to obtain an ODE system of the form (3.49). This ODE system is solved by the Singly Diagonally Implicit Runge-Kutta Method (SDIRK) given by the Butcher array [75]

$$\begin{array}{c|ccc} \omega & \omega & & \\ \frac{1}{2}(1+\omega) & \frac{1}{2}(1-\omega) & \omega & \\ 1 & \frac{1}{4}(-1+16\omega-6\omega^2) & \frac{1}{4}(5-20\omega+6\omega^2) & \omega \\ \hline & \frac{1}{4}(-1+16\omega-6\omega^2) & \frac{1}{4}(5-20\omega+6\omega^2) & \omega \end{array}$$

with $\omega = 0.4358665215$ being a root of $6\omega^3 - 18\omega^2 + 9\omega - 1 = 0$. This third-order numerical integration scheme is relevant to our problem. For one, it is simple and inexpensive in the context of industrial software development. For another, it provides the A-stability and L-stability[4] properties. These will be essential when using more sophisticated droplet models such as Schiller and Nauman's drag model [160], where the ODE becomes nonlinear and the coupling is stiffer.

3.3.2 Arbitrary Lagrange Euler formalism

In contrast to previous EMSM-related works [120, 87] where calculations were settled on fixed meshes, the realistic configurations considered in our case—injection in combustion engines with a moving piston—command to carry out computations over moving meshes. The most common technique to cope with this new constraint is the Arbitrary Lagrange Euler (ALE) formalism, which was introduced [78] in the context of single-velocity fluid flows. Let us see how to adapt the ALE philosophy to the EMSM model, in which two velocity fields co-exist.

We introduce a new referential frame, attached to the grid points, in which the coordinates are denoted by $\boldsymbol{\chi}$. This frame is, a priori, neither the material (Lagrangian) configuration nor the laboratory (Eulerian) configuration $\boldsymbol{x}$. Instead, it moves at the imposed velocity $\boldsymbol{w}$ with respect to the laboratory. Let $\boldsymbol{x} = \boldsymbol{x}(t, \boldsymbol{\chi})$ be the correspondence between the moving frame and the laboratory frame. This correspondence is determined by

$$\partial_t \boldsymbol{x} = \boldsymbol{w}. \tag{3.52}$$

Let $J_d = \det(\nabla_{\boldsymbol{\chi}} \boldsymbol{x})$ be the dilatation rate. Then, it is a classical result that J_d evolves in time according to

$$\partial_t J_d = J_d \nabla_{\boldsymbol{x}} \cdot \boldsymbol{w}. \tag{3.53}$$

In the ALE formalism, J_d will act as a new scalar unknown subject to (3.53). To properly account for two-velocity mixtures, we propose to copy J_d into a second scalar unknown J_g, governed by

$$\partial_t J_g = J_g \nabla_{\boldsymbol{x}} \cdot \boldsymbol{w}. \tag{3.54}$$

The idea is then to consider J_d and J_g as two independent fields, since each phase has its own velocity. We are now ready to perform a change of variables from $(t, \boldsymbol{x})$ to $(t, \boldsymbol{\chi})$.

[4]The solution of the ODE $dy/dt = \lambda y$, with $\mathrm{Re}(\lambda) < 0$, is stable in the sense that $y(t) \to 0$ as $t \to +\infty$. A numerical scheme $y_{n+1} = R(\lambda \Delta t) y_n$ is said to be A-stable if it reproduces this decay property, i.e., if $|R(z)| < 1$ for all $\mathrm{Re}(z) < 0$. Furthermore, the method is said to be L-stable if stiff modes are highly damped, that is, if $R(z) \to 0$ as $\mathrm{Re}(z) \to -\infty$.

Standard calculations [37] show that system (3.21)–(3.22) is equivalent to the following problem.

- For the spray, find $(J_d, \boldsymbol{m}, \boldsymbol{u_d}) = (J_d, m_0, m_1, \dots, m_N, \boldsymbol{u_d})$ such that

$$\partial_t(J_d) + J_d\nabla_{\boldsymbol{x}}\cdot(\boldsymbol{u_d}-\boldsymbol{w}) - J\nabla_{\boldsymbol{x}}\cdot(\boldsymbol{u_d}) = 0, \tag{3.55a}$$

$$\partial_t(J_d m_0) + J_d\nabla_{\boldsymbol{x}}\cdot(m_0(\boldsymbol{u_d}-\boldsymbol{w})) = -\ KJ_d\tilde{n}(\boldsymbol{m}, S=0), \tag{3.55b}$$

$$\partial_t(J_d m_1) + J_d\nabla_{\boldsymbol{x}}\cdot(m_1(\boldsymbol{u_d}-\boldsymbol{w})) = -\ KJ_d m_0, \tag{3.55c}$$

$$\vdots \qquad \vdots \qquad\qquad \vdots$$

$$\partial_t(J_d m_N) + J_d\nabla_{\boldsymbol{x}}\cdot(m_N(\boldsymbol{u_d}-\boldsymbol{w})) = -NKJ_d m_{N-1}, \tag{3.55d}$$

$$\partial_t(J_d m_1\boldsymbol{u_d}) + \underbrace{J_d\nabla_{\boldsymbol{x}}\cdot(m_1\boldsymbol{u_d}\otimes(\boldsymbol{u_d}-\boldsymbol{w}))}_{\text{C}} \underbrace{\qquad}_{\text{B}} = -\ \underbrace{K J_d m_0\boldsymbol{u_d} + \tfrac{18\pi}{\rho} J_d\mu_g m_0(\boldsymbol{u_g}-\boldsymbol{u_d})}_{\text{A}}. \tag{3.55e}$$

- For the gas, find $(J_g, \rho_g, \boldsymbol{u_g}, E_g)$ such that

$$\partial_t(J_g) + J_g\nabla_{\boldsymbol{x}}\cdot((\boldsymbol{u_g}-\boldsymbol{w})) - J_g\nabla_{\boldsymbol{x}}\cdot(\boldsymbol{u_g}) = 0, \tag{3.56a}$$

$$\partial_t(J_g\rho_g) + J_g\nabla_{\boldsymbol{x}}\cdot(\rho_g(\boldsymbol{u_g}-\boldsymbol{w})) = J_g\tilde{\mathfrak{S}}^{\rho}, \tag{3.56b}$$

$$\partial_t(J_g\rho_g\boldsymbol{u_g}) + J_g\nabla_{\boldsymbol{x}}\cdot(\rho_g\boldsymbol{u_g}\otimes(\boldsymbol{u_g}-\boldsymbol{w})) + J_g\nabla_{\boldsymbol{x}}\cdot(P_g\boldsymbol{I}-\boldsymbol{\Sigma}_g) = J_g\tilde{\mathfrak{S}}^{\rho\boldsymbol{u}}, \tag{3.56c}$$

$$\partial_t(J_g\rho_g E_g) + \underbrace{J_g\nabla_{\boldsymbol{x}}\cdot(\rho_g E_g(\boldsymbol{u_g}-\boldsymbol{w}))}_{\text{C}} + \underbrace{J_g\nabla_{\boldsymbol{x}}\cdot((P_g\boldsymbol{I}-\boldsymbol{\Sigma}_g)\cdot\boldsymbol{u_g})}_{\text{B}} = \underbrace{J_g\tilde{\mathfrak{S}}^{\rho e}}_{\text{A}}. \tag{3.56d}$$

As earlier, $(\tilde{\mathfrak{S}}^{\rho}, \tilde{\mathfrak{S}}^{\rho\boldsymbol{u}}, \tilde{\mathfrak{S}}^{\rho e})$ are either zero (one-way coupling) or given by (3.23) (two-way coupling). The unknowns

$$\mathbb{U}_d = (J_d, \boldsymbol{m}, \boldsymbol{u_d}) \qquad \text{and} \qquad \mathbb{U}_g = (J_g, \rho_g, \boldsymbol{u_g}, E_g), \tag{3.57}$$

must be viewed as functions of $(t, \boldsymbol{\chi})$. In practice, we never have to handle the space variable $\boldsymbol{\chi}$, since by appropriate integration over control volumes in the $(t, \boldsymbol{\chi})$-frame, we can bring every thing back to the $(t, \boldsymbol{x})$-frame. Besides, we insist that although J_d and J_g remain identical in the unsplit system, they should be regarded as two distinct quantities. This viewpoint will be useful for the splitting procedure, in the course of which J_d may differ from J_g.

3.3.3 Elements of time-space discretization

To update the variables of (3.55)–(3.56) from time t^n to $t^{n+1} = t^n + \Delta t$, the algorithm goes through 3 stages, or *phases*, traditionally called A, B and C. This is depicted by the

diagram

$$(\mathbb{U}_d^n, \mathbb{U}_g^n) \xrightarrow[\Delta t]{\text{A}} (\mathbb{U}_d^A, \mathbb{U}_g^A) \xrightarrow[\Delta t]{\text{B}} (\mathbb{U}_d^B, \mathbb{U}_g^B) \xrightarrow[\Delta t]{\text{C}} (\mathbb{U}_d^{n+1}, \mathbb{U}_g^{n+1}). \tag{3.58}$$

Far from being a mere algebraic decomposition, each stage does have a most natural physical meaning. In this respect, the ALE formalism is powerful even for a fixed mesh ($\boldsymbol{w} = 0$). Starting from $J_d^n = J_g^n$, one will generally have

$$J_d^A = J_g^A, \quad J_d^B \neq J_g^B, \quad J_d^{n+1} = J_g^{n+1}. \tag{3.59}$$

To gain more insight into this splitting strategy, let us review some features of each phase.

In phase A, since $\partial_t J_d = \partial_t J_g = 0$, the dilatation rates J_d and J_g can be simplified from the equations. These boil down to (3.41)–(3.42) and can be solved as explained in §3.3.1 for the two-way coupling and A.1.1 for the one-way coupling.

In phase B, we have to deal with two uncoupled systems, namely,

$$\partial_t(J_d) - J_d \nabla_{\boldsymbol{x}} \cdot (\boldsymbol{u_d}) = 0, \tag{3.60a}$$
$$\partial_t(J_d \boldsymbol{m}) = 0, \tag{3.60b}$$
$$\partial_t(J_d m_1 \boldsymbol{u_d}) = 0, \tag{3.60c}$$

for the spray, and

$$\partial_t(J_g) - J_g \nabla_{\boldsymbol{x}} \cdot (\boldsymbol{u_g}) = 0, \tag{3.61a}$$
$$\partial_t(J_g \rho_g) = 0, \tag{3.61b}$$
$$\partial_t(J_g \rho_g \boldsymbol{u_g}) + J_g \nabla_{\boldsymbol{x}} \cdot (P_g \boldsymbol{I} - \boldsymbol{\Sigma}_g) = 0, \tag{3.61c}$$
$$\partial_t(J_g \rho_g E_g) + J_g \nabla_{\boldsymbol{x}} \cdot ((P_g \boldsymbol{I} - \boldsymbol{\Sigma}_g) \cdot \boldsymbol{u_g}) = 0. \tag{3.61d}$$

for the gas. We refer the readers to A.1.2 for the full space-time discretization of the spray system (3.60). Here, we highlight some of its properties at the continuous level. First, note that the intermediate equations (3.60b) can be readily solved to give

$$\boldsymbol{m}^B = \frac{J_d^A}{J_d^B} \boldsymbol{m}^A, \tag{3.62}$$

which implies that $\boldsymbol{m}^B \in \mathfrak{M}_{N+1}$ as soon as $\boldsymbol{m}^A \in \mathfrak{M}_{N+1}$, $J_d^A > 0$ and provided that $J_d^B > 0$. At the continuous level, phase B seems to be consistent with the realizability of moments. But the real difficulty lies in the fact that the hyperbolic system (3.60) is resonant. As a matter of fact, any subsystem

$$\partial_t(J_d) - J_d \nabla_{\boldsymbol{x}} \cdot (\boldsymbol{u_d}) = 0, \tag{3.63a}$$
$$\partial_t(J_d m_k) = 0, \tag{3.63b}$$
$$\partial_t(\boldsymbol{u_d}) = 0, \tag{3.63c}$$

extracted from (3.60), can be interpreted as the Lagrangian version of the pressureless gas system

$$\partial_t(m_k) + \nabla_{\boldsymbol{x}} \cdot (m_k \boldsymbol{u_d}) = 0, \tag{3.64a}$$
$$\partial_t(m_k \boldsymbol{u_d}) + \nabla_{\boldsymbol{x}} \cdot (m_k \boldsymbol{u_d} \otimes \boldsymbol{u_d}) = 0. \tag{3.64b}$$

The mathematical properties of pressureless gas dynamics have been investigated by many authors, notably by Bouchut [14, 13]. Since no pressure term acts on the velocity field to prevent particle accumulation, high density moving concentrations called *δ-shocks* are expected to develop. This behavior is due to the mono-kinetic assumption made on the spray velocity field in part 3.2, where we choose a Dirac delta function for the spray velocity distribution.

As far as the gas system (3.61) is concerned, it is none other than the Navier-Stokes gas dynamics in Lagrangian coordinates. The physics contained in this Lagrangian setting is essentially acoustics. Several numerical schemes are available for (3.61). We have chosen to rely on the one implemented in IFP-C3D. Details at the fully discrete level can be found in the KIVA report by Amsden et al. [4] or a relaxation variant by Coquel et al. [27].

In phase C, we also have two uncoupled systems, namely,

$$\begin{aligned}
&\partial_t(J_d) && + J_d\nabla_{\boldsymbol{x}}\cdot(\boldsymbol{u_d}-\boldsymbol{w}) && = 0 && \text{(3.65a)}\\
&\partial_t(J_d m_0) && + J_d\nabla_{\boldsymbol{x}}\cdot(m_0(\boldsymbol{u_d}-\boldsymbol{w})) && = 0, && \text{(3.65b)}\\
&\partial_t(J_d m_1) && + J_d\nabla_{\boldsymbol{x}}\cdot(m_1(\boldsymbol{u_d}-\boldsymbol{w})) && = 0, && \text{(3.65c)}\\
&\vdots && \vdots && \vdots && \\
&\partial_t(J_d m_N) && + J_d\nabla_{\boldsymbol{x}}\cdot(m_N(\boldsymbol{u_d}-\boldsymbol{w})) && = 0, && \text{(3.65d)}\\
&\partial_t(J_d m_1\boldsymbol{u_d}) && + J_d\nabla_{\boldsymbol{x}}\cdot(m_1\boldsymbol{u_d}\otimes(\boldsymbol{u_d}-\boldsymbol{w})) && = 0, && \text{(3.65e)}
\end{aligned}$$

for the spray, and

$$\begin{aligned}
&\partial_t(J_g) && + J_g\nabla_{\boldsymbol{x}}\cdot((\boldsymbol{u_g}-\boldsymbol{w})) && = 0, && \text{(3.66a)}\\
&\partial_t(J_g\rho_g) && + J_g\nabla_{\boldsymbol{x}}\cdot(\rho_g(\boldsymbol{u_g}-\boldsymbol{w})) && = 0, && \text{(3.66b)}\\
&\partial_t(J_g\rho_g\boldsymbol{u_g}) && + J_g\nabla_{\boldsymbol{x}}\cdot(\rho_g\boldsymbol{u_g}\otimes(\boldsymbol{u_g}-\boldsymbol{w})) && = 0, && \text{(3.66c)}\\
&\partial_t(J_g\rho_g E_g) && + J_g\nabla_{\boldsymbol{x}}\cdot(\rho_g E_g(\boldsymbol{u_g}-\boldsymbol{w})) && = 0. && \text{(3.66d)}
\end{aligned}$$

for the gas. We refer the readers to A.1.3 for the full space-time discretization of the spray system (3.65). To meet the challenge of preserving the realizability condition $\boldsymbol{m}^{n+1} \in \mathfrak{M}_{N+1}$, we follow Kah et al. [87].

Equations (3.66) of the gas system imply the pure advection of $(\rho_g, \rho_g u_g, \rho_g E_g)$ at velocity $\boldsymbol{u_g} - \boldsymbol{w}$ by means of similar calculations. Here, the challenge is to preserve positivity for the density ρ_g and the internal energy e_g. Again, first-order schemes meet the requirements but are not accurate enough. Higher order schemes have to equipped with additional treatment. The problem is all the trickier as IFP-C3D uses a staggered grid. The readers are referred to [12] for more details.

3.4 Verification of two claimed features for the new EMSM

As this work aims at extending two previous contributions [120, 87], we focus here on the illustration of EMSM two new capabilities, two-way coupling and moment transport

in the ALE context, by means of some simple test cases. The test cases we consider below are directly inspired from those of [120, 87]. The numerical values assigned to various quantities have been calibrated so as to be representative of the upcoming injection calculations.

3.4.1 Source terms for two-way coupling

In order to test the method for phase A developed in §3.3.1, we concentrate on 0-D cases; phases B and C have been deactivated and analytical solutions can be found. In the two following test cases, the initial data (at $t = 0$) share the common values

$$\rho_d = 760\,\mathrm{kg/m^3}, \qquad u_d = -1\,\mathrm{m/s}, \qquad T_d = 293\,\mathrm{K}, \qquad \mu_g = 1.99 \cdot 10^{-5}\,\mathrm{kg/m/s}, \tag{3.67a}$$

$$\rho_g = \quad 1\,\mathrm{kg/m^3}, \qquad u_g = \quad 1\,\mathrm{m/s}, \qquad T_g = 293\,\mathrm{K}. \tag{3.67b}$$

Since our ultimate goal is to provide a Eulerian alternative for ICE applications, it would be meaningful to make an analogy between the 0-D cases here and the 2-D injection cases of §3.6. To put it another way, it would be nice to have comparable dimensionless numbers, but the problem arises as to how a reference length could be defined for a 0-D case. We have chosen to take the injector diameter $L_0 = 8 \cdot 10^{-3}\,\mathrm{m}$. We set $U_0 = u_g(t = 0) = 1\,\mathrm{m/s}$ for the reference speed and assume that the viscosity $\mu_g(T_g)$ is a constant $\mu_{g,0}$ that does not depend on T_g. In addition to the Reynolds and Stokes numbers, it is also customary to define

$$\Phi_{\mathsf{v}} = \frac{1}{6\pi^{1/2}} m_{3/2}, \qquad \Phi_{\mathsf{m}} = \frac{1}{6\pi^{1/2}} \frac{\rho_d}{\rho_g} m_{3/2}, \tag{3.68}$$

as respectively the volume fraction and the mass loading. In terms of dimensionless quantities, the initial data (3.67) and the initial value of $m_{3/2}$ have been prepared so that

$$\mathsf{Re} = 3.05 \cdot 10^5, \qquad \Phi_{\mathsf{v}} = 1.31 \cdot 10^{-3}, \qquad \Phi_{\mathsf{m}} = 1. \tag{3.69}$$

This implies

$$m_{3/2}(t = 0) = 1.4 \cdot 10^{-2}. \tag{3.70}$$

Let us now focus on the calculation of the Stokes number St of the two-phase flow. From (3.32), the gas-phase characteristic time scale is calculated as $\tau_{g,0} = 8 \cdot 10^{-3}\,\mathrm{s}$. The characteristic time scale τ_d associated to polydisperse spray dynamics is in function of the reference size S_0 and defined as

$$S_0 = \frac{m_{3/2}(t = 0)}{m_{1/2}(t = 0)}, \tag{3.71}$$

which is equal to the initial mean size of the polydisperse distribution, also converts to a reference radius expressed as $r_0 = (S_0/4\pi)^{1/2}$. This choice for S_0 is particulary important since the drag dynamics are driven through the mean size of the polydisperse distribution, as deduced from Eq.(3.45d).

In the following, one will work with different size distributions under a size phase space respecting $S \in [0, S_{max}]$ and $S_{max} = 8.04 \cdot 10^{-8}\,\mathrm{m^2}$ is the maximum size. This implies different S_0 and St for each distribution.

3.4.1.1 Drag force alone

The first numerical experiment, with $K = 0$, is set up to assess numerical stability. As no evaporation comes in to change the size distribution, it is justified to consider a constant distribution in size of droplets

$$n(t = 0, S) = n_0 \mathbf{1}_{[0,S_{max}]}(S), \tag{3.72}$$

where n_0 is chosen so that $m_{3/2}(t = 0) = \int_{\mathbb{R}^+} S^{3/2} n(t = 0, S)\,\mathrm{d}S = \frac{2}{5} n_0 S_{max}^{5/2}$ has the prescribed value (3.70). From n_0, we can deduce

$$m_{1/2}(t = 0) = \int_{\mathbb{R}^+} S^{1/2} n(t = 0, S)\,\mathrm{d}S = \frac{2}{3} n_0 S_{max}^{3/2}. \tag{3.73}$$

From the previous definition for $m_{3/2}(0)$, Eq.(3.73) and Eq.(3.71), the reference size of the distribution is computed as $S_0 = \frac{3}{5} S_{max}$.

The analytical solution is derived as follows. It is obvious that $K = 0$ implies $\partial_t m_{1/2} = \partial_t m_{3/2} = 0$. Because $\partial_t \rho_g = 0$, the total momentum conservation $\partial_t(\rho_g u_g + \frac{1}{6\pi^{1/2}} \rho_d m_{3/2} u_d) = 0$ can be divided by ρ_g and then integrated to yield $u_g = -\Phi_{\mathsf{m}} u_d + \psi$, with $\psi = 0$ thanks to the initial data. Moreover, Φ_{m} remains constant in time. A little algebra shows then that

$$\partial_t u_d = -(1 + \Phi_{\mathsf{m}}) \frac{18\pi\mu_{g,0}}{\rho_d} \frac{m_{1/2}(0)}{m_{3/2}(0)} u_d = -(1 + \Phi_{\mathsf{m}}) \frac{1}{\tau_d} u_d. \tag{3.74}$$

The solution of (3.74) is the decaying exponential

$$u_d(t) = u_d(0) \exp\left(-\frac{t}{\tau_0^\flat}\right), \qquad \text{with } \tau_0^\flat = \frac{\tau_d}{(1 + \Phi_{\mathsf{m}})}. \tag{3.75}$$

This represents a two-way coupled velocity relaxation due to the drag between the phases at relatively high mass loading.

At the numerical level, the stability property of SDIRK depends only the ratio $\Delta t/\tau_0^\flat$. However, we prefer working with the more convenient ratio $\mathsf{Dt} = \Delta t/\tau_d = \Delta t/(\tau_{g,0}\mathsf{St})$, which we call the dimensionless time-step. In this case, as $S_0 = 4.74405 \cdot 10^{-8}$, leading to $\tau_d = 3.204 \cdot 10^{-2}$ and $\mathsf{St} = 4.005$. Smaller Dt leads to more accurate solutions in time. Simulations are run from $t = 0$ to $t = 0.5\,\mathrm{s}$. and results are displayed in Fig. 3.1. The numerical solution is in excellent agreement with the analytical one for a small enough time-step $\Delta t = 10^{-3}$ with $\mathsf{Dt} = 0.0312$. Even when $\Delta t = 10^{-1}$ with $\mathsf{Dt} = 3.12$, a stable solution is obtained, in which the velocities are slightly oscillating but relaxing toward the proper equilibrium.

3.4.1.2 Drag force and evaporation

The second numerical experiment, with $K = 2{\cdot}10^{-8}\,\mathrm{m}^2/\mathrm{s}$, is set up to assess the prediction capability of the numerical integrator, as well as the accuracy of the fractional moment

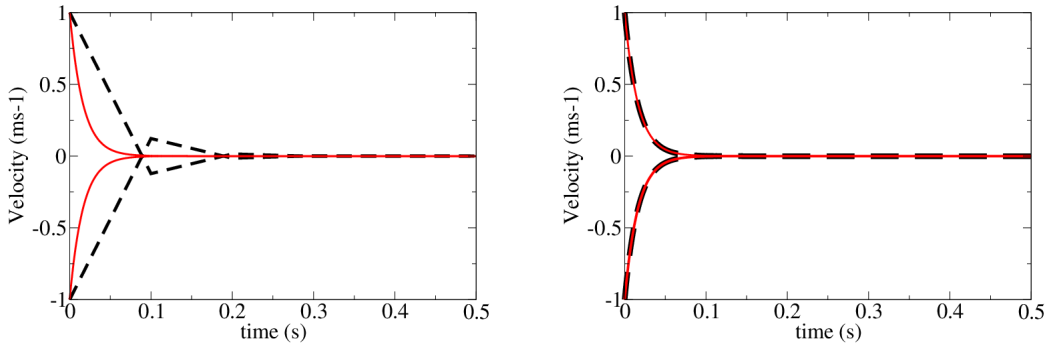

Figure 3.1: Evolution of spray and gas velocities according to the SDIRK method (black dashed line) and the exact solution (solid red line). The time-step Δt is taken to be 10^{-1} s (left) and 10^{-3} s (right).

reconstructor. The impact of the nonzero value of K can be captured by the characteristic evaporation time

$$\tau_v = \frac{S_0}{K} = 0.066098\,\mathrm{s} \tag{3.76a}$$

and its ratio by that of the gas

$$\mathsf{K_v} = \frac{\tau_v}{\tau_{g,0}} = 8.26225. \tag{3.76b}$$

For evaporation to have a sensible effect, we consider an exponential distribution in size of droplets

$$n(t=0,S) = n_0 \exp\left(-\frac{3}{2}\frac{S}{S_0}\right), \tag{3.77}$$

in such a way that S_0 is the mean surface defined by Eq.(3.71). We also define a maximal droplet size in a quite arbitrary way by $S_{max} = 60S_0$ which makes $n\,(t=0,S_{max})$ almost vanish. n_0 is chosen so that
$m_{3/2}(t=0) = \int_{\mathbb{R}^+} S^{3/2} n(t=0,S)\,\mathrm{d}S = n_0 (S_{max}/\beta)^{5/2} \int_{\mathbb{R}^+} \varsigma^{3/2} \exp(-\varsigma)\,\mathrm{d}\varsigma$ has the prescribed value (3.70). From n_0, we can deduce

$$m_{1/2}(t=0) = \int_{\mathbb{R}^+} S^{1/2} n(t=0,S)\,\mathrm{d}S = n_0 \left(\frac{2S_0}{3}\right)^{3/2} \int_{\mathbb{R}^+} \varsigma^{1/2} \exp(-\varsigma)\,\mathrm{d}\varsigma. \tag{3.78}$$

The analytical solution is derived as follows. Starting from $\partial_t n - K\partial_S n = 0$, we have $n(t,S) = n(0,S+Kt)$. By virtue of (3.77), $n(t,S) = n(0,S)\exp(-\frac{3}{2}Kt/S_0)$. Therefore,

$$m_{1/2}(t) = m_{1/2}(0)\exp(-\frac{3}{2}Kt/S_0), \qquad m_{3/2}(t) = m_{3/2}(0)\exp(-\frac{3}{2}Kt/S_0). \tag{3.79}$$

Inserting (3.79) in $\partial_t \rho_g = \frac{1}{4\pi^{1/2}}\rho_d K m_{1/2}$ results in

$$\rho_g(t) = \rho_g(0) + \frac{\rho_d m_{3/2}(0)}{6\pi^{1/2}}[1 - \exp(-\beta Kt/S_{max})]. \tag{3.80}$$

Equations (3.79) and (3.80) confirm the expectation that due to evaporation, the spray mass concentration $\frac{1}{6\pi^{1/2}}\rho_d m_{3/2}$ should decrease and the gas density ρ_g should increase.

The momentum conservation $\partial_t(\rho_g u_g + \frac{1}{6\pi^{1/2}}\rho_d m_{3/2} u_d) = 0$ is integrated to give $\rho_g u_g + \frac{1}{6\pi^{1/2}}\rho_d m_{3/2} u_d = \Gamma$, with $\Gamma = 0$ thanks to the initial data. Thus, $u_g = -\phi_m u_d$ where

$$\phi_m(t) := \frac{\rho_d}{6\pi^{1/2}}\frac{m_{3/2}(t)}{\rho_g(t)} = \frac{\Phi_{\mathsf{m}}\exp(-\frac{3}{2}Kt/S_0)}{1+\Phi_{\mathsf{m}}[1-\exp(-\frac{3}{2}Kt/S_0)]} \tag{3.81}$$

is now a function of time. Note that $\phi_m(0) = \Phi_{\mathsf{m}}$ defined in §3.4.1.1. Combining $\partial_t(m_{3/2}) = -\frac{3}{2}Km_{1/2}$ with $\partial_t(m_{3/2}u_d) = -\frac{3}{2}Km_{1/2}u_d - \frac{18\pi\mu_{g,0}}{\rho_d}m_{1/2}(u_g - u_d)$ and using (3.81), we end up with

$$\partial_t u = -(1+\phi_m(t))\frac{18\pi\mu_{g,0}}{\rho_d}\frac{m_{1/2}(t)}{m_{3/2}(t)}u_d = -(1+\phi_m(t))\frac{1}{\tau_d}u_d. \tag{3.82}$$

The solution of (3.82) is then

$$u_d(t) = u_d(0)\exp\left(-\frac{t}{\tau_d}\right)\left[1+\Phi_m\left(1-\exp\left(-\frac{3Kt}{2S_0}\right)\right)\right]^{-\dfrac{2S_0}{3K\tau_d}} \tag{3.83}$$

Equations (3.83) underscore a nonlinear exponential velocity relaxation due to the drag force.

Simulations are run from $t = 0$ to $t = 0.5\,\mathrm{s}$. The results are displayed in Fig. 3.2. The dimensionless time-step still has the same definition $\mathsf{Dt} = \Delta t/\tau_d$ as before. According to the considered size distribution, the characteristic spray dyamic time scale and Stokes number for the mean droplet size $S_0 = 1.32196\cdot 10^{-9}$ are computed as $\tau_d = 8.92815\cdot 10^{-4}$ and $\mathsf{St} = 0.11160$ respectively. An accurate set of computed results, with relative errors below 1 % for all quantities, is obtained for time step $\Delta t = 10^{-3}$ with $\mathsf{Dt} = 1.12007$. The solution remains stable even for larger time-steps leading to a very robust numerical scheme with proper prediction of the asymptotic states.

3.4.2 Transport of moments in one-way coupling

To test the method for phase C presented in §A.1.3, we concentrate on 1-D cases, for which a one-way coupling dedicated prototype has been written using the ALE formalism. This prototype works with dimensionless units, and therefore all variables in this subsection will be nondimensional. To alleviate the notations, we shall deliberately omit the $*$-superscript.

3.4.2.1 Evaporating aerosol

The first numerical experiment is aimed at demonstrating the possibility of transporting and evaporating an aerosol, as well as the need for a second-order scheme on a moving grid. The particles are considered as tracers, or *passive scalars*, for the gas phase. In

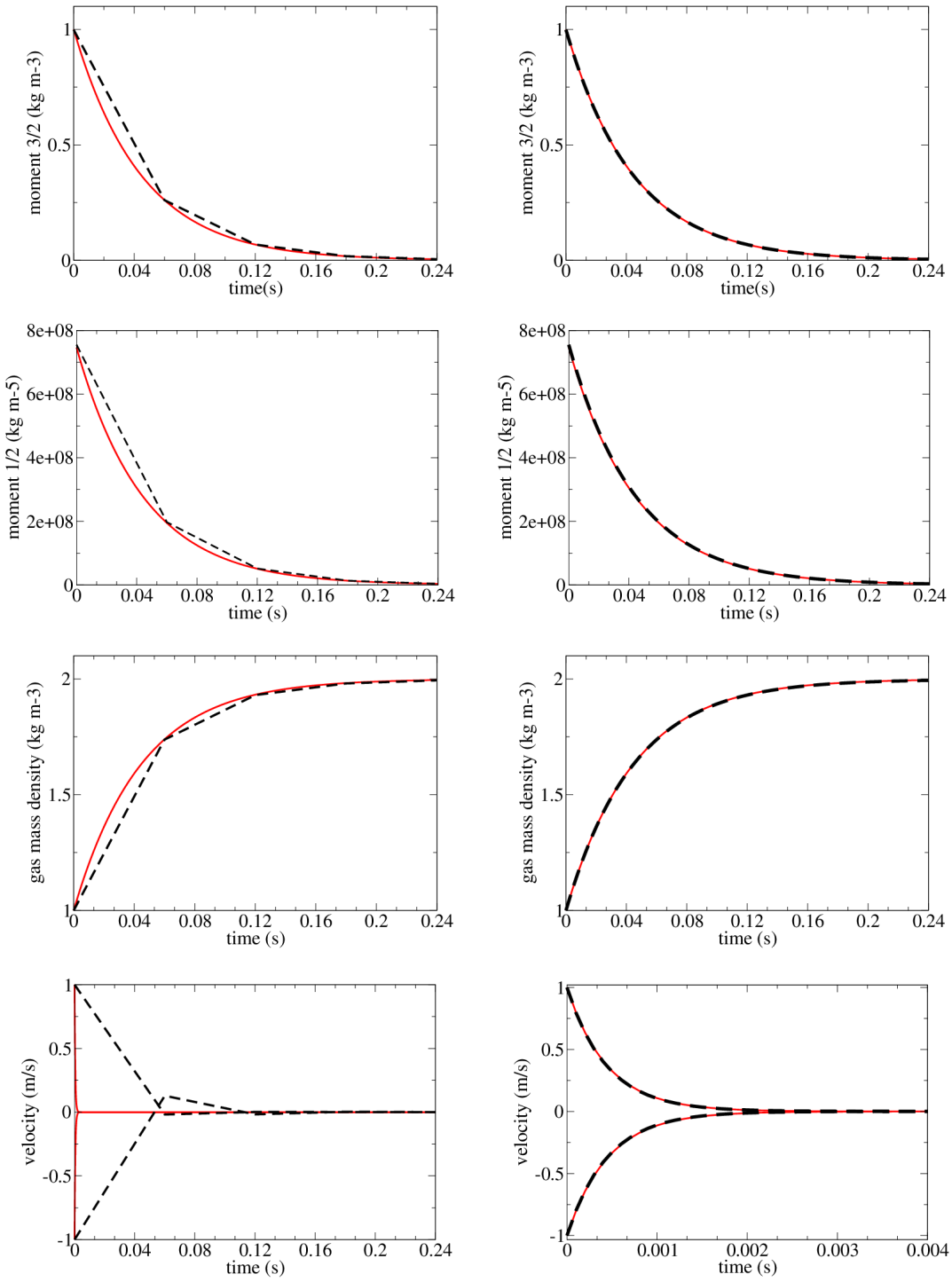

Figure 3.2: Evolution of various spray and gas properties. Results from analytical (solid red lines) and numerical (dashed black lines) solutions. Cases for $\Delta t = 0.06\,\mathrm{s}$ (left column), for $\Delta t = 10^{-3}\,\mathrm{s}$ (right column). Top row: moment of order $m_{3/2}$; second row: moment of order $m_{1/2}$; third row: gas mass density ρ_g; bottom row: velocities u_d and u_g.

other words, instead of having a momentum balance giving $\partial_t(m_1 u)$, we simple-mindedly force $u = u_g$. Consequently, the phase C equations for the aerosol are

$$\partial_t(J_g) \quad + J_g \partial_x(u_g - w) \quad = 0, \tag{3.84a}$$
$$\partial_t(J_g \boldsymbol{m}) + J_g \partial_x(\boldsymbol{m}(u_g - w)) = 0. \tag{3.84b}$$

The gas is initiated as the Riemann data

$$(P_g, \rho_g, u_g)(t = 0, x) = (3, 1, 1) - (2, \tfrac{7}{8}, 0)\mathbf{H}(x - \tfrac{1}{2}), \tag{3.85}$$

where $\mathbf{H}$ stands for the Heaviside function. The aerosol has an initial NDF equal to

$$n(t = 0, x, S) = \mathbf{1}_{[0,1]}(S)\,[1 - \tfrac{7}{8}\mathbf{H}(x - \tfrac{1}{2})], \tag{3.86}$$

The reason why $\rho_g(0, x)$ has been set identical to $m_0(0, x) = \int_{\mathbb{R}^+} n(0, x, S)\,\mathrm{d}S$ is for their profiles to be easily comparable. The initial data are plotted in Fig. 3.3-left.

The Neumann boundary conditions are applied at the boundaries of the space interval $[0, 1]$, which is discretized by a uniform mesh of 200 cells. Some attention must be paid to the choice of the time-step. Indeed, the time-step is determined at the beginning of the resolution, prior to phase A. Therefore, we can at best control $|{u_g}^n - w^n|\Delta t/\Delta x^n$. However, during phases A and B, both u_g and Δx undergo changes, so that the CFL condition (A.27) may be violated in phase C, in terms of $|{u_g}^B - w^n|\Delta t/\Delta x^B$.

It is wise to start with a non-evaporating simulation in which $K = 0$, just to check that waves are correctly propagated. Figure 3.3-right depicts the analytical and computed solutions in (ρ_g, m_0) at $t = 0.1$. Of course, m_2 and m_3 are also solved, but not shown here. The moment m_0 even seems to be less dissipated than the density ρ_g. The first conclusion is that the ALE method gives convincing results as far as transport and acoustic phenomena are concerned.

We are now ready to switch to a genuinely evaporating case with $K = 2$. Figure 3.4-left plots the solution at $t = 0.1$. It shows that, in addition to being propagated and contrary to the gas density ρ_g, the droplet number density m_0 is also attenuated by a rate of about 2, going from 1 to 0.8 for x small enough, say, $x < 0.2$. This observation can be explained by inspecting the right-hand side of the equation $\partial_t(m_0) + \partial_x(m_0 u_d) = -Kn(S = 0)$. Assuming $u_d = u_g =: u$ remains uniform for x small enough, we have $n(t, x, S) = n(0, x - ut, S + Kt)$ from $\partial_t n + u\partial_x n - K\partial_S n = 0$. Therefore, $n(t, x, S = 0) = n(0, x - ut, Kt)$ and according to (3.86), $n(0, x - ut, Kt) = 1$ as long as $t < 1/K$ and $x - ut < 0.5$. Hence, $-Kn(S = 0) = -2$ for x small enough.

Figure 3.4-right displays the results for m_0 of the same test case, but comparing a first-order scheme with the second-order scheme. The accuracy of these schemes is compared on a fixed grid but also in a moving grid. The grid is subject to a uniformly oscillating motion

$$w(t, x) = 4\pi \cos(20\pi t), \tag{3.87a}$$

which creates sinusoidal trajectories

$$x(t, \chi) = \chi + 0.2 \sin(20\pi t). \tag{3.87b}$$

The curved are zoomed in on the interface region. For a fixed grid, the second-order scheme is already more accurate than the first-order. But the interest of a second-order scheme becomes obvious when the grid moves. In our case, the high grid velocity leads to small CFL numbers for the fluids. Therefore the profile of m_0 is much more diffused with the first-order scheme than with the second-order scheme.

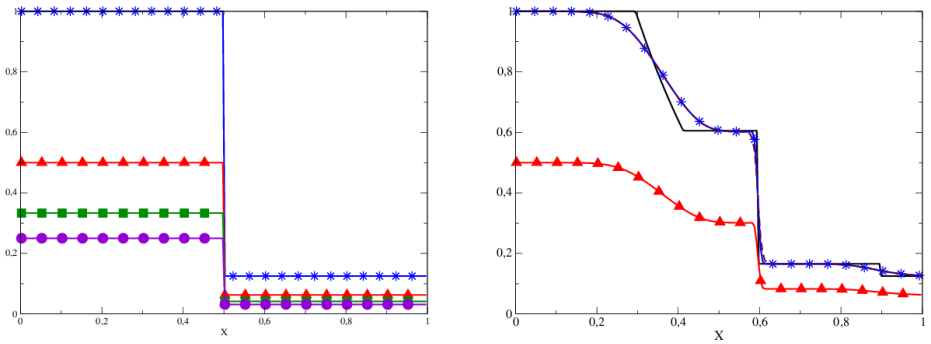

Figure 3.3: *Left*: Initial data for the moments m_0 (blue line with stars), m_1 (red line with triangles), m_2 (green line with squares), m_3 (purple line with circles). *Right*: Solution of the Riemann problem at $t = 0.1$ for non-evaporating particles.

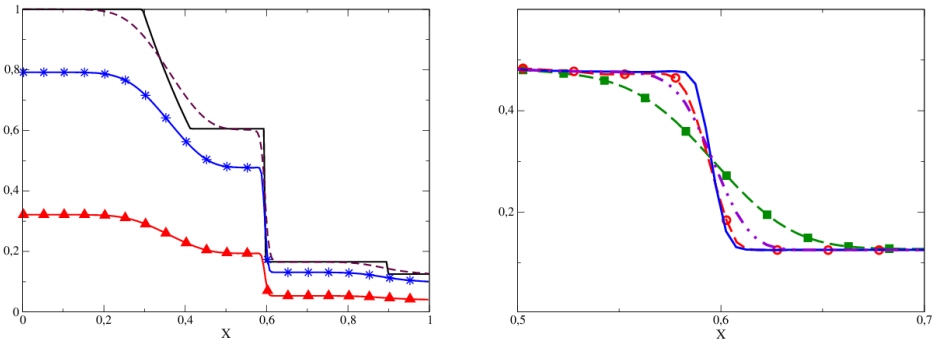

Figure 3.4: *Left*: Solution of the Riemann problem at $t = 0.1$ for evaporating particles, containing the exact ρ_g (solid black line), the computed ρ_g (dashed brown line), the computed m_0 (blue curve with circles) and m_1 (red curve with triangles). *Right*: Close-up on the interfacial area and comparison between various solutions for m_0, namely, second-order solution without mesh movement (solid blue line), second-order solution with mesh movement (dashed red line), first-order solution without mesh movement (dotted-dashed purple line), first-order solution with mesh movement (green line with squares).

3.4.2.2 Non-evaporating spray

The second numerical experiment is aimed at demonstrating the stability as well as the good level of accuracy of the transport scheme in a staggered grid for a non-evaporating

spray. In particular, we want to show that the convection solver is general and does not presume any type of NDF. For that purpose, we consider the NDF

$$n(t=0,x,S) = \left[(1-2x)^2 \sin(\pi S) + 4x(1-x)\exp(-10S)\right] \mathbf{1}_{[0,1]}(S)\, \mathbf{1}_{[0,0.5]}(x), \tag{3.88}$$

which is a convex combination of $\sin(\pi S)$ and $\exp(-10S)$ for $x \in [0, 0.5]$. The moments associated to this NDF are subject to a discontinuous initial velocity

$$u_d(t=0,x) = 0.5 + 1.5\mathbf{H}(x-0.25). \tag{3.89}$$

Periodic boundary conditions are applied at the boundaries of the space interval $[0, 1]$, which is discretized by a uniform mesh of 200 cells. The analytical solution is the translation of the two parts of the density profile corresponding to each value of the velocity. Figure 3.5-left displays the initial condition for the size moments and the velocity.

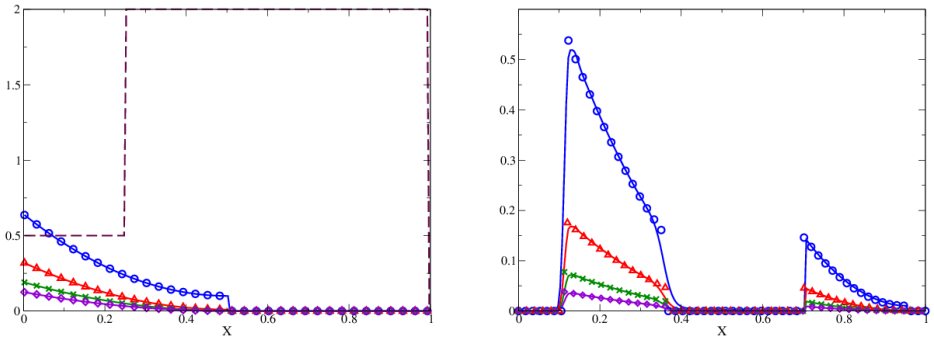

Figure 3.5: Evolution of a spray in a discontinuous velocity field. *Left*: Initial data for the moments and the velocity. *Right*: Analytical solutions (markers) and computed solutions (lines) at time $t = 0.225$ in the first four moments, i.e., m_0 (blue), m_1 (red), m_2 (green), m_3 (purple).

At $t = 0.225$, the initial distribution breaks into two parts, as shown in Fig. 3.5-right. Vacuum is created at the prescribed velocity discontinuity. The computed moments are represented by solid lines in decreasing order, meaning that the highest curve stands for the 0th-order moment, and the lowest curve stands for the 3rd-order moment. Their analytical counterparts are represented by markers. The numerical solution is seen to match the analytical one very accurately. We underline that the proposed model and numerical method with built-in realizability condition have provided a robust way of treating the coupled dynamics and evaporation of a polydisperse spray carried by a gaseous flow field, even within the moving mesh framework, the appearance of vacuum zones of droplets and with potentially very stiff source terms treated implicitly.

3.5 Implementation of EMSM in IFP-C3D

3.5.1 A glimpse of IFP-C3D

Over the past several years, the IFP-C3D code [12] has been developed at IFP Energies nouvelles for the numerical simulation of advanced internal combustion engines. IFP-

C3D involves a great many intricate physical and chemical processes, most prominently transient and multidimensional, for multicomponent mixtures of gases undergoing mixing, ignition, reactions, heat transfer, and turbulence. These numerous options can be individually activated or deactivated by input switches, which makes IFP-C3D a versatile tool for engineers. As far as liquid spray is concerned, it was previously incorporated in IFP-C3D with a Lagrangian approach called *stochastic parcel* [74].

The most salient feature of IFP-C3D is its capability to tackle engine geometries with arbitrarily shaped moving piston, valves or other actuators. To accomplish this, IFP-C3D resorts to a staggered grid whose hexahedral or tetrahedral cells build up an unstructured mesh. Thermodynamic variables are located at the cell-centers, while velocity vectors are located at the nodes. Such a choice is meant to make the mesh motion unambiguous: the vertices are simply moved to new user-specified positions. The price to be paid for such a convenience with respect to mesh motion is some awkwardness in discretizing the momentum balance equations over the dual mesh.

As expounded in §3.3.2 and §3.3.3, each time-step in IFP-C3D consists of three phases:

- In phase A, source terms of the chemical reactions on gas[5], of the Lagrangian fuel injection spray and of the spark ignition are calculated.
- In phase B, all the diffusive and acoustic terms are solved implicitly, with first the species mass, internal energy term, and turbulent terms. The method introduced in [137] is retained in its fully implicit version. The coupled implicit equations (momentum, temperature and pressure) are solved with the SIMPLE algorithm [182]: this is called the PVT (Pressure Temperature Velocity) loop.
- In phase C, the outcomes of phase B are remapped in order to match the imposed new grid. The corresponding linear convection equations are solved explicitly, so as to enhance accuracy with respect to kinematic phenomena. Limited slope reconstruction is considered via dimensional splitting, which gives rise to the so-called Quasi Second Order Upwind Scheme (QSOU) [4]. Subcycles may have to be introduced in order to ensure the CFL condition.

3.5.2 Validation in one-way coupling configurations

In light of the numerical method outlined in §3.3 and §A.1, we have added to IFP-C3D the ability to simulate a Eulerian spray using the EMSM model. This implementation is validated through a range of test cases, the two most crucial of which are presented below in the one-way coupling configuration. In §3.6, an injection case of a polydisperse droplet spray will be done in a two-way coupling framework integrated in the ALE algorithm and compared with the Lagrangian result.

3.5.2.1 Scheme robustness through mesh movement

The objective of this test case is to ensure that the implemented model is stable with mesh movement. The evolution of homogeneous fields of liquid and gas are considered in

[5] auto-ignition, combustion, post-oxidation, chemical equilibrium, etc.

a closed high pressure cell. The bottom boundary of this cell corresponds to a moving piston being at the bottom dead center. The gas is taken as air, and the particles are initially stationary. No ignition occurs, and no thermal effect is considered. Also, no special treatment of the boundary is considered. The computation ends after a revolution of the crank, with the *crank angle degree* (cad) ranging in $[-180°, 180°]$. The high pressure cell and the movement of the piston are described in Fig. 3.6.

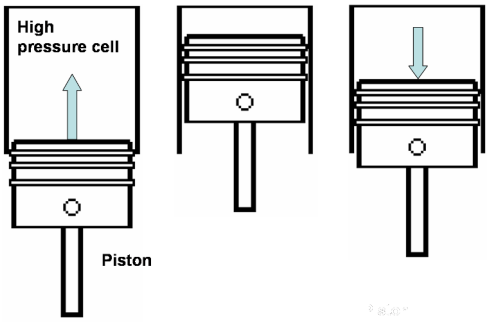

Figure 3.6: Piston movement during the computation. The computation starts at cad $= -180°$ and ends at cad $= 180°$.

The boundary conditions are $(\boldsymbol{u_d} - \boldsymbol{w}) \cdot \boldsymbol{n} = 0$ on the surface of the piston, and $\boldsymbol{u_d} \cdot \boldsymbol{n} = 0$ at the upper edge of the domain. The size distribution is constant and similar to the one-dimensional tests with an aerosol. During the compression and expansion of the high pressure cell, the computational cell volumes change is homothetic. The results are displayed for the number density m_0 and the surface density m_1 with a 1200-cell grid (30×40). Computations are successively run for an aerosol and a spray. Figure 3.7-left displays the results for the moments, in the case of an aerosol, at cad $= -100°$, $-30°$, $50°$, $180°$. In the various graphs, the distance where the value of the moments is null is the distance traveled by the piston. These graphs show that the flow stays homogeneous during the whole computation. This is a typical case where the operator splitting done in the algorithm of IFP-C3D is legitimate since the speed of sound is at least one order of magnitude higher than the convective speed of the fluid. In fact, the speed of sound exceeds 300 m/s. At the same time, with a rating of 1200 rpm, and a stroke of about 10 cm, the piston average velocity and that of the dragged fluid is much smaller than the speed of sound in the gas. Mass conservation imposes that the gas density and consequently the particle number increases as the piston heads to the top dead center, because the volume of the high pressure cell decreases, Fig. 3.7-left (top right), Fig. 3.7-left (bottom left). The moments recover their initial values at the end of the computation which corresponds to the end of the expansion stroke.

Figure 3.7-right displays results for a spray at different instants. The first two (cad $= -100°$ and cad $= -30°$) correspond to the compression of the high pressure cell. The two following ones (cad $= 50°$ and cad $= 180°$) correspond to the expansion of the domain. The case of a spray is dramatically different from the previous one. Indeed inertial particles within the infinite Stokes limit are considered now, since no interaction with the gas phase is taken into account. They stick to the piston as it moves upward.

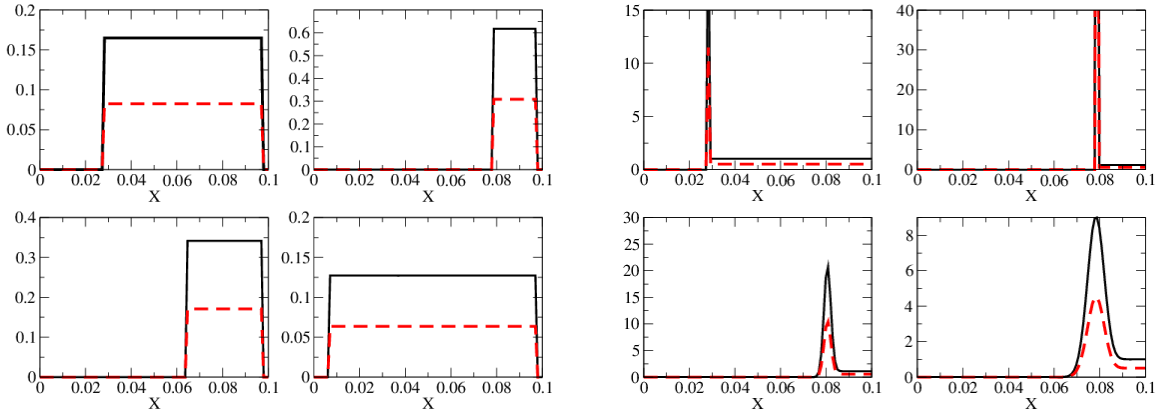

Figure 3.7: *Left*: Results in the case of an aerosol, for m_0 (solid black line) and m_1 (dashed red line). Results for cad $= -100°, -30°, 50°, 180°$. *Right*: Results in the case of a spray, for m_0 (solid black line) and m_1 (dashed red line). Results for cad $= -100°$, $-30°$, $50°$, $180°$.

This behavior is observed in Fig. 3.7-right (top) and is responsible for the singularity present at the piston surface. Meanwhile, the moment field downstream of the piston is unchanged. This is a direct consequence of the assumption made for pressureless gas dynamics, wherein the speed of sound is null, and consequently no pressure wave modifies the field. In Fig. 3.7-right (bottom), the δ-shock moves forward relatively to the mesh. The enlargement of the δ-shock has two explanations. The first one is the numerical diffusion. Secondly, the computational cell volume expansion contributes to the δ-shock enlargement. Meanwhile, upstream of the δ-shock, in the wake of the piston, a vacuum zone is created, which is the expected behavior.

3.5.2.2 Spray dynamics through evaporation and drag, comparison with MUSES3D

The objective of this test case is to study and validate the behavior of spray particles, undergoing evaporation and drag. Therefore no mesh movement is considered. The chosen test case involves the Taylor-Green vortices for the gas velocity field in a square and periodic domain, wherein a motionless droplet cloud is initiated, which can be seen in Fig. 3.8. The results obtained with IFP-C3D are validated by comparison with the results obtained for the same configuration with the MUSES3D code, an academic solver for polydisperse spray [30], wherein the EMSM model has been implemented and validated [87].

The velocity field then writes

$$\boldsymbol{u_g}(x,y) = U_0\left(-\sin\frac{2\pi x}{L_0}\cos\frac{2\pi y}{L_0},\ \cos\frac{2\pi x}{L_0}\sin\frac{2\pi y}{L_0}\right). \tag{3.90}$$

The characteristic droplet diameter is taken as 100 µm which amounts to a Stokes number of 1.4

Four different instants are represented. The results obtained with the IFP-C3D code are compared to the ones obtained with the MUSES3D code at $t = 1$, Fig. 3.9, $t = 1.4$, Fig. 3.10, and $t = 2$, Fig. 3.11. The field displayed is m_0, size moment of order zero, equal to the total droplet number.

Since the droplet cloud is initialized in two different vortices, a main part is dragged in the top-left vortex, whereas a small part is dragged by the top-right vortex, as seen at $t = 1$. The droplet Stokes number is much higher than the critical Stokes number St_c, below which the particles stay in the vortices, so that their characteristics do not cross. At $t = 1.4$, particles are ejected from the vortices because of the periodic boundary conditions, especially particles dragged by the top-left vortex which enter the bottom-right vortex. In this region, the gas velocity field direction is opposed to the droplet velocity one. As seen at $t = 2$, this leads to the creation of a discontinuity in the velocity and thus to the formation of a δ-shock in the particle size moment field. We reiterate that this is a typical effect of the pressureless gas formalism used in the EMSM model. Meanwhile, the residual portion of the small part dragged by the top-right vortex is ejected from this vortex and enters the δ-shock.

Although the code structures are very different, one can assess that the level of similarity between the results given by the two codes is very high. Indeed there are three paramount differences between the numerical schemes implemented in MUSES3D and in IFP-C3D. The first one concerns the formalism used. The MUSES3D code is an academic solver dedicated to spray resolution in an Eulerian formalism, whereas in IFP-C3D the ALE formalism is implemented. Secondly, the numerical scheme for transport in physical space is second order in space and time in the MUSES3D code, whereas it is only first order in the IFP-C3D code. This is the reason why the moment field is more diffused at time $t = 1, 1.4$ and 2. Finally, in the structured MUSES3D code, a dimensional splitting algorithm handles transport in multi-dimensions, whereas in the IFP-C3D code which is an unstructured code, it is fully multi-dimensional. This is why, at time $t = 2$, in the result given with MUSES3D, the particles, dragged by their inertia, penetrate further in the bottom-right vortex than in the result given in the IFP-C3D code. Nevertheless, this comparison case is a success and validates the implementation of the EMSM model in the IFP-C3D code in terms of spray dynamics through transport coupled to drag and evaporation.

3.6 Feasibility of injection computations with IFP-C3D

The 2D test-case involved in section 3.5 was dedicated to an academic framework where the gas-phase is considered to be frozen and the cloud of polydisperse droplets initially at zero velocity is driven by the gas. However, this study is not enough to prove the ability of moment methods to reproduce correct and stable simulations for a more complicated application. Moreover, in the context of industrial applications such as the direct injection of the liquid fuel in an internal combustion engine, it is required to capture the gas-phase entrainment by the polydisperse spray. Therefore, the efficiency of the two-way coupling methodology developed in subsection 3.3.1 needs to be investigated under the

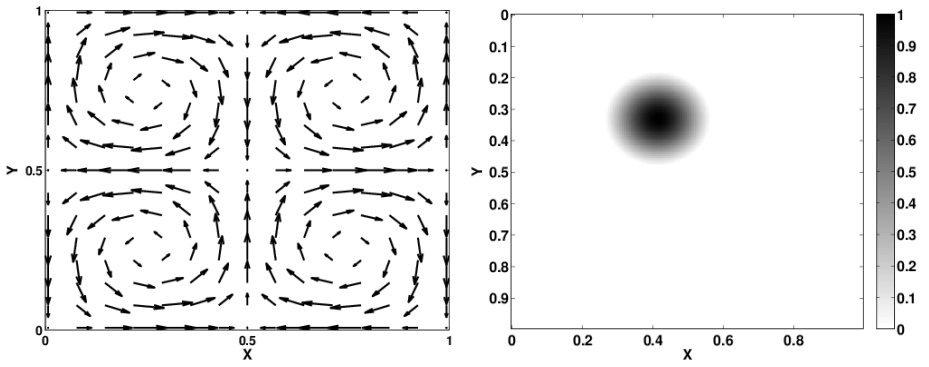

Figure 3.8: *Left*: Taylor-Green configuration for the gaseous flow. *Right*: initial condition for the moment m_0 of the spray.

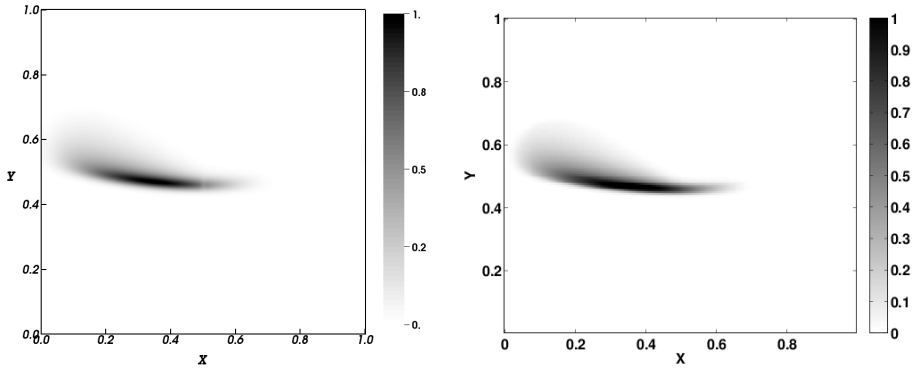

Figure 3.9: Results for m_0 at time $t = 1$. *Left*: with IFP-C3D. *Right*: with MUSES3D.

injection computations with IFP-C3D. Let us recall that injection parameters for the spray should be chosen such that the mass loading ratio Φ_m and the spray volume fraction Φ_v determining the validity of the two-way coupling, as highlighted by in [7]. Yet, the issue of spatial discretization accounts for a difficult task. The finite volume method on staggered grids [102] along with the mesh motion through ALE formalism can be considered as major numerical difficulties within the framework of engine simulations, tackled in the industrial software IFP-C3D [12]. Moreover, the moment space conservation issue through EMSM still needs to be approved. In this section, one considers a 2-D injection of the gas-spray mixture in a gas filled chamber. Actually, the test case is chosen such that one has the corresponding experimental data for a thin, polydisperse and collisionless spray under the turbulent dispersion of droplets [58]. However, we will limit our study to a laminar flow regime. The industrial software IFP-C3D [12] dedicated to reactive compressible flows will be used for such simulations. In the following, the test case, including both spray and gas properties, will be first described. The main aim being to verify the full Eulerian description of the dispersed phase with respect to Lagrangian particles [47], one will then introduce the methodology to correctly initialize both Eulerian and Lagrangian fields at the beginning of each computation. Finally, injection results will be discussed. The effect of mean droplet size with and without evaporation will be investigated.

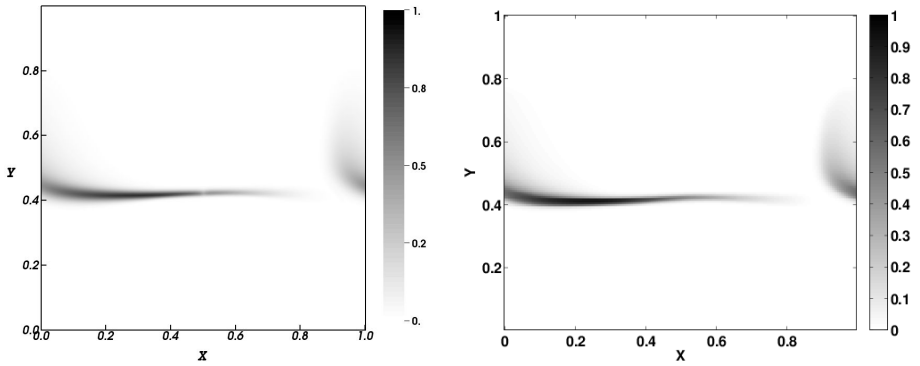

Figure 3.10: Results for m_0 at time $t = 1.4$. *Left*: with IFP-C3D. *Right*: with MUSES3D.

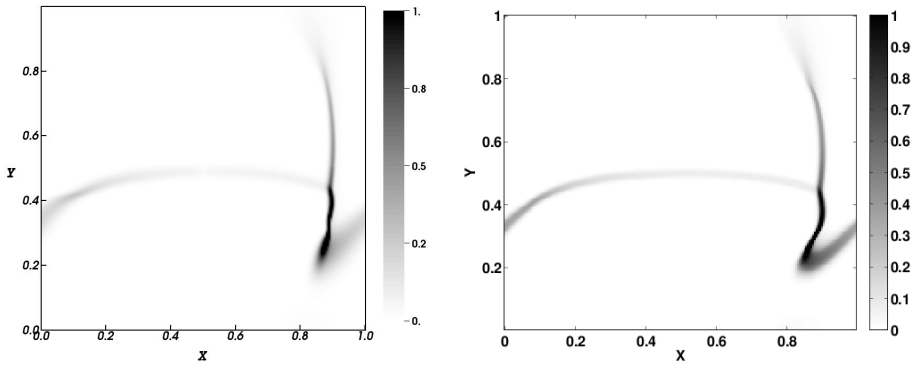

Figure 3.11: Results for m_0 at time $t = 2$. *Left*: with IFP-C3D. *Right*: with MUSES3D.

3.6.1 Description of the test case

The computations are run with a polydisperse droplet population governed by the Rosin-Rammler distribution [155]

$$f(r) = q\frac{r^{q-1}}{r_{\mathrm{SMR}}^{q}} \exp\left(-\frac{r^{q}}{r_{\mathrm{SMR}}^{q}}\right), \tag{3.91}$$

where r is the particle radius, r_{SMR} is the Sauter mean radius (SMR), and q is a coefficient determining the sharpness of the distribution. The distribution considered here is the one with $q = 3.5$, see Fig. 3.12.

The computations are run with the geometry presented in Fig. 3.13. This is proportional to a two-dimensional mesh in the y- and x-axes, respectively. This 2-D plan is composed of square cells with a length of 0.25 mm (320 cells in the x-direction, and 800 cells in the y-direction). Yet two cells with a length of 0.5 mm along the z-axis had to be kept since IFP-C3D software is a 3-D code. The 32×16 cell additional part at the top of the mesh is dedicated to the injection type inlet condition. Periodic boundary conditions are set on faces orthogonal to the z-axis, and free exit boundary conditions are set for the part localized at $y = 0$, $x = 40\,\mathrm{mm}$ and $x = -40\,\mathrm{mm}$. The cases presented in this section involve injection of a fuel spray and gas with velocity $u_{\mathrm{inj}} = 18\mathrm{m/s}$. The ambient gas phase is taken as air, with initial pressure $P_g = 10^5\,\mathrm{Pa}$, temperature $T_g = 293\,\mathrm{K}$, and

viscosity $\mu_g = 1.99\ 10^{-5}\,\mathrm{kg/m/s}$, whereas the fuel is taken as the $C_{14}H_{30}$ species, with a density $\rho_d = 763\,\mathrm{kg/m^3}$. Some other initial thermodynamic quantities can be found in Table 3.1.

$C_{p,g}$	1014.047 J/kg/K
$C_{v,g}$	724.660 J/kg/K
γ_g	1.399
e_g	21318.245 J/kg
R_g	8.314
$C_{v,d}$	1435.909 J/kg/K
e_d	−59784.881 J/kg

Table 3.1: Values of heat capacity in constant pressure of the gas $C_{p,g}$, in constant volume of the gas $C_{v,g}$ and the fuel spray $C_{v,d}$. Specific internal energies of the gas e_g and the spray e_d, the perfect gas constant R_g and the ratio $\gamma_g = C_{p,g}/C_{v,g}$.

To characterize the spray / gas interaction regime, we introduce a characteristic length $L_0 = 8 \cdot 10^{-3}\,\mathrm{mm}$ which is the injection diameter and a characteristic corresponding time $\tau_{g,0} = L_0/u_{\mathrm{inj}}$ for the gas flow. In our case, the mean droplet diameter being significant for the study of the disperse phase, the characteristic dynamic time scale for the droplet population is given as a function of the SMR number

$$\tau_0 = \frac{2\rho_d r_{\mathrm{SMR}}^2}{9\mu_{g,0}} \tag{3.92}$$

We also define some dimensionless numbers such as the fractional volume occupied by the dispersed phase Φ_v and the Stokes number St expressed as the ratio of the droplet dynamic time response τ_0 over the gas characteristic time $\tau_{g,0}$.

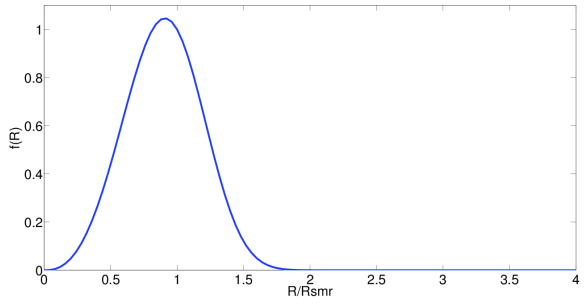

Figure 3.12: Illustration of Rosin-Rammler distributions actually used in the computations.

3.6.2 Initialization strategy of both Eulerian and Lagrangian computations

Since our aim is to conduct accurate comparisons between Lagrangian and Eulerian simulations, some preliminary computations are required to determine injection boundary conditions. Given the value of injected liquid volume fraction α_d and the distribution function shown in Fig. 3.12, one can compute moments of the distribution at injection for Eulerian simulations. However, in IFP-C3D, the injection of Lagrangian particles is controlled by the total liquid mass m_l, the injection time length t_{inj} and the injector radius r_{inj}. To have the same injection conditions in Lagrangian cases, we first compute the mass flow rate for a given inlet velocity and inlet volume fraction by the formula

$$\dot{m}_l = \Phi_{\mathsf{v}} \rho_d u_{\text{inj}} S \tag{3.93}$$

where S is the injection section for the two-phase flow and $\rho_d S$ corresponds to the injection section for the Lagrangian particles. From the latter, r_{inj} can be easily calculated. Moreover, from the knowledge of t_{inj}, m_l is deduced from

$$m_l = \dot{m}_l t_{\text{inj}} \tag{3.94}$$

Lagrangian particles are injected in the middle of each of the 64 cell face belonging to the inlet condition, which leads to a total of 64 injectors. Since the mesh is a 2-D plane, the radius and the injection section related to each injector remain same.

r_{SMR}	5 µm	20 µm
St	0.479	7.67
Φ_{v}	$2.51 \cdot 10^{-4}$	$2.51 \cdot 10^{-4}$
Φ_{m}	0.191	0.191
τ_v	$1.4 \cdot 10^{-2}$ s	$1.4 \cdot 10^{-2}$ s
τ_v/τ_0	65.7	4.14

Table 3.2: Dimensionless characteristic values at injection: Stokes numbers St, spray volume fraction Φ_{v} and mass loading Φ_{m} are computed through the Sauter mean radius r_{SMR}.

3.6.3 Discussion on injection simulations

In the context of injection simulations, the two-way coupling effects on flow dynamics can not be neglegted when the mass ratio of the dispersed phase over the gas phase becomes significant. Moreover, inertial droplets inside a distribution have a low response to changes in the gas whereas light particles barely follows the carrier gas phase. The spray dispersion is thus influenced by the size of the droplets. In internal combustion engines, a broad range of fuel droplet sizes needs to be considered. We run injection simulations under two types of droplet distributions characterized by different Sauter mean radius r_{SMR} but the same mass loading Φ_{m} or volume fraction Φ_{v}, as observed in Table 3.2. These initial

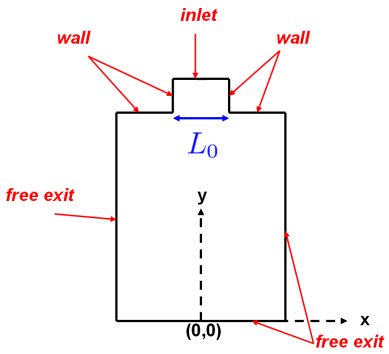

Figure 3.13: Illustration of the 2-D plane geometry and boundary conditions

characteristic numbers are chosen such that droplet-droplet interactions can be assumed to be neglected. Note that, we adopt a simple d^2 evaporation law of droplets under a constant evaporation time τ_v for both low and high inertia droplets. The ratio of the evaporation time over the characteristic droplet time τ_v/τ_0, observed in Table 3.2, shows that the spray with high inertia droplets undergoes a faster evaporation.

For each distribution, we run separately four simulations. Two of them are dedicated to Lagrangian description of droplets whereas the other two are devoted to the full Eulerian resolution of the dispersed flow. Note that for each method, there are two possibilities; the spray being either evaporating or not. The initial spray mass flow rate is taken as $2.76 \cdot 10^{-5}$ kg/s. A total number of 6.4 millions numerical particles, insuring the convergence of the Lagrangian solution, is injected to the domain.

In the following, results are displayed for a simulation time of $1.4 \cdot 10^{-2}$ s. The latter also corresponds to the characteristic evaporation time τ_v, as shown in Table 3.2. Each figure contains results from both Eulerian and Lagrangian resolutions of the fuel spray.

3.6.4 Injection of low inertia droplets

Injection results in the case of a light droplet population with Sauter mean radius $r_{\text{SMR}} = 5\mu$m are illustrated in Figures 3.14 and 3.15. The fields of spray volume fractions and spray velocity for both Lagrangian and Eulerian sprays are quite similar. The global droplets dynamics is well reproduced. Let us note that the front of Lagrangian spray is sharper than the Eulerian one.

The fuel vapor field is also very well represented, as seen through Fig. 3.15. This shows that the mass density modification in the gas due to the evaporation between phases are well captured through the two-way coupling algorithm. Moreover, the gas velocity field driven by the Eulerian spray is qualitatively similar to the one driven by the Lagrangian spray, see Fig. 3.14. Although the spray and the vapor penetration lengths are slightly different as shown in Fig. 3.17, there is a good quantitative compromise between both approaches. The spray and vapor dispersions along the injection width is also very well captured despite small differences, as plotted in Fig. 3.16.

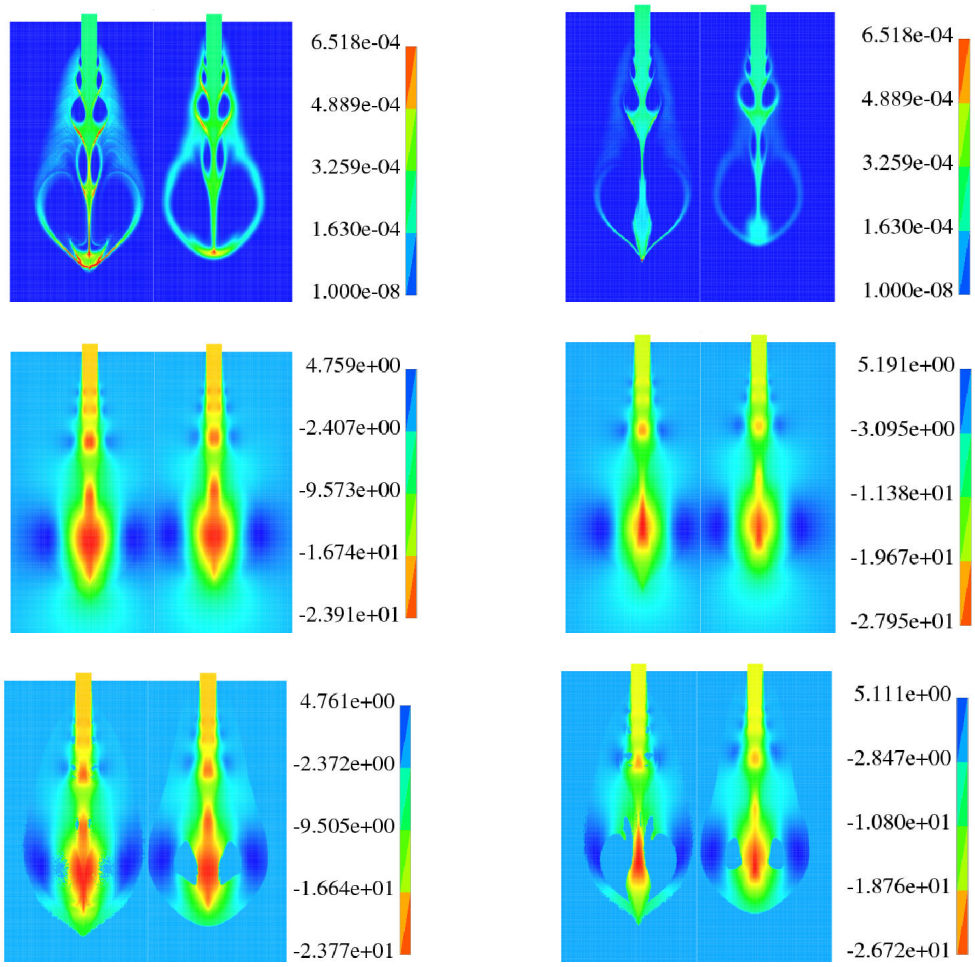

Figure 3.14: Results for a droplet population of $r_{\mathrm{SMR}} = 5\mu\mathrm{m}$ at time $1.4 \cdot 10^{-2}\,\mathrm{s}$. *Left*: Spray without evaporation. *Right*: Spray with constant evaporation velocity. Spray volume fraction (top row), gas velocity along the y-axis (middle row), spray velocity along the y-axis (bottom row). In each panel, Lagrangian spray is displayed on the left side whereas Eulerian on the right side.

3.6.5 Injection of high inertia droplets

In case of a droplet population with $r_{\mathrm{SMR}} = 20\mu\mathrm{m}$, results from fields of spray volume fraction, spray velocity, gas velocity are illustrated in Fig. 3.18, whereas Fig. 3.19 shows the field of vaporized fuel mass fraction. Through spray velocity and spray volume fraction fields, differences between Eulerian and Lagrangian sprays can be observed. There is a high concentration of Eulerian droplets at the front side of the spray. This situation can be argued through the fact that the presureless gas formalism is adopted for the spray modeling where the spray momentum equation is weakly hyperbolic without any diffusion terms. But this is not enough to explain the real situation since for low inertia droplets the pressureless approach was working perfectly. The second issue is that, in real situations, droplets with different sizes and different velocities can cross. Therefore, from

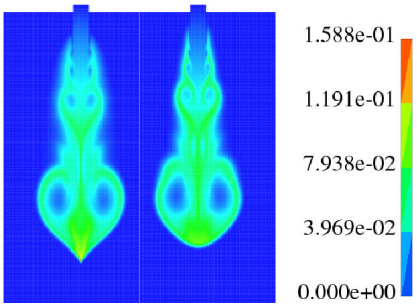

Figure 3.15: Evaporated fuel mass fraction inside the gas-phase for a droplet population of $r_{\mathrm{SMR}} = 5\mu\mathrm{m}$ under a constant evaporation velocity at time $1.4 \cdot 10^{-2}\,\mathrm{s}$. In the panel, Lagrangian spray is displayed on the left side whereas Eulerian is displayed on the right side.

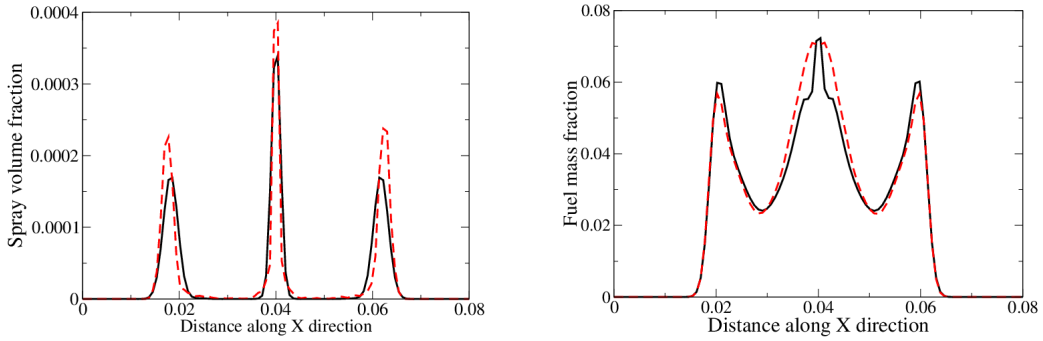

Figure 3.16: Results from 1-D plots, taken along the x-direction which center point on y-axis is 12 diameter far from the injector, in case of a droplet population of $r_{\mathrm{SMR}} = 5\mu\mathrm{m}$. Results from Eulerian (solid black lines) and Lagrangian (dashed red lines) solutions. *Left*: Spray volume fraction for droplets without evaporation. *Right*: Evaporated fuel mass fraction for evaporating droplets with a constant evaporation velocity.

the modeling point of view, the droplet trajectory crossing effect needs to be taken into account. Yet, the EMSM method has proven to fail to simulate that type of configurations. This failure stems from the assumption that all droplets located in the same cell have the same velocity. However, high inertia droplets cannot be considered to have the same velocity, since the drag force between phases is strongly conditioned by the droplet size. So one can conclude that the high droplet concentration observed for Eulerian spray leads to some non physical solutions. Yet, the core of the Eulerian spray is quite similar to the Lagrangian one. Moreover, the high droplet accumulation is drastically reduced in the case of evaporating droplets. The field of evaporated fuel mass fraction between the Lagrangian and the Eulerian sprays, as shown in Fig. 3.19, matches quite well.

As illustrated in Fig. 3.20, the quantitative evaluation for non evaporating spray along the injection width shows an important gap in spray volume fraction field. However, the Eulerian fuel vapor width tends to the Lagrangian solution, when evaporation is considered. Figure 3.21 implies that the sudden increase in Eulerian spray volume fraction

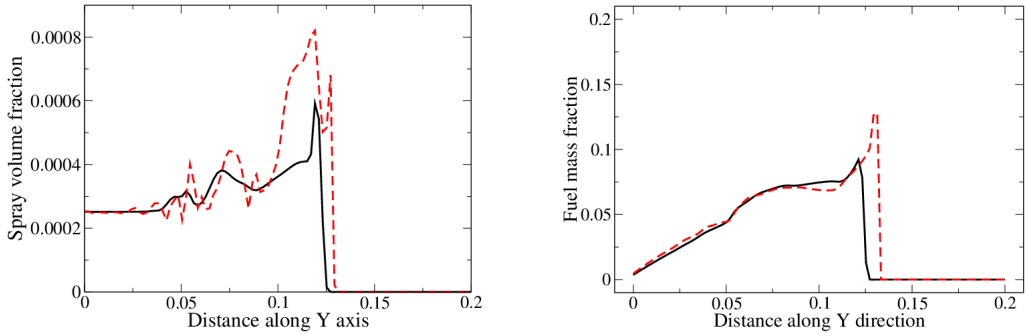

Figure 3.17: Results from 1-D plots, taken along the y-axis see Figure 3.13, in case of a droplet population of $r_{\mathrm{SMR}} = 5\mu\mathrm{m}$. Results from Eulerian (solid black lines) and Lagrangian (dashed red lines) solutions. *Left*: Spray volume fraction for droplets without evaporation. *Right*: Evaporated fuel mass fraction for evaporating droplets with a constant evaporation velocity.

at the front side of the spray is not observed for the field of evaporated fuel mass fraction. This behavior is expected since the evaporation leads to a decreasing droplet inertia where the mono-kinetic assumption without the polydispersity in velocity, works quite well. This situation is likely to occur, because in normal ICE engine operating conditions, the fuel droplet evaporation takes place under high temperatures and pressures.

3.6.6 Concluding remarks on injection simulations

In this section, the unexplored issue which is the ability of EMSM moment method to tackle the two-way polydisperse interactions of droplets with the surrounding gas phase has been revealed. The method has been proved to be stable and accurate, preserving the moment space, within the multi-dimensional context. Through its rigorous comparison with the widely used Lagrangian method, promising results towards ICE engine injection applications have been obtained. The good accuracy on the fuel vapor field and gas phase properties shows that Eulerian method is in equal footing with the Lagrangian method. Although all these achievements have been carried out under a 2-D injection test case with motionless geometry. The simulations were done under the fully coupled two-way formalism integrated in the ALE algorithm as presented in the previous sections.

3.7 Conclusion

Throughout this paper, we have explained how to adapt the EMSM model and its associated numerical methods from the one-way to the two-way coupling framework and from fixed to moving grids. The challenge here is to respect the strong stability conditions inherent to the model in order to provide robustness without introducing a loss of both computational efficiency and accuracy by enforcing the stability conditions a posteriori.

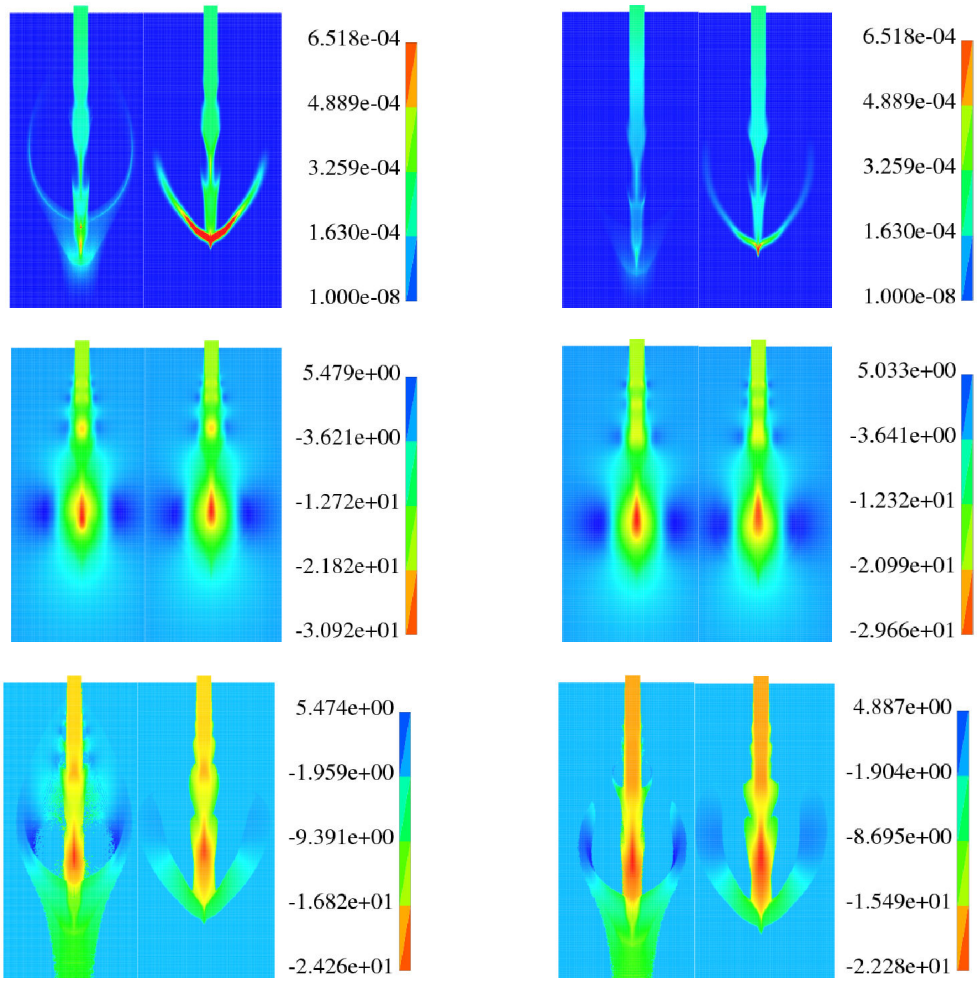

Figure 3.18: Results for a droplet population of $r_{\mathrm{SMR}} = 20\mu\mathrm{m}$ at time $1.4 \cdot 10^{-2}\,\mathrm{s}$. *Left*: Spray without evaporation. *Right*: Spray with with constant evaporation velocity. Spray volume fraction (top row), gas velocity field along the y-axis (middle row), spray velocity along the y-axis (bottom row). In each panel, Lagrangian spray is displayed on the left side whereas Eulerian is displayed on the right side.

A significant part of this work has consisted in implementing the EMSM model in the IFP-C3D code, an industrial software solving reactive compressible flows in unstructured grids and dedicated to engine computations. By extensive numerical simulations, we have shown that injection cases can be handled.

High order moment methods are able to describe polydispersity without discretizing the size phase space into sections, contrary to sectional/multi-fluid methods. But the methods suggested in the literature [130, 65] face some limitations preventing their use in the applications we target. In this respect, the EMSM model can be considered a breakthrough both in terms of modeling, with a new and efficient way to describe polydispersity and in terms of numerical methods, with a low level of artificial dissipation while maintaining the realizability condition and the maximum principle. It currently represents

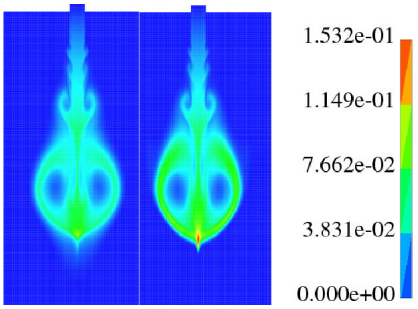

Figure 3.19: Evaporated fuel mass fraction inside the gas-phase for a droplet population of $r_{\mathrm{SMR}} = 20\mu\mathrm{m}$ under a constant evaporation velocity at time $1.4 \cdot 10^{-2}\,\mathrm{s}$. In the panel, Lagrangian spray is displayed on the left side whereas Eulerian is displayed on the right side.

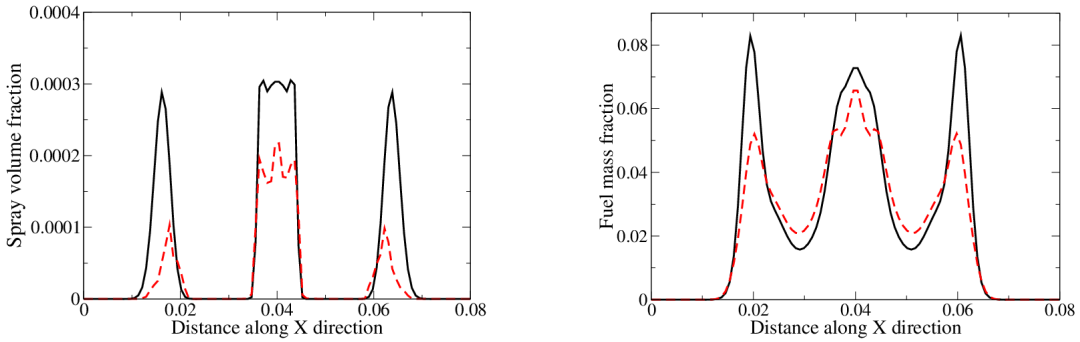

Figure 3.20: The results from 1-D plots, taken along the x-direction which center point on Y axis is 12 diameter far from the injector, in case of a droplet population of $r_{\mathrm{SMR}} = 20\mu\mathrm{m}$. Results from Eulerian (solid black lines) and Lagrangian (dashed red lines) solutions. *Left*: Spray volume fraction for droplets without evaporation. *Right*: Evaporated fuel mass fraction for evaporating droplets with a constant evaporation velocity.

an important source of ongoing investigations, which widens its range of applicability. Resolving one additional moment transport equation, Vié et al. [189] has introduced the ability of describing a correlation between the size and the velocity variable. Hence, the type of flows described by the EMSM model should describe flows with particles having a larger Stokes number. This extended model has been denoted CSVM model (Coupled Size and Velocity Moment) model. Furthermore, the use of the model and methods developed in this paper in order to treat size polydispersity can be used beyond a mono-kinetic assumption for the particle velocity distribution within the framework of direct numerical simulation. Indeed, the same ideas can be used in order to treat a set of larger Stokes numbers when particle trajectory crossing has to be taken into account, either deterministically such as in [83, 119] using QMOM in velocity phase space, even if it leads to weakly hyperbolic systems of conservation laws and potential singularities [20], or statistically such as in [188, 187], or even treating both types such as in [19, 18]. Besides, it can also be used in the context of turbulence modeling, for example in a RANS framework [53].

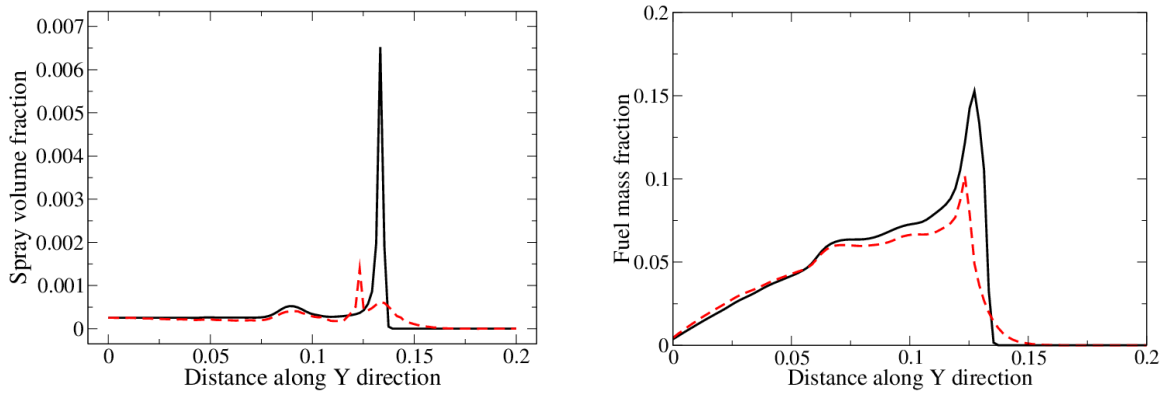

Figure 3.21: Results from 1-D plots, taken along the y-axis see Figure 3.13, in the case of a droplet population of $r_{\mathrm{SMR}} = 20\mu\mathrm{m}$. Results from Eulerian (solid black lines) and Lagrangian (dashed red lines) solutions. *Left*: Spray volume fraction for droplets without evaporation. *Right*: Evaporated fuel mass fraction for evaporating droplets with a constant evaporation velocity.

Chapter 4

Numerical analysis of a two-way coupled Eulerian high order moment method for the simulation of polydisperse evaporating sprays

The advances associated with this chapter are written in an article in preparation for a submission to Journal of Computational Physics [55]

- *O. Emre, F. Laurent, S. de Chaisemartin, S. Jay, and M. Massot, Numerical analysis of a two-way coupled Eulerian high order moment method for the simulation of polydisperse evaporating sprays*, paper in preparation for a submission in Journal of Computational Physics

4.1 Introduction

In several industrial applications such as automotive engines, gas turbines or turbojet engines, the direct injection of the liquid inside a combustion chamber has a great influence on both fuel consumption and pollutant production. Actually, the two-phase flow generated from the injection is generally very complex. The flow in the dense zone close to the injector is called separate-phase flow whereas it is qualified as disperse-phase flow far downstream of the injector. From the modeling point of view, the liquid phase involved in the dense zone is always described by Eulerian methods while its modeling can be carried out through either Eulerian or Lagrangian methods in case of disperse-phase flows. Lagrangian methods are widely adopted in industrial applications since they provide a high numerical efficiency [47]. Their implementation on computing softwares is also quite easy. However, the high number of particles required for them to be really accurate increases the simulation cost. They also introduce numerical diffusion associated with the repartition of the mass, momentum and energy at the droplet locations onto the gas Eulerian grid. Moreover, they require significant effort in numerical algorithm implementation on parallel architectures, to guarantee a good load balance between the processors. Therefore, the Eulerian description is considered as an alternative option. Its coupling with the gas phase

is natural and it is also well-suited for massively parallel computations. However, most of the Eulerian methods face the difficulty of taking into account the polydisperse character in size of droplets and its impact on the two-way interactions between phases. In that context, there has been a first attempt originally initiated by Tambour et al. [73], which is then extended by Laurent et al [94]. The development of multi-fluid model so-called sectional approach from the Boltzmann type spray equation [193, 194] has been a fruitful achievement in describing the spray polydispersity. Its great efficiency for DNS computations has been also assessed [30]. However, the cost of the discretization in size phase space is high and still results in numerical diffusion since the method is first order in size discretization [93]. Therefore, in terms of computational cost, the possibility of high order moment method considering a single size section is attractive. It goes back to moment methods either like Quadrature Method of Moment (QMOM) where the dynamics of moments are evaluated after closing the source terms using quadrature methods [123, 196] or Direct Quadrature Method of Moment (DQMOM) wherein equations are directly written on the quadrature weights and abscissas, which describe the reconstructed distribution function having the same moments [65]. Such methods have proved to be very efficient in a number of configurations. But, they are not able to accurately predict the evaporating flux at zero droplet size, which is a point-wise value to be reconstructed from the set of moments. Consequently, further studies have been undertaken and have lead to a proper treatment of the evaporation term. Within this framework, the Eulerian Multi Size Moment (EMSM) method developed by Kah et al. [83] has been a breakthrough in terms of accuracy for the quantitative prediction of evaporating polydisperse spray [120, 87]. In his work, Kah et al. proposed a size-velocity moment method with the reconstruction through maximum entropy of the size distribution in one section and its associated numerical strategy [120]. Moreover, a great potential for ICE type applications has been proved [86]. Through the present contribution, one focuses on a Eulerian resolution strategy of the disperse phase at the downstream region of the injector. Within the dilute spray assumption, the rate of collisions between droplets being not significant, the liquid-liquid interactions do not occur. On the other hand, the notable inertia of droplets conditioned by their size along with the droplet evaporation phenomena prompted by the normal engine operating conditions make challenging the resolution of the two-way interaction between phases. Mass, momentum and energy exchanges between the polydisperse spray and the compressible occur under stiff conditions, involving very small characteristic time scales which can prompt stability and accuracy problems for simulations. This issue has been recently tackled in [84] through a stable and accurate two-way coupling numerical resolution strategy, while preserving the realizability of moment transports. Moreover, its accuracy in the context of 2-D injection simulations under the industrial code IFP-C3D [12], as compared to the widely used Lagrangian approach has been qualitatively and quantitatively validated. However, a rigorous numerical analysis of the new two-way coupling still needs to be assessed. All the achievements done in [84] were in the context of d-square constant evaporation law of droplets. Yet the method should be generalized and studied under more complicated time dependent evaporation laws widely used in ICE applications [2]. Through the present work, we thus aim at bringing a general two-way coupling approach compatible for an industrial software IFP-C3D, while discussing about the accuracy of the resolution strategy under realistic evaporation laws. The remainder

of the paper is organized as follows. In section 4.2, the kinetic spray modeling is first presented, along with explicit expressions for drag, evaporation and heat source terms. Then the EMSM model is presented. The generalized two-way coupling model is derived within the context of Arbitrary Lagrangian Eulerian (ALE) formalism, taking into account energy equation on the spray and the heat exchange term between phases. In section 4.3, the order of accuracy related to the evaporation scheme developed in [120] has been first discussed in this paper and the possible errors influencing the order of the scheme are highlighted. Afterwards, the global strategy for the two-way coupling resolution is given both in case of a constant and time dependent evaporation laws. In section 4.4, the two-way coupling strategy has been evaluated through homogeneous test-cases under both constant and time dependent evaporation laws within the framework of realistic configurations. Moreover, the convergence study of the method has been conducted in both cases. Finally, the method has been tested under the industrial code IFP-C3D, considering a time-dependent evaporation law. The aim here is to study the accuracy of the method through comparisons with widely used Lagrangian approach [47]. Then we finish with a conclusion and perspectives in section 4.6.

4.2 Eulerian polydisperse spray modeling in the gas

The purpose of this section is to derive a macroscopic system of equations from a fluid kinetic model for a dilute spray in a gaseous flow, in the same way as in a companion paper [84], but with more complex models for the droplets (evaporation and heating). In the context of an Arbitrary Lagrangian and Eulerian (ALE) formalism, the phase transport can then be isolated, showing its main properties, the rest of the algorithm, especially the transport in physical space, being detailed in [84].

4.2.1 Eulerian Multi-Size Moment (EMSM) method

In the present contribution, one deals with a dilute two-phase flow regime, composed of evaporating polydisperse droplets in a gas, with a typic volume fraction such that $\Phi_v \ll 10^{-2}$. In that context, the droplets can be described at the kinetic level by a Williams-Boltzmann Equation (WBE) from which the EMSM macroscopic model will be derived.

4.2.1.1 Kinetic description of the spray inside the gas

The spray can be described thanks to the statistical formalism originally proposed in [193] for combustion and atomization applications. It consists of defining the number density function (NDF) f of the spray, where $f(t, \boldsymbol{x}, \boldsymbol{u}, S, T)\,\mathrm{d}\boldsymbol{x}\mathrm{d}\boldsymbol{u}\mathrm{d}S\mathrm{d}T$ accounts for the number of droplets occupying a volume of $\mathrm{d}\boldsymbol{x}$ around a space location $\boldsymbol{x}$, with a velocity in a $\mathrm{d}\boldsymbol{u}$-neighborhood of $\boldsymbol{u}$, with a temperature in a $\mathrm{d}T$-neighborhood of T, with a size in surface a $\mathrm{d}S$-neighborhood of S.

For considered diluted sprays, the collision frequency of droplets is much smaller than the characteristic length, in such a way that droplet-droplet collisions can be neglected. Moreover, inertial forces prompted by relative velocities between droplets and the gas

are not very high compared to droplet surface tension forces. It is therefore appropriate to neglect the droplet break-up phenomenon. The evolution of NDF is then conducted through the following expression of collisionless WBE [193, 194]

$$\partial_t f + \nabla_{\boldsymbol{x}} \cdot (\boldsymbol{u} f) - \partial_S \left(R_S f\right) + \nabla_{\boldsymbol{u}} \cdot (\boldsymbol{F} f) + \partial_T \cdot (Q f) = 0, \tag{4.1}$$

with $\boldsymbol{F}$ the drag force per unit mass, R_S the evaporation rate per unit mass and Q is the heating rate per unit mass. These terms are required to be closed through models taking into account physical phenomena at droplet scale. The drag is typically modeled under Stokes law

$$\boldsymbol{F}\left(t, \boldsymbol{x}, \boldsymbol{u}, S\right) = \frac{\boldsymbol{u_g} - \boldsymbol{u}}{\tau_d}, \qquad \tau_d = \frac{\rho_d S}{18 \pi \mu_g}, \tag{4.2}$$

with τ_d the dynamic time scale associated to the droplet of size S, $\boldsymbol{u_g}$ the gas velocity at droplet location, ρ_d the density of the liquid fuel occupying droplets and μ_g the gas dynamic viscosity. Let us recall that, in case where droplets Reynolds number Re_d is high, some corrections of type Schiller-Naumann or Ranz-Marshall are required to be taken into account in τ_d [160, 56].

In the literature, models for terms R_S and Q are typically deduced from the film theory based on the resolution of conservation equations relative to an isolated spherical droplet evaporating inside the gas. In the one way coupling context, the heat transfer from the gas to each droplet is assumed to occur under only conduction and convection phenomena. In the present work, one will consider infinite conductivity model which assume that the temperature is spatially uniform in the droplet but depend on time [164]. The evaporation and the heat transfer terms can then be given by:

$$R_S\left(t, \boldsymbol{x}, \boldsymbol{u}, S, T\right) = 4\pi \frac{\rho_g}{\rho_d} \mathrm{Sh_c} D_{Y_F} \ln\left(1 + \mathrm{B_M}\right) \tag{4.3}$$

and

$$Q\left(t, \boldsymbol{x}, \boldsymbol{u}, S, T\right) = 6\pi \frac{\rho_g}{\rho_d S C_{p,l}} \mathrm{Sh_c} D_{Y_F} \ln\left(1 + \mathrm{B_M}\right) \left(\frac{C_{p,g}\left(T_g(\infty) - [T]_s\right)}{\mathrm{B_T}} - \mathrm{L}_v \right), \tag{4.4}$$

with ρ_g the gas density, $T_g(\infty)$ the gas temperature beyond the diffusive thermal boundary layer, $[T]_s$ the temperature at the droplet surface, $C_{p,g}$ the gaseous specific heat capacity at constant pressure, ρ_d the liquid density, $C_{p,l}$ the liquid specific heat at constant pressure, D_{Y_F} the Fick's law binary diffusion coefficient, L_v the latent heat of vaporization, $\mathrm{Sh_c}$ the convective modified Sherwood number, $\mathrm{B_M}$ the Spalding dimensionless mass transfer number and $\mathrm{B_T}$ the Spalding dimensionless heat transfer number. Let us give expressions for the Spalding numbers and the relation between them:

$$\mathrm{B_M} = \frac{[Y_F]_s - [Y_F]_\infty}{1 - [Y_F]_s}, \qquad \mathrm{B_T} = \frac{\rho_g u_s C_{p,g}}{h_c}, \qquad \mathrm{B_T} = \left(\mathrm{B_M} + 1\right)^{\frac{\mathrm{Sh_c}}{\mathrm{Nu_c}} \frac{\mathrm{Sc}}{\mathrm{Pr}}}, \tag{4.5}$$

with $[Y_F]_s$ the fuel mass fraction at the droplet surface, $[Y_F]_\infty$ the fuel mass fraction beyond the diffusive mass boundary layer, h_c the convective modified heat transfer coefficient, $\mathrm{Nu_c}$ the convective modified Nusselt number, Sc the Schmitt number, Pr the Prandtl number.

According to the film theory, the convection prompted by the relative velocity between the gas and the droplet reduces boundary layers around the droplets. Therefore some corrections on Sherwood and Nusselt numbers are required.

The description of the gas phase in the context of compressible, multi-species reactive flows is given by the classical Navier Stokes conservation equations for mass, species, momentum and total energy [140], with added source terms from the spray which is diluted enough to neglect its volume occupation:

$$\partial_t(\rho_g) + \nabla_{\boldsymbol{x}} \cdot (\rho_g \boldsymbol{u_g}) = \mathfrak{S}^{\rho}, \tag{4.6a}$$

$$\partial_t(\rho_g Y_k) + \nabla_{\boldsymbol{x}} \cdot (\rho_g \boldsymbol{u_g} Y_k) = \nabla_{\boldsymbol{x}} \cdot (\rho_g D_k \nabla_{\boldsymbol{x}} (Y_k)) + \mathfrak{S}^{Y_k}, \tag{4.6b}$$

$$\partial_t(\rho_g \boldsymbol{u_g}) + \nabla_{\boldsymbol{x}} \cdot (\rho_g \boldsymbol{u_g} \otimes \boldsymbol{u_g} + P_g I) = \nabla_{\boldsymbol{x}} \cdot (\rho_g \tau) + \mathfrak{S}^{\rho \boldsymbol{u}}, \tag{4.6c}$$

$$\partial_t(\rho_g E_g) + \nabla_{\boldsymbol{x}} \cdot (\rho_g E_g \boldsymbol{u_g} + P_g \boldsymbol{u_g}) = \nabla_{\boldsymbol{x}} \cdot (\rho_g \tau \boldsymbol{u_g}) - \nabla_{\boldsymbol{x}} \cdot \mathbf{q} + \mathfrak{S}^{\rho E}, \tag{4.6d}$$

with ρ_g the gas density, E_g the total energy of the gas, P_g gas pressure, τ the gas viscous tensor, $\mathbf{q}$ energy flux, Y_k is the mass fraction of species k. The system (6.13) is closed through the state equation for perfect fluids. Source terms are given by:

$$\mathfrak{S}^{\rho} = \int\int\int \frac{\rho_d}{4\sqrt{\pi}} S^{1/2} R_S f \, \mathrm{d}S \, \mathrm{d}T \, \mathrm{d}\boldsymbol{u}, \tag{4.7a}$$

$$\mathfrak{S}^{Y_k} = \delta_{k,F} \mathfrak{S}^{\rho}, \tag{4.7b}$$

$$\mathfrak{S}^{\rho \boldsymbol{u}} = -\int\int\int \frac{\rho_d}{6\sqrt{\pi}} S^{3/2} \boldsymbol{F} f \, \mathrm{d}S \, \mathrm{d}T \, \mathrm{d}\boldsymbol{u} + \int\int\int \frac{\rho_d}{4\sqrt{\pi}} S^{1/2} \boldsymbol{u} R_S f \, \mathrm{d}S \, \mathrm{d}T \, \mathrm{d}\boldsymbol{u}, \tag{4.7c}$$

$$\mathfrak{S}^{\rho e} = \int\int\int \frac{\rho_d}{4\sqrt{\pi}} e\,(T)\, S^{1/2} R_S f \, \mathrm{d}S \, \mathrm{d}T \, \mathrm{d}\boldsymbol{u} - \int\int\int \frac{\rho_d}{6\sqrt{\pi}} S^{3/2} Q f \mathrm{d}S \mathrm{d}T \mathrm{d}\boldsymbol{u}, \tag{4.7d}$$

where $\delta_{k,F}$ is equal to one when k refers to the fuel species and zero otherwise. Then, the diphasic flow is described by the fluid kinetic model (6.1,6.13,4.7).

4.2.1.2 Non-isothermal EMSM model

The Eulerian Multi Size Moment Method (EMSM) was formulated in [120, 87, 84] with simple models for the droplets. In particular, the droplet heating was not considered. Here, the derivation of the EMSM equations is done again but in the case of the infinite conductivity model, describing the evolution of the droplet temperature T. The state function is then chosen as the internal energy which only depends on temperature and reads $e(T) = e_0 + \int_{T_0}^{T} C_{v,l}(T)\mathrm{d}T$, where $C_{v,l}(T)$ is the liquid fuel heat capacity at constant volume and the index 0 accounts for the reference state.

The first derivation step consists in reducing the size of the phase space to the only droplet size variable, by only considering the following moments in the velocity and temperature variables: the number density $n = \iint f \mathrm{d}\boldsymbol{u}\, \mathrm{d}T$, the average momentum $n\boldsymbol{u_d} = \iint f \boldsymbol{u} \mathrm{d}\boldsymbol{u}\, \mathrm{d}T$ and the average internal energy $ne_d = \iint f e(T)\, \mathrm{d}\boldsymbol{u}\, \mathrm{d}T$ [94], which then depend on $(t, \boldsymbol{x}, S)$. Let us now define an effective temperature T_d such that $e(T_d) = e_d$. In order to close the so-called "semi-kinetic" system of equation on n, $n\boldsymbol{u_d}$ and ne_d, the following assumptions are introduced:

[HVT1] For each droplet size S, at a given point $(t,\boldsymbol{x})$, the only characteristic velocity and the only characteristic temperature are respectively $\boldsymbol{u_d}(t,\boldsymbol{x},S)$ and $T_d(t,\boldsymbol{x},S)$.

[HVT2] The velocity dispersion around $\boldsymbol{u_d}(t,\boldsymbol{x},S)$ and the temperature dispersion around $T_d(t,\boldsymbol{x},S)$ are zero whatever the point $(t,\boldsymbol{x},S)$.

It is equivalent to presume the following form of the NDF:

$$f(t,\boldsymbol{x},\boldsymbol{u},T,S) = n(t,\boldsymbol{x},S)\delta(\boldsymbol{u}-\boldsymbol{u_d}(t,\boldsymbol{x},S))\delta(T-T_d(t,\boldsymbol{x},S)). \tag{4.8}$$

The semi-kinetic system is then obtained by integrating Eq.(6.1) with respect to $(\boldsymbol{u},T)$ after multiplying it by 1, $\boldsymbol{u}$ and $e(T)$. Thanks to the monokinetic assumption (4.8), this leads to:

$$\partial_t n + \nabla_{\boldsymbol{x}}\left(n\boldsymbol{u_d}\right) = \partial_S\left(nR_d\right), \tag{4.9a}$$
$$\partial_t\left(n\boldsymbol{u_d}\right) + \nabla_{\boldsymbol{x}}\left(n\boldsymbol{u_d}^2\right) = \partial_S\left(nR_d\boldsymbol{u_d}\right) + n\boldsymbol{F}_d, \tag{4.9b}$$
$$\partial_t\left(ne_d\right) + \nabla_{\boldsymbol{x}}\left(n\boldsymbol{u_d}e_d\right) = \partial_S\left(nR_de_d\right) + nC_{v,l}\left(T_d\right)Q_d, \tag{4.9c}$$

with

$$R_d = R_S\left(t,\boldsymbol{x},\boldsymbol{u_d},S,T_d\right), \qquad Q_d = Q\left(t,\boldsymbol{x},\boldsymbol{u_d},S,T_d\right), \qquad \boldsymbol{F}_d = F\left(t,\boldsymbol{x},\boldsymbol{u_d},S\right) \tag{4.10}$$

the $(t,\boldsymbol{x},S)$ dependance of $\boldsymbol{u_d}$ and T_d being skipped for legibility reasons.

The next step consists in taking size moments of Eq. (6.6). Let us precise that since an accurate description of the droplet dynamics and thermal behavior conditioned by size is beyond the scope of this present contribution, we only consider, here, one averaged velocity and one averaged temperature, assuming that there is no dependance of $\boldsymbol{u_d}$ and T_d on droplet size: $\boldsymbol{u_d}\left(t,\boldsymbol{x},S\right) = \boldsymbol{u_d}\left(t,\boldsymbol{x}\right)$ and $T_d\left(t,\boldsymbol{x},S\right) = T_d\left(t,\boldsymbol{x}\right)$. The size moments are denoted as

$$m_k = \int_0^{S_{max}} S^k f\left(t,\boldsymbol{x},S\right)\mathrm{d}S,$$

the index k varying between 0 and 3. We first take moments of (4.9a) in size of order 0 up to 3. Then we both take the size moment of order one of (4.9b) and (4.9c) respectively. The new system at macroscopic level becomes as follows

$$\partial_t m_0 + \nabla_{\boldsymbol{x}}\left(m_0\boldsymbol{u_d}\right) = -n\left(S=0\right)R_d, \tag{4.11a}$$
$$\partial_t m_1 + \nabla_{\boldsymbol{x}}\left(m_1\boldsymbol{u_d}\right) = \mathfrak{S}_{m_1}, \tag{4.11b}$$
$$\partial_t m_2 + \nabla_{\boldsymbol{x}}\left(m_2\boldsymbol{u_d}\right) = \mathfrak{S}_{m_2}, \tag{4.11c}$$
$$\partial_t m_3 + \nabla_{\boldsymbol{x}}\left(m_3\boldsymbol{u_d}\right) = \mathfrak{S}_{m_3}, \tag{4.11d}$$
$$\partial_t m_1\boldsymbol{u_d} + \nabla_{\boldsymbol{x}}\left(m_1\boldsymbol{u_d}^2\right) = \mathfrak{S}_{m_1\boldsymbol{u_d}}, \tag{4.11e}$$
$$\partial_t m_1 e_d + \nabla_{\boldsymbol{x}}\left(m_1\boldsymbol{u_d}e_d\right) = \mathfrak{S}_{m_1e_d}, \tag{4.11f}$$

with, skipping the $(t, \boldsymbol{x})$ dependance:

$$\mathfrak{S}_{m_k} = -\int_0^{S_{max}} kS^{k-1} R_d(S) n(S) \mathrm{d}S, \tag{4.12a}$$

$$\mathfrak{S}_{m_1 \boldsymbol{u_d}} = -\boldsymbol{u_d} \int_0^{S_{max}} R_d(S) n(S) \mathrm{d}S + \int_0^{S_{max}} S \boldsymbol{F}_d(S) n(S) \mathrm{d}S \tag{4.12b}$$

$$\mathfrak{S}_{m_1 e_d} = -e_d \int_0^{S_{max}} R_d(S) n(S) \mathrm{d}S + C_{v,l}\left(T_d\right) \int_0^{S_{max}} S Q_d(S) n(S) \mathrm{d}S. \tag{4.12c}$$

In system (4.11), the main issues concern the closure of the terms at the right hand side of Eq. (4.11), especially the one of Eq. (4.11a) which requires the knowledge of the pointwise value of the NDF at $S = 0$. Let us remark that, in the case of a Stokes law for the drag and with no correction on Sherwood and Nusselt numbers, R_d, $S\,\boldsymbol{F}_d$ and $S\,Q_d$ are independent of S and the source terms $\mathfrak{S}_{m_k}$, $\mathfrak{S}_{m_1 \boldsymbol{u_d}}$ and $\mathfrak{S}_{m_1 e_d}$ are closed since they are expressed through transported size moments. The source terms of gaseous equation also still have to be closed. They are written here:

$$\mathfrak{S}^{\rho} = \int_0^{S_{max}} \frac{\rho_d}{4\sqrt{\pi}} S^{1/2} R_d(S) n(S)\ \mathrm{d}S, \tag{4.13a}$$

$$\mathfrak{S}^{Y_k} = \delta_{k,F} \mathfrak{S}^{\rho}, \tag{4.13b}$$

$$\mathfrak{S}^{\rho \boldsymbol{u}} = -\int_0^{S_{max}} \frac{\rho_d}{6\sqrt{\pi}} S^{3/2} \boldsymbol{F}_d(S) n(S)\ \mathrm{d}S + \boldsymbol{u_d} \int_0^{S_{max}} \frac{\rho_d}{4\sqrt{\pi}} S^{1/2} R_d(S) n(S)\ \mathrm{d}S, \tag{4.13c}$$

$$\mathfrak{S}^{\rho e} = e_d \int \frac{\rho_d}{4\sqrt{\pi}} S^{1/2} R_S\left(S\right) n\left(S\right)\ \mathrm{d}S - C_{v,l} \int \frac{\rho_d}{6\sqrt{\pi}} S^{3/2} Q\left(S\right) n\left(S\right) \mathrm{d}S. \tag{4.13d}$$

4.2.2 Two-way coupling through EMSM method

The resolution of the complete system (6.13) and (4.11) can be achieved through an operator splitting. In case of fixed meshes, a separation between the transport in phase space (through drag, evaporation heating) and the transport in physical space can be envisioned as done for the two-size moment multi-fluid model in [41], only the phase space transport coupling equations for the spray to equations for the gaseous phase. In the context of moving meshes adopted here, the chosen splitting is based on the Arbitrary Lagrangian and Eulerian (ALE) formalism, the first stage (phase A) of which is also the transport in phase space, as explained below. We will see the main properties of this system, which will determine the way we will resolve it.

4.2.2.1 Arbitrary Lagrangian and Eulerian (ALE) formalism

In the context of realistic internal combustion engine configurations where moving parts add additional complexity to the resolution of the two-phase flow under mesh motion, a common resolution technique used is the Arbitrary Lagrange Euler (ALE) formalism, which was introduced [78] in the context of single-velocity fluid flows and adapted to the EMSM model in which two velocity fields co-exist [84], but in a case of simple models for droplets. According to ALE, the complete resolution of equation systems (6.13) and (4.11)

is achieved through the operator splitting that consists in dealing separately different operators into three steps (phases): the first two steps named after also, Lagrangian phases, begin with the resolution of source terms (phase A). In that step, the volume of a mesh cell do not evolve. Then follows the resolution of acoustic-diffusion terms (phase B) while the cell size changing, following the fluid flow velocity evolution. Finally it ends up with the Eulerian projection of physical quantities into cells (phase C). Let us precise that no further discussion will be conducted on ALE formalism in this chapter since detailed information is available in Chapter 3.

The scope of the present contribution being the two-way coupling resolution of the polydisperse evaporating spray with the gas phase which accounts for source terms in (6.13) and (4.11), we therefore deal with only phase A resolution of ALE in the reminder of the paper. Let us remind that the extension of the EMSM method to the ALE formalism in a one-way framework as well as the detailed treatment of spray convection through a kinetic based numerical scheme can be found in [84] and [87] respectively. In the following, let us show the system of equations in phase A. Vectors of conserved variables being $\boldsymbol{U}_d = \big(m_0, m_1, m_2, m_3, m_1\mathbf{u_d}, m_1 e_d\big)$ and $\boldsymbol{U}_g = \big(\rho_g, \rho_g Y_k, \rho_g \boldsymbol{u_g}, \rho_g E_g\big)$, our subproblem can be written:

$$\begin{aligned} \mathrm{d}_t \boldsymbol{U}_g &= \boldsymbol{F}_A \\ \mathrm{d}_t \boldsymbol{U}_d &= \boldsymbol{G}_A \end{aligned} \tag{4.14}$$

with, $\boldsymbol{F}_A = \big(\mathfrak{S}^{\rho}, \mathfrak{S}^{Y_k}, \mathfrak{S}^{\rho \boldsymbol{u}}, \mathfrak{S}^{\rho E}\big)$ and $\boldsymbol{G}_A = \big(-R_d n(S=0), \mathfrak{S}_{m_1}, \mathfrak{S}_{m_2}, \mathfrak{S}_{m_3}, \mathfrak{S}_{m_1 \boldsymbol{u_d}}, \mathfrak{S}_{m_1 e_d}\big)$, source terms being given by Eq. (4.13) and Eq. (4.12). It is then a local system of ODEs.

4.2.2.2 Source terms reconstruction and global conservation of the two-phase system in phase A

There are three major issues with system (4.14).

The first one concerns the space in which the variables evolve. Indeed, the vector $\boldsymbol{m} = (m_0, m_1, m_2, m_3)^t$ is used, which is a vector of the four first moments on $[0, S_{max}]$ of a positive distribution. It then live in a space defined by:

$$\mathcal{M}([0, S_{max}]) = \left\{ \begin{array}{l} \boldsymbol{m} = (m_0, m_1, m_2, m_3)^t \in (\mathbb{R}_*^+)^4; \quad m_0 > 0 \\ \\ p_1(\boldsymbol{m}) \in]0,1[,\ p_2(\boldsymbol{m}) \in]0,1[,\ p_3(\boldsymbol{m}) \in]0,1[\end{array} \right\}, \tag{4.15}$$

where $p_1(\boldsymbol{m})$, $p_2(\boldsymbol{m})$ and $p_3(\boldsymbol{m})$ are the canonical moments [38] given by:

$$p_1(\boldsymbol{m}) = \frac{m_1}{S_{max} m_0}, \tag{4.16}$$

$$p_2(\boldsymbol{m}) = \frac{m_2 m_0 - m_1^2}{m_1 (S_{max} m_0 - m_1)}, \tag{4.17}$$

$$p_3(\boldsymbol{m}) = \frac{(S_{max} m_0 - m_1)(m_1 m_3 - m_2^2)}{S_{max}(m_0 m_2 - m_1^2)(S_{max} m_1 - m_2)}. \tag{4.18}$$

This space is the interior of the moment space defined for example in [120]. It is quite complex but convex. The fact that the vector $\boldsymbol{m}$ belongs to this space $\mathcal{M}([0, S_{max}])$ is

called the realizability condition. If this condition is not satisfied, the system will not be able to be closed.

The second issue concerns the closure of the source terms. Indeed, the disappearance flux of droplets through evaporation is required to be determined through the knowledge of $n\,(S=0)$. For an accurate evaluation of this flux, Massot et al. [120] has proposed the following approach: an approximation of the distribution $n\,(S)$ is reconstructed from its first integer moments. This means solving finite Hausdorff moment problem that is finding one positive number density function n with its corresponding moments on $[0, S_{max}]$ equal to the sequence $\boldsymbol{m} = (m_0, m_1, m_2, m_3)^t$. This problem has an infinity of solutions as soon as $\boldsymbol{m}$ belongs to the moment space $\mathcal{M}([0, S_{max}])$, previously defined, i.e. the realizability is satisfied. Among these solutions, we choose the distribution denoted $S \mapsto \tilde{n}(\boldsymbol{m}, S)$ maximizing Shannon entropy [120]. It is called the entropy maximization reconstruction. Thanks to this method, the evaporative flux of polydisperse spray is evaluated. Moreover, depending on physical models provided for terms such as $\boldsymbol{F}$, R_S and Q through expressions (4.2), (4.3) and (4.4) respectively, the other source terms can usually not be directly expressed as a function of the moments. The reconstructed NDF by entropy maximization $\tilde{n}(\boldsymbol{m}, .)$ allows us to close them.

The last issue is the momentum and energy conservations of the global system. Let us define the mass density of the spray, $m_{3/2}$, as well as the fractional moment $m_{1/2}$, which will naturally appear in drag force for Stokes law for example:

$$m_{3/2}\,(t,S) = \int \rho_d \frac{S^{3/2}}{6\sqrt{\pi}} n\,(t,S)\,\mathrm{d}S, \qquad m_{1/2}\,(t,S) = \int \rho_d \frac{S^{1/2}}{6\sqrt{\pi}} n\,(t,S)\,\mathrm{d}S \tag{4.19}$$

Integrating the semi-kinetic system (6.6) with respect to S after multiplying it by $\rho_d S^{3/2}/(6\sqrt{\pi})$ leads to the following conservation equations:

$$\begin{aligned} &\mathrm{d}_t\left(\rho_g + m_{3/2}\right) &&= 0, \qquad \mathrm{d}_t\left(\rho_g\, Y_F + m_{3/2}\right) = 0, \\ &\mathrm{d}_t\left(\rho_g \boldsymbol{u_g} + m_{3/2}\boldsymbol{u_d}\right) &&= 0, \qquad \mathrm{d}_t\left(\rho_g e_g + m_{3/2} e_d\right) = 0, \end{aligned} \tag{4.20}$$

where $e_g = E_g - \frac{1}{2}\|\boldsymbol{u_g}\|^2$ is the internal energy of the gas and while $m_1\boldsymbol{u_d}$ and $m_1 e_d$ are considered in Eqs. (4.11e) and (4.11f) or in system (4.14). To respect these conditions, system (4.14) is modified. First, the total mass conservation equation is considered instead of the gas density equation and the same thing is done for the fuel conservation. Second, equations on $m_1\boldsymbol{u_d}$ and $m_1 e_d$ are replaced by equations on $m_{3/2}\boldsymbol{u_d}$ and $m_{3/2} e_d$. Finally, the internal energy conservation is substituted to the total energy conservation for the gaseous phase in order to better separate the velocity $\boldsymbol{u_g}$ from other thermodynamical variables. For the sake of simplicity, let do not consider convective correction terms in R_d

and Q_d and write down the equation system involved in the two-way coupling modeling:

$$
\begin{aligned}
\mathrm{d}_t m_0 &= -\tilde{n}\,(\boldsymbol{m}, 0)\, R_d && \text{(4.21a)}\\
\mathrm{d}_t m_1 &= -m_0 R_d && \text{(4.21b)}\\
\mathrm{d}_t m_2 &= -2 m_1 R_d && \text{(4.21c)}\\
\mathrm{d}_t m_3 &= -3 m_2 R_d && \text{(4.21d)}\\
\mathrm{d}_t \left(\rho_g + m_{3/2}\right) &= 0 && \text{(4.21e)}\\
\mathrm{d}_t \left(\rho_g Y_F + m_{3/2}\right) &= 0 && \text{(4.21f)}\\
\mathrm{d}_t \left(m_{3/2}\, \boldsymbol{u_d}\right) &= \frac{\boldsymbol{u_g} - \boldsymbol{u_d}}{\tau_d^*}\, m_{1/2} - \frac{3}{2}\, m_{1/2}\, R_d\, \boldsymbol{u_d} && \text{(4.21g)}\\
\mathrm{d}_t \left(\rho_g\, \boldsymbol{u_g}\right) &= -\frac{\boldsymbol{u_g} - \boldsymbol{u_d}}{\tau_d^*}\, m_{1/2} + \frac{3}{2}\, m_{1/2}\, R_d\, \boldsymbol{u_d} && \text{(4.21h)}\\
\mathrm{d}_t \left(m_{3/2}\, e_d\left(T_d\right)\right) &= C_{v,l}\left(T_d\right)\, Q_d^*\, m_{1/2} - \frac{3}{2} m_{1/2}\, R_d\, e_d\, \left(T_d\right) && \text{(4.21i)}\\
\mathrm{d}_t \left(\rho_g\, e_g\left(T_g\right)\right) &= -C_{v,l}\left(T_d\right)\, Q_d^*\, m_{1/2} + \frac{3}{2} m_{1/2}\, R_d\, e_d\, \left(T_d\right) && \text{(4.21j)}
\end{aligned}
$$

where $\tau_d^* = \tau_d / S$, $Q_d^* = Q_d S$. In case where convective correction terms were considered for evaporation and heating, or in the drag force, the source terms would still be written in an integral form, which would have to be numerically computed.

4.2.2.3 Stiffness issue of the two-phase flow

The disperse flow modeled through the system of ODE (4.21) involves complex physics. This is a bottleneck problem for precise and stable simulations under rapid physical variations. Drag, heat and evaporation phenomena, each of them being associated to different time scales, can occur simultaneously. Moreover, the size of droplets continuously decreasing due to evaporation yields very small characteristic times. In that context, There are two crucial points needed to be highlighted for the numerical resolution of the two-way coupled system:

- Classical methods can no longer guarantee the stability in case where the integration time step of the simulation remains greater than characteristic time scales associated to disappearing droplets. This aspect requires both the unconditional stability and the high accuracy.
- The time integration for the high order size moments in the context of the two-way coupling system is not straightforward since the realizability is a mandatory task.

In the next section, a stable and precise numerical integration strategy, preserving the complex size moment space, will be discussed.

4.3 Numerical strategy in phase A of ALE

We focus here on system (4.21). The aim of this part is to design a robust and accurate strategy for its resolution, especially preserving realizability condition. Before dealing

with the general case, the simplified case of a constant evaporation rate is considered. Indeed, this case induces a decoupling of the equations on size moments and mass density, allowing the use of the kinetic scheme developed in [120]. The key point is then to solve the rest of the equations, which depend on fractional size moments, with a method able to cope with their stiffness. Then, a strategy will then be able to be developed in the general case, where all equations can be coupled.

4.3.1 Time integration strategy in case of a constant evaporation law

In this part, a constant evaporation rate R_d is considered. It is the case when the temperature inside the droplet is considered as constant and uniform, in such a way that Eq. (4.21i) does not exist and the gas phase energy equation is evolved only due to the constant evaporation. But anyway, we still deal with these energy equations since the algorithm developed here will be used as a part of the one developed for the general case.

4.3.1.1 Resolution of system on size moments

Here, the system (4.21a-4.21d) on $\boldsymbol{m}$ is decoupled from the rest of the equations. The kinetic scheme developed in [120] is able to solve it in a way preserving the realizability condition. This scheme is based on an integral form of the equations:

$$\exp(t\,R_d\,A)\,\boldsymbol{m}(t) = \boldsymbol{m}(0) - \int_0^{tR_d} \tilde{n}\left(\boldsymbol{m}\left(\beta\right),0\right) \begin{bmatrix} 1 \\ \beta \\ \beta^2 \\ \beta^3 \end{bmatrix} \mathrm{d}\beta, \tag{4.22}$$

where A is the nilpotent matrix appearing in system (4.21a-4.21d) and has the following property:

$$A = \begin{bmatrix} 0 & 0 & 0 & 0 \\ 1 & 0 & 0 & 0 \\ 0 & 2 & 0 & 0 \\ 0 & 0 & 3 & 0 \end{bmatrix}, \qquad \forall x, S \in \mathbb{R} \quad \exp(xA) \begin{bmatrix} 1 \\ S \\ S^2 \\ S^3 \end{bmatrix} = \begin{bmatrix} 1 \\ (S+x) \\ (S+x)^2 \\ (S+x)^3 \end{bmatrix}. \tag{4.23}$$

Let us notice that $\tilde{n}(\boldsymbol{m}\left(\beta\right),0)$ represents the value at $S=0$ of the reconstruction by entropy maximization done from the moment vector $\boldsymbol{m}(\beta)$ at time β. If $\tilde{n}$ were the exact solution of the kinetic equation $\partial_t n - R_d \partial_S n = 0$ from which the system (4.21a-4.21d) is derived, then it could be replaced by $\tilde{n}(\boldsymbol{m}\left(0\right),\beta)$. This last value is then used in the following definition of an approximation $\tilde{\boldsymbol{m}}$ of $\boldsymbol{m}$, which will be used to write the numerical scheme:

$$\exp(t\,R_d\,A)\,\tilde{\boldsymbol{m}}(t) = \boldsymbol{m}(0) - \Psi_-(t), \qquad \Psi_-(t) = \int_0^{tR_d} \tilde{n}\left(\boldsymbol{m}\left(0\right),\beta\right) \begin{bmatrix} 1 \\ \beta \\ \beta^2 \\ \beta^3 \end{bmatrix} \mathrm{d}\beta. \tag{4.24}$$

Moreover, we can remark that the multiplication by $\exp(-t\,R_d\,A)$ can be done through the computation of the weights w_i and abscissas S_i of a two-node quadrature and through the property (4.23) on A. So, from known moment vector $\boldsymbol{m}^n$ at a time t^n, the new moment vector $\boldsymbol{m}^{n+1}$ at time $t^{n+1} = t^n + \Delta t$ is obtained in the following way:

1. The reconstruction $\tilde{n}^n$ is provided from moments $\boldsymbol{m}^n$ by entropy maximization and the flux Ψ_- is computed as its moments on $[0, \Delta t R_d]$.

2. A two nodes quadrature of $\boldsymbol{m}^n - \Psi_-$ is done: weights w_i and abscissas S_i for $i = 1, 2$ are computed such that $m_k = \sum_{i=1}^{3} w_i S_i^k$ for $k = 0, 1, 2, 3$.

3. Moment vector $\boldsymbol{m}^{n+1}$ corresponds then to the weights w_i and the abscissas $S_i - \Delta t R_d$: $m_k^{n+1} = \sum_{i=1}^{3} w_i (S_i - \Delta t R_d)^k$ for $k = 0, 1, 2, 3$

Since $\boldsymbol{m}^n - \Psi_-$ belongs to moment space $\mathcal{M}([\Delta t R_d, S_{max}])$, the abscissas S_i of its quadrature belongs to $]\Delta t R_d, S_{max}[$, which insures that $\boldsymbol{m}^{n+1}$ belong to the moments space $\mathcal{M}([0, S_{max}])$.

Let us discuss the accuracy of this scheme. For that, the numerical approximation is compared to the exact solution $\boldsymbol{m}$ of system (4.21a-4.21d), which is closed by the entropy maximization reconstruction. The local error can then be described by the difference between the exact solution $\boldsymbol{m}(\Delta t)$ at time Δt and its approximation $\tilde{\boldsymbol{m}}(\Delta t)$ by the previously described scheme, with the same initial value $\boldsymbol{m}(0)$:

$$\boldsymbol{m}(\Delta t) - \tilde{\boldsymbol{m}}(\Delta t) = \exp(-\Delta t\, R_d\, A) \int_0^{\Delta t R_d} (\tilde{n}(\boldsymbol{m}(\beta), 0) - \tilde{n}(\boldsymbol{m}(0), \beta)) \begin{bmatrix} 1 \\ \beta \\ \beta^2 \\ \beta^3 \end{bmatrix} \mathrm{d}\beta \quad (4.25)$$

$$= \int_0^{\Delta t R_d} (\tilde{n}(\boldsymbol{m}(\beta), 0) - \tilde{n}(\boldsymbol{m}(0), \beta)) \begin{bmatrix} 1 \\ (\beta - \Delta t\, R_d) \\ (\beta - \Delta t\, R_d)^2 \\ (\beta - \Delta t\, R_d)^3 \end{bmatrix} \mathrm{d}\beta. \quad (4.26)$$

Since $\tilde{n}(\boldsymbol{m}(\beta), 0)$ and $\tilde{n}(\boldsymbol{m}(0), \beta)$ coincides at $\beta = 0$, this local error is of order $(O(\Delta t^2), O(\Delta t^3), O(\Delta t^4), O(\Delta t^5))^t$. So, assuming its stability, the scheme is globally at least first order accurate. More precisely, let us focus on the difference $\tilde{n}(\boldsymbol{m}(\beta), 0) - \tilde{n}(\boldsymbol{m}(0), \beta)$. It is related to the error done by solving system (4.21a-4.21d) instead of the kinetic equation directly. However, from Eq. (4.24), the value of $\tilde{\boldsymbol{m}}(\Delta t)$ can be given by:

$$\tilde{\boldsymbol{m}}(\Delta t) = \exp(-\Delta t\, R_d\, A) \int_{\Delta t R_d}^{S_{max}} \tilde{n}(\boldsymbol{m}(0), \beta) \begin{bmatrix} 1 \\ \beta \\ \beta^2 \\ \beta^3 \end{bmatrix} \mathrm{d}\beta$$

$$= \int_0^{S_{max} - \Delta t R_d} \tilde{n}(\boldsymbol{m}(0), S + \Delta t R_d) \begin{bmatrix} 1 \\ S \\ S^2 \\ S^3 \end{bmatrix} \mathrm{d}S. \quad (4.27)$$

So, if $\tilde{n}(\boldsymbol{m}(0), S) = \sum_{i=0}^{3} \lambda_i S^i$ would be zero for $S > S_{max}$, the function $\tilde{n}(\boldsymbol{m}(0), S+\Delta t R_d)$ would be the reconstruction by entropy maximization of $\tilde{\boldsymbol{m}}(\Delta t)$, thanks to Eq. (4.27) and by unicity of such reconstruction. Since it is a solution of the kinetic equation, $\tilde{\boldsymbol{m}}(\Delta t)$ would also coincide with $\boldsymbol{m}(\Delta t)$ (they are some solutions of the same ODE system with the same initial condition). Unfortunately, $\tilde{n}(\boldsymbol{m}(0), S)$ can not be zero for $S > S_{max}$, but it can be very small, especially if the integration domain is large enough. One can then presume that the error will be very small for the distribution having a reconstruction by entropy maximization very small on $[S_{max}, +\infty[$.

4.3.1.2 Global strategy

The previous scheme gives then an approximation of the moments vector $\boldsymbol{m}$ at each time step. From it, the reconstruction by entropy maximization allows to compute $m_{3/2}$ and also $m_{1/2}$, evaluating the integrals through Gauss-Legendre quadrature methods on 24 quadrature points [120, 125]. Moreover, the mass conservation gives values of ρ_g and $\rho_g Y_F$. Then, only equations (4.21g)-(4.21j) on $\mathbf{U} = \left(m_{3/2}\ \boldsymbol{u_d}, \rho_g \boldsymbol{u_g}, m_{3/2} e_d, \rho_g e_g\right)^t$ remain to be solved. Let us denotes it

$$\mathrm{d}_t \mathbf{U} = G(\boldsymbol{m}, U). \tag{4.28}$$

The dependance of the right hand side of this system on $\boldsymbol{m}$ reflects its dependance on fractional moments $m_{3/2}$ and $m_{1/2}$ and on ρ_g and $\rho_g Y_F$, which are computed from $\boldsymbol{m}$. This non-linear ODE system being possibly stiff, an adapted method has to be used. A-stable and L-stable type implicit Runge Kutta methods (IRK) provide both stable and accurate resolution of this kind of problem [75]. Among many existing IRK, the methods called Singly Diagonally Implicit Runge-Kutta Method (SDIRK) can respect this stability requirement while taking advantage of a more user-friendly numerical algorithm for an implementation in commercial codes than other existing methods [75]. This kind of method can be represented by its Butcher table

$$\begin{array}{c|cccc} c_1 & \omega & & & \\ c_2 & a_{2,1} & \omega & & \\ \vdots & \vdots & \ddots & \ddots & \\ c_s & a_{s,1} & \dots & a_{s,s-1} & \omega \\ \hline & b_1 & \dots & b_{s-1} & b_s \end{array} \tag{4.29}$$

where s is the number of stages in SDIRK. From an initial value $\mathbf{U}^n$, the resolution of the system (4.28) during each stage of SDIRK, that is during the sub-time step $\Delta t_i = c_i \Delta t$, with Δt is the simulation time step and $c_i < 1$, is then given by:

$$\mathbf{U}_i - \Delta t \omega \mathbf{G}\left(\boldsymbol{m}_i, \mathbf{U}_i\right) = \mathbf{U}^n + \Delta t \sum_{j=1}^{i-1} a_{ij} \mathbf{G}\left(\boldsymbol{m}_j, \mathbf{U}_j\right), \tag{4.30}$$

where the value of the moment vector $\boldsymbol{m}_j$ at stage j is given by the algorithm given in section 4.3.1.1. Upon the completion of stages, the final solution is computed by the following expression:

$$\mathbf{U}^{n+1} = \mathbf{U}^n + \Delta t \sum_{j=1}^{s} b_j \mathbf{G}\left(\boldsymbol{m}_j, \mathbf{U}_j\right). \tag{4.31}$$

Let us give further insights on the choice of SDIRK method. In the context of industrial code development, a CPU time efficient numerical scheme is needed. In the literature, there exists a third order A-stable and L-stable SDIRK method, given by the following Butcher table:

$$\begin{array}{c|ccc} \omega & \omega & & \\ \frac{1}{2}(1+\omega) & \frac{1}{2}(1-\omega) & \omega & \\ 1 & \frac{1}{4}(-1+16\omega-6\omega^2) & \frac{1}{4}(5-20\omega+6\omega^2) & \omega \\ \hline & \frac{1}{4}(-1+16\omega-6\omega^2) & \frac{1}{4}(5-20\omega+6\omega^2) & \omega \end{array}$$

with $\omega = 0.4358665215$ being a root of $6\omega^3 - 18\omega^2 + 9\omega - 1 = 0$. In section 4.4 and 4.5, we will therefore make use of this third order SDIRK method for testing the new numerical strategy developed in this section.

4.3.2 Time integration strategy in case of a time-dependent evaporation law

In the general case, ρ_g and $\rho_g Y_F$ are still seen as functions of $\boldsymbol{m}$, since they are deduced from $m_{3/2}$ by mass conservation and $m_{3/2}$ is computed from the moment vector $\boldsymbol{m}$ through the reconstruction by entropy maximization. Then, system (4.21) can be expressed by the following way:

$$\mathrm{d}_t \boldsymbol{m} = \mathbf{F}\left(\boldsymbol{m}, \phi\left(\boldsymbol{m}, \mathbf{U}\right)\right), \tag{4.32a}$$

$$\mathrm{d}_t \mathbf{U} = \mathbf{G}\left(\boldsymbol{m}, \mathbf{U}, \phi\left(\boldsymbol{m}, \mathbf{U}\right)\right), \tag{4.32b}$$

with $\mathbf{U} = \left(m_{3/2}\ \boldsymbol{u_d}, \rho_g \boldsymbol{u_g}, m_{3/2} e_d(T_d), \rho_g e_g(T_g)\right)^t$. The function ϕ represents the evaporation rate R_d, depending on $\boldsymbol{m}$ through its dependance on ρ_g and Y_F and depending on $\mathbf{U}$ through its dependance on T_d.

This case is rather complicated since ϕ in (4.32) is not constant and the computation of $\boldsymbol{m}_i$ in each stage of SDIRK requires the simultaneous computation of $\mathbf{U}_i$, the system (4.32) being fully coupled. However, for the sake of preserving the moment space, a fully coupled resolution is not straightforward and we therefore propose to keep the same numerical integration strategy presented in part 4.3.1. This requires to use a decoupled approach for the time integration of (4.32). Thus, we come down to the previous case by considering constant value of the evaporation rate ϕ inside a time step.

To illustrate the potential accuracy failure of this strategy in the context of time depending evaporation laws and the way to obtain a second order of accuracy, we use the same strategy as in [44]. Then, supposing that all functions are sufficiently differentiable in all their variables and using the Taylor expansion of the true solution of (4.32), one

can write the value of the solution after a time step Δt from initial time t_0:

$$\boldsymbol{m}(t_0+\Delta t) = \boldsymbol{m}_0 + \Delta t \mathbf{F}(\boldsymbol{m}_0,\phi_0) + \frac{\Delta t^2}{2}\left[\partial_{\boldsymbol{m}}\mathbf{F}\mathbf{F} + \partial_\phi \mathbf{F}\partial_{\boldsymbol{m}}\phi\mathbf{F} + \partial_\phi\mathbf{F}\partial_{\mathbf{U}}\phi\mathbf{G}\right]_{\boldsymbol{m}_0,U_0,\phi_0} + O(\Delta t^3), \tag{4.33a}$$

$$\begin{aligned}\mathbf{U}(t_0+\Delta t) =& \mathbf{U}_0 + \Delta t\mathbf{G}(\boldsymbol{m}_0,\mathbf{U}_0,\phi_0)\\ &+ \frac{\Delta t^2}{2}\left[\partial_{\boldsymbol{m}}\mathbf{G}\mathbf{F} + \partial_{\mathbf{U}}\mathbf{G}\mathbf{G} + \partial_\phi\mathbf{G}\partial_{\boldsymbol{m}}\phi\mathbf{F} + \partial_\phi\mathbf{G}\partial_{\mathbf{U}}\phi\mathbf{G}\right]_{\boldsymbol{m}_0,\mathbf{U}_0,\phi_0} + O(\Delta t^3),\end{aligned} \tag{4.33b}$$

with $\boldsymbol{m}_0 = \boldsymbol{m}(t_0)$, $\mathbf{U}_0 = \mathbf{U}(t_0)$ and $\phi_0 = \phi(\boldsymbol{m}_0,\mathbf{U}_0)$.

A second order in time resolution of system (4.32) must then verify (4.33) locally for each Δt. In the context of decoupled approach, ϕ is taken constant inside a time step. This amounts to solve:

$$\mathrm{d}_t\bar{\boldsymbol{m}} = \mathbf{F}\left(\bar{\boldsymbol{m}},\phi^*\right) \tag{4.34a}$$

$$\mathrm{d}_t\bar{\mathbf{U}} = \mathbf{G}\left(\bar{\boldsymbol{m}},\bar{\mathbf{U}},\phi^*\right), \qquad t\in\,]t_0,t_0+\Delta t], \tag{4.34b}$$

with fixed $\phi^* = \phi^*(t^*)$ for $t^*\in[t_0,t_0+\Delta t]$ and $\bar{\boldsymbol{m}}(t_0) = \boldsymbol{m}_0$.

The most common technique considers $t^* = t_0$, which implies previously computing ϕ^* from values of $\mathbf{U}$ and $\boldsymbol{m}$ taken at the initial time t_0: $\phi^* = \phi_0$. This can leads to the following Taylor development:

$$\boldsymbol{m}(t_0+\Delta t) = \boldsymbol{m}_0 + \Delta t\mathbf{F}(\boldsymbol{m}_0,\phi_0) + \frac{\Delta t^2}{2}\left[\partial_{\boldsymbol{m}}\mathbf{F}\mathbf{F}\right]_{\boldsymbol{m}_0,U_0,\phi_0} + O(\Delta t^3), \tag{4.35a}$$

$$\mathbf{U}(t_0+\Delta t) = \mathbf{U}_0 + \Delta t\mathbf{G}(\boldsymbol{m}_0,\mathbf{U}_0,\phi_0) + \frac{\Delta t^2}{2}\left[\partial_{\boldsymbol{m}}\mathbf{G}\mathbf{F} + \partial_{\mathbf{U}}\mathbf{G}\mathbf{G}\right]_{\boldsymbol{m}_0,\mathbf{U}_0,\phi_0} + O(\Delta t^3), \tag{4.35b}$$

to be compared with (4.33). It is then clear that the system is locally second order accurate and then globally first order accurate. However, it can be solved with algorithm described in the previous section.

In the case where the used schemes to solve (4.34) were second order accurate, a second order solution can be obtained by considering $t^* = t_0 + \dfrac{\Delta t}{2}$, in the same way that in [44]. Indeed, the Taylor development of the solution would be the same as in the fully coupled case, as soon as we have a first order estimation of ϕ^*. This one can be obtained by the use of the previously described first order scheme on a time step $\dfrac{\Delta t}{2}$. However, the evaporation scheme is only first order accurate, as explained in section 4.3.1.1. But it can be very accurate if the entropy maximization reconstruction is very small on $[S_{max},+\infty[$. In this case, one can hope to obtain numerically a second order of convergence with this strategy.

4.4 Homogeneous test cases

In this section, one is looking for conducting some preliminary test cases to study the numerical strategy developed in section 4.3 for the two-way coupling of polydisperse evaporating droplets with the gas. The main focus will be on the stability and the accuracy

of the time integration. It is therefore appropriate to focus on, all at once, the resolution of the system in phase A rather than complete conservation equation system which will be further investigated in section 4.5. This accounts for dealing with an homogeneous 0D case where all gradients are null. In the reminder, we will first of all give a brief introduction on common characteristic of test cases presented in this section and then deeply focus on each of them successively. In the first test case, one aims at validating the new numerical strategy when the order of the method is not expected to be influenced by the evaporation law, that is, we will consider a constant d-square evaporation of droplets. The second test case will help us to analysis our numerical method under more complicated evaporation laws also adopted for injection simulations of droplets under industrial codes. Indeed, ambient gas pressure and temperature along with the amount of vapor fuel presented in a combustion chamber can significantly influence the evaporation rate which can lead, in extreme case, severe CFD simulation problems such as the stability and the accuracy. For both test cases described above, the evaporation velocity will be computed through Eq.(4.3). For the sake of simplicity, no heat transfer between phases will be conducted, leading $Q = 0$ in Eq.(4.4).

Let us present the initial droplet distribution used in the simulations. For the sake of consistency with injection simulations investigated in section 4.5, we are adopting a Rosin Rammler distribution given by the following equation under the dimensionless formulation:

$$n\left(\bar{S}\right) = \frac{1}{2} q_{rr} 16^{\frac{q_{rr}}{2}} (S)^{\frac{q_{rr}}{2}-1} \exp\left[-\left(16\bar{S}\right)^{\frac{q_{rr}}{2}}\right] \tag{4.36}$$

with the constant $q_{rr} = 3.5$ determining the sharpness of the distribution and the dimensionless size phase variable $\bar{S} \in [0, 1]$. Therefore initial dimensionless moment set can be given as $\bar{\boldsymbol{m}} = (\bar{m}_0, \bar{m}_1, \bar{m}_2, \bar{m}_3)^t$. Working with $\bar{\boldsymbol{m}}$ helps us to minimize numerical errors while reconstructing the distribution function $\tilde{n}$ using Newton iterations. Yet in the context of industrial CFD code development, the dimensional formalism is rather adopted. Our strategy is therefore to keep dimensionless formalism on transported moment $\bar{\boldsymbol{m}}$ and reconstruct dimensional fractional moments required for the two-way coupling. Thanks to the following expression and through the knowledge of characteristic droplet number per volume of the spray and the maximum size of the droplet distribution, it is straightforward to express the dimensional moments through non-dimensional moments:

$$m_k = N_0 S_{max}^k \bar{m}_k \tag{4.37}$$

where N_0 is the characteristic number of droplets. The configuration chosen for 0D simulations is very important since the thermodynamics encountered in a classical diesel/gasoline engine can have a significant impact on both characteristic time scales of polydisperse droplets and the two-way coupling dynamics between phases. To illustrate the effectiveness of the numerical strategy developed in this paper, one focuses on a test-case where both the evaporation and the dynamic time scales are initially at the same order of magnitude. We thus focus in the following both gas and spray thermodynamics given in Table 4.1.

The gas pressure P_g, the gas temperature T_g, species mass fractions Y_k inside the gas, the vapor pressure P_v and the liquid fuel temperature T_d will allow us to compute the

evaporation velocity R_d of droplets. However more properties for the gas phase such as the diffusion coefficient D_{Y_F} appeared in Equation (4.3) and the heat capacity at constant volume $C_{v,g}$ required for the computation of the spray temperature from the internal energy, are needed. Therefore, during computations we are calculating these properties through routines provided by Chemkin [88].

	Y_{O_2}	Y_{N_2}	$Y_{C_7H_{16}}$	$T\,(K)$	$P_g\,(MPa)$	$\rho\,(kg/m^3)$	$P_v\,(MPa)$	$\nu_g\,(m^2/s)$
gas	0.21	0.79	-	800	0.1	0.43822	-	$4.15\ 10^{-5}$
fuel	-	-	1	373	-	622.79340	0.59508	-

Table 4.1: Initial thermodynamic data relative to the ambient gas and the liquid fuel composed of n-heptane C_7H_{16}.Y_k represents the mass fraction of the specie k.

In the following, let us detail the two test cases and comment on results.

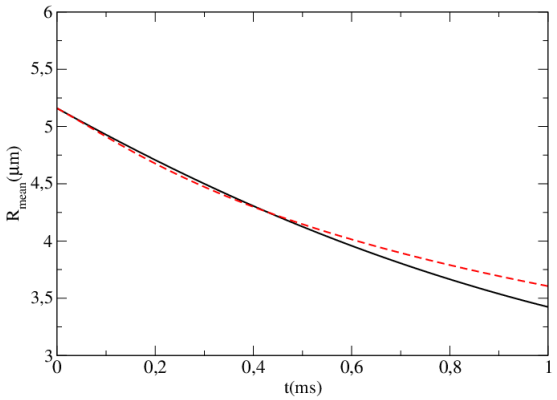

Figure 4.1: *The spray mean radius evolution through time, given for cases of constant evaporation (solid line) and time-dependent evaporation (dashed line)*

4.4.1 0-D test case of evaporating polydisperse spray under the d-square constant evaporation law

In this first test case, the evaporation velocity is computed through properties given in Table 4.1 at the beginning of the simulation. This implies a constant evaporation velocity R_S but with variable characteristic evaporation time τ_v since the mean droplet radius given through the formula

$$r_{mean} = \sqrt{\frac{m_{3/2}}{4\pi m_{1/2}}}. \tag{4.38}$$

is decreasing in time as plotted in Figure 4.1. It is also noticed, in Figure 4.2, that the order of magnitude between dynamic and evaporation characteristic times is the same, at initial time. Under a time step $\Delta t = 10^{-6}s$, the simulation is run up to the time

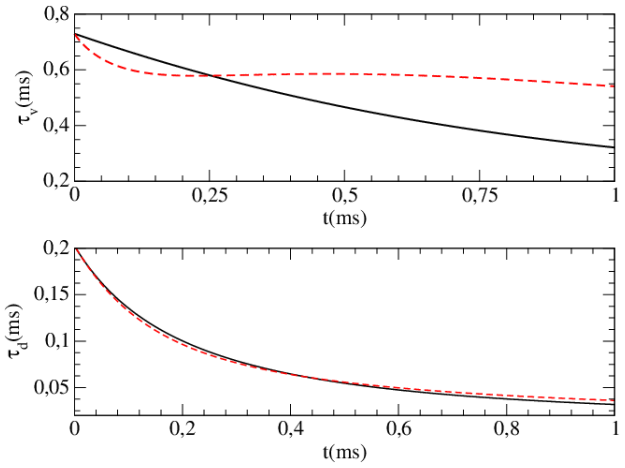

Figure 4.2: *Evolution of the characteristic evaporation time τ_v (upper graph) and the characteristic dynamic time scale τ_d (lower graph) based on the spray mean size. Evolution under a time-dependent evaporation law (dashed line) and under a the dynamic time τ_d (solid line).*

0.001s which is bigger than the initial evaporation time of the mean spray radius. Let us emphasize that, this time step is considered to give a reference solution since an analytical solution of the two-way coupling under the Rosin-Rammler distribution does not exist.

At the final time, about 96% of the spray mass is evaporated as seen in Figure 4.3. When it comes to the gas thermodynamics which follow the perfect gas equation of state, the temperature T_g and the pressure P_g are decreased respectively to about 407K and to about 0.78MPa while the vapor mass fraction and the gas mass density go up to about6.44 10^{-1} and about 1.23 kg/m3 respectively, as plotted in Figure 4.4. The initial mass loading being high, the velocity relaxation between two phases happens at velocity $u_r = -0.3$ m/s which is more closer to the initial spray velocity than the initial gas velocity, as observed in Figure 4.5. For the sake of the accuracy and the stability investigation of the numerical strategy, one has been interested in numerical solutions under different time steps. Remark that the characteristic evaporation time scale is about 3.5 times greater than the characteristic dynamic time scale at the initial time. Under such small differences between two time scales, it is important to focus on time steps smaller and greater than the smallest time scale that is the dynamic time scale of droplets. If one considers that the smallest time step $\Delta t = 10^{-6}s$ is the reference one, the solution under the time scale $\Delta t = 2.5\ 10^{-4}s > \tau_d(t = 0)$ has a correct and stable behavior while converging to the reference velocity as seen in Figure 4.5. Yet this coarse time step is not so small compared to the characteristic evaporation time $\tau_v(t = 0)$ and is expected to influence the accuracy of thermodynamics such as the gas pressure and temperature, and the fuel vapor mass fraction. Figure 4.4 shows that both gas thermodynamics and the fuel vapor fraction evolution under the coarse time step is well captured as compared to the reference solution. Moreover, even if the velocity relaxation time between phases is not captured, the natural equilibrium state is well predicted under a stable computation as plotted in Figure 4.5.

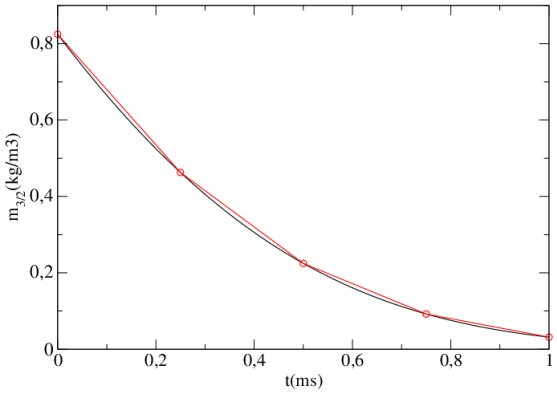

Figure 4.3: *Spray density concentration (moment of order* $3/2$*) evolution under the constant evaporation. Solutions are given under the time steps* $\Delta t = 10^{-6}s$ *(Solid line) and* $\Delta t = 2.4910^{-3}s$ *(empty squares).*

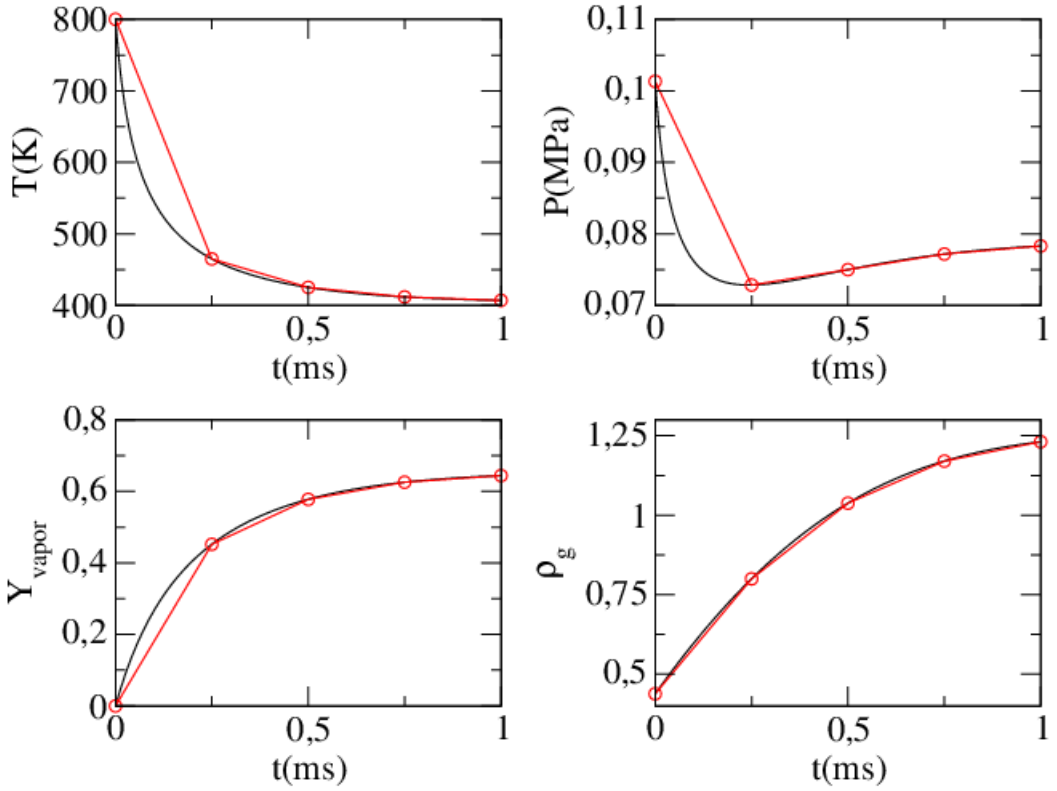

Figure 4.4: *Gas phase thermodynamics and vapor mass fraction against time,under the constant evaporation. Gas temperature* T_g *(top left), gas pressure* P_g *(top right), vapor mass fraction* $Y_{C_7H_{16}}$*(down left) and gas mass density (down right). Results under* $\Delta t = 2.49\ 10^{-3}s$ *are plotted by empty squares whereas solid lines correspond to the solution with* $\Delta t = 10^{-6}s$*.*

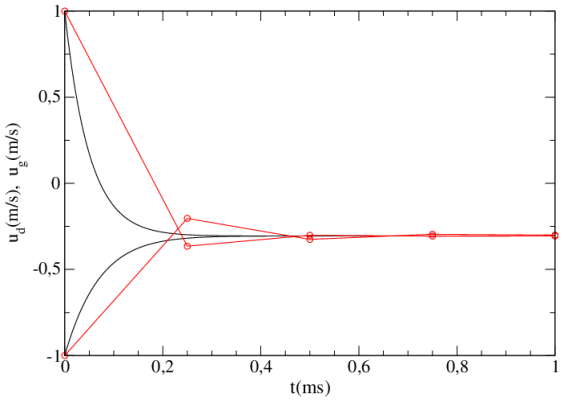

Figure 4.5: *Velocity evolution under the constant evaporation. Gas velocity when* $\Delta t = 10^{-6}s$ *(solid line),* $\Delta t = 10^{-5}s$ *(empty circles) and spray velocity when* $\Delta t = 10^{-6}$ *(dashed line),* $\Delta t = 10^{-5}s$ *(empty squares).*

4.4.2 Variable (realistic) d-square law of evaporation

In this case, the drift velocity R_d is computed at each time step Δt through Equation (4.3), implying a time-dependency through the evolutions for the ambient pressure, the ambient temperature and the vapor mass fraction. Under this unique consideration as compared to the previous test case discussed in part 4.4.1, one runs the same homogeneous simulations. Like the constant evaporation case, one considers the simulation under a time step $\Delta t = 10^{-6}s$ as a reference solution and $\Delta t = 2.5\ 10^{-4}s > \tau_d(t = 0)$ the coarse solution. The results are discussed in the following.

The fact that the pressure and the temperature keep going down and the vapor mass fraction tends to increase towards its saturation value leads a complicated evaporation time scale evolution. As shown in Figure 4.2, the evaporation time scale firstly decreases then tends to flatten out, before decreasing slowly. At the final time 0.001s, the remaining spray mass is about 8%, as illustrated in Figure 4.6. It is concluded that in this case about 4% more spray mass remain at the final simulation time than in the constant evaporation case. The profiles for gas-phase thermodynamics plotted in Figure 4.7 are similar to same variables under a constant evaporation law given through Figure 4.4. Yet the ambient temperature T_g decreases about 0.5% less, the ambient pressure decreases about 2.8% more, the vapor mass fraction and the gas-phase mass density increase about 1.4% and 3.8% less respectively than in the constant evaporation case.

Let us now investigate results under the coarse solution. As observed in figures 4.6, 4.7 and 4.8, solutions remain stable. The velocity profiles remain almost the same as the constant evaporation case. Yet in terms of the gas-phase thermodynamics and the spray mass density, one can qualitatively observe that the coarse solution is less accurate in case with time-dependent evaporation than the case with constant evaporation.

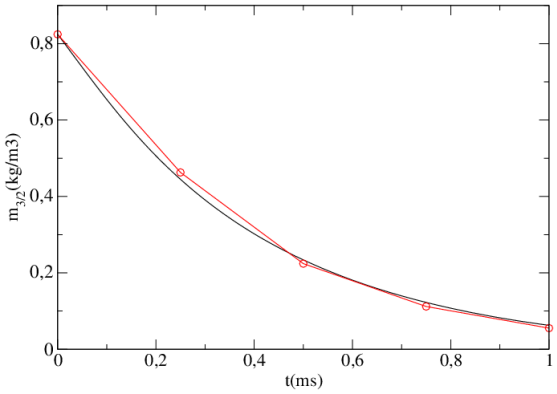

Figure 4.6: *Spray density concentration (moment of order 3/2) evolution under the time dependent evaporation. Solutions are given under the time steps* $\Delta t = 10^{-6}s$ *(Solid line) and* $\Delta t = 2.4910^{-3}s$ *(empty squares).*

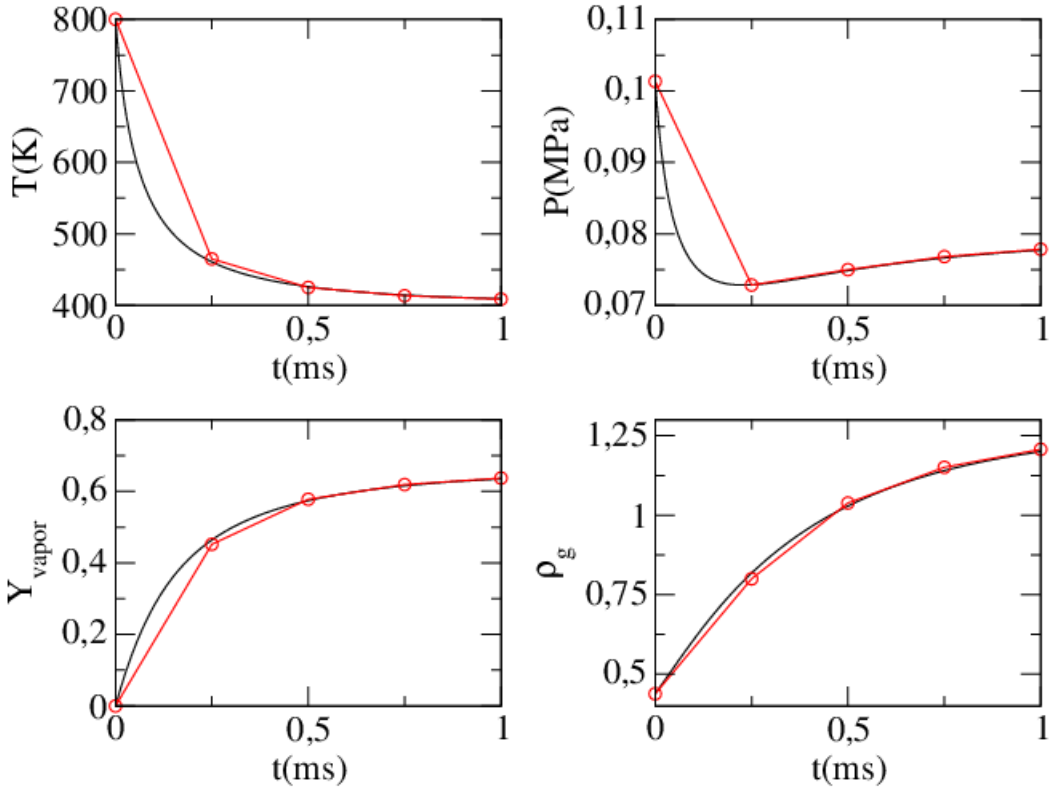

Figure 4.7: *Gas phase thermodynamics and vapor mass fraction against time,under the time dependent evaporation. Gas temperature* T_g *(top left), gas pressure* P_g *(top right), vapor mass fraction* $Y_{C_7H_{16}}$ *(down left) and gas mass density (down right). Results under* $\Delta t = 2.49\ 10^{-3}s$ *are plotted by empty squares whereas solid lines correspond to the solution with* $\Delta t = 10^{-6}s$.

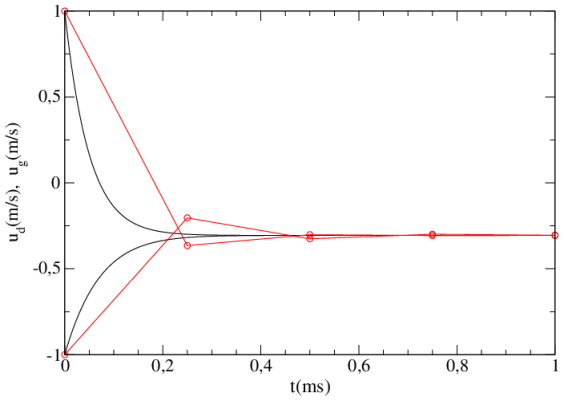

Figure 4.8: *Velocity evolution under the time dependent evaporation. Gas velocity when* $\Delta t = 10^{-6}s$ *(solid line),* $\Delta t = 10^{-5}s$ *(empty circles) and spray velocity when* $\Delta t = 10^{-6}s$ *(dashed line),* $\Delta t = 10^{-5}s$ *(empty squares).*

4.4.3 Order of convergence study of the numerical scheme

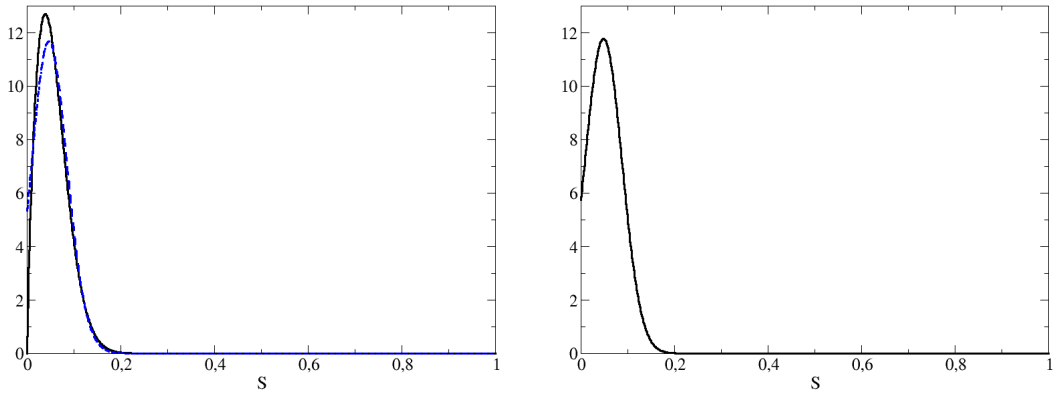

Figure 4.9: *(left) Rosin Rammler distribution (dashed line) and its reconstruction by entropy maximization (solid line); (right) initial distribution given by (4.39) "close" to the Rosin Rammler distribution*

Let us first analyze the error done with the evaporation scheme. The initial distribution in the Rosin Rammler one, given by Eq. (4.36) and plotted on figure 4.9-left. For the sake of simplicity, we use the dimensionless formulation and the corresponding evaporation rate is then equal to 1. A reference solution is computed by the resolution of the scheme with a very small time steps $\Delta t = 10^{-5}$ (10 times smaller than the smaller one used for the other computations). On figure 4.10, one can find the maximal value of the error between the simulation done for several time steps and the reference solution. The order of accuracy is clearly equal to one. However, the accuracy is very good, with a maximal

error of 10^{-4} on the moments.

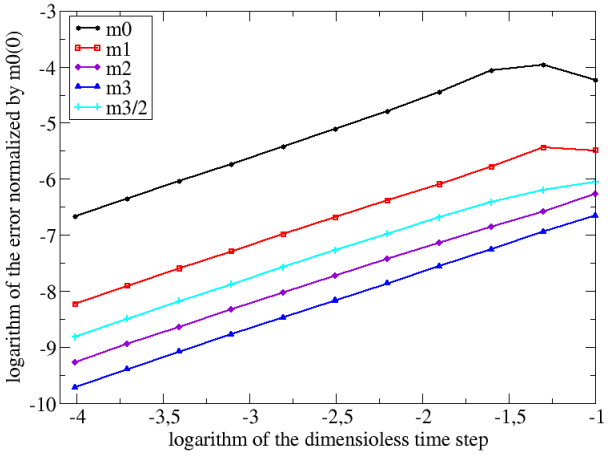

Figure 4.10: *Logarithm of the error on the moments m_0, m_1, m_2, m_3 and $m_{3/2}$ normalized by the initial value of m_0 as a function of the time step Δt.*

The entropy maximization reconstruction of the Rosin Rammler distribution is plotted on figure 4.9-left. It can be seen that its value at the bound $\bar{S} = 1$ of the integration interval is about 0.0034. It is not negligible and the reconstructed distribution can not be a solution of the kinetic problem, as explained in section 4.3.1.1. Let us then modify this distribution and introduce the following one:

$$n_0(\bar{S}) = \exp(1.75 + 30\,\bar{S} - 315\,\bar{S}^2 + 3\,\bar{S}^3). \tag{4.39}$$

It is plotted on figure 4.9-right and coincide with its reconstruction by entropy maximization. Moreover, its value at $\bar{S} = 1$ is largely smaller that the double precision of the computer. The simulation shows that, for this distribution, the error of the evaporation scheme is smaller that 10^{-11} time the initial value or m_0. So, as presumed in section 4.3.1.1, the error is very small for this distribution having a reconstruction by entropy maximization very small on $[S_{max}, +\infty[$.

But let us now analyze the error of the global scheme conducted under the same physics studied in part 4.4.1. Similarly done for the previous error analysis on the evaporation scheme only, we take the reference solution such to be 10 times smaller than the smaller one used for the other computations. Yet let us recall that in this case, we are in a dimensional variables framework and the reference time step is taken as $\Delta t = 10^{-8}$s. Moreover, the simulations are run up to a final time 10^{-4}s which remaining below the initial values for characteristic times τ_d and τ_v, which are illustrated in Figure 4.2. Several simulations are run under a time step $\Delta t \in [10^{-7}s, 10^{-5}s]$ and the error graphs are plotted through Figure 4.11. The right graph plots the absolute errors relative to quantities the moment of order 3/2, $m_{3/2}$, the gas velocity $\boldsymbol{u_g}$ and the spray velocity $\boldsymbol{u_d}$ involved in the two-way coupling equations under a constant evaporation law. The moment $m_{3/2}$ has

the first order of accuracy with very small errors as also observed in the previous study. Under the coarsest time step, the moment $m_{3/2}$ is of three order of magnitude more precise than both the gas and the spray velocities. However, velocities are converging to their reference solutions faster than the moment 3/2 for smaller time steps under a greater slope, verifying a third order of accuracy. This is a promising result since the order of the SDIRK scheme is preserved, despite the lower order associated to the evaporation scheme. On the other hand, results are less accurate under a time dependent evaporation law. All of three variables of interest converging under a first order of accuracy. More importantly, the associated errors are of three order of magnitude more important than their counterparts under a constant evaporation case, at the most refined time step Δt. This is an expected situation since the evaporation velocity is kept constant during a time step Δt.

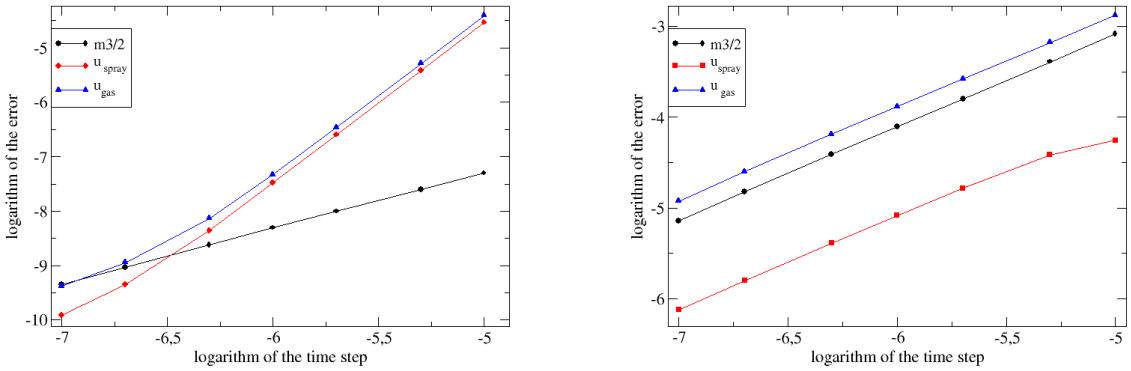

Figure 4.11: *Error studies for the two-way coupling model: logarithm of the error on the moment $m_{3/2}$, the spray velocity u_d, the gas velocity u_g as a function of the time step Δt. Results from a constant d-square evaporation law given on the left graph, whereas from a time dependent d-square evaporation law by the right graph.*

4.5 2D Injection simulations in IFP-C3D code

One aims at investigating our two-way coupling strategy in case where a multidimensional framework is considered. The main target being an ICE application, one will study the direct injection of a two-phase flow, composed of a cloud of polydisperse droplets inside the gas, to a chamber initially filled by a motionless gas. Let us recall that the experimental set-up proposed in [58] to focus on spray injection has been an appropriate inspiration to validate the Eulerian two-way coupling model under the industrial software IFP-C3D [12] where a 2D geometry and a regular mesh were considered [84]. In this last paper, both qualitative and quantitative comparisons between widely used Lagrangian description of

the spray under IFP-C3D and the newly implemented Eulerian high order moment method (EMSM) of evaporating polydisperse spray model have been successfully achieved. Yet the polydisperse spray evaporation followed a constant d-square law. The goal is now to extent this work to a case where a time depending d-square evaporation law which is more realistic and taking advantage of gas-phase thermodynamics is activated. This will be achieve through the link between homogeneous test cases conducted in section 4.4 and injection test cases discussed in this section. In the following, a brief insight on IFP-C3D software will be first given. Afterwards, the test-case will be presented. Finally the discussion on results under both Eulerian and Lagrangian descriptions of the spray will be conducted.

4.5.1 A short description of IFP-C3D software

Over the past several years, the IFP-C3D code [12] has been developed at IFP Énergies nouvelles for the numerical simulation of advanced internal combustion engines. IFP-C3D involves a great many intricated physical and chemical processes, most prominently transient multidimensional multicomponent gases undergoing mixing, ignition, reactions, heat transfer, and turbulence. These numerous options can be individually activated or deactivated by input switches, which makes IFP-C3D a versatile tool for engineers. As far as liquid spray is concerned, it was previously incorporated in IFP-C3D with a Lagrangian approach called *stochastic parcel* [74].

The most salient feature of IFP-C3D is its capability to tackle engine cylinders with arbitrarily shaped and moving piston geometries. To accomplish this, IFP-C3D resorts to a staggered grid whose hexahedral cells build up an unstructured mesh. Thermodynamic variables are located at the cell-centers, while velocity vectors are located at the nodes. Such a choice is meant to make the mesh motion unambiguous: the vertices are simply moved to new user-specified positions. The price to be paid for such a convenience with respect to mesh motion is some awkwardness in discretizing the momentum balance equations over the dual mesh.

Following the ALE formalism detailed in part 4.2.2.1, each time-step in IFP-C3D consists of three phases.

- In phase A, source terms of the chemical reactions on gas[1], of the Lagrangian fuel injection spray and of the spark ignition are calculated.
- In phase B, all the diffusive and acoustic terms are solved implicitly, with first the species mass, internal energy term, and turbulent terms. The method introduced in [137] is retained in its fully implicit version. The coupled implicit equations (momentum, temperature and pressure) are solved with the SIMPLE algorithm [182]: this is called the PVT (Pressure Temperature Velocity) loop.
- In phase C, the outcomes of phase B are remapped in order to match the imposed new grid. The corresponding linear convection equations are solved explicitly, so as to enhance accuracy with respect to kinematic phenomena. Limited slope reconstruction is considered via dimensional splitting, which gives rise to the so-called

[1] auto-ignition, combustion, post-oxidation, chemical equilibrium, etc.

Quasi Second Order Upwind Scheme (QSOU) [4]. Subcycles may have to be introduced in order to ensure the CFL condition.

4.5.2 Discussion on injection simulations

The complete description of the 2D injection test-case is found in [84]. It basically consists of injecting a two-phase flow involving polydisperse spray and the gas. The injected volume fraction of the spray is 2.51 10^{-4} while its mass fraction is 0.19151 . Both the gas and the spray are injected at the same velocity $u = 18m/s$ through an injection diameter of 8mm. The typical size of cells composing the mesh is 0.25mm. The injected size distribution function is the same as the one presented through Eq. (4.36). More details on initial and boundary conditions, and spray and gas properties are presented in [84]. Yet the initial gas temperature in the chamber and at the inlet boundary condition is taken as 800K as done for homogeneous test-cases presented in section 4.4. The heat transfer between phases will be omitted and the evaporation law will follow the model given by the expression (4.3) while the Stokes law will guide the velocity relaxation through drag force. In the following, one will look forward to validating the Eulerian two-way coupling model under a time dependent evaporation law. The strategy will be the same as done in [84], that is, comparing results from Eulerian and Lagrangian descriptions of the polydisperse spray. Note that the characteristic size of the spray given through the Sauter Mean Radius (SMR) has been revealed to impact the injection dynamics in [84]. Therefore, one will focus on the effect of the two-way coupling on both low and high inertia droplets.

4.5.2.1 Injection of low inertia droplets

Injection results in the case of a low inertia droplet population with Sauter mean radius $SMR = 5\mu m$ are illustrated in Figures 4.12, 4.13 and 4.14. The fields of gas and spray velocities are in a very good agreement between Lagrangian and Eulerian simulations, as illustrated in Figure 4.12. Yet some differences are observed in the fields of the spray volume fraction, the fuel-vapor mass fraction and the gas-phase temperature. Although the penetration length is the same between the Lagrangian and Eulerian results, the size of the biggest structure inside the spray-phase is smaller in the Lagrangian case, as observed through Figure 4.13. Moreover, the droplet concentration at the front of the spray is more remarkable for the Lagrangian spray then the Eulerian one. As a conclusion, the evaporated fuel occupy less space in Lagrangian case then the Eulerian case. In the latter, the fuel vapor is less dense as shown through the figure 4.13. Since the fuel is more dense in case of the Lagrangian spray, locally, the gas-phase temperature goes down faster, as observed in the figure 4.14.

4.5.2.2 Injection of high inertia droplets

Injection results in the case of a high inertia droplet population with Sauter mean radius $SMR = 20\mu m$ are illustrated in Figures 4.15, 4.16 and 4.17. As highlighted in [84], the monokinetic assumption for the Eulerian spray, that is, unique velocity for all droplets in a cell does not allow to capture droplet trajectory crossings (PTC). Yet it is known

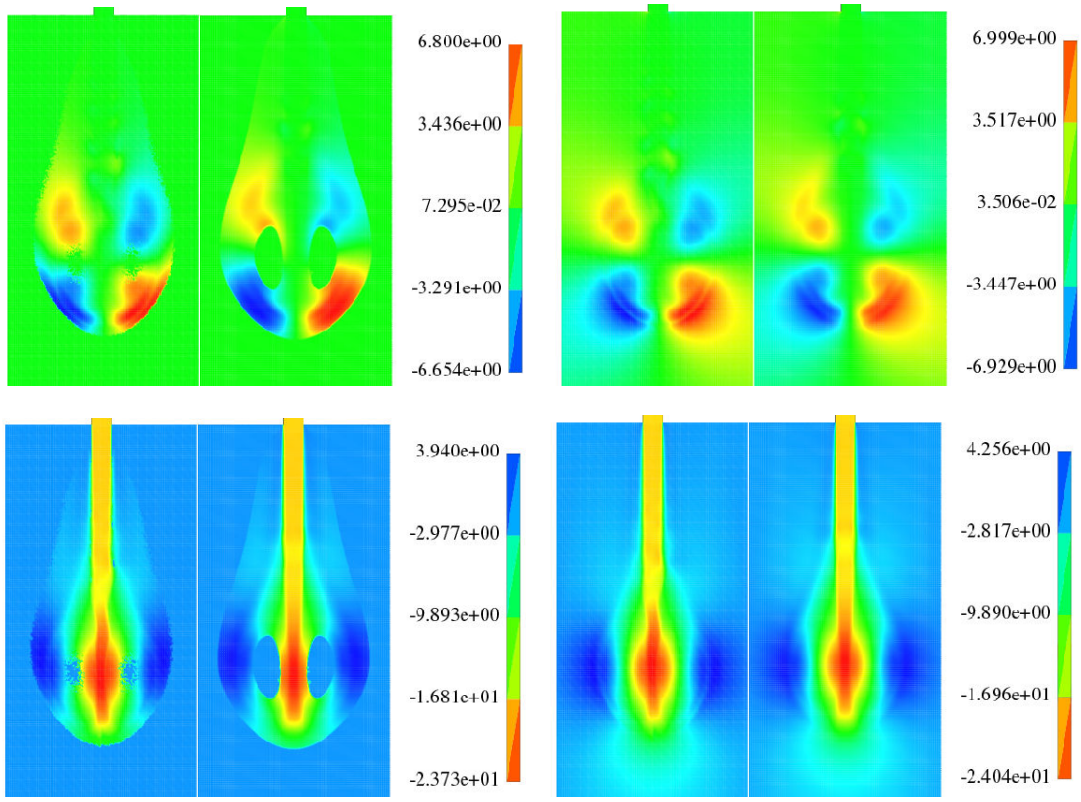

Figure 4.12: Results for a droplet population of SMR = $5\mu m$ at time $1.4 \cdot 10^{-2}$s. Left: spray-phase velocities. Right: gas-phase velocities. velocity component along x-axis (top row), velocity component along the y-axis (bottom row). In each panel, Lagrangian spray is displayed on the left side whereas Eulerian on the right side

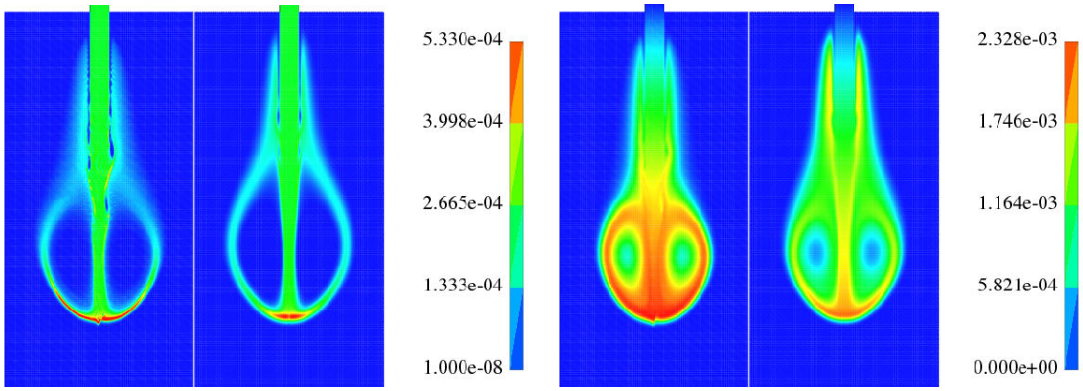

Figure 4.13: Results for a droplet population of SMR = $5\mu m$ at time $1.4 \cdot 10^{-2}$s. Left: spray-phase volume fraction. Right:fuel vapor mass fraction.In each panel, Lagrangian spray is displayed on the left side whereas Eulerian on the right side

that the PTC is more important in case of inertial droplets which relaxation time with

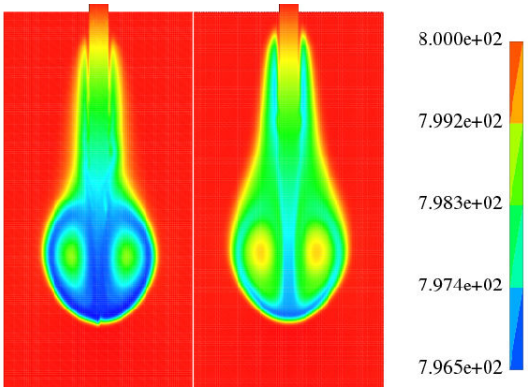

Figure 4.14: The gas-phase temperature field for a droplet population of SMR = $5\mu m$ at time $1.4 \cdot 10^{-2}$s. In each panel, Lagrangian spray is displayed on the left side whereas Eulerian on the right side

the surrounding gas velocity is higher then low inertia droplets. This implies multiple droplet velocities in a cell. The Lagrangian description captures well the PTC so that the differences in the field of velocity, observed in Figure 4.15, come from the fact that Eulerian approach could not capture such PTC. Moreover, this lack of the Eulerian method is observed also in the spray volume fraction field illustrated through Figure 4.16. Yet the vapor fuel mass fraction and the gas temperature fields are quite similar between different description of the spray. This is an encouriging results for combustion applications.

4.6 Conclusion and perspectives

Through this paper, the Eulerian two-way coupling model between the polydisperse spray and the compressible gas originally developed in [84] has been generalized for realistic cases with time-dependent evaporation laws widely used in Internal Combustion Engine applications. In terms of numerical achievements, the order of accuracy related to the evaporation scheme developed in [120] has been revealed for the first time. Through homogeneous test cases, the scheme has been shown to be at least first order. The same study has been conducted on the global scheme. Under the constant evaporation, both gas and spray velocities are proven to respect the third order of accuracy of the SDIRK scheme, involved in the time integration of the momentum equations. This is due to the fact that the absolute errors related to the kinetic evaporation scheme are very small. The mid-time step technique originally developed in [44] has been succesfully integrated to our two-way coupling strategy, leading to very accurate and encouraging results in case of time-dependent realistic evaporation laws. Moreover, the stability of the global scheme under time-dependent evaporation law has been validated. The Eulerian two-way coupling model has been also investigated through 2-D injection simulations in the industrial code IFP-C3D software, under a time-dependent evaporation law. Its qualitative comparison to the widely used Lagrangian simulation of particles has yielded encouraging results.

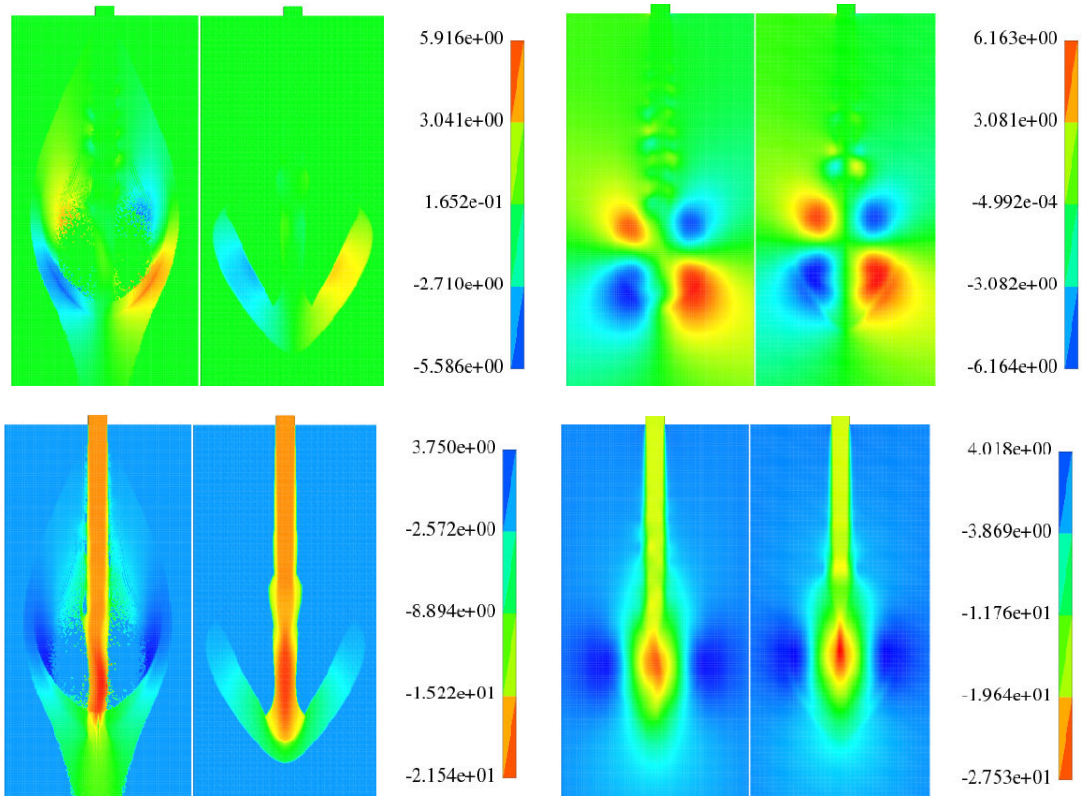

Figure 4.15: Results for a droplet population of SMR = $20\mu m$ at time $1.4 \cdot 10^{-2}$s. Left: spray-phase velocities. Right: gas-phase velocities. Velocity component along x-axis (top row), velocity component along the y-axis (bottom row). In each panel, Lagrangian spray is displayed on the left side whereas Eulerian on the right side

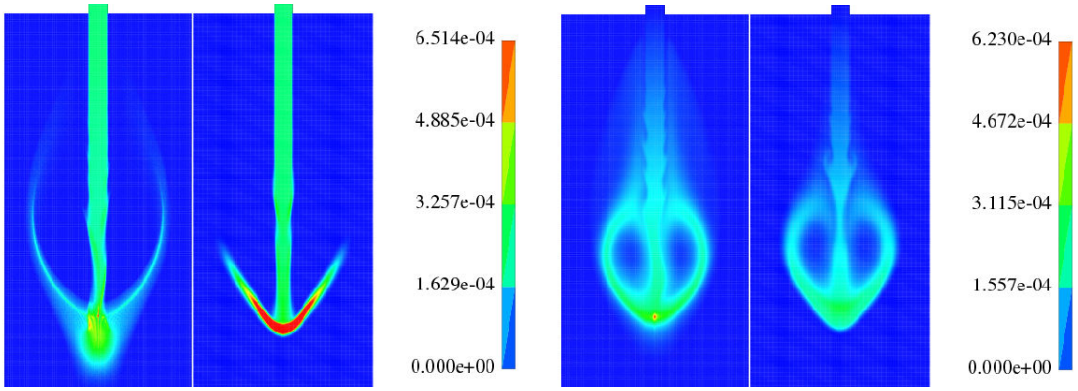

Figure 4.16: Results for a droplet population of SMR = $20\mu m$ at time $1.4 \cdot 10^{-2}$s. Left: spray-phase volume fraction. Right:fuel vapor mass fraction.In each panel, Lagrangian spray is displayed on the left side whereas Eulerian on the right side

As far as the perspectives are concerned, the method of Duarte et al. [44] is required

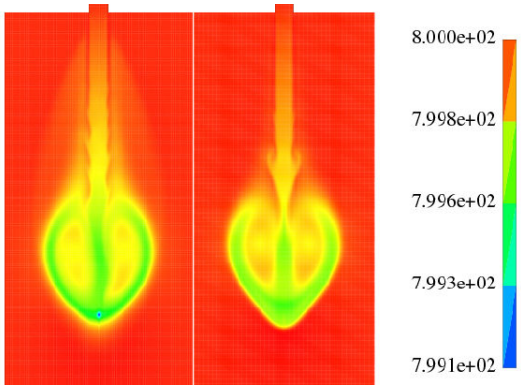

Figure 4.17: The gas-phase temperature field for a droplet population of SMR = $20\mu m$ at time $1.4 \cdot 10^{-2}$s. In each panel, Lagrangian spray is displayed on the left side whereas Eulerian on the right side

to be integrated in IFP-C3D software and qualitatively verified through comparisons with Lagrangien method.

Chapter 5

Implementation of the two-way coupled EMSM algorithm in IFP-C3D code for 3-D simulations

The results from 3-D simulations in this chapter are my contribution to an article accepted for a publication in Atomization and Sprays [54]

- *O. Emre, D. Kah, S. Jay, Q.-H. Tran, A. Velghe, S. de Chaisemartin, R.O. Fox, F. Laurent, M. Massot, Eulerian Moment Methods for Automotive Sprays*, accepted for a publication in Atomization and Sprays.

5.1 Introduction

This chapter presents the ability of the two-way coupled polydisperse Eulerian method to handle stiff injection conditions under a three dimensional test-case simulated through IFP-C3D software. Yet before going into details of this configuration, first the implementation effort done in IFP-C3D needs to be investigated. In fact, the IFP-C3D code structure, based on the 3D model resolution thanks to the ALE operator splitting formalism to deal with moving geometries and the finite volume integration strategy on the staggered grid can be considered as bottleneck issues. Moreover, the routines required for the parallelization through MPI, further complicate the integration of the two-way coupled EMSM algorithm. Therefore one will first focus on how the numerical algorithm is integrated in the IFP-C3D software. Let us remind that in 4.5.1, the general numerical method adopted in IFP-C3D code under ALE formalism has been already explained in details. Therefore, in section 5.2, one will directly go through details on the implementation carried out in the IFP-C3D code itself. Then, the 3D test-case of the high pressure direct injection will be presented and discussed in section 5.3.

5.2 Implementation of the two-way coupled EMSM method

Implementations related to the EMSM method under one-way coupling approach have been already available in the V211 version of the IFP-C3D code [83]. This section thus presents the numerical developments upgrading the code IFP-C3D to a two-way coupled polydisperse Eulerian spray solver for the version V300. First, the data structure and the initialization procedure will be described. Then, the numerical algorithm of the two-way coupling in phase A of the code will be presented.

5.2.1 Data structure

The data structure required for the one-way coupled Eulerian polydisperse spray is already available in [83]. Yet implementing the two-way coupling algorithm involves more arrays for a couple of raisons:

- Besides transported integer size moments, one needs to define arrays for the fractional size moments of order 1/2 and 3/2 used for the two-way coupling strategy.
- The fact that the global time integration strategy for the coupled gas-spray equation system is conducted through the use of an implicit Runge Kutta method (SDIRK), values belonging to different SDIRK stages need to be stored.
- As discussed in part 4.3.1, in the original EMSM algorithm, as far as the size distribution function is constructed through the transported integer moments, one would upgrade new values for the moments after the evaporation procedure. Yet this algorithm has undergone some simple modifications within the two-way coupling framework since the moment reconstruction and the evaporation routines are treated

in a decoupled manner. This is due to the fact that the fractional moment 3/2 needs to be computed through the Maximum Entropy reconstruction to calculate the conserved quantity in the spray momentum equation, before calling the two-way coupling algorithm. Then, at each stage of SDIRK, one first calls the evaporation routine before the moment reconstruction. This requires a dynamic allocation of the array of Lagranges multipliers.

The principal arrays required, to move from the one-way to the two-way coupled EMSM method are:

```
real(kind(0.d0)),allocatable, dimension(ncells,nmom) :: spdmom_3d2
real(kind(0.d0)),allocatable, dimension(ncells,nmom) :: lagrmu
real(kind(0.d0)),allocatable, dimension(ncells) :: spdmom_1d2

real(kind(0.d0)), allocatable, dimension (rknbr_S) :: rkcoefb
real(kind(0.d0)), allocatable, dimension (rknbr_S) :: rkcoefc
real(kind(0.d0)), allocatable, dimension (rknbr_S,rknbr_S) :: rkcoefaa

real(kind(0.d0)), allocatable, dimension (rk_dim,rk_dim,rknbr_S,nod) :: M_Jac

real(kind(0.d0)), allocatable, dimension (rk_dim,nod) :: rk_sol_x
real(kind(0.d0)), allocatable, dimension (rk_dim,nod) :: rk_sol_y
real(kind(0.d0)), allocatable, dimension (rk_dim,nod) :: rk_sol_z

real(kind(0.d0)), allocatable, dimension (rk_dim,rknbr_S,nod) :: rk_To_x
real(kind(0.d0)), allocatable, dimension (rk_dim,rknbr_S,nod) :: rk_To_y
real(kind(0.d0)), allocatable, dimension (rk_dim,rknbr_S,nod) :: rk_To_z
```

nmom is the number of transported integer size moments whereas *ncells* and *nod* are respectively the total cell and node numbers of the grid, *rknbr_S* the number of stage in the SDIRK time integration scheme, *rk_dim* the dimension of the two-way coupled momentum system of equation per space dimension. The arrays *spdmom_3d2, spdmom_1d2,lagrmu* denote respectively the fractional moments of order 3/2, 1/2 and the Lagranges multipliers. Arrays *rkcoefaa, rkcoefb, rkcoefc* correspond respectively to a,b,c in the butcher table given through Eq. 4.29. *M_Jac* is the Jacobien matrix of the two-way coupled momentum equation system. Arrays *rk_To_x, rk_To_y, rk_To_z* respresent intermediate solutions of the momentum system of equations throughout the SDIRK scheme according to x, y and z spacial coordinates respectively. Finally, arrays *rk_sol_x, rk_sol_y, rk_sol_z* respresent final solutions of the momentum system of equations computed over a global simulation time step, according to x, y and z spacial coordinates respectively.

5.2.2 Initialization

This paragraph presents the new options introduced in the code during the initialization procedure:

- idigazcoupl: This switch must be equal to 1 for a two-way coupling Eulerian polydisperse spray resolution
- SMR_euler: If idigazcoupl is activated, this is necessary to define the Sauter Mean Radius of the polydisperse spray distribution as an inlet boundary condition.
- Nbdrop: If idigazcoupl is activated, dimensional number of droplets injected through the inlet boundary condition.
- idievap_coeff: the constant dimensional evaporation velocity associated to the Eulerian polydisperse spray.

5.2.3 Numerical Scheme in phase A

As the two-way coupling between the polydisperse spray and the gas occurs through source terms in the two-phase equation system, the numerical strategy has been implemented in phase A of IFP-C3D code. The associated resolution is conducted in the routine called *emsm_gaz_polydisp_cpl* called by the main routine *c3d* of IFP-C3D.

Algorithm 1 Illustration of phase A routine for the resolutiong of the two-way coupled EMSM system

procedure ***emsm_gaz_polydisp_cpl***
...
% *compute Gauss Legendre quadrature points*
call gauleg(...);
...
% *compute Lagranges Multipliers and* $m_{3/2}$
call initial_entropy_maximum(...);
...
% *exchange data (*$\rho_{g,i}$*,* ΔV_i*,* $m_{3/2,i}$*) among all processors*
call exchangeBndData;
...
% *calculate Y_1,j and Y_2,j*
compute Eq.(5.1);
...
% *mass and momentum coupling via Implicit Runge Kutta algorithm*
call RungeKutta(Delta t);
...
% *exchange data (*$\rho_{g,i}$*,* ΔV_i*,* $m_{3/2,i}$*) among all processors*
call exchangeBndData;
...
% *upgrade u_d,j and u_g,j*
compute Eq.(5.1);
...
end procedure ***emsm_gaz_polydisp_cpl***

In routine *emsm_gaz_polydisp_cpl* illustrated through Algorithm 1, there are basically three steps:

- Step 1: First, abcissas and weights according to Gauss-Legendre quadrature method are computed. Then the Lagrange multipliers and the fractional moment $m_{3/2}$ are evaluated through the Maximum entropy method and the transported integer size moments. Let us remind that before proceeding to the two-way coupling resolution loop, one should reconstruct the conserved quantities for the momentum equation system. Because the numerical discretization in IFP-C3D is conducted through the staggered grid approach, all the quantities except the velocities are defined on cell centers. Yet, since velocities are defined on grid nodes, the resolution of the momentum equation system is also conducted on nodes in IFP-C3D. That is to say, it is necessary to reconstruct conserved quantities on nodes as well. Let us remind that these conserved quantities are expressed as $Y_1 = \int_V m_{3/2} u_d \mathrm{d}V$ and $Y_2 = \int_V \rho_g u_g \mathrm{d}V$ within the framework of finite volume approach, with V is an elementary cell volume. Therefore, one should construct Y_1 and Y_2 in phase A as follows:

$$Y_{1,j} = u_{d,j} \frac{1}{N_{cells}} \sum_{i}^{N_{cells}} m_{3/2,i} \Delta V_i \tag{5.1a}$$

$$Y_{2,j} = u_{g,j} \frac{1}{N_{cells}} \sum_{i}^{N_{cells}} \rho_{g,i} \Delta V_i \tag{5.1b}$$

  where the index j represents node centered values whereas the index i are for cell centered quantities. N_{cells} is the number of neighbor cells around the node j. ΔV_i is the volume of cell i. In (5.1), the sum is performed to compute at grid nodes both the spray and the gas mass. Let us also precise that, in the context of domain decomposition through MPI formalism, neighbor cells can be treated under different processors, requiring a data exchange before anys reconstructions through Eq.(5.1).

- Step 2: time integration through SDIRK loop over the global time step. This is done thanks to the routine *RungeKutta* which will be further presented in the following.

- Step 3: upgrading the velocities through the knowledge of mass and momentum conserved quantities. This step requires to use again (5.1).

Algorithm 2 Illustration of SDIRK scheme

procedure ***RungeKutta*** ...
% *SDIRK looping*
do k= 1 **to** S;
...
⟶ **call** euler_polydisp_cpl;
...
⟶ **do** j=1 **to** nod;
...
% *intermediate solution of Eq.(5.2)*
⟶ **compute** $Y^k_{1,j}$ and $Y^k_{2,j}$
⟶ **end do**
end do
...
% *final solution of Eq.(5.2) at* Δt
do j=1 **to** nod;
⟶ **compute** $Y_{1,j}$ and $Y_{2,j}$
end do
...
end procedure ***RungeKutta***

The subroutine *RungeKutta*, illustrated in Algorithm 2, is the core of the global two-way coupled EMSM integration scheme over the IFP-C3D simulation time step Δt. Within each Runge Kutta stage k over S stages, following computations are conducted:

- First for each cell i, the evaporation scheme is conducted, leading to an upgrade in integer and fractional moments but also the gas-phase mass density. This step is treated through routine *euler_polydisp_cpl*. Afterwards, the coefficients of the Jacobien Matrix associated to the two-way coupled momentum equation system, given through Eq.4.21, is calculated on grid nodes. For a better understanding of this algorithm, let us focus on the following expression of the momentum system given under the finite volume formalism

$$\begin{aligned} \mathrm{d}_t Y_{1,j} = &\left(\frac{Y_{2,j}}{\frac{1}{N_{cells}} \sum_i^{N_{cells}} \rho_{g,i} \Delta V_i} - \frac{Y_{1,j}}{\frac{1}{N_{cells}} \sum_i^{N_{cells}} m_{3/2,i} \Delta V_i} \right) \frac{1}{N_{cells}} \sum_i^{N_{cells}} \frac{m_{3/2,i}}{\tau_d^*} \Delta V_i \\ &- \frac{3}{2} Y_{1,j} \frac{\sum_i^{N_{cells}} m_{3/2,i} R_d \Delta V_i}{\sum_i^{N_{cells}} m_{3/2,i} \Delta V_i} \end{aligned} \tag{5.2a}$$

$$\begin{aligned} \mathrm{d}_t Y_{2,j} = &- \left(\frac{Y_{2,j}}{\frac{1}{N_{cells}} \sum_i^{N_{cells}} \rho_{g,i} \Delta V_i} - \frac{Y_{1,j}}{\frac{1}{N_{cells}} \sum_i^{N_{cells}} m_{3/2,i} \Delta V_i} \right) \frac{1}{N_{cells}} \sum_i^{N_{cells}} \frac{m_{3/2,i}}{\tau_d^*} \Delta V_i \\ &+ \frac{3}{2} Y_{1,j} \frac{\sum_i^{N_{cells}} m_{3/2,i} R_d \Delta V_i}{\sum_i^{N_{cells}} m_{3/2,i} \Delta V_i} \end{aligned} \tag{5.2b}$$

  where the sum on cells i in the vicinity of each node j is carried out in routine *euler_polydisp_cpl* as well.

- As far as the first step is achieved, through a loop on grid nodes, the system (5.2) is resolved in a coupled manner, as presented through the numerical strategy in section 4.3.1.

5.3 High pressure injection conditions: 3D configuration

The present test case is intended to assess the capacity of the two-way coupled EMSM model to be operated under realistic injection conditions for practical Diesel applications. The test case features a 3D dimensional simulation of a 200 μm diameter single hole injector inside a cylinder (60 mm diameter and 60 mm height), typical of a test cell geometry for actual Diesel injectors which implies very different spatial scales.

The mesh refinement is illustrated in Fig. 5.1. The smallest cells size inside the injector are about $\pm$ 5 μm.

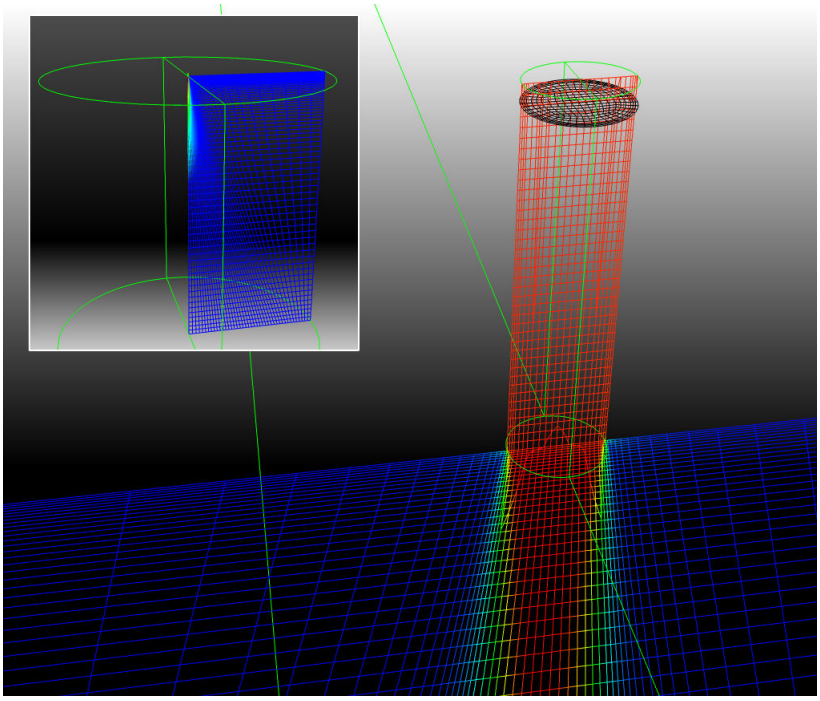

Figure 5.1: Injector hole geometry and chamber. One can notice the refined boundary condition of the injection device revealing the multiscale nature of the addressed case.

The spray is injected at a velocity of 100 ms^{-1} in a quiescent ambiant atmosphere (P_{ch}=1bar,T_{ch}=293 K). This introduces very stiff conditions due to the strong gradients related to the dynamics of injection and the density ratios between the liquid and the surrounding gas. The fully coupled EMSM model described in the previous sections is tested under these conditions. The standard $k-\epsilon$ model is activated in the gaseous phase [141]. The volume fraction at the injection boundary is that of a disperse spray ($\alpha_l \simeq 10^{-2}$) as the physics represented by the model does not include any dense effects at this stage. One can notice that, in spite of the very stiff conditions, the model is very robust. The smallest timesteps are of the order of 10^{-8} sec. The computation lasts 16 hours for a total physical time simulated of 4 ms and was conducted on 128 processors.

Results in Figures 5.2 and 5.3 show how the spray develops from the onset of injection where a disperse phase assumption is made down to the fully developed spray region in the

far field of the injector. Figure 5.2 shows the liquid volume fraction spatial distribution very close to the injector outlet. A typical cone shape distribution is observed due to the mixing with the surrounding gas. The qualitative aspect of the injected spray distribution and evaporated fuel distibution matches those issued from observations of classical high pressure injected spray. Due to the two-way coupling method described above, the high velocity liquid jet generates turbulent energy in the gas through macroscopic air entrainment at the tip of the injector (Figure 5.4).

The two-way coupled numerical approach will be extended in a future work to handle complex evaporation and drag laws which are classicaly used in engine spray conditions. This will permit quantitative comparisons with real spray measurements.

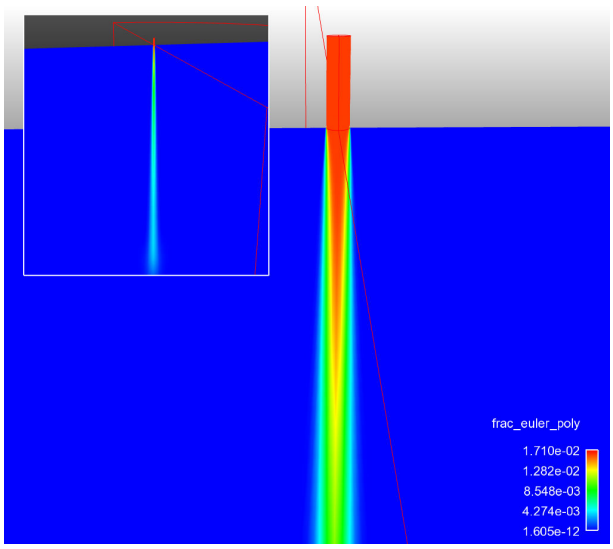

Figure 5.2: Eulerian volume fraction of liquid computed with the EMSM approach.

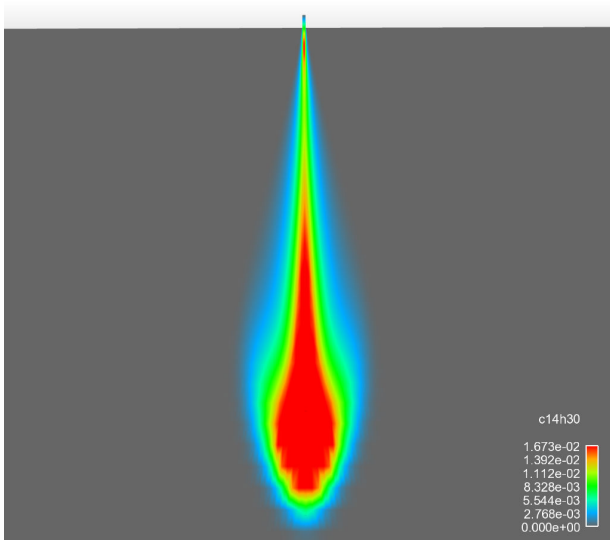

Figure 5.3: Gaseous fuel mass fraction evaporated with the EMSM approach.

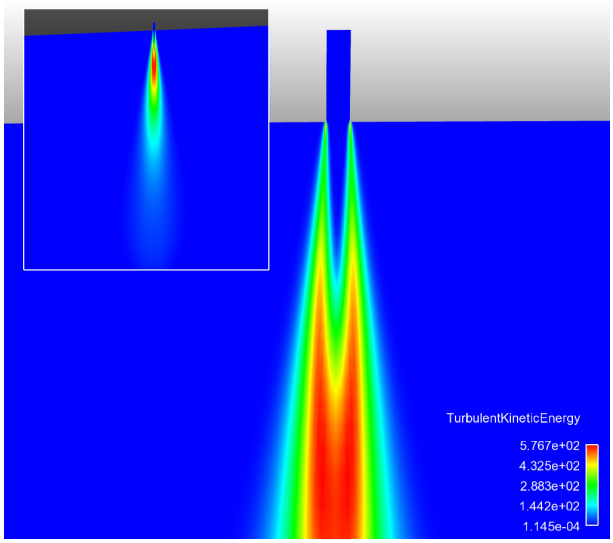

Figure 5.4: Gaseous turbulent kinetic energy related to high jet velocities

Figure 5.5 represents the evolution of the liquid and vapor concentrations at different axial positions. One can notice an opening of the spray jet along the injection direction. The fuel vapour distribution follows that of the liquid with higher concentrations on the jet axis. One can observe that vapour is entrained in the periphery of the jet which can be attributed to the turbulent transport of gaseous species. Figure 5.6 confirms that the highest vapour concentration is located in the front of the jet whereas the liquid concentration continuously decreases along the jet axis under the evaporation process. A higher vapour fuel concentration is observed in the near injector region and can be explained by the evaporation of the smallest droplets.

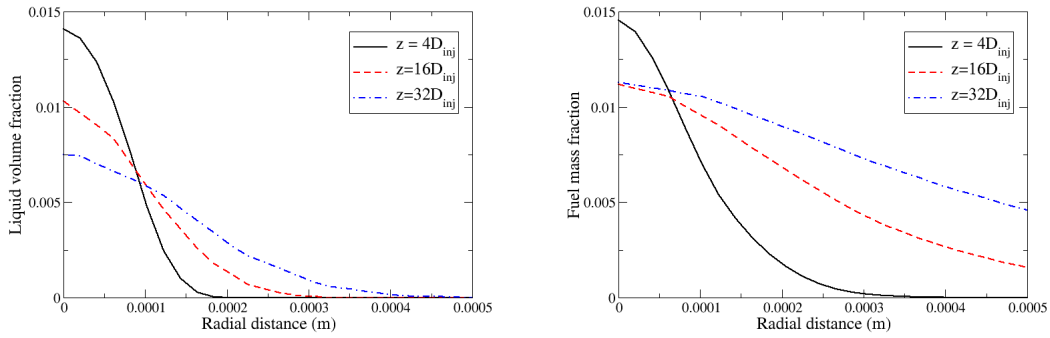

Figure 5.5: Radial profile of liquid volume fraction (left) and evaporated fuel mass fraction (right) at different axial positions : z=4D_{inj}, z=16D_{inj}, z=32D_{inj}.

From these results, one can deduce penetration lengths for the liquid and for the gas which are the relevant quantities of practical interest for engine simulations. Figure 5.7 presents the liquid penetration based on the average liquid volume fraction of the poly-

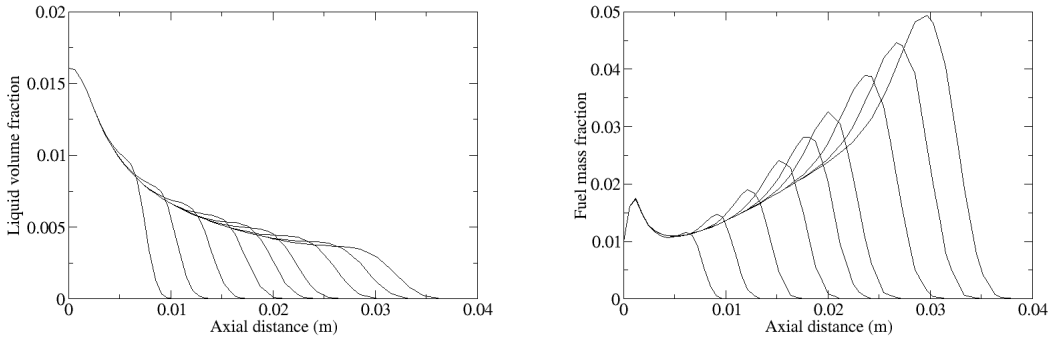

Figure 5.6: Axial profile of liquid volume fraction (left) and evaporated fuel mass fraction (right) at different consecutive instants between t=0 (start of injection) and t=2.4 ms.

disperse spray. It is calculated at an axial position where 10^{-3} of the maximum value of the volume fraction is reached. Different initial condition on the spray volume fraction is tested with variation between a low volume fraction $\alpha_{liq} = 10^{-4}$ to a higher volume fraction $\alpha_{liq} = 10^{-2}$. For this last case two combinations of Sauter mean radius and droplet number are tested resulting in the same spray volume fraction : (SMR=20μm, N=5.05810^{11}) and (SMR=5μm, N=3.2310^{13}). One can notice that for these last two conditions the spray penetration is much more important as the overall inertia of the spray is higher. In this case high inertia case, the penetration is most important for the spray having the biggest droplets. This is what can be expected on a qualitative level.

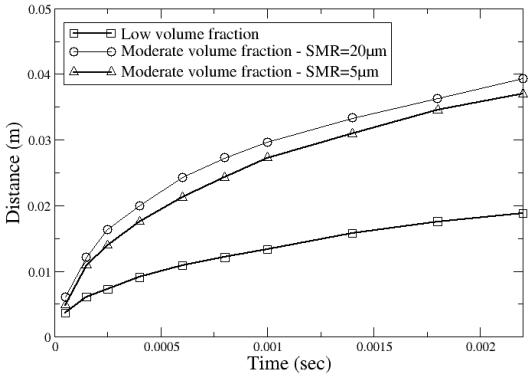

Figure 5.7: Liquid jet penetration with time for different initial conditions on charge : low charge ($\Phi_v = 10^{-4}$) - moderate charge ($\Phi_v = 10^{-2}$) with two r_{SMR} values : 5μm and 20 μm.

Chapter 6

Turbulence modeling of polydisperse interactions between the spray and the gas through the Eulerian high order moment method

This chapter is from the text of the article published in the scientific journal Flow Turbulence and Combustion [53]:

- O. Emre, R. Fox, M. Massot, S. de Chaisemartin, S. Jay, and F. Laurent, Towards Eulerian modeling of a polydisperse evaporating spray under realistic internal-combustion-engine conditions, Flow, Turbulence and Combustion, 93 (2014), pp. 689-722

6.1 Introduction

In internal combustion engines (ICE), the direct injection of the liquid fuel jet inside the combustion chamber has a great influence on both fuel consumption and pollutant production. The dynamics of the jet being very fast, one observes rapid temporal and spatial variations of mass, momentum and energy of the flow inside the chamber. Moreover, the phase change prompted by the evaporation of the fuel along with the turbulent character of the flow further complicates the physics. The liquid jet is composed of a dense zone near the injector and a dispersed zone with a cloud of droplets, also called a spray, downstream of the injector. Many previous works have addressed the modeling of the two-phase flow composed of the gas and liquid droplets. For such simulations, Lagrangian methods have been widely adopted since they provide high numerical efficiency [47]. Furthermore, their implementation in computing software is also quite straightforward. However, the high number of particles required for statistical convergence increases the simulation cost. Lagrangian methods also introduce numerical difficulties related to the coupling with the Eulerian grid used for the gas phase around the droplets and the dense zone of the spray. Moreover, they face difficulties on parallel architectures due to possible heterogeneous load balancing between the processors [71]. Given these shortcomings of Lagrangian methods,

the Eulerian description is considered as a promising alternative. However, the precise description of the polydispersity and of the two-way turbulent interaction of evaporating droplets with the surrounding gas phase at a reasonable cost remain a challenge for Eulerian methods. Moreover, satisfying the moment method stability constraints is complicated due to the rapid variations occurring inside the flow domain. Nevertheless, some pioneering work has been carried out in the context of one-way coupling [83, 120, 87].

The Eulerian Multi-Size Moment (EMSM) method, derived from the Williams-Boltzmann kinetic model [193] and developed in [83, 120, 87], has shown promising potential for fuel-injection applications based on academic configurations [86]. Its dedicated numerical scheme, respecting the moment stability constraints, treats precisely the evaporating droplets and requires less computational effort as compared to other methods [87]. Moreover, two major advances towards industrial applications have been recently achieved [87, 84]. The first is the adaptation of EMSM method to an unstructured, staggered moving grid under the Arbitrary Lagrangien Eulerian (ALE) numerical formalism. The second is the development of a stable and accurate numerical strategy for treating the polydisperse two-way coupling of the evaporating spray with its surrounding gas, while respecting the conservation of moment space, i.e., the stability requirement of the method. All these developments have been integrated into the industrial computational fluid dynamics (CFD) software IFP-C3D dedicated to compressible reactive flows under ICE conditions. Verification tests between the Eulerian and Lagrangian descriptions of the spray under injection conditions with a d^2-constant evaporation law and two-way coupled polydisperse droplets have been successfully carried out [84]. However, the issue of turbulent droplet dispersion and its impact on two-way coupling dynamics still needs to be addressed to move towards more realistic engine conditions. These topics are the focus of this work.

The reminder of this paper is organized by the following way. The second section discusses the derivation of an Eulerian-Eulerian model, within the framework of laminar two-phase flows composed of an evaporating polydisperse spray and a compressible gas. The correct behavior of the energy partition in the spray phase for the turbulence modeling requires taking into account the granular temperature effect (also called uncorrelated motion), as highlighted first in [59]. This accounts for considering a poly-kinetic velocity distribution at the kinetic level. Based on this idea, first the original monokinetic EMSM model is extended to poly-kinetic in the context of laminar flow, through a transport equation for the granular temperature. The gas phase is modeled with the compressible Navier-Stokes equation. The third section is devoted to a new Reynolds-averaged (RA) turbulence model derived from the two-phase model presented in the second section. This is based on the same philosophy introduced in [64] for two-way coupled monodisperse flows. Here, one must deal with new terms and equations that arise due to size moment equations of the polydisperse evaporating spray and the gas-phase internal energy equation. To overcome this bottleneck, new closure models are provided and discussed. The fourth section is dedicated to homogeneous test cases. First, the new model is qualitatively validated as compared to the test case of [59] for one-way coupling and then the extension to two-way coupling is studied for both evaporating and non-evaporating sprays. Next, the model is investigated under the conditions typical of high-pressure direct injection in ICE applications. Finally, some relevant conclusions along with several insights on future

work are discussed in section five.

6.2 Modeling approach

A cloud of droplets undergoing Brownian motion (i.e., a spray) can be described using the statistical formalism originally proposed by [193] for combustion and atomization applications. This formalism is appropriate for the disperse-flow regime where inertial forces, leading to a nonzero relative velocity between a droplet and the gas, are not very large compared to droplet surface-tension forces, characterized by a small Weber number $\mathsf{We} < 12$, and is appropriate for dilute sprays, which have a large droplet mean free path with respect to the characteristic length of the flow (i.e., Knudsen number $\mathrm{Kn} > 0.1$). In this context, droplets can be assumed to be roughly spherical, and their number concentration can be described using a number density function (NDF). The NDF f is defined such that $f(t, \boldsymbol{x}, \boldsymbol{u}, S, T)\mathrm{d}\boldsymbol{x}\mathrm{d}\boldsymbol{u}\mathrm{d}S\mathrm{d}T$ represents the number of droplets residing in the small volume $[\boldsymbol{x}, \boldsymbol{x} + \mathrm{d}\boldsymbol{x}]$ having velocities between $[\boldsymbol{u}, \boldsymbol{u} + \mathrm{d}\boldsymbol{u}]$, sizes (i.e., surface area) between $[S, S + \mathrm{d}S]$, and temperatures between $[T, T + \mathrm{d}T]$ at time t. The evolution equation for the NDF, first introduced in [194], is

$$\partial_t f + \nabla_{\boldsymbol{x}} \cdot (\boldsymbol{u} f) - \partial_S \left(R_S f\right) + \nabla_{\boldsymbol{u}} \cdot (\boldsymbol{F} f) = 0 \tag{6.1}$$

where $\boldsymbol{F}$ is the drag force per unit mass, and $R_S \geq 0$ is the drift velocity due to evaporation. In this work, the spray is assumed to be collisionless at the far downstream of the injector since the spray volume fraction is very small $\Phi_{\mathsf{v}} < 10^{-3}$. Moreover, the assumption of a d^2-evaporation law makes the heat-exchange term negligible. Therefore Eq. (6.1) contains no additional terms (e.g., for coalescence or heat transfer). For the sake of simplicity, the drag term is assumed to obey Stokes law:

$$\boldsymbol{F} = \frac{1}{\tau_d}\left(\boldsymbol{u_g} - \boldsymbol{u}\right) \quad \text{with} \quad \tau_d = \frac{\rho_d S}{18\pi\mu_g} \tag{6.2}$$

where τ_d is the dynamic time scale associated with droplets of size S, $\boldsymbol{u_g}$ is the gas velocity seen by droplets, ρ_d is the material density of the fuel droplets, which is assumed constant, and μ_g is the gas dynamic viscosity.

As in [94], an assumption on the form of f for closure at the kinetic level must be made. Here we assume, as done in [116, 150] , that the velocity dispersion around the mean velocity $\boldsymbol{u_d}$ is independent of size such that f takes the following form:

$$f\left(t, \boldsymbol{x}, S, \boldsymbol{u}\right) = n\left(t, \boldsymbol{x}, S\right)\phi\left(\boldsymbol{u} - \boldsymbol{u_d}\left(t, \boldsymbol{x}\right)\right) \tag{6.3}$$

where ϕ is an isotropic Gaussian distribution:

$$\phi(\boldsymbol{u}) = \frac{1}{\left(4\pi\Theta/3\right)^{3/2}} \exp\left(-\frac{3\boldsymbol{u}^2}{4\Theta}\right). \tag{6.4}$$

The macroscopic variable $\Theta(t, \boldsymbol{x})$, which describes isotropic velocity dispersion due to the nonzero Stokes number of the droplets, is expressed as a function of the droplet velocity as

$$\Theta = \frac{1}{2}\int \boldsymbol{u}^2 \phi\left(\boldsymbol{u}\right) d\boldsymbol{u}. \tag{6.5}$$

We refer to Θ as the granular temperature of the droplets. In the framework of the moment approach, semi-kinetic equations are derived, integrating the moments of the NDF over droplet velocity phase space. Taking velocity moments of order 0, 1 and 2 of Eq. (6.1), the following system is obtained:

$$\partial_t n + \nabla_{\boldsymbol{x}} \cdot n\boldsymbol{u_d} = R_S \partial_S n, \tag{6.6a}$$

$$\partial_t n\boldsymbol{u_d} + \nabla_{\boldsymbol{x}} \cdot n\left(\boldsymbol{u_d} \otimes \boldsymbol{u_d} + P_d I\right) = n\frac{\boldsymbol{u_g} - \boldsymbol{u_d}}{\tau_d} + R_S \partial_S n\boldsymbol{u_d}, \tag{6.6b}$$

$$\partial_t n\left(\frac{\boldsymbol{u_d}^2}{2} + \Theta\right) + \nabla_{\boldsymbol{x}} \cdot n\boldsymbol{u_d}\left(\frac{\boldsymbol{u_d}^2}{2} + \Theta + P_d\right) = n\frac{\boldsymbol{u_g} \cdot \boldsymbol{u_d} - 2\Theta - \boldsymbol{u_d}^2}{\tau_d} + R_S \partial_S n\left(\frac{\boldsymbol{u_d}^2}{2} + \Theta\right). \tag{6.6c}$$

The pressure tensor $P_d I$ is a second-order isotropic tensor, which is related to Θ by

$$P_d = \frac{2}{3}\Theta \tag{6.7}$$

where the value of Θ is found from Eq. (6.6c).

System (6.6) still contains terms that are functions of the size phase space variable S. To retain information on the size distribution, we follow the classic approach of moment methods and establish conservation equations for the macroscopic quantities defined as

$$m_k = \int S^k n(t, \boldsymbol{x}, S) dS \quad \text{for } 0 \leq k \leq 3 \tag{6.8}$$

where k is an integer and m_k denotes moments of order k of the size distribution. Through successive integrations in S^k of Eq. (6.6a) and in S of Eq. (6.6b), we can obtain conservation equations for a polydisperse spray [83]. Note that the term Θ can be closed by integrating in S over Eq. (6.6c). The final spray governing equations are given by

$$\partial_t m_0 + \nabla_{\boldsymbol{x}} \cdot m_0\boldsymbol{u_d} = R_S n(t, \boldsymbol{x}, S = 0), \tag{6.9a}$$

$$\partial_t m_1 + \nabla_{\boldsymbol{x}} \cdot m_1\boldsymbol{u_d} = \mathcal{M}, \tag{6.9b}$$

$$\partial_t m_2 + \nabla_{\boldsymbol{x}} \cdot m_2\boldsymbol{u_d} = -2R_S m_1, \tag{6.9c}$$

$$\partial_t m_3 + \nabla_{\boldsymbol{x}} \cdot m_3\boldsymbol{u_d} = -3R_S m_2, \tag{6.9d}$$

$$\partial_t m_1\boldsymbol{u_d} + \nabla_{\boldsymbol{x}} \cdot \left(m_1\boldsymbol{u_d}^2 + m_1 P_d I\right) = \boldsymbol{\mathcal{A}} + \mathcal{M}\boldsymbol{u_d}, \tag{6.9e}$$

$$\partial_t m_1 E + \nabla_{\boldsymbol{x}} \cdot \left(m_1\boldsymbol{u_d}E + m_1 P_d\boldsymbol{u_d}\right) = \mathcal{E} + \mathcal{M}E \tag{6.9f}$$

where total energy and the source terms on the right-hand side are defined by

$$E = \frac{\boldsymbol{u_d}^2}{2} + \Theta, \tag{6.10a}$$

$$\mathcal{M} = -R_S m_0, \tag{6.10b}$$

$$\boldsymbol{\mathcal{A}} = m_0\frac{\boldsymbol{u_g} - \boldsymbol{u_d}}{\tau_d^*}, \tag{6.10c}$$

$$\mathcal{E} = m_0\frac{\boldsymbol{u_g} \cdot \boldsymbol{u_d} - 2E}{\tau_d^*}. \tag{6.10d}$$

where $\tau_d^* = \tau_d/S$. Remark that Eq. (6.9f) represents the total energy including both the kinetic energy and the granular temperature contributions. Also remark that a separate equation for the granular temperature can be obtained after manipulating system (6.9):

$$\partial_t m_1 \Theta + \nabla_{\boldsymbol{x}} \cdot m_1 \boldsymbol{u_d} \Theta + m_1 P_d \nabla_{\boldsymbol{x}} \cdot \boldsymbol{u_d} = \mathcal{U} + \mathcal{M}\Theta \tag{6.11}$$

with

$$\mathcal{U} = -\frac{2\Theta m_0}{\tau_d^*}. \tag{6.12}$$

In any case, system (6.9) represents a closed mesoscale description of the fuel spray that is coupled to governing equations for the gas phase.

Let us recall that assuming $\Theta = 0$ in system (6.9) yields the conservation equations for the classical monokinetic EMSM model [83] with a single unclosed term $n(S = 0)$ in Eq. (6.9a). This flux term represents the disappearance of droplets due to evaporation. For an accurate evaluation of this flux, a continuous representation of $n(S)$ must be found from data for the integer moments. Reconstructing this profile requires solving the finite Hausdorff moment problem on the interval $[0, 1]$, i.e., finding a positive NDF n belonging to the moment sequence $(m_0, \ldots, m_k)^t$ [38]. The existence of such an NDF is called the realizability condition. Otherwise the moments of the NDF are said to be corrupted leading to the immediate crash of the simulation. Although the set of all possible moments, called moment space, has a complex geometry in $\mathbb{R}^N$, a solution of this problem, preserving the moment space, has been developed in [120]. This solution is based on reconstructing the NDF $\tilde{n}(m_0, \ldots, m_k, S)$ using entropy maximisation of the moment sequence $(m_0, \ldots, m_k)^t$ and an associated numerical scheme for the evaporation. Using this method, Eq. (6.9a) is closed and the evaporative flux of a polydisperse spray can be evaluated using a kinetic scheme that preserves the moment space.

The description of the gas phase in the context of compressible, multi-species reactive flows is given by the classical Navier-Stokes conservation equations for mass, species, momentum and total energy [140]:

$$\partial_t \rho_g + \nabla_{\boldsymbol{x}} \cdot \rho_g \boldsymbol{u_g} = \mathfrak{S}^{\rho} \tag{6.13a}$$

$$\partial_t \rho_g \boldsymbol{u_g} + \nabla_{\boldsymbol{x}} \cdot (\rho_g \boldsymbol{u_g} \otimes \boldsymbol{u_g} + P_g I) = \nabla_{\boldsymbol{x}} \cdot \rho_g \boldsymbol{\tau} + \mathfrak{S}^{\rho \boldsymbol{u}} \tag{6.13b}$$

$$\partial_t \rho_g E_g + \nabla_{\boldsymbol{x}} \cdot (\rho_g E_g \boldsymbol{u_g} + P_g \boldsymbol{u_g}) = \nabla_{\boldsymbol{x}} \cdot \rho_g \boldsymbol{\tau} \cdot \boldsymbol{u_g} - \nabla_{\boldsymbol{x}} \cdot \mathbf{q} + \mathfrak{S}^{\rho E} \tag{6.13c}$$

where ρ_g is the gas density, E_g the total energy of the gas, P_g the gas pressure, $\boldsymbol{\tau}$ the gas viscous-stress tensor, and $\mathbf{q}$ the energy flux. System (6.13) is closed using the equation of state for an ideal gas:

$$P_g = \rho_g R T_g. \tag{6.14}$$

The viscous-stess tensor is closed in the context of the Navier-Stokes equation for Newtonian fluids using

$$\boldsymbol{\tau} = \nu_g \left[\nabla_{\boldsymbol{x}} \boldsymbol{u_g} + (\nabla_{\boldsymbol{x}} \boldsymbol{u_g})^t \right] - \frac{2}{3} \nu_g \left(\nabla_{\boldsymbol{x}} \cdot \boldsymbol{u_g} \right) I \tag{6.15}$$

where ν_g is the kinematic viscosity of the gas. The energy flux is given by

$$\mathbf{q} = \lambda_g \nabla_{\boldsymbol{x}} T_g + \rho_g \sum_{k=1}^{n_s} h_k D_k \nabla_{\boldsymbol{x}} Y_k \tag{6.16}$$

where n_s is the number of chemical species, λ_g the thermal conductivity, h_k the specific enthalpy associated with species k, and D_k the gas mass diffusion coefficient. The internal energy evolution of the gas is governed by

$$\partial_t \rho_g e_g + \nabla_{\boldsymbol{x}} \cdot \rho_g e_g \boldsymbol{u_g} = -P_g \nabla_{\boldsymbol{x}} \cdot \boldsymbol{u_g} + \rho_g \boldsymbol{\tau} : \nabla_{\boldsymbol{x}} \boldsymbol{u_g} - \nabla_{\boldsymbol{x}} \cdot \mathbf{q} + \mathfrak{S}^{\rho e} \tag{6.17}$$

where $e_g = E_g - \frac{1}{2}\boldsymbol{u_g}^2$ is the internal energy of the gas. In the literature, the tensor $\boldsymbol{\tau}$ is shown to contain the gas velocity fluctuations due to droplet wakes leading to a pseudo-turbulent kinematic viscosity [176]. However, we assume the latter to be null in this work since we deal with a linear Stokes drag law that does not take into account wakes created by droplets. This assumption is appropriate for small droplets and is consistent with our treatment of velocity dispersion.

System (6.13) and Eq. (6.17) are written in the framework of a two-phase flow in the presence of a cloud of droplets. The disperse phase is assumed to be dilute enough such that its influence on the gas phase can be described by source terms in the gas-phase governing equations. Indeed, the kinetic model in Eq. (6.1) provides these source terms, which represent the variation of mass density due to evaporation, variation of momentum of the spray due to evaporation and the drag force, and the variation of the total/internal energy due to spray evaporation with uniform droplet temperature. These source terms are given, respectively, by

$$\mathfrak{S}^{\rho} = \frac{3}{2} R_S m_{1/2}, \tag{6.18a}$$

$$\mathfrak{S}^{\rho \boldsymbol{u}} = -m_{1/2} \frac{\boldsymbol{u_g} - \boldsymbol{u_d}}{\tau_d^*} + \frac{3}{2} R_S m_{1/2} \boldsymbol{u_d}, \tag{6.18b}$$

$$\mathfrak{S}^{\rho E} = -m_{1/2} \frac{\boldsymbol{u_g} \cdot \boldsymbol{u_d} - 2E}{\tau_d^*} + \frac{3}{2} R_S m_{1/2} E, \tag{6.18c}$$

from which (using Eqs. (6.13a) and (6.13b)) the internal energy source term is found to be

$$\mathfrak{S}^{\rho e} = \left(\frac{2}{\tau_d^*} + \frac{3}{2} R_S \right) m_{1/2} \Theta_g \tag{6.19}$$

where the gas-phase velocity dispersion is defined by

$$\Theta_g = \frac{1}{2} \left(\boldsymbol{u_d} - \boldsymbol{u_g} \right)^2 + \Theta. \tag{6.20}$$

Note that $\mathfrak{S}^{\rho e} \geq 0$ so that internal energy is transferred from the droplet phase to the gas phase due both to a nonzero relative velocity and to velocity dispersion. Once in the gas phase, this internal energy contributes directly to increasing the gas temperature, as opposed to generating gas-phase turbulent kinetic energy (TKE).

Systems (6.9) and (6.13), along with the coupling terms in (6.18), provide a complete mesoscale description of the two-phase flow. In practice, the solution to these systems under ICE conditions will be highly turbulent and thus the computational cost of solving the mesoscale model will be very high. Therefore, to make the model tractable for realistic ICE conditions, it will be necessary to introduce a turbulence model, which is the topic of the next section.

6.3 Turbulence models for spray and gas phases

The aim of this section is to apply the Reynolds-averaging (RA) philosophy, originally introduced for the two-way coupled monodisperse flow in [64], to the two-way coupled polydisperse flow [84]. The exact derivation of RA transport equations both for the compressible Navier-Stokes equation and the moment equations will be given below. As done in [64], let us define the following RA and phase-average (PA) quantities appearing in the RA equations.

- RA moments: $\langle m_0 \rangle, \langle m_1 \rangle, \langle m_2 \rangle, \langle m_3 \rangle$.
- RA number of disappearing droplets: $\langle n(t, \boldsymbol{x}, 0) \rangle$.
- PA velocities: $\langle m_1 \boldsymbol{u_d} \rangle = \langle m_1 \rangle \langle \boldsymbol{u_d} \rangle_d$ and $\langle \rho_g \boldsymbol{u_g} \rangle = \langle \rho_g \rangle \langle \boldsymbol{u_g} \rangle_g$.
- Spray-phase PA granular temperature: $\langle m_1 \Theta \rangle = \langle m_1 \rangle \langle \Theta \rangle_d$.
- Gas-phase PA internal energy: $\langle \rho_g e_g \rangle = \langle \rho_g \rangle \langle e_g \rangle_g$.
- Spray-phase PA Reynolds-stress tensor: $\langle m_1 \boldsymbol{u_d}'' \boldsymbol{u_d}'' \rangle = \langle m_1 \rangle \langle \boldsymbol{u_d}'' \boldsymbol{u_d}'' \rangle_d$.
- Gas-phase PA Reynolds-stress tensor: $\langle \rho_g \boldsymbol{u_g}''' \boldsymbol{u_g}''' \rangle = \langle \rho_g \rangle \langle \boldsymbol{u_g}''' \boldsymbol{u_g}''' \rangle_g$.
- Spray-phase PA total granular energy:

$$\langle m_1 E \rangle_d = \langle m_1 \rangle \langle E \rangle_d = \langle m_1 \rangle \left(\frac{1}{2} \langle \boldsymbol{u_d} \cdot \boldsymbol{u_d} \rangle_d + \langle \Theta \rangle_d \right) = \langle m_1 \rangle \left(K + k_d + \langle \Theta \rangle_d \right) \quad (6.21)$$

  with $K = \frac{1}{2} \langle \boldsymbol{u_d} \rangle_d \cdot \langle \boldsymbol{u_d} \rangle_d$ the mean kinetic energy and $k_d = \frac{1}{2} \langle \boldsymbol{u_d}'' \cdot \boldsymbol{u_d}'' \rangle_d$ the spray-phase TKE.

- Gas-phase PA total energy:

$$\langle \rho_g E_g \rangle = \langle \rho_g \rangle \langle E_g \rangle_g = \langle \rho_g \rangle \left(\frac{1}{2} \langle \boldsymbol{u_g} \cdot \boldsymbol{u_g} \rangle_g + \langle e_g \rangle_g \right) = \langle \rho_g \rangle \left(K_g + k_g + \langle e_g \rangle_g \right) \quad (6.22)$$

  with $K_g = \frac{1}{2} \langle \boldsymbol{u_g} \rangle_g \cdot \langle \boldsymbol{u_g} \rangle_g$ the mean kinetic energy and $k_g = \frac{1}{2} \langle \boldsymbol{u_g}''' \cdot \boldsymbol{u_g}''' \rangle_g$ the gas-phase TKE.

The next step is consider the RA versions of systems (6.9) and (6.13) with appropriate turbulence closures.

6.3.1 Reynolds-average equations for the spray

6.3.1.1 RA moment equations

The RA moment equations are found by applying the RA to Eqs. (6.9a), (6.9b), (6.9c) and (6.9d). Let us state at the outset that the modeling of physical phenomena related

to turbulent diffusive fluxes coming from size-velocity correlations is beyond the scope of this work. Thus, we assume that the following relation holds for the size moments:

$$\frac{\langle m_k' A\rangle}{\langle m_k\rangle} = \frac{\langle m_1' A\rangle}{\langle m_1\rangle} \tag{6.23}$$

with A is any random quantity belonging to either the gas or spray phase. In words, this assumption means that whatever the index k, the correlation can expressed in terms of m_1. This assumption implies that the size-velocity correlations leading to turbulent diffusive fluxes appearing in the RA moment equations (see Eq. (B.11) in the appendix) are null. Therefore, the RA moment equations reduce to

$$\partial_t \langle m_0\rangle + \nabla_{\boldsymbol{x}} \cdot \langle m_0\rangle \langle \boldsymbol{u_d}\rangle_d = R_S \langle n(t,\boldsymbol{x},0)\rangle\,, \tag{6.24a}$$
$$\partial_t \langle m_1\rangle + \nabla_{\boldsymbol{x}} \cdot \langle m_1\rangle \langle \boldsymbol{u_d}\rangle_d = \langle \mathcal{M}\rangle\,, \tag{6.24b}$$
$$\partial_t \langle m_2\rangle + \nabla_{\boldsymbol{x}} \cdot \langle m_2\rangle \langle \boldsymbol{u_d}\rangle_d = -2R_S \langle m_1\rangle\,, \tag{6.24c}$$
$$\partial_t \langle m_3\rangle + \nabla_{\boldsymbol{x}} \cdot \langle m_3\rangle \langle \boldsymbol{u_d}\rangle_d = -3R_S \langle m_2\rangle\,, \tag{6.24d}$$

and thus the spatial fluxes of the RA moments depend only on the spray-phase PA velocity $\langle \boldsymbol{u_d}\rangle_d$.

6.3.1.2 Spray-phase mean momentum equation

Taking the RA of (6.9e) yields

$$\partial_t \langle m_1\rangle \langle \boldsymbol{u_d}\rangle_d + \nabla_{\boldsymbol{x}} \cdot \langle m_1\rangle \left(\langle \boldsymbol{u_d}\rangle_d \otimes \langle \boldsymbol{u_d}\rangle_d + \langle \boldsymbol{u_d}''\boldsymbol{u_d}''\rangle_d + \frac{2}{3}\langle\Theta\rangle_d I \right) = \langle \boldsymbol{\mathcal{A}}\rangle + \langle \mathcal{M}\boldsymbol{u_d}\rangle\,. \tag{6.25}$$

The spray-phase Reynolds-stress tensor is closed using a turbulent-viscosity model:

$$\langle \boldsymbol{u_d}''\boldsymbol{u_d}''\rangle_d = -2\nu_{d,t}\left(S_d - \frac{1}{3}\nabla_{\boldsymbol{x}} \cdot \langle \boldsymbol{u_d}\rangle_d I \right) + \frac{2}{3}k_d I \tag{6.26}$$

where

$$S_d = \frac{1}{2}\left[\nabla_{\boldsymbol{x}} \langle \boldsymbol{u_d}\rangle_d + (\nabla_{\boldsymbol{x}} \langle \boldsymbol{u_d}\rangle_d)^t\right]. \tag{6.27}$$

For later use, we also define

$$\bar{S}_d = S_d - \frac{1}{3}\nabla_{\boldsymbol{x}} \cdot \langle \boldsymbol{u_d}\rangle_d I. \tag{6.28}$$

The turbulent viscosity of the spray phase is defined by

$$\nu_{d,t} = C_{d,\mu}\frac{k_d^2}{\varepsilon_d}. \tag{6.29}$$

Models for the spray-phase TKE k_d and TKE dissipation rate ε_d will be described below.

The full expression for the source terms on the right-hand side of Eq. (6.25) is given in Eqs. (B.13) and (B.14). Note that correlations containing the turbulent drag term $(1/\tau_d^*)'$

can be neglected in the framework of Stokes drag with a small relative velocity between the phases. Moreover, the use of the model in (6.23) reduces the RA momentum source terms to the following expressions:

$$\langle \boldsymbol{\mathcal{A}} \rangle = \langle m_0 \rangle \left\langle \frac{1}{\tau_d^*} \right\rangle \left(\langle \boldsymbol{u_g} \rangle_g - \langle \boldsymbol{u_d} \rangle_d + \frac{\langle m_1' \boldsymbol{u_g}' \rangle}{\langle m_1 \rangle} - \frac{\langle \rho_g' \boldsymbol{u_g}' \rangle}{\langle \rho_g \rangle} \right) \tag{6.30}$$

and

$$\langle \mathcal{M} \boldsymbol{u_d} \rangle = -R_S \langle m_0 \rangle \langle \boldsymbol{u_d} \rangle_d . \tag{6.31}$$

Remark that further simplifications can be introduced to reduce the number of unclosed correlations in (6.30). The term $\langle \rho_g' \boldsymbol{u_g}' \rangle / \langle \rho_g \rangle$, referred to as the turbulent gas density flux, can be rewritten by adopting the low-Mach-number flow approximation, i.e., neglecting correlations between the compressibility and the turbulence in the gas phase:

$$\frac{\langle \alpha_d' \boldsymbol{u_g}' \rangle}{\langle 1 - \alpha_d \rangle} = -\frac{\langle \rho_g' \boldsymbol{u_g}' \rangle}{\langle \rho_g \rangle}. \tag{6.32}$$

Combining relations (6.30) and (6.32), replacing m_1 by the moment of order 3/2 through expression (6.23) to get the spray volume fraction α_d, the following relation results

$$\frac{\langle m_1' \boldsymbol{u_g}' \rangle}{\langle m_1 \rangle} - \frac{\langle \rho_g' \boldsymbol{u_g}' \rangle}{\langle \rho_g \rangle} = \frac{\langle \alpha_d' \boldsymbol{u_g}' \rangle}{\langle 1 - \alpha_d \rangle \langle \alpha_d \rangle}. \tag{6.33}$$

The term $\langle \alpha_d' \boldsymbol{u_g}' \rangle$, referred to as the turbulent drift due to preferential segregation of droplets, can be closed through a turbulent-flux model:

$$\langle \alpha_d' \boldsymbol{u_g}' \rangle = -\frac{\nu_{g,t}}{\mathrm{Sc}_{g,d}} \nabla_{\boldsymbol{x}} \langle \alpha_d \rangle + C_g \langle \alpha_d \rangle \langle 1 - \alpha_d \rangle \left(\langle \boldsymbol{u_d} \rangle_d - \langle \boldsymbol{u_g} \rangle_g \right) \tag{6.34}$$

where $\nu_{g,t}$ is the turbulent viscosity of the gas, defined by

$$\nu_{g,t} = C_{g,\mu} \frac{k_g^2}{\varepsilon_g}, \tag{6.35}$$

and $\mathrm{Sc}_{g,d}$ the turbulent Schmidt number of the spray in the presence of the gas phase, taken as a constant in the case of small droplets but depending on the Stokes number for inertia droplets. Models for the gas-phase TKE k_g and TKE dissipation rate ε_g will be described below. Equation (6.30) can then be rewritten in closed form as

$$\langle \boldsymbol{\mathcal{A}} \rangle = \langle m_0 \rangle \left\langle \frac{1}{\tau_d^*} \right\rangle \left(\langle \boldsymbol{u_g} \rangle_g - \langle \boldsymbol{u_d} \rangle_d + \boldsymbol{u}_c \right) \tag{6.36}$$

where the drift velocity is defined by

$$\boldsymbol{u}_c = C_g \left(\langle \boldsymbol{u_d} \rangle_d - \langle \boldsymbol{u_g} \rangle_g \right) - \frac{\nu_{g,t} \nabla_{\boldsymbol{x}} \langle \alpha_d \rangle}{\mathrm{Sc}_{g,d} \langle \alpha_d \rangle \langle 1 - \alpha_d \rangle}. \tag{6.37}$$

Note that since $0 \leq C_g < 1$, the mean drag is lower due to preferential concentration in a turbulent flow.

The final form for the RA spray momentum equation is

$$\partial_t \langle m_1 \rangle \langle \boldsymbol{u_d} \rangle_d + \nabla_{\boldsymbol{x}} \cdot \langle m_1 \rangle \left[\langle \boldsymbol{u_d} \rangle_d \otimes \langle \boldsymbol{u_d} \rangle_d - 2\nu_{d,t} \bar{S}_d + \frac{2}{3} \left(k_d + \langle \Theta \rangle_d \right) I \right] = \langle m_0 \rangle \left\langle \frac{1}{\tau_d^*} \right\rangle \left(\langle \boldsymbol{u_g} \rangle_g - \langle \boldsymbol{u_d} \rangle_d + \boldsymbol{u}_c \right) - R_S \langle m_0 \rangle \langle \boldsymbol{u_d} \rangle_d \quad (6.38)$$

where we have used the equality $\langle P_d \rangle_d = 2 \langle \Theta \rangle_d / 3$. Note that turbulence introduces the diffusive flux with coefficient $\nu_{d,t}$ on the left-hand side, and modifies the momentum exchange terms of the right-hand side of Eq. (6.38). Likewise, in a turbulent flow, the total effective pressure in the droplet phase is proportional to $(\langle \Theta \rangle_d + k_d)$.

6.3.1.3 Spray-phase granular temperature equation

The RA granular temperature equation is

$$\partial_t \langle m_1 \rangle \langle \Theta \rangle_d + \nabla_{\boldsymbol{x}} \cdot \langle m_1 \rangle \left(\langle \Theta \rangle_d \langle \boldsymbol{u_d} \rangle_d + \langle \Theta'' \boldsymbol{u_d}'' \rangle_d \right) = - \langle m_1 \rangle \frac{2}{3} \langle \Theta \rangle_d \nabla_{\boldsymbol{x}} \cdot \langle \boldsymbol{u_d} \rangle_d - \langle m_1 \rangle \langle P_d \nabla_{\boldsymbol{x}} \cdot \boldsymbol{u_d}'' \rangle_d + S^{\Theta}. \quad (6.39)$$

where the source term is given by

$$S^{\Theta} = \langle \mathcal{U} \rangle + \langle \mathcal{M}\Theta \rangle . \quad (6.40)$$

The term $\langle P_d \nabla_{\boldsymbol{x}} \cdot \boldsymbol{u_d}'' \rangle_d$, which corresponds to the spray TKE dissipation, leads to

$$\langle P_d \nabla_{\boldsymbol{x}} \cdot \boldsymbol{u_d}'' \rangle_d = -\varepsilon_d \quad (6.41)$$

where ε_d is the spray-phase TKE dissipation rate. Following the modeling considerations introduced above, the source term for the granular temperature S^{Θ} becomes

$$\langle \mathcal{U} \rangle = -2 \langle m_0 \rangle \left\langle \frac{1}{\tau_d^*} \right\rangle \langle \Theta \rangle_d \quad (6.42)$$

and

$$\langle \mathcal{M}\Theta \rangle = -R_S \langle m_0 \rangle \langle \Theta \rangle_d . \quad (6.43)$$

The term $\langle \Theta'' \boldsymbol{u_d}'' \rangle_d$ in Eq. (6.39) is the turbulent granular-temperature flux. Its closure can be achieved using a gradient-diffusion model:

$$\langle \Theta'' \boldsymbol{u_d}'' \rangle_d = -\frac{\nu_{d,t}}{\mathrm{Pr}_{d,t}} \nabla_{\boldsymbol{x}} \langle \Theta \rangle_d \quad (6.44)$$

where $\mathrm{Pr}_{d,t}$ is the turbulent Prandtl number.

The first term on the right-hand side of (6.39) is the production term due to mean velocity gradients whereas the second term is the production term coming from TKE dissipation. The final equation for the granular temperature is

$$\partial_t \langle m_1 \rangle \langle \Theta \rangle_d + \nabla_{\boldsymbol{x}} \cdot \langle m_1 \rangle \left(\langle \Theta \rangle_d \langle \boldsymbol{u_d} \rangle_d - \frac{\nu_{d,t}}{\mathrm{Pr}_{d,t}} \nabla_{\boldsymbol{x}} \langle \Theta \rangle_d \right) = - \langle m_1 \rangle \frac{2}{3} \langle \Theta \rangle_d \nabla_{\boldsymbol{x}} \cdot \langle \boldsymbol{u_d} \rangle_d + \langle m_1 \rangle \varepsilon_d - 2 \langle m_0 \rangle \left\langle \frac{1}{\tau_d^*} \right\rangle \langle \Theta \rangle_d - R_S \langle m_0 \rangle \langle \Theta \rangle_d . \quad (6.45)$$

Note that in a turbulent flow the principal production term for PA granular temperature is the one involving ε_d, which increases with increasing Reynolds number.

6.3.1.4 Spray-phase total granular energy equation

The RA total granular equation found from (6.9f) is

$$\partial_t \langle m_1 \rangle \langle E \rangle_d + \nabla_{\boldsymbol{x}} \cdot \langle m_1 \rangle \left(\langle E \rangle_d \langle \boldsymbol{u_d} \rangle_d + \langle E \boldsymbol{u_d}'' \rangle_d + \frac{2}{3} \langle \Theta \rangle_d \langle \boldsymbol{u_d} \rangle_d \right) = - \nabla_{\boldsymbol{x}} \cdot \langle m_1 \rangle \frac{2}{3} \langle \Theta \boldsymbol{u_d}'' \rangle_d + \left\langle S^E \right\rangle \tag{6.46}$$

where $\left\langle S^E \right\rangle$ is the RA source term. There are several unclosed term in this expression, such as the turbulent total granular energy flux $\langle E \boldsymbol{u_d}'' \rangle_d$. Note that using the properties of PA, this term can be rewritten as

$$\langle E \boldsymbol{u_d}'' \rangle_d = \langle \boldsymbol{u_d}'' \boldsymbol{u_d}'' \rangle_d \cdot \langle \boldsymbol{u_d} \rangle_d + \frac{1}{2} \langle \boldsymbol{u_d}'' \boldsymbol{u_d}'' \cdot \boldsymbol{u_d}'' \rangle_d + \langle \Theta'' \boldsymbol{u_d}'' \rangle_d . \tag{6.47}$$

Terms $\langle \boldsymbol{u_d}'' \boldsymbol{u_d}'' \cdot \boldsymbol{u_d}'' \rangle_d$ and $\langle \Theta \boldsymbol{u_d}'' \rangle_d$ together account for the spray-phase energy flux whose closure model needs to be consistent with the spray-phase Reynolds-stress tensor:

$$\frac{1}{2} \langle \boldsymbol{u_d}'' \boldsymbol{u_d}'' \cdot \boldsymbol{u_d}'' \rangle_d + \frac{2}{3} \langle \Theta \boldsymbol{u_d}'' \rangle_d = - \frac{\nu_{d,t}}{\sigma_{d,t}} \nabla_{\boldsymbol{x}} k_d - \frac{2 \nu_{d,t}}{3 \mathrm{Pr}_{d,t}} \nabla_{\boldsymbol{x}} \langle \Theta \rangle_d \tag{6.48}$$

where $\sigma_{d,t} = 5/3$ is a model constant (Rumsey 2009).

The source term contributions due to drag and evaporation on the right-hand side of Eq. (6.46) lead to

$$\left\langle S^E \right\rangle = \langle m_0 \rangle \left\langle \frac{1}{\tau_d^*} \right\rangle \left(\langle \boldsymbol{u_g}''' \cdot \boldsymbol{u_d}'' \rangle_d - 2 k_d \right) + \langle \mathcal{U} \rangle + \langle \boldsymbol{\mathcal{A}} \rangle \cdot \langle \boldsymbol{u_d} \rangle_d - R_S \langle m_0 \rangle (K + k_d) + \langle \mathcal{M} \Theta \rangle . \tag{6.49}$$

The covariance term $\langle \boldsymbol{u_g}''' \cdot \boldsymbol{u_d}'' \rangle_d$ appearing in the drag term is important for capturing the TKE exchange between phases. In the case of point particles, Fox [64] proposes the following model (in agreement with the DNS of Fevrier et al. [59]):

$$\langle \boldsymbol{u_g}''' \cdot \boldsymbol{u_d}'' \rangle_d = 2 \beta (\mathsf{St}) (k_g k_d)^{1/2} \tag{6.50}$$

where $\beta \approx 1$ in the case of low to moderate Stokes number droplets.

The final RA total granular energy equation is

$$\begin{aligned} \partial_t \langle m_1 \rangle \langle E \rangle_d + \nabla_{\boldsymbol{x}} \cdot \langle m_1 \rangle \left[\langle E \rangle_d \langle \boldsymbol{u_d} \rangle_d + \frac{2}{3} \left(\langle \Theta \rangle_d + k_d \right) \langle \boldsymbol{u_d} \rangle_d - \langle \boldsymbol{u_d} \rangle_d \cdot 2 \nu_{d,t} \bar{S}_d \right] = \\ \nabla_{\boldsymbol{x}} \cdot \langle m_1 \rangle \left(\frac{5 \nu_{d,t}}{3 \mathrm{Pr}_{d,t}} \nabla_{\boldsymbol{x}} \langle \Theta \rangle_d + \frac{\nu_{d,t}}{\sigma_{d,t}} \nabla_{\boldsymbol{x}} k_d \right) - R_S \langle m_0 \rangle \left(K + k_d + \langle \Theta \rangle_d \right) \\ + \langle m_0 \rangle \left\langle \frac{2}{\tau_d^*} \right\rangle \left[\beta (k_g k_d)^{1/2} - k_d - \langle \Theta \rangle_d \right] + \langle m_0 \rangle \left\langle \frac{1}{\tau_d^*} \right\rangle \left(\langle \boldsymbol{u_g} \rangle_g - \langle \boldsymbol{u_d} \rangle_d + \boldsymbol{u}_c \right) \cdot \langle \boldsymbol{u_d} \rangle_d . \end{aligned} \tag{6.51}$$

Note that the TKE dissipation rate does not appear on the right-hand side of this expression because the total granular energy includes the sum of the TKE and the granular energy and the role of TKE dissipation rate is to transform spray-phase TKE into $\langle \Theta \rangle_d$.

6.3.1.5 Spray-phase mean kinetic energy

Multiplying Eq. (6.38) by the mean spray velocity $\langle \boldsymbol{u_d} \rangle_d$ gives rise to the following mean kinetic energy equation after some manupulations:

$$\partial_t \langle m_1 \rangle K + \nabla_{\boldsymbol{x}} \cdot \langle m_1 \rangle \left[K \langle \boldsymbol{u_d} \rangle_d + \frac{2}{3} \left(\langle \Theta \rangle_d + k_d \right) \langle \boldsymbol{u_d} \rangle_d - \langle \boldsymbol{u_d} \rangle_d \cdot 2\nu_{d,t} \bar{S}_d \right] = - \Pi^K - R_S \langle m_0 \rangle K + \langle m_0 \rangle \left\langle \frac{1}{\tau_d^*} \right\rangle \left(\langle \boldsymbol{u_g} \rangle_g - \langle \boldsymbol{u_d} \rangle_d + \boldsymbol{u}_c \right) \cdot \langle \boldsymbol{u_d} \rangle_d \quad (6.52)$$

where the spray-phase fluctuating energy production due to the mean spray velocity is defined by

$$\Pi^K = \langle m_1 \rangle \left[2\nu_{d,t} \bar{S}_d : \bar{S}_d - \frac{2}{3} \left(\langle \Theta \rangle_d + k_d \right) \nabla_{\boldsymbol{x}} \cdot \langle \boldsymbol{u_d} \rangle_d \right]. \quad (6.53)$$

Equation (6.52) can be used to find the transport equation for the spray-phase TKE.

6.3.1.6 Spray-phase fluctuating energy

As pointed out above, both the velocity dispersion and the uncorrelated motion of droplets contribute to the fluctuations around the mean velocity. The fluctuating energy is thus the sum of the spray-phase TKE and granular energy:

$$\kappa = \langle \Theta \rangle_d + k_d. \quad (6.54)$$

The expression for the fluctuating energy transport is straightforward. Subtracting (6.52) from (6.51) gives rise to the fluctuating energy equation:

$$\partial_t \langle m_1 \rangle \kappa + \nabla_{\boldsymbol{x}} \cdot \langle m_1 \rangle \left(\kappa \langle \boldsymbol{u_d} \rangle_d - \frac{5\nu_{d,t}}{3\mathrm{Pr}_{d,t}} \nabla_{\boldsymbol{x}} \langle \Theta \rangle_d - \frac{\nu_{d,t}}{\sigma_{d,t}} \nabla_{\boldsymbol{x}} k_d \right) = \Pi^K - R_S \langle m_0 \rangle \kappa + \langle m_0 \rangle \left\langle \frac{2}{\tau_d^*} \right\rangle \left[\beta \left(k_g k_d \right)^{1/2} - \kappa \right]. \quad (6.55)$$

The right-hand side of this expression has production due to the mean flow and exchange terms with the gas phase due to evaporation and drag.

6.3.1.7 Spray-phase turbulent kinetic energy

As noted above, the spray-phase fluctuating energy has two contributions. We therefore obtain the spray-phase TKE equation by subtracting (6.45) from (6.55):

$$\partial_t \langle m_1 \rangle k_d + \nabla_{\boldsymbol{x}} \cdot \langle m_1 \rangle k_d \left(\langle \boldsymbol{u_d} \rangle_d - \frac{\nu_{d,t}}{\sigma_{d,t}} \nabla_{\boldsymbol{x}} \ln k_d - \frac{\nu_{d,t}}{\mathrm{Pr}_{d,t}} M_d \nabla_{\boldsymbol{x}} \ln \langle \Theta \rangle_d \right) = \Pi_d^k - \langle m_1 \rangle \varepsilon_d - R_S \langle m_0 \rangle k_d + \langle m_0 \rangle \left\langle \frac{2}{\tau_d^*} \right\rangle \left[\beta \left(k_g k_d \right)^{1/2} - k_d \right] \quad (6.56)$$

where

$$M_d = \frac{2 \langle \Theta \rangle_d}{3k_d}, \quad (6.57)$$

and the spray-phase TKE production due to the mean spray velocity is

$$\Pi_d^k = \langle m_1 \rangle \left(2\nu_{d,t} \bar{S}_d : \bar{S}_d - \frac{2}{3} k_d \nabla_{\boldsymbol{x}} \cdot \langle \boldsymbol{u_d} \rangle_d \right). \tag{6.58}$$

Note that the spray-phase TKE dissipation rate now appears with the correct sign on the right-hand side of (6.56). The remaining terms represent exchanges with the gas phase due to evaporation and drag. As discussed in [64], there are no TKE production terms for the spray phase due to drag or evaporation. The ratio M_d will be small at high-Reynolds numbers for small-Stokes-number droplets, and can often be neglected.

6.3.1.8 Spray-phase turbulent kinetic energy dissipation

In the model for ε_d, empirical constants originated from DNS and experimental studies on classical single-phase flows need to be carefully modified in the case of two-phase flows. The reason is that the turbulence associated with each phase is produced at different integral scales. For example, the spray-phase TKE is not only produced by the gradient of the mean velocity but also through the coupling term $\langle \boldsymbol{u_g}''' \cdot \boldsymbol{u_d}'' \rangle_d$. This implies that the spray-phase TKE dissipation rate can be either higher or lower compared to the gas-phase turbulent scales. It is therefore important to choose reasonable values for the constants in the model for ε_d. By analogy with Eq. (6.56), we model the TKE dissipation using

$$\begin{aligned} &\partial_t \langle m_1 \rangle \varepsilon_d + \nabla_{\boldsymbol{x}} \cdot \langle m_1 \rangle \varepsilon_d \left(\langle \boldsymbol{u_d} \rangle_d - \frac{\nu_{d,t}}{\sigma_{d,\epsilon}} \nabla_{\boldsymbol{x}} \ln \varepsilon_d - \frac{\nu_{d,t}}{\mathrm{Pr}_{d,t}} M_d \nabla_{\boldsymbol{x}} \langle \Theta \rangle_d \right) = \\ &C_{d,\epsilon}^1 \frac{\varepsilon_d}{k_d} \Pi_d^k - C_{d,\epsilon}^2 \langle m_1 \rangle \frac{\varepsilon_d^2}{k_d} - C_{d,\epsilon}^5 R_S \langle m_0 \rangle \varepsilon_d + C_{d,\epsilon}^3 \langle m_0 \rangle \left\langle \frac{2}{\tau_d^*} \right\rangle \left[\beta_\epsilon \left(\varepsilon_g \varepsilon_d \right)^{1/2} - \varepsilon_d \right] \end{aligned} \tag{6.59}$$

where $C_{d,\epsilon}^1$, $C_{d,\epsilon}^2$, $C_{d,\epsilon}^3$, $C_{d,\epsilon}^5$, β_ϵ and $\sigma_{d,\epsilon}$ are constants. Note that in this model, the evaporation and drag terms are written in terms of the TKE dissipation rates, and not as source terms. This modification from the classical two-phase turbulence model leads to a more robust formulation [64].

6.3.2 Reynolds-average equations for gas phase

The RA source terms seen by the gas phase contain numerous correlations that can lead to confusion when deriving RA gas equations. We thus prefer to work with some new expressions for these source terms given in (6.18). Let us first define

$$\mathcal{M}_g = \frac{3}{2} R_S m_{1/2}, \qquad \boldsymbol{\mathcal{A}}_g = -m_{1/2} \frac{\boldsymbol{u_g} - \boldsymbol{u_d}}{\tau_d^*}, \tag{6.60}$$

and then we rewrite the gas-phase governing equations using these definitions. Given the assumptions made concerning the velocity-size correlations in (6.23), working with (6.60) is entirely equivalent to working with the original moments.

6.3.2.1 Gas-phase continuity equation

Applying the RA to Eq. (6.13a) yields

$$\partial_t \langle \rho_g \rangle + \nabla_{\boldsymbol{x}} \cdot \langle \rho_g \rangle \langle \boldsymbol{u_g} \rangle_g = \langle \mathcal{M}_g \rangle . \tag{6.61}$$

This equation is closed.

6.3.2.2 Gas-phase momentum equation

The gas-phase PA momentum equation is found from (6.13b):

$$\partial_t \langle \rho_g \rangle \langle \boldsymbol{u_g} \rangle_g + \nabla_{\boldsymbol{x}} \cdot \left[\langle \rho_g \rangle \left(\langle \boldsymbol{u_g} \rangle_g \otimes \langle \boldsymbol{u_g} \rangle_g + \langle \boldsymbol{u_g}''' \boldsymbol{u_g}''' \rangle_g \right) + \langle P_g \rangle I \right] = \nabla_{\boldsymbol{x}} \cdot \langle \rho_g \rangle \langle \boldsymbol{\tau} \rangle_g + \langle \mathfrak{S}^{\rho \boldsymbol{u}} \rangle \tag{6.62}$$

with

$$\langle \mathfrak{S}^{\rho \boldsymbol{u}} \rangle = \langle \mathcal{M}_g \boldsymbol{u_d} \rangle + \langle \boldsymbol{\mathcal{A}}_g \rangle . \tag{6.63}$$

The RA viscous-stress tensor is

$$\langle \boldsymbol{\tau} \rangle_g = \langle \nu_g \rangle_g \left[\nabla_{\boldsymbol{x}} \langle \boldsymbol{u_g} \rangle_g + \left(\nabla_{\boldsymbol{x}} \langle \boldsymbol{u_g} \rangle_g \right)^t - \frac{2}{3} \nabla_{\boldsymbol{x}} \cdot \langle \boldsymbol{u_g} \rangle_g I \right] + \left\langle \nu_g''' \left[\nabla_{\boldsymbol{x}} \boldsymbol{u_g}''' + (\nabla_{\boldsymbol{x}} \boldsymbol{u_g}''')^t \right] - \frac{2}{3} \nu_g''' \nabla_{\boldsymbol{x}} \cdot \boldsymbol{u_g}''' I \right\rangle_g \tag{6.64}$$

where the second contribution is neglected in compressible turbulence models. For the sake of simplicity, we define

$$\bar{S}_g = S_g - \frac{1}{3} (\nabla_{\boldsymbol{x}} \cdot \langle \boldsymbol{u_g} \rangle_g) I \quad \text{and} \quad S_g = \frac{1}{2} \left[\nabla_{\boldsymbol{x}} \langle \boldsymbol{u_g} \rangle_g + (\nabla_{\boldsymbol{x}} \langle \boldsymbol{u_g} \rangle_g)^t \right] . \tag{6.65}$$

In the literature, it is common to combine the RA viscous-stress tensor with the gas-phase Reynolds-stress tensor $\langle \boldsymbol{u_g}''' \boldsymbol{u_g}''' \rangle_g$, for which closure is achieved through a turbulent-viscosity model. Therefore, it is convenient to express the total stress tensor as

$$\langle \boldsymbol{u_g}''' \boldsymbol{u_g}''' \rangle_g - \langle \boldsymbol{\tau} \rangle_g = -2 \left(\langle \nu_g \rangle_g + \nu_{g,t} \right) S_g + \frac{2}{3} k_g I. \tag{6.66}$$

The source terms accounting for drag and evaporation are, respectively,

$$\langle \boldsymbol{\mathcal{A}}_g \rangle = - \left\langle m_{1/2} \right\rangle \left\langle \frac{1}{\tau_d^*} \right\rangle \left(\langle \boldsymbol{u_g} \rangle_g - \langle \boldsymbol{u_d} \rangle_d + \boldsymbol{u}_c \right) \tag{6.67}$$

and

$$\langle \mathcal{M}_g \boldsymbol{u_d} \rangle = R_S \left\langle m_{1/2} \right\rangle \langle \boldsymbol{u_d} \rangle_d . \tag{6.68}$$

The final form for the gas-phase RA momentum equation is

$$\partial_t \langle \rho_g \rangle \langle \boldsymbol{u_g} \rangle_g + \nabla_{\boldsymbol{x}} \cdot \langle \rho_g \rangle \left[\langle \boldsymbol{u_g} \rangle_g \otimes \langle \boldsymbol{u_g} \rangle_g + \left(\frac{2}{3} k_g + R \langle T_g \rangle_g \right) I \right] = + \nabla_{\boldsymbol{x}} \cdot \langle \rho_g \rangle \left[2 \left(\langle \nu_g \rangle_g + \nu_{g,t} \right) \bar{S}_g \right] + \frac{3}{2} R_S \left\langle m_{1/2} \right\rangle \langle \boldsymbol{u_d} \rangle_d - \left\langle m_{1/2} \right\rangle \left\langle \frac{1}{\tau_d^*} \right\rangle \left(\langle \boldsymbol{u_g} \rangle_g - \langle \boldsymbol{u_d} \rangle_d + \boldsymbol{u}_c \right) . \tag{6.69}$$

Note that the exchange terms on the right-hand side have the opposite sign as the corresponding terms in the spray-phase momentum equation. By construction, the total mean momentum of the two-phase system is conserved.

6.3.2.3 Gas-phase total energy equation

Reynolds averaging the total energy equation for the gas phase (6.13c) yields the following expression:

$$\partial_t \langle\rho_g\rangle \langle E_g\rangle_g + \nabla_{\boldsymbol{x}} \cdot \left[\langle\rho_g\rangle \left(\langle E_g\rangle_g \langle \boldsymbol{u_g}\rangle_g + \langle E_g \boldsymbol{u_g}'''\rangle_g\right) + \langle P_g\rangle \langle \boldsymbol{u_g}\rangle_g + \langle P_g \boldsymbol{u_g}'''\rangle\right] = + \nabla_{\boldsymbol{x}} \cdot \langle\rho_g\rangle \left(\langle\boldsymbol{\tau}\rangle_g \langle \boldsymbol{u_g}\rangle_g + \langle \boldsymbol{\tau}''' \boldsymbol{u_g}'''\rangle_g\right) - \nabla_{\boldsymbol{x}} \cdot \langle \mathbf{q}\rangle + \left\langle \mathfrak{S}^{\rho E}\right\rangle . \quad (6.70)$$

The turbulent total energy flux can be decomposed as follows:

$$\langle E_g \boldsymbol{u_g}'''\rangle_g = \langle \boldsymbol{u_g}\rangle_g \cdot \langle \boldsymbol{u_g}''' \boldsymbol{u_g}'''\rangle_g + \frac{1}{2}\langle \boldsymbol{u_g}''' \boldsymbol{u_g}''' \cdot \boldsymbol{u_g}'''\rangle_g + \left\langle e_g''' \boldsymbol{u_g}'''\right\rangle_g - \frac{\langle P_g \boldsymbol{u_g}'''\rangle}{\langle\rho_g\rangle}. \quad (6.71)$$

Consistent with the velocity flux, the turbulent fluxes can be grouped together and modeled as

$$\frac{1}{2}\langle \boldsymbol{u_g}''' \boldsymbol{u_g}''' \cdot \boldsymbol{u_g}'''\rangle_g - \langle \boldsymbol{\tau}''' \boldsymbol{u_g}'''\rangle_g = -\left(\nu_g + \frac{\nu_{g,t}}{\sigma_{g,t}}\right) \nabla_{\boldsymbol{x}} k_g \quad (6.72)$$

where $\sigma_{g,t}$ is a constant whose value depends on the turbulence model.

The final expression for the gas-phase PA total energy is

$$\begin{aligned}\partial_t \langle\rho_g\rangle \langle E_g\rangle_g + \nabla_{\boldsymbol{x}} \cdot \langle\rho_g\rangle &\left[\langle E_g\rangle_g \langle \boldsymbol{u_g}\rangle_g - \frac{\nu_{g,t}}{\mathrm{Pr}_{g,t}} \nabla_{\boldsymbol{x}} \langle e_g\rangle_g - \left(\nu_g + \frac{\nu_{g,t}}{\sigma_{g,t}}\right) \nabla_{\boldsymbol{x}} k_g\right] \\ + \nabla_{\boldsymbol{x}} \cdot \langle\rho_g\rangle &\left[\left(R\langle T_g\rangle_g + \frac{2}{3}k_g\right)\langle \boldsymbol{u_g}\rangle_g - 2\left(\nu_{g,t} + \langle\nu_g\rangle_g\right)\bar{S}_g \cdot \langle \boldsymbol{u_g}\rangle_g\right] + \nabla_{\boldsymbol{x}} \cdot \langle \mathbf{q}\rangle = \\ &\frac{3}{2} R_S \langle m_{1/2}\rangle \left(K + k_d + \langle\Theta\rangle_d\right) - \langle m_{1/2}\rangle \left\langle \frac{2}{\tau_d^*}\right\rangle \left[\beta \left(k_g k_d\right)^{1/2} - k_d - \langle\Theta\rangle_d\right] \\ &- \langle m_{1/2}\rangle \left\langle \frac{1}{\tau_d^*}\right\rangle \left(\langle \boldsymbol{u_g}\rangle_g - \langle \boldsymbol{u_d}\rangle_d + \boldsymbol{u}_c\right) \cdot \langle \boldsymbol{u_d}\rangle_d . \end{aligned} \quad (6.73)$$

As with the mean momentum, the total energy of the two-phase system is conserved by the exchange terms.

6.3.2.4 Gas-phase internal energy equation

Taking the RA of Eq. (6.17) leads to

$$\begin{aligned}\partial_t \langle\rho_g\rangle \langle e_g\rangle_g + \nabla_{\boldsymbol{x}} \cdot \langle\rho_g\rangle &\left(\langle e_g\rangle_g \langle \boldsymbol{u_g}\rangle_g + \left\langle e_g''' \boldsymbol{u_g}'''\right\rangle_g\right) = -\langle P_g\rangle \nabla_{\boldsymbol{x}} \cdot \left(\langle \boldsymbol{u_g}\rangle_g - \frac{\left\langle \rho_g' \boldsymbol{u_g}'\right\rangle}{\langle\rho_g\rangle}\right) \\ - \left\langle P_g' \nabla_{\boldsymbol{x}} \cdot \boldsymbol{u_g}'\right\rangle + \langle\rho_g\rangle &\left(\langle\boldsymbol{\tau}\rangle_g : \nabla_{\boldsymbol{x}} \langle \boldsymbol{u_g}\rangle_g + \langle \boldsymbol{\tau}''' : \nabla_{\boldsymbol{x}} \boldsymbol{u_g}'''\rangle_g\right) - \nabla_{\boldsymbol{x}} \cdot \langle \mathbf{q}\rangle + \langle \mathfrak{S}^{\rho e}\rangle . \end{aligned} \quad (6.74)$$

The internal energy turbulent flux is closed through a gradient-diffusion model:

$$\left\langle e_g''' \boldsymbol{u_g}''' \right\rangle_g = -\frac{\nu_{g,t}}{\mathrm{Pr}_{g,t}} \nabla_{\boldsymbol{x}} \left\langle e_g \right\rangle_g \tag{6.75}$$

where $\mathrm{Pr}_{g,t}$ is the gas-phase turbulent Prandtl number. The gas-phase TKE dissipation rate produces a source term in the internal energy equation. This is due to $\left\langle P_g' \nabla_{\boldsymbol{x}} \cdot \boldsymbol{u_g}' \right\rangle - \left\langle \rho_g \right\rangle \left\langle \boldsymbol{\tau}''' : \nabla_{\boldsymbol{x}} \boldsymbol{u_g}''' \right\rangle_g$ whose closure is achieved by the following equality

$$\left\langle P_g' \nabla_{\boldsymbol{x}} \cdot \boldsymbol{u_g}' \right\rangle - \left\langle \rho_g \right\rangle \left\langle \boldsymbol{\tau}''' : \nabla_{\boldsymbol{x}} \boldsymbol{u_g}''' \right\rangle_g = - \left\langle \rho_g \right\rangle \varepsilon_g \tag{6.76}$$

where ε_g is the TKE dissipation rate in the gas phase. The RA source term is

$$\begin{aligned} \left\langle \mathfrak{S}^{\rho e} \right\rangle = & \left(\left\langle \frac{2}{\tau_d^*} \right\rangle + \frac{3}{2} R_S \right) \left\langle m_{1/2} \right\rangle \left(K - \left\langle \boldsymbol{u_g} \right\rangle_g \cdot \left\langle \boldsymbol{u_d} \right\rangle_d + K_g \right) \\ & + \left(\left\langle \frac{2}{\tau_d^*} \right\rangle + \frac{3}{2} R_S \right) \left\langle m_{1/2} \right\rangle \left(k_d - \left\langle \boldsymbol{u_g}''' \cdot \boldsymbol{u_d}'' \right\rangle_d + k_g + \left\langle \Theta \right\rangle_d \right) \\ & - \left(\left\langle \frac{2}{\tau_d^*} \right\rangle + \frac{3}{2} R_S \right) \left\langle m_{1/2} \right\rangle \left[\frac{\left\langle \alpha_d' \boldsymbol{u_g}''' \right\rangle}{\left\langle \alpha_d \right\rangle \left\langle 1 - \alpha_d \right\rangle} \cdot \left(\left\langle \boldsymbol{u_d} \right\rangle_d - \left\langle \boldsymbol{u_g} \right\rangle_g \right) - \frac{1}{2} \frac{\left\langle \alpha_d' \boldsymbol{u_g}''' \cdot \boldsymbol{u_g}''' \right\rangle}{\left\langle \alpha_d \right\rangle \left\langle 1 - \alpha_d \right\rangle} \right]. \end{aligned} \tag{6.77}$$

The triple correlation $\left\langle \alpha_d' \boldsymbol{u_g}''' \cdot \boldsymbol{u_g}''' \right\rangle$ in (6.77) represents correlations between the spray volume fraction and the gas-phase TKE. This term is likely to be negative (i.e., the more inertial the droplets, the faster they segregate away from regions of high gas vorticity), but we will assume it is small and neglect it.

Introducing the turbulence models gives rise to final gas-phase RA internal energy equation:

$$\begin{aligned} \partial_t \left\langle \rho_g \right\rangle \left\langle e_g \right\rangle_g + \nabla_{\boldsymbol{x}} \cdot \left\langle \rho_g \right\rangle & \left(\left\langle e_g \right\rangle_g \left\langle \boldsymbol{u_g} \right\rangle_g - \frac{\nu_{g,t}}{\mathrm{Pr}_{g,t}} \nabla_{\boldsymbol{x}} \left\langle e_g \right\rangle_g + \frac{\left\langle \mathbf{q} \right\rangle}{\left\langle \rho_g \right\rangle} \right) = \Pi_g^e + \left\langle \rho_g \right\rangle \varepsilon_g \\ & + \left(\left\langle \frac{2}{\tau_d^*} \right\rangle + \frac{3}{2} R_S \right) \left\langle m_{1/2} \right\rangle \left[K - \left\langle \boldsymbol{u_g} \right\rangle_g \cdot \left\langle \boldsymbol{u_d} \right\rangle_d + K_g + k_d \right] \\ & + \left(\left\langle \frac{2}{\tau_d^*} \right\rangle + \frac{3}{2} R_S \right) \left\langle m_{1/2} \right\rangle \left[k_g + \left\langle \Theta \right\rangle_d - 2\beta \left(k_g k_d \right)^{1/2} \right] \\ & - \left(\left\langle \frac{2}{\tau_d^*} \right\rangle + \frac{3}{2} R_S \right) \left\langle m_{1/2} \right\rangle \boldsymbol{u}_c \cdot \left(\left\langle \boldsymbol{u_d} \right\rangle_d - \left\langle \boldsymbol{u_g} \right\rangle_g \right) \end{aligned} \tag{6.78}$$

where

$$\Pi_g^e = -\tilde{\Pi}_g^e - \left\langle \rho_g \right\rangle R \left\langle T_g \right\rangle_g \nabla_{\boldsymbol{x}} \cdot \left\langle \boldsymbol{u_g} \right\rangle_g + 2 \left\langle \rho_g \right\rangle \left\langle \nu_g \right\rangle_g \bar{S}_g : \bar{S}_g \tag{6.79}$$

is the production of gas-phase internal energy through the mean velocity, and

$$\tilde{\Pi}_g^e = - \left\langle \rho_g \right\rangle R \left\langle T_g \right\rangle_g \nabla_{\boldsymbol{x}} \cdot \left\langle \alpha_d \right\rangle \boldsymbol{u}_c \tag{6.80}$$

is the contribution due to the drift velocity generated by preferential concentration. Note that the contribution of the mean velocities in the exchange term can be rewritten as

$$K - \left\langle \boldsymbol{u_g} \right\rangle_g \cdot \left\langle \boldsymbol{u_d} \right\rangle_d + K_g = \frac{1}{2} \left(\left\langle \boldsymbol{u_g} \right\rangle_g - \left\langle \boldsymbol{u_d} \right\rangle_d \right)^2, \tag{6.81}$$

which is strictly positive. Likewise, the TKE contributions can be rewritten as $(k_d^{1/2} - k_d^{1/2})^2 + 2(1-\beta)(k_d k_d)^{1/2}$ with $\beta \leq 1$. Thus, the exchange terms act to increase the gas-phase PA internal energy.

6.3.2.5 Gas-phase mean kinetic energy equation

The gas-phase mean kinetic energy is known from the gas-phase PA velocity. It can be found by multiplying the gas-phase PA momentum equation (6.69) by $\langle \boldsymbol{u_g} \rangle_g$:

$$\begin{aligned}\partial_t \langle \rho_g \rangle K_g + \nabla_{\boldsymbol{x}} \cdot \langle \rho_g \rangle \left[\left(K_g + R \langle T_g \rangle_g + \frac{2}{3} k_g \right) \langle \boldsymbol{u_g} \rangle_g - 2 \left(\nu_{g,t} + \langle \nu_g \rangle_g \right) \bar{S}_g \cdot \langle \boldsymbol{u_g} \rangle_g \right] \\ = \langle \rho_g \rangle \left[\left(R \langle T_g \rangle_g + \frac{2}{3} k_g \right) I - 2 \left(\nu_{g,t} + \langle \nu_g \rangle_g \right) \bar{S}_g \right] : \nabla_{\boldsymbol{x}} \langle \boldsymbol{u_g} \rangle_g \\ - \langle m_{1/2} \rangle \left\langle \frac{1}{\tau_d^*} \right\rangle \left(\langle \boldsymbol{u_g} \rangle_g - \langle \boldsymbol{u_d} \rangle_d + \boldsymbol{u}_c \right) \cdot \langle \boldsymbol{u_g} \rangle_g + \frac{3}{2} R_S \langle m_{1/2} \rangle \left(\langle \boldsymbol{u_d} \rangle_d \cdot \langle \boldsymbol{u_g} \rangle_g - K_g \right).\end{aligned} \tag{6.82}$$

This expression can now be used to find the equation for the gas-phase TKE.

6.3.2.6 Gas-phase turbulent kinetic energy equation

Using the equality $\langle E_g \rangle_g = \langle e_g \rangle_g + K_g + k_g$, the gas-phase TKE can be easily found by subtracting the gas-phase internal energy equation (6.78) and the gas-phase mean kinetic energy equation (6.82) from the total energy equation (6.73):

$$\begin{aligned}\partial_t \langle \rho_g \rangle k_g + \nabla_{\boldsymbol{x}} \cdot \langle \rho_g \rangle k_g \left[\langle \boldsymbol{u_g} \rangle_g - \left(\nu_g + \frac{\nu_{g,t}}{\sigma_{g,t}} \right) \nabla_{\boldsymbol{x}} \ln k_g \right] = \\ \Pi_g^k + \tilde{\Pi}_g^e + \Pi_c^k - \langle \rho_g \rangle \varepsilon_g + \langle m_{1/2} \rangle \left(\left\langle \frac{2}{\tau_d^*} \right\rangle + 3 R_S \right) \left[\beta \left(k_g k_d \right)^{1/2} - k_g \right] \\ + \frac{3}{2} R_S \langle m_{1/2} \rangle k_g\end{aligned} \tag{6.83}$$

where

$$\Pi_g^k = \langle \rho_g \rangle \nu_{g,t} \bar{S}_g : \bar{S}_g - \frac{2}{3} \langle \rho_g \rangle k_g \nabla_{\boldsymbol{x}} \cdot \langle \boldsymbol{u_g} \rangle_g \tag{6.84}$$

is the gas-phase TKE production due to mean velocity gradients, and

$$\Pi_c^k = \langle m_{1/2} \rangle \left(\left\langle \frac{1}{\tau_d^*} \right\rangle + \frac{3}{2} R_S \right) \max \left[0, \boldsymbol{u}_c \cdot \left(\langle \boldsymbol{u_d} \rangle_d - \langle \boldsymbol{u_g} \rangle_g \right) \right] \tag{6.85}$$

is a TKE production term due to two-way coupling and the preferential concentration of droplets in a turbulent flow. Note that the coupling terms in (6.83) are asymmetric with respect to those in (6.56) for the spray phase. This is caused by the preferential concentration of droplets: under such circumstances the gas seen by droplets has different statistics than the gas itself [64]. Nevertheless, in shear-driven flows such as fuel jets in ICE injectors, the main TKE production term will be Π_g^k.

6.3.2.7 Gas-phase turbulent kinetic energy dissipation equation

By analogy with Eq. (6.83), the gas-phase TKE dissipation rate is found from

$$\partial_t \langle\rho_g\rangle \varepsilon_g + \nabla_{\boldsymbol{x}} \cdot \langle\rho_g\rangle \varepsilon_g \left[\langle \boldsymbol{u_g}\rangle_g - \left(\nu_g + \frac{\nu_{g,t}}{\sigma_{g,\epsilon}}\right)\nabla_{\boldsymbol{x}} \ln \varepsilon_g\right] = \frac{\varepsilon_g}{k_g}\left(C^1_{g,\epsilon}\Pi^k_g + C^6_{g,\epsilon}\tilde{\Pi}^e_g\right) + \frac{\varepsilon_d}{k_d}C^4_{g,\epsilon}\Pi^k_c - C^2_{g,\epsilon}\langle\rho_g\rangle\frac{\varepsilon_g^2}{k_g} + C^3_{g,\epsilon}\langle m_{1/2}\rangle\left(\left\langle\frac{2}{\tau^*_d}\right\rangle + 3R_S\right)\left[\beta_\epsilon\left(\varepsilon_g\varepsilon_d\right)^{1/2} - \varepsilon_g\right] + C^5_{g,\epsilon}\frac{3}{2}R_S\langle m_{1/2}\rangle\varepsilon_g \quad (6.86)$$

where $\sigma_{g,\epsilon}$, $C^1_{g,\epsilon}$, $C^2_{g,\epsilon}$, $C^3_{g,\epsilon}$, $C^4_{g,\epsilon}$, $C^5_{g,\epsilon}$ and $C^6_{g,\epsilon}$ are model constants.

6.3.3 Final remarks

The variables and the corresponding transport equations solved for each phase in the CFD code are as follows.

- Spray phase:
  1. RA moments $\langle m_k\rangle$ for $k \in (0,1,2,3)$ – (6.24).
  2. PA velocity $\langle \boldsymbol{u_d}\rangle_d$ – (6.38).
  3. PA fluctuating energy κ – (6.55).
  4. TKE k_d – (6.56).
  5. TKE dissipation rate ε_d – (6.59).
- Gas phase:
  1. RA density $\langle\rho_g\rangle$ – (6.61).
  2. PA velocity $\langle \boldsymbol{u_g}\rangle_g$ – (6.69).
  3. PA internal energy $\langle e_g\rangle_g$ – (6.78).
  4. TKE k_g – (6.83).
  5. TKE dissipation rate ε_g – (6.86).

As in the case of laminar flow, the RA moments are used to reconstruct the RA droplet-size NDF $\langle n(t,\boldsymbol{x},S)\rangle$, which is needed to close the phase-space flux term in (6.24a) and to find other moments such as $\langle m_{1/2}\rangle$. In the turbulence models, the model constants are set at the standard values used in free-shear flows such as turbulent jets.

6.4 Homogeneous turbulence of two-phase polydisperse flows

The this section we apply the multiphase turbulence model derived in Sec. 6.2 to a simple test case, namely, homogeneous two-phase turbulence. The most important point is to

capture the correct behavior of the total energy partition between the evaporating spray and the compressible gas in the context of two-way coupling. In [64] the effectiveness of the closures proposed for the turbulent velocity correlations between phases $\langle \boldsymbol{u_g}''' \cdot \boldsymbol{u_d}'' \rangle_d = 2\beta(k_g k_d)^{1/2}$ has been shown in the context of one-way and two-way coupling of collisionless monodisperse droplets with an incompressible gas. The model showed good agreement with the total fluctuating energy expression first given in [175], and provided results comparable with [59] for the partition between the spray-phase TKE k_d and the granular temperature $\langle \Theta \rangle_d$. Here we focus on the extension of these results to a more complicated framework with a polydisperse spray and two-way coupling. In order to simplify the analysis of the different flow regimes, we first present a dimensionless homogeneous system of equations. We then focus on selected test cases, which highlight the turbulence model predictions for different flow conditions relevant to ICE sprays. In the first case, we are interested in the energy partition for a polydisperse, non-evaporating spray with frozen gas turbulence, similar to [64, 59]. The second case considers two-way coupling effects on the energy partition for both evaporating and non-evaporating sprays. After these preliminary studies, the third case considers conditions relevant to direct-injection ICE applications.

6.4.1 Dimensionless equations for homogeneous turbulent flow

A summary of the equations needed for the two-phase turbulence model with polydisperse evaporating sprays is given in Sec. 6.3.3. By neglecting all terms representing spatial transport, a simplified set of equation suitable for time-evolving homogeneous flow is found. We can define the following reference quantities: turbulent kinetic energy k_∞, material density of the liquid inside the droplets $\rho_{l,\infty}$, material density of the gas $\rho_{l,\infty}$, kinematic viscosity of the gas $\nu_{g,\infty}$, maximum droplet size S_0, number per volume of droplets n_0, and the integral time scale of the gas-phase turbulence $\tau_g = k_\infty/\varepsilon_g(0)$ where $\varepsilon_g(0)$ is the value the gas-phase TKE dissipation rate at time zero. The dimensionless quantities appearing in the homogeneous model are as follows:

$$
\begin{aligned}
\overline{k}_g &= \frac{k_g}{k_\infty}, & \overline{k}_d &= \frac{k_d}{k_\infty}, & \overline{\varepsilon}_g &= \frac{\varepsilon_g \tau_g}{k_\infty}, & \overline{\varepsilon}_d &= \frac{\varepsilon_d \tau_g}{k_\infty}, & \overline{\rho}_g &= \frac{\langle \rho_g \rangle}{\rho_{g,\infty}}, \\
\overline{x} &= \frac{x}{\sqrt{k_\infty}\tau_g}, & \overline{t} &= \frac{t}{\tau_g}, & \overline{\boldsymbol{u}}_g &= \frac{\langle \boldsymbol{u}_g \rangle_g}{\sqrt{k_\infty}}, & \overline{\boldsymbol{u}}_d &= \frac{\langle \boldsymbol{u}_d \rangle_d}{\sqrt{k_\infty}}, & \overline{S} &= \frac{S}{S_0}, \\
\overline{R}_S &= \frac{R_S \tau_g}{S_0}, & \overline{\nu}_g &= \frac{\nu_g}{\nu_{g,\infty}}, & \overline{\bar{S}_d} &= \tau_g \bar{S}_d, & \overline{\bar{S}_g} &= \tau_g \bar{S}_g, & \overline{e}_g &= \frac{\langle e_g \rangle_g}{k_\infty}, \\
\overline{\nu}_{g,t} &= \frac{\nu_{g,t}}{\nu_{g,\infty}\mathsf{Re}}, & \overline{\nu}_{d,t} &= \frac{\nu_{d,t}}{\nu_{g,\infty}\mathsf{Re}}, & \overline{\rho}_d &= \frac{\langle \rho_d \rangle}{\rho_{d,\infty}}, & \overline{m}_k &= \frac{\langle m_k \rangle}{S_0^k n_0}, & \overline{n} &= \frac{\langle n \rangle\, S_0}{n_0}
\end{aligned}
\tag{6.87}
$$

where $\mathsf{Re} = k_\infty \tau_g / \nu_{g,\infty}$ is the turbulence Reynolds number [141].

In the following, we work with dimensionless RA equations, omitting the bars on variables of the mean two-phase flow as well as the RA and PA brackets (e.g., $m_k = \langle m_k \rangle$)

for clarity. The dimensionless RA moment equations are given by

$$\mathrm{d}_t m_0 = -\, n(t,\boldsymbol{x},0) R_S, \tag{6.88a}$$
$$\mathrm{d}_t m_1 = -\, m_0 R_S, \tag{6.88b}$$
$$\mathrm{d}_t m_2 = -\, m_1 R_S, \tag{6.88c}$$
$$\mathrm{d}_t m_3 = -\, m_2 R_S. \tag{6.88d}$$

The dimensionless continuity equation for the gas phase is

$$\mathrm{d}_t \rho_g = \frac{3}{2} \Phi_{\mathsf{m}} m_{1/2} R_S \tag{6.89}$$

with the dimensionless mass loading $\Phi_{\mathsf{m}} = \rho_{d,\infty} S_0^{3/2} n_0 / \rho_{g,\infty}$. The dimensionless RA mean momentum equations are

$$\mathrm{d}_t \Phi_{\mathsf{m}} m_{3/2} \boldsymbol{u_d} = \frac{\Phi_{\mathsf{m}} m_{1/2}}{\mathsf{St}} (1 - C_g) (\boldsymbol{u_g} - \boldsymbol{u_d}) - \frac{3}{2} \Phi_{\mathsf{m}} m_{1/2} R_S \boldsymbol{u_d}, \tag{6.90a}$$
$$\mathrm{d}_t \rho_g \boldsymbol{u_g} = -\, \frac{\Phi_{\mathsf{m}} m_{1/2}}{\mathsf{St}} (1 - C_g) (\boldsymbol{u_g} - \boldsymbol{u_d}) + \frac{3}{2} \Phi_{\mathsf{m}} m_{1/2} R_S \boldsymbol{u_d} \tag{6.90b}$$

where St is the Stokes number relative to the droplet size S_0. The reader can note that the total mean momentum of the two-phase system is constant. The dimensionless RA internal-energy equation for the gas phase is

$$\mathrm{d}_t \rho_g e_g = \left(\frac{2}{\mathsf{St}} + \frac{3}{2} R_S \right) \Phi_{\mathsf{m}} m_{1/2} \left[\left(\frac{1}{2} - C_g \right) (\boldsymbol{u_g} - \boldsymbol{u_d})^2 + k_g - 2\beta (k_g k_d)^{1/2} + \kappa \right] + \frac{\Pi_g^e}{\mathsf{Re}} + \rho_g \varepsilon_g \tag{6.91}$$

where the production term due to molecular dissipation of mean shear Π_g^e will be non-zero for free-shear flow but otherwise is null. Note that the right-hand side of this equation should always non-negative since the gas-phase internal energy never decreases, which implies that $C_g \leq 1/2$.

The dimensionless system of conserved quantities representing fluctuations in the spray phase is

$$\mathrm{d}_t m_{3/2} \kappa = \Pi^K + \frac{2}{\mathsf{St}} m_{1/2} \left[\beta (k_g k_d)^{1/2} - \kappa \right] - \frac{3}{2} R_S m_{1/2} \kappa \tag{6.92a}$$
$$\mathrm{d}_t m_{3/2} k_d = \Pi_d^k - m_{3/2} \varepsilon_d + \frac{2}{\mathsf{St}} m_{1/2} \left[\beta (k_g k_d)^{1/2} - k_d \right] - \frac{3}{2} R_S m_{1/2} k_d \tag{6.92b}$$
$$\mathrm{d}_t m_{3/2} \varepsilon_d = C_{d,\epsilon}^1 \frac{\varepsilon_d}{k_d} \Pi_d^k - C_{d,\epsilon}^2 m_{3/2} \frac{\varepsilon_d^2}{k_d} + C_{d,\epsilon}^3 \frac{2}{\mathsf{St}} m_{1/2} \left[\beta_\epsilon (\varepsilon_g \varepsilon_d)^{1/2} - \varepsilon_d \right] - C_{d,\epsilon}^5 \frac{3}{2} R_S m_{1/2} \varepsilon_d \tag{6.92c}$$

where $\Pi^K = \Pi_d^k$ are the dimensionless production terms due to turbulent dissipation of mean shear in the spray phase. The dimensionless system of conserved quantities

representing the turbulent fluctuations in the gas phase is

$$\begin{aligned}\mathrm{d}_t\rho_g k_g =&\Pi_g^k - \rho_g\varepsilon_g + \left(\frac{2}{\mathsf{St}} + 3R_S\right)\Phi_{\mathsf{m}} m_{1/2}\left[\beta\left(k_g k_d\right)^{1/2} - k_g\right] \\ &+ \left(\frac{1}{\mathsf{St}} + \frac{3}{2}R_S\right)\Phi_{\mathsf{m}} m_{1/2} C_g\left(\boldsymbol{u_g} - \boldsymbol{u_d}\right)^2 + \frac{3}{2}R_S\Phi_{\mathsf{m}} m_{1/2} k_g \qquad (6.93a)\\ \mathrm{d}_t\rho_g\varepsilon_g =&C_{g,\epsilon}^1\frac{\varepsilon_g}{k_g}\Pi_g^k - C_{g,\epsilon}^2\rho_g\frac{\varepsilon_g^2}{k_g} + C_{g,\epsilon}^3\left(\frac{2}{\mathsf{St}} + 3R_S\right)\Phi_{\mathsf{m}} m_{1/2}\left[\beta_\epsilon\left(\varepsilon_g\varepsilon_d\right)^{1/2} - \varepsilon_g\right] \\ &+ C_{g,\epsilon}^4\frac{\varepsilon_d}{k_d}\left(\frac{1}{\mathsf{St}} + \frac{3}{2}R_S\right)\Phi_{\mathsf{m}} m_{1/2} C_g\left(\boldsymbol{u_g} - \boldsymbol{u_d}\right)^2 + C_{g,\epsilon}^5\frac{3}{2}R_S\Phi_{\mathsf{m}} m_{1/2}\varepsilon_g \qquad (6.93b)\end{aligned}$$

where Π_g^k is the dimensionless production term due to turbulent dissipation of mean shear in the gas phase. In the following, we consider $C_{g,\epsilon}^1 = C_{d,\epsilon}^1 = 1.44$, $C_{g,\epsilon}^2 = C_{d,\epsilon}^2 = 1.92$, $C_{g,\epsilon}^3 = C_{d,\epsilon}^3 = 1.55$, $C_{g,\epsilon}^4 = 2.11$, $C_{g,\epsilon}^5 = C_{d,\epsilon}^5 = 1.55$, and $C_g = 0.3$. The values of the remaining production terms are set equal to zero unless noted otherwise.

6.4.2 Example results for fluctuating energy partition with decaying turbulence

In order to validate the spray-phase energy partition for polydisperse droplets, we use the three one-way-coupling cases in [59], originally conducted for monodisperse droplets. These cases use three sets of initial conditions: (i) $\kappa(0) = 1$, $k_d(0) = 1$; (ii) $\kappa(0) = 0$, $k_d(0) = 0$; and (iii) $\kappa(0) = 0.83$, $k_d(0) = 0$. The gas-phase turbulence is frozen and set as $k_g = 1$. The mean velocities are equal $\boldsymbol{u_g} = \boldsymbol{u_d}$, and remain so for all time due to the abscence of gravity. For the case with initial value $k_d(0) = 1$, we use the initial value $\varepsilon_d(0) = 2$. Otherwise we use $\varepsilon_d(0) = 0$ when $k_d(0) = 0$ for the sake of consistency. For monodisperse droplets in [59], a Stokes number equal to $\mathsf{St}_m = 0.81$ is employed. This value corresponds to the Stokes number to the time scale relative to the mean droplet size of the polydisperse distribution over the (constant) gas integral time scale τ_g. For convenience, we set $\tau_g = 1$, leading to a gas-phase turbulence energy dissipation of $\varepsilon_g = 1$.

For the following simulations, the values for β and β_ϵ are fixed to 0.8, as suggested in [64], since this provides the correct steady-state results for κ as compared to [175] and the correct energy partition as found in [59]. Moreover, the following Rosin-Rammler function is used to characterize the droplet size distribution in the spray:

$$n\left(S\right) = \frac{1}{2}q_{rr}16^{q_{rr}/2}S^{\frac{q_{rr}}{2}-1}\exp\left[-\left(16S\right)^{q_{rr}/2}\right] \qquad (6.94)$$

with the constant $q_{rr} = 3.5$ determining the sharpness of the distribution and the dimensionless size phase variable $S \in [0, 1]$. According to this distribution, the largest droplet size is equal to $S_0 = 16S_{mean}$ where S_{mean} is the mean droplet size. This yields a characteristic Stokes number of $\mathsf{St} = 16\mathsf{St}_m$.

Recall that for one-way coupling of polydisperse droplets with a frozen gas phase, only the system (6.92) with $\Pi^K = \Pi_d^k = 0$ is solved. Results are plotted in Fig. 6.1. The spray energy partition is a good agreement with Fig. 3 in [64], and the small differences in the

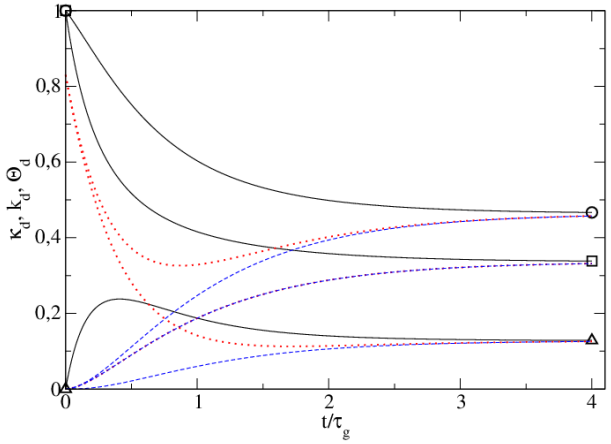

Figure 6.1: Dynamics of the dimensionless non-evaporating spray-phase energy components with frozen gas-phase turbulence (one-way coupling). Curves correspond to three initial conditions: (i) solid lines, (ii) dashed lines, and (iii) stars. Curves corresponding to the fluctuating energy κ, the spray-phase kinetic energy k_d and the granular temperature Θ are respectively denoted through circle, square and triangle symbols.

steady-state values are due to the polydispersity of the droplets in Fig. 6.1. In summary, the turbulence model proposed in [64] has been successfully extended to the Eulerian high-order moment method for polydisperse droplets.

Two-way coupled interactions require the complete turbulence model given by (6.92) and (6.93) for a non-evaporating spray and (6.92), and (6.93) and (6.88) for an evaporating spray. As with one-way coupling, production terms involving mean gradients are set to zero, i.e., $\Pi^K = \Pi^k_d = \Pi^k_g = 0$. The mass loading number is set to $\Phi_\mathsf{m} = 0.4$ for both non-evaporating and evaporating cases, and the evaporation velocity is taken as $R_S = 10\mathsf{St}$ for the evaporating case.

Results for a non-evaporating spray are plotted in Figs. 6.2 and 6.3. In contrast to the spray energy partition observed for one-way coupling, the normalized values in Fig. 6.2 show that the granular energy decreases towards zero while the spray-phase TKE moves towards the total fluctuating energy. Moreover, the gas-phase turbulence dissipates into gas-phase internal energy since no production term due to the mean flow are considered. Furthermore, the spray mass is not high enough to generate significant turbulence inside the gas phase. However, let us underline the small effect of initial spray fluctuating energy on the gas phase as observed in the internal energy profiles, which are not the same for different spray initial conditions and increase with κ.

Results for an evaporating spray are plotted in Figs. 6.4, 6.5 and 6.6. In this case, time $t = 8$ corresponds to the characteristic evaporation time for the mean droplet radius of the distribution. The spray-phase energy partition displayed in Fig. 6.5 is very similar to the case with a non-evaporating spray despite some small differences. When it comes to the gas phase, although the internal energy profiles do not change much, the final values decrease for each initial condition, since the spray evaporation heats the gas phase. Moreover, it is observed that the gas-phase TKE remains the same as compared to the non-evaporating case. This proves that the turbulence generation in the gas due to the

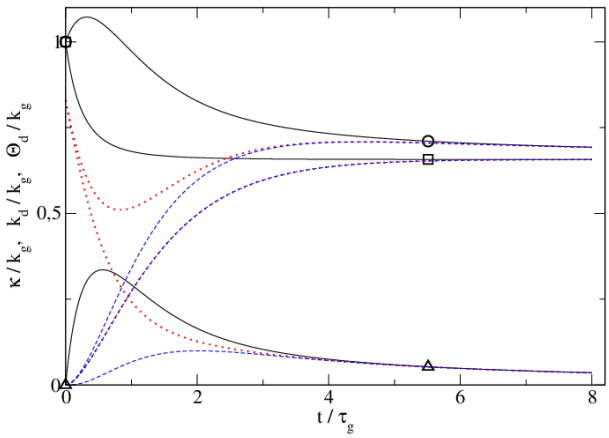

Figure 6.2: Dynamics of the normalized non-evaporating spray-phase energy components with two-way coupling. Curves correspond to three initial conditions: (i) solid black lines, (ii) dashed blue lines, (iii) red dots. Curves corresponding to the fluctuating energy κ, the spray-phase kinetic energy k_d and the granular temperature Θ are respectively denoted through circle, square and triangle symbols.

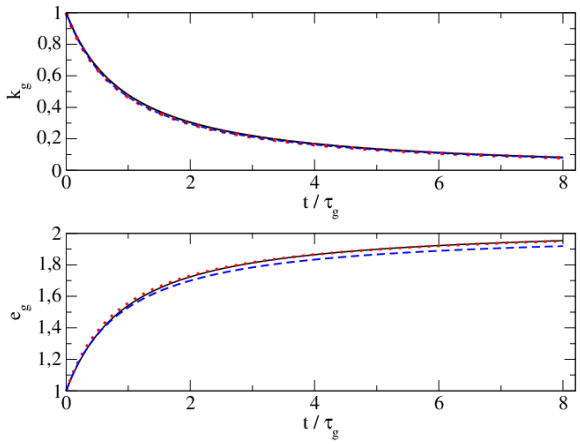

Figure 6.3: Dynamics of the gas-phase energy components for non-evaporating droplets with two-way coupling. Curves correspond to gas-phase TKE (top) and gas-phase internal energy (bottom) for three initial conditions: (i) solid black lines, (ii) dashed blue lines, (iii) red dots.

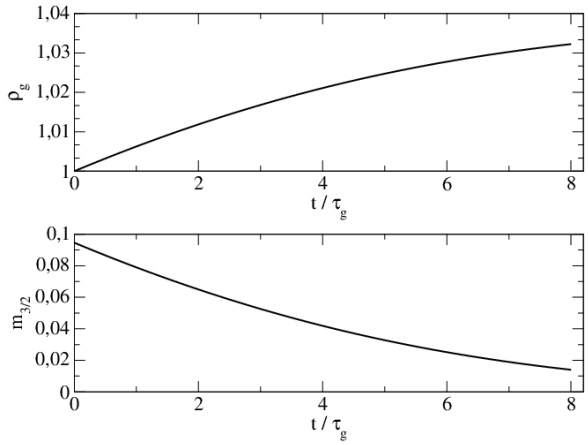

Figure 6.4: Gas-phase density evolution (top) and spray density concentration (bottom) with polydisperse evaporating droplets.

droplet presence is going down since droplets are disappearing but the evaporation creates some turbulence in the gas, counterbalancing the former.

In summary, the test cases without turbulence source terms due to mean velocity gradients but with different initial energy distributions illustrate that the two-phase turbulence model with evaporating droplets behaves as might be expected from the behavior observed with frozen gas-phase turbulence. In general, the turbulence decay observed for the gas phase is only slightly altered by the presence of the spray. Nevertheless, the numerical method used to reconstruct the NDF from the RA moments works equally well as it did for the laminar cases in our earlier work.

6.4.3 Example results for typical ICE flow conditions

The complete turbulence model will eventually be implemented in an industrial CFD code [12] and validated for high-pressure direct injection simulations of ICE applications. The scope of this section is to verify the feasibility of using the turbulence model under typical ICE operating conditions [77]. In the combustion chamber of a typical diesel engine, the gas-phase turbulence is mainly produced by the high-speed direct injection of the fuel spray. Due to the significant velocity difference between the gas and the injected liquid fuel, the spray phase is nearly laminar near the nozzle and the associated spray-phase TKE is very small. However, the droplet flow regime, having strong interactions with the turbulent gas phase, becomes turbulent farther from the injector nozzle. Therefore, we will focus on a two-phase flow regime composed of a fully-developed gas-phase turbulent jet interacting with a nearly laminar spray phase composed of polydisperse droplets. Injection velocities for each phase and other relevant quantities needed to initialize the time-evolving simulations are representative of ICE conditions.

To obtain the characteristic initial data for ICE conditions, an injection test case, representing Spray-H conditions in [1], has been computed using the IFP-C3D software [12], adopting a Lagrangian description of polydisperse droplets [133]. The relevant characteristic values are the gas-phase TKE k_g, gas-phase TKE dissipation ε_g, the spray-phase

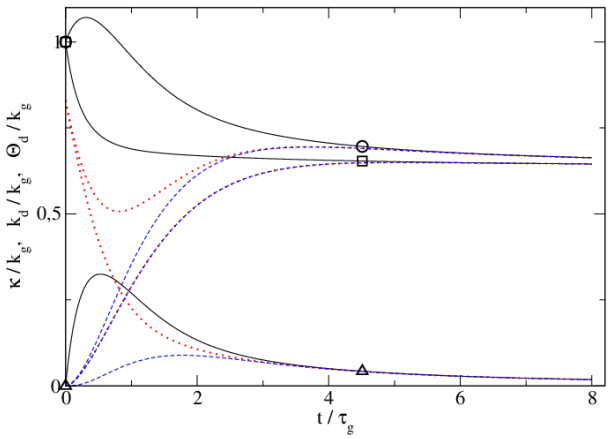

Figure 6.5: Dynamics of the normalized evaporating spray-phase energy components. Curves correspond to three initial conditions: (i) solid black lines, (ii) dashed blue lines, (iii) red dots. Curves corresponding to the fluctuating energy κ, the spray-phase kinetic energy k_d and the granular temperature Θ are respectively denoted through circle, square and triangle symbols.

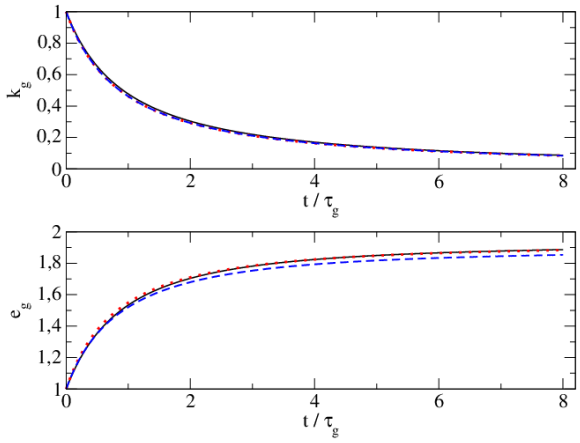

Figure 6.6: Dynamics of the gas-phase energy components with evaporating droplets. Curves correspond to gas-phase TKE (top) and gas-phase internal energy (bottom) for three initial conditions: (i) solid black lines, (ii) dashed blue lines, (iii) red dots.

Table 6.1: Parameters characterizing the dense zone of the disperse phase under ICE conditions. Values for inlet velocity u, TKE k, TKE dissipation rate ε, and the volume fraction α are given for each phase whereas r_{smr} denotes the Sauter mean radius (SMR) of the spray and ν_g is the gas-phase viscosity.

	u (m/s)	k (m^2/s^2)	ε (m^2/s^3)	α	r_{smr} (μm)	ν_g (m^2/s)
gas	71	111	2×10^6	1	-	4.15×10^{-5}
spray	156	1	10	5×10^{-3}	25	-

Table 6.2: Characteristic inflow values for turbulent disperse-phase flow under ICE conditions. $\tau_{S,smr}$ and $\tau_{d,smr}$ are the evaporation and drag times, respectively, based on the spray Sauter mean radius (SMR). $\tau_\eta = (\nu_g/\varepsilon_g)^{1/2}$ and $\mathsf{St}_\eta = \tau_{d,smr}/\tau_\eta$ are the Kolmogorov time scale and Stokes number, respectively. $\mathsf{St}_S = \tau_{S,smr}/\tau_g$ is the evaporation number. All values are based on the initial conditions give in Table 6.1.

$\tau_{S,smr}$ (s)	$\tau_{d,smr}$ (s)	τ_g (s)	τ_η (s)	Re	St	St_η	St_S
3×10^{-3}	4×10^{-5}	5.55×10^{-5}	4.56×10^{-6}	148	0.721	8.77	54.1

volume fraction α_d, the mean droplet radius r_{smr}, characteristic evaporation time scale $\tau_{S,smr}$ and the drag time scale $\tau_{d,smr}$ associated with the spray. These are obtained from the IFP-C3D simulation results and are used as initial conditions for our time-evolving homogeneous simulation. Table 6.1 provides the relevant data. These values are employed to compute the dimensionless numbers given in Table 6.2 characterizing the disperse-flow regime. Note that the drag and integral time scales are comparable, while the evaporation time scale is two orders of magnitude larger. Also note that the Stokes number St is nearly unity, indicating that particle trajectory crossing (represented by Θ in our model) will be important at the turbulence integral scale. In a self-similar turbulent jet, the turbulence Reynolds number ($\mathsf{Re} = k_g^2/(\nu_g \varepsilon_g)$) is constant and τ_g increases along the centerline (i.e., with time in our model). Thus, with one-way coupling, the Stokes numbers would decrease in the non-evaporating case due to the change in τ_g. Obviously, the decrease in Stokes number will be more rapid with evaporating droplets due to the decrease in $\tau_{d,smr}$.

The conceptual difference between the Lagrangian description of the droplets used to characterize the turbulent disperse-phase flow and the Eulerian turbulent model developed in this work do not allow us to extract directly the values for spray-phase TKE k_d and its dissipation rate ε_d from the IFP-C3D simulation results. Nevertheless, the integral time scale associated with the spray-phase TKE should be comparable to the gas-phase integral time scale τ_g in the injection zone where the velocity difference between phases is significant. Therefore, we set $k_d = \kappa = 1$ and $\varepsilon_d = 10$ as the initial state of the spray-phase turbulence. Note that these values are much smaller than in the gas phase, and correspond to nearly laminar flow. The initial polydisperse droplet size distribution follows the function defined by Eq. (6.94).

Although we are considering a homogeneous case, energy production terms due to

mean velocity gradients in the gas phase need to be taken into consideration since the direct injection process is modeled as a free-shear flow for the gas-phase turbulence [141]. It is therefore appropriate to provide closures for these production terms, considering a constant turbulence Reynolds number as is observed for single-phase turbulent jets [141]. For this purpose, we deduce an analytical expression for Π_g^k in Eq. (6.93) and Eq. (6.92), respectively, corresponding to a self-similar turbulent jet:

$$\Pi_g^k = \left(\frac{2 - C_{g,\epsilon}^2}{2 - C_{g,\epsilon}^1}\right) \rho_g \varepsilon_g, \quad \Pi_d^k = \left(\frac{2 - C_{d,\epsilon}^2}{2 - C_{d,\epsilon}^1}\right) m_{3/2} \varepsilon_d. \tag{6.95}$$

In the absence of two-way coupling, this expression for Π_g^k will yield a constant turbulence Reynolds number as expected for a turbulent jet [141]. However, due to two-way coupling, the turbulence Reynolds number under ICE conditions will vary with time (or distance from the nozzle). The model for Π_d^k is taken in analogy to the gas phase.

In the following, three time-dependent homogeneous cases are considered, based on the following initial conditions: (i) single-phase gas flow, (ii) two-phase flow of a compressible gas and a non-evaporating polydisperse spray and (iii) two-phase flow composed of a compressible gas and an evaporating polydisperse spray. Case (i) is a reference case for a self-similar turbulent jet where the data corresponds to the centerline turbulence statistics moving with the mean velocity. Case (ii) uses the same initial conditions as case (i) but with $R_S = 0$, and thus illustrates the effect of two-way coupling due to drag on the turbulence statistics. Finally, case (iii) shows the additional effect of droplet evaporation on two-way coupling. For reference, the mean velocities and the spray density concentration are shown in Fig. 6.7 as a function of dimensionless time. (In all figures, the time is made dimensionless by the initial gas-phase integral time scale.) Note that the mean momentum equations (see, e.g., Eq. (6.90)) do not contain terms corresponding to the spread of the turbulent jet, which would lower the mean velocities. Thus, the mean velocities plotted in Fig. 6.7 can be thought of as normalized values relative to the centerline jet velocity. In any case, from Fig. 6.7 we can observe that for the two spray cases the mean velocities are nearly equal for $t \geq 4\tau_g$. The fact that the two spray cases have nearly the same velocity profiles is due to the relatively slow evaporation rate for case (iii) as seen from the slow decrease in the spray density concentration.

Figures 6.8 and 6.9 present the evolution of the turbulence Reynolds number and gas-phase energies, respectively, for each case. As expected due to the modeling assumptions for Π_g^k and Π_d^k, in case (i) the turbulence Reynolds number remains constant although the gas-phase TKE decreases with time. For cases (ii) and (iii), the turbulence Reynolds number first increases and decreases sharply at the beginning of the simulation and then slowly decreases. This behavior comes from the fact that the presence of droplets increases significantly the gas-phase TKE k_g due to two-way coupling (i.e., the source terms in Eq. (6.93) involving C_g). It can also be remarked that the gas-phase internal energy increases up to ~ 8 from 0.5 for cases (ii) and (iii), whereas it remains quite low for case (i). This difference comes from the two-way coupling source terms, especially due to the mean velocity difference between the two phases shown in Fig. 6.7, which has a significant effect on the gas-phase turbulence.

In Fig. 6.10, the spray-phase energy partition and the TKE dissipation rates are given

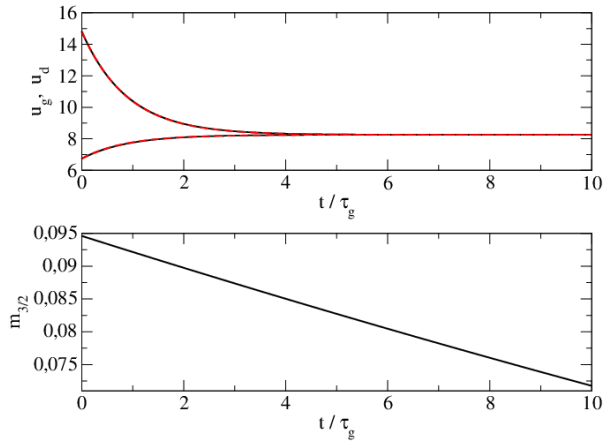

Figure 6.7: Mean velocities versus time (top) for cases (ii) (solid black lines) and (iii) (dashed red lines). Spray density concentration $m_{3/2}$ versus time for case (iii) (dashed red lines).

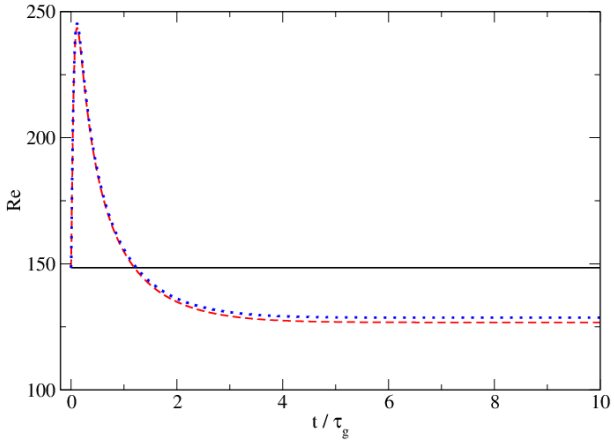

Figure 6.8: Turbulence Reynolds number Re versus time. Cases (i) solid black lines, (ii) dashed red lines, and (iii) blue dots.

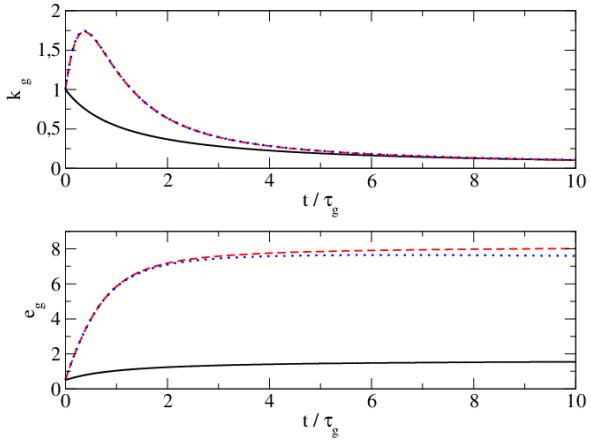

Figure 6.9: Dimensionless gas-phase TKE k_g (top) and gas-phase internal energy e_g (bottom) versus time. Cases (i) solid black lines, (ii) dashed red lines, and (iii) blue dots.

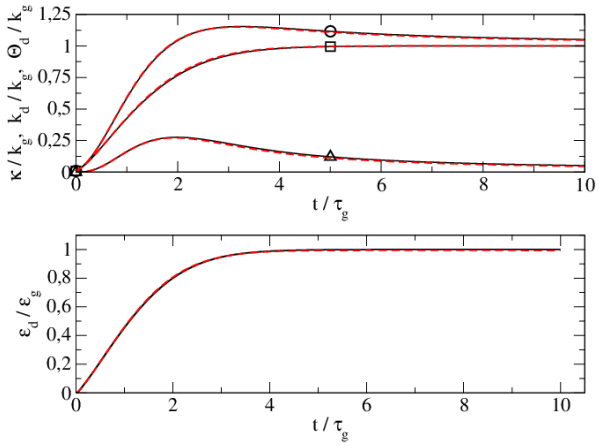

Figure 6.10: Normalized total fluctuating energy κ (top, circle), spray-phase TKE k_d (top, square), granular temperature Θ (top, triangle) and spray-phase TKE dissipation ε_d (bottom) versus time. Cases (ii) (solid black lines) and (iii) (dashed red lines).

for cases (ii) and (iii). It can be observed that the complete relaxation between the gas and spray does not take place since the the normalized spray-phase TKE k_d remains below one. Nonetheless, the energy partition seems reasonable since the granular temperature Θ tends to diminish while the spray-phase TKE k_d and the total fluctuating energy κ become closer and approach k_g with time. Note the differences between cases (ii) and (iii) are minimal due to the relatively slow evaporation of droplets in case (iii). Overall, the spray-phase turbulence is driven by the energy exchange terms from the gas phase due to drag, although as seen in Fig. 6.9 the presence of droplets significantly increases the gas-phase turbulence and, hence, leads to turbulence in the spray phase.

6.5 Conclusions

Within the context of two-phase turbulence modeling for ICE applications, the main purpose of the present contribution is to apply the Reynolds-averaging (RA) philosophy, originally introduced for two-way coupled monodisperse flows in [64], to two-way coupled polydisperse flows with evaporating droplets and a compressible gas [84]. For clarity, we have considered only the simplest forms for drag model through Stokes law and d^2-constant evaporation law for the droplets. However, the generalization to more complex models should be straightforward.

In the context of homogeneous two-phase turbulence, the new model has been investigated for polydispere droplets with both one-way and two-way coupling. The realizability condition of EMSM method has been successfully respected, validating the adequacy of the new turbulence modeling approach with high-order moment methods in the presence of spray evaporation. Moreover, it has been qualitatively validated as compared to work done in [59] within the framework of one-way coupling. The correct behavior of the energy partition in the two-phase flow has been also observed for two-way coupled evaporating and non-evaporating sprays. As far as industrial applications are concerned, the model has been studied under realistic characteristic scales and values provided from the data

of 3D injection simulations (spray-h conditions [1]) in the industrial CFD code IFP-C3D [12]. The latter work gave some significant insights on the underlying physics although it lacks of quantitative validations.

Given these achievements, the model is now ready to be implemented in an industrial software (i.e. IFP-C3D [12]). However, further effort is required for its numerical resolution using the ALE formalism for moving geometries. Let us recall that for laminar two-phase flows, the two-way coupled EMSM method had been successfully implemented in [84] using a pressure-less gas formalism for its resolution. However, the fact that there are many gradients arising from the turbulence model renders the task more complicated. As soon as the numerical implementation is complete, the turbulence model should be tested under realistic injection conditions and quantitatively validated against experimental data.

Chapter 7

General conclusions and perspectives

Within the framework of high-fidelity CFD simulations dedicated to High Pressure Direct Injection in internal combustion engines (ICE), the main focus of this PhD work has been the two-phase flow modeling of the evaporating polydisperse spray composed of spherical droplets and the compressible gas, the flow regime encountered at far downstream of the injector. Following the project of IFP Energies nouvelles to simulate the full injection process in a consistent way, the Eulerian description for the spray has been adopted instead of the widely used Lagrangian approach. Among few Eulerian models able to describe accurately both the polydispersity and the evaporation characteristics of droplets, a kinetic based Eulerian high order moment method called Eulerian Multi-Size Moment (EMSM) method has been demonstrated, through the PhD of Kah [83] to be very promising for industrial application. Yet for a better understanding of underlying physics, driving two-phase combustion regimes and pollutant formation, more studies needed to be carried out. In that context, the work conducted in the present PhD contribution was expected to answer three major questions:

- In the context of one-way coupling of polydisperse spray with the gas, that is, the simple effect of the gas on the spray, some fundamental results had been obtained in [83] under laminar flow regimes. Yet its extension to a two-way coupling framework was an unexplored issue and presents two major difficulties. First, although both the gas and the spray were described through the Eulerian approach at macroscopic level, there are still some fundamental modeling differences between them. Second, the realizability condition required to be respected for the EMSM along with the numerical stability issues associated to fast dynamic time scales encountered in a realistic flow are considered to be some major difficulties from the numerical resolution point of view.

- In realistic ICE under high turbulence intensity, the Kolmogorov length scale of the flow is very small and makes prohibitive DNS simulations. To overcome this difficulty, industrial codes use either LES or Reynolds Averaging (RA) formalism for the turbulence flow modeling. In the IFPC3D code, the two-way coupling between the gas and the polydisperse evaporating spray were required to be extended to the RA formalism. Yet taking into account the effect of the gas-phase turbulence on droplet dynamics, the turbulence modulation in the gas due to presence of droplets

and the issue of polydispersity were considered as major bottlenecks points, requiring a new RA model.

- In the context of industrial simulations, the EMSM method had been successfully extended to a moving mesh formalism and implemented in IFPC3D software, respecting the unstructured nature of the code. It had been proven efficient for injection applications under a 2D geometry, laminar and one-way coupling context.Yet its feasibility under the two-way coupling extension, the typical 3D engine geometry and the realistic injection boundary conditions were required to be validated.

Thanks to the present PhD thesis, all these bottleneck points required to be resolved towards realistic ICE studies have been successfully addressed in three chapters. In Chapter 3 which is entirely devoted to the investigation of the two-way polydisperse coupling modeling of the evaporating spray with the compressible gas, taking into account a numerical formalism for moving geometries and under a simply evaporation law. The effectiveness of the new numerical strategy dedicated to the two-way coupling has been demonstrated from theoretical point of view and validated under more practical framework through an implementation in the industrial CFD software IFP-C3D dedicated to compressible reactive flows in ICE. In Chapter 4, the two-way coupling modeling has been extended to more applicative cases through the consideration of a realistic droplet evaporation. A rigorous numerical analysis has been conducted for both simple and realistic evaporation of polydisperse droplets. The effect of the realistic evaporation has been investigated under the IFP-C3D. Moreover, the feasibility of the the two-way polydisperse coupling modeling of the evaporating spray with the compressible and turbulent gas under a typical 3D ICE geometry and a more realistic velocity boundary conditions for the injection has been studied in Chapter 5. In Chapter 6, firstly, the extension of the two-way coupling modeling to the RANS framework has been conducted through a rigorous derivation of equations by means of the Reynolds averaging technique and some effective closures have been proposed. The new model has been tested and validated under some homogeneous test-cases.

The achievements of the thesis can be classify into following three sections:

- In terms of modeling (point of view):
  - the two-way polydisperse coupling model, composed of the original EMSM method for the spray description and the compressible Navier Stokes equations for the gas-phase, which involves some non transported moments is successfully closed through the use of the maximum entropy technique and respecting the mass and momentum conservation of the global two-phase system.
  - the extension of the two-way coupling to the turbulence modeling under the Reynolds average formalism, has been achieved through a close collaboration with Rodney Rox. The fluctuating energy partitions inside the spray phase has been validated as compared to theoretical work done in [64, 175]. Moreover, the fact that the velocity distribution is taken as an Isotropic Gaussian distribution rather then the monokinetic one originally adopted in EMSM method, this work can be considered as a fruitful achievement in taking into account the phenomenon of homo-PTC.

- In terms of numerical development (point of view)
  - Through theoretical evaluations, the new two-way coupling resolution strategy developed in this thesis has been proved to guarantee the stability while providing a good accuracy and respecting the realizability condition. This aspect is particularly important since the global time step of the simulation is not conditioned by the fastest scale of the two-way coupling (i.e. the dynamic time scale of very small evaporating droplets).
  - In Chapter 4, a detailed numerical analysis of the two-way coupling numerical strategy showed that a third order accuracy for spray and gas velocities and the first order of accuracy for spray and gas density concentrations have been obtained. Despite the first order, results were very accurate as compared to reference solutions.
  - The numerical strategy has been successfully implemented in unstructured industrial CFD code for compressible and reactive flows IFP-C3D.
- In terms of injection simulations
  - the new Eulerian two-way coupled polydisperse spray, available in IFP-C3D code, has been compared to the widely used Lagrangian approach in the context of a 2D geometry. Results issued from the comparisons have been very encouraging for combustion applications since both the spray and the gas phases (i.e fuel vapor partition in the domain) are both qualitatively and quantitatively very well captured by the Eulerian method.
  - Results from the 3-D configuration under the realistic injection conditions have given rise to promising qualitative results.

As far as the perspectives of this work are concerned, three types of extensions can be envisioned:

- Given the achievements of two-way turbulent polydisperse coupling between the spray and the gas, the model should be implemented in the industrial code IFP-C3D [12]. However, further effort is required for its numerical resolution using the ALE formalism for moving geometries. Let us recall that all the development conducted through EMSM method in IFP-C3D was in the context of pressure-less gas formalism. Yet the new k-ε Reynolds averaged turbulence model, based on polykinetic approach implies many gradient terms which require to be correctly resolved. This issue requires thus some numerical efforts. As soon as the numerical resolution through ALE is achieved, first, some preliminary test-cases should be conducted and quantitative comparisons with either DNS simulations or experimental studies need to be done. Although the latter work was conducted in [64] for monodisperse flows, the new closure models for correlations arise form the polydispersity, the gas-phase compressiblity and the evaporation are required to be validated. The next step would be to carry on the same validation strategy under ICE applications. Thanks to an appropriate engine configuration, the new method should be compared to both

the existing turbulence model for Lagrangian Stochastic particles in IFP-C3D and the experimental results.

- It has been shown in Chapter 4 that the order of accuracy of the two-way coupling strategy should be increased to deal with realistic evaporation models with a dependency on time. Yet although it is the first order scheme in evaporation which is for instance implemented in IFP-C3D, results are promising as compared to reference Lagrangian simulations. But the implementation of the second order scheme discussed in Chapter 4 is important to deal with time scales related to the broad range of engine ambiant conditions. Moreover, the necessity of taking into account the size-velocity correlations for large inertia droplets have been discussed so far in this PhD. It is therefore essential to extent the two-way coupling method, integrating both modeling and numerical functionalities introduced in [189]. After, all these numerical developments, a rigorous study on CPU time of the two-way coupling resolution should be done compared to a reference method widely used for the industrial simulations.

- Following the ambitious project of IFP Energies nouvelles to simulate, in a consistent way, the complete injection in ICE, the Eulerian polydisperse spray developed in [83] should be coupled to a separate-phase breakup model. Let us recall that it is possible to bypass the modeling of dense injection zones, calculating approximate boundary conditions for a Eulerian disperse-phase model [108]. Yet, due to the very complex and the unsteady behavior of ligaments and the liquid core near injector, the full Eulerian resolution of the dense zone is required [104, 105]. Therefore the transition zone between pure disperse and pure separated-phases should be modeled and a numerical coupling strategy should be envisaged.

References

[1] *Engine combustion network data archive, http://www.sandia.gov/ecn/.*

[2] B. Abramzon and W. A. Sirignano, *Droplet vaporisation model for spray combustion calculations*, International Journal of Heat and Mass Transfer, 9 (1989), pp. 1605–1618.

[3] G. Allaire, S. Clerc, and S. Kokh, *A five-equation model for the simulation of interfaces between compressible fluids*, J. Comput. Phys., 181 (2002), pp. 577–616.

[4] A. Amsden, P. J. O'Rourke, and T. D. Butler, *KIVA II: A computer program for chemically reactive flows with sprays*, Tech. Rep. LA-11560-MS, Los Alamos National Laboratory, Los Alamos, New Mexico, 1989.

[5] S. V. Apte, S. Martin, and S. A. Patankar, *A numerical method for fully resolved simulation (FRS) of rigid particle-flow interactions in complex flows*, Journal of Computational Physics, 228 (2009), pp. 2712 – 2738.

[6] M. R. Baer and J. W. Nunziato, *A two-phase mixture theory for the deflagration-to-detonation transition (DDT) in reactive granular materials*, Int. J. Multiphase Flow, 12 (1986), pp. 861–889.

[7] S. Balachandar and J. K. Eaton, *Turbulent dispersed multiphase flow*, Ann. Rev. Fluid Mech., 42 (2010), pp. 111–133.

[8] F. Bayoro, *Prise en compte de l'écoulement du liquide dans l'injecteur dans la modélisation des jets de carburant diesel, raport de thèse à mi-parcours*, tech. rep., IFP Energies nouvelles, 2008.

[9] R. BenDakhlia, *Combustion stationnaire et instationnaire de mlanges diphasiques*, PhD thesis, Ecole Centrale Paris, 2001.

[10] C. Berthon, *Numerical approximations of the 10-moment Gaussian closure*, Math. Comp., 75 (2006), pp. 1809–1831.

[11] G. A. Bird, *Molecular gas dynamics and the direct simulation of gas flows*, Oxford Science Publications, 42 (1994).

[12] J. Bohbot, N. Gillet, and A. Benkenida, *IFP-C3D: an unstructured parallel solver for reactive compressible gas flow with spray*, Oil Gas Sci. Tech., 64 (2009), pp. 309–335.

[13] F. Bouchut, *On zero pressure gas dynamics*, in Advances in kinetic theory and computing, vol. 22 of Ser. Adv. Math. Appl. Sci., World Science Publisher, River Edge, NJ, 1994, pp. 171–190.

[14] F. Bouchut, S. Jin, and X. Li, *Numerical approximations of pressureless and isothermal gas dynamics*, SIAM J. Numer. Anal., 41 (2003), pp. 135–158.

[15] S. Bougrine, *Modlisation 0D de la combustion des carburants alternatifs dans les moteurs à allumage commandé*, PhD thesis, Ecole Centrale Paris, 2012.

[16] J. Capecelatro and O. Desjardins, *An Euler-Lagrange strategy for simulating particle-laden flows*, J. Comp. Phys., 238 (2013), pp. 1–31.

[17] A. Cervone, S. Manservisi, R. Scardovelli, and S. Zaleski, *A geometrical predictor-corrector advection scheme and its application to the volume fraction function*, Journal of Computational Physics, 228 (2009), pp. 406 – 419.

[18] C. Chalons, R. O. Fox, F. Laurent, M. Massot, and A. Vié, *A multi-Gaussian quadrature-based moment method for dispersed multiphase flows*, Submitted (HAL), (2013).

[19] C. Chalons, R. O. Fox, and M. Massot, *A multi-Gaussian quadrature method of moments for gas-particle flows in a LES framework*, in Proceedings of the Summer Program 2010, Center for Turbulence Research, Stanford University, Stanford, 2010, pp. 347–358.

[20] C. Chalons, D. Kah, and M. Massot, *Beyond pressureless gas dynamics: quadrature-based velocity moment models*, Commun. Math. Sci., 10 (2012), pp. 1241–1272.

[21] S. Chapman and T. G. Cowling, *The Mathematical Theory of Non-Uniform Gases*, Cambridge Mathematical Library, 1970.

[22] V. L. Chenadec and H. Pitsch, *A 3D Unsplit Forward/Backward Volume-of-Fluid Approach and Coupling to the Level Set Method* , Journal of Computational Physics, 233 (2013), pp. 10–33.

[23] ——, *A monotonicity preserving conservative sharp interface flow solver for high density ratio two-phase flows*, Journal of Computational Physics, 249 (2013), pp. 185 – 203.

[24] J. Chesnel, T. Menard, J. Reveillon, and F.-X. Demoulin, *Subgrid analysis of liquid jet atomization*, Atomization and Sprays, 21 (2011), pp. 41–67.

[25] J. Chesnel, J. Reveillon, T. Menard, and F.-X. Demoulin, *Large eddy simulation of liquid jet atomization*, Atomization and Sprays, 21 (2011), pp. 711–736.

[26] R. Clift, J. R. Grace, and M. E. Weber, *Bubbles, Drop and Particles*, Academic Press, New York, 1978.

[27] F. Coquel, Q. L. Nguyen, M. Postel, and Q. H. Tran, *Entropy-satisfying relaxation method with large time-steps for Euler IBVPs*, Math. Comp., 79 (2010), pp. 1493–1533.

[28] C. T. Crowe, M. Sharma, and D. Stock, *The particle-source-in cell (PSI-CELL) model for gas-droplet flows*, J. Fluids Eng., 99 (1977), pp. 325–332.

[29] C. T. Crowe, M. Sommerfeld, and Y. Tsuji, *Multiphase Flows with droplets and particles*, CRC Press, Boca Raton, Florida, 1998.

[30] S. de Chaisemartin, *Eulerian models and numerical simulation of turbulent dispersion for polydisperse evaporating sprays*, PhD thesis, Ecole Centrale Paris, France, 2009. `http://tel.archives-ouvertes.fr/tel-00443982/en/`.

[31] S. de Chaisemartin, L. Fréret, D. Kah, F. Laurent, R. Fox, J. Reveillon, and M. Massot, *Eulerian models for turbulent spray combustion with polydispersity and droplet crossing*, C. R. Mécanique, 337 (2009), pp. 438–448. Special Issue Combustion for Aerospace Propulsion.

[32] J. M. Delhaye and J. L. Achard, *On the averaging operators introduced in a two-phase flow modeling*, in Proceedings CSNI Specialist Meeting in transient two-phase flow, 1976, pp. 5–84.

[33] F.-X. Demoulin, P. Beau, G. Blokkeel, A. Mura, and R. Borghi, *A new model for turbulent flows with large density fluctuations: application to liquid atomization*, Atomization and Sprays, 17 (2007), pp. 315–345.

[34] J. Derksen, *Dense suspensions-solid–liquid interactions at the particle scale*, Progress in Computational Fluid Dynamics, an International Journal, 12 (2012), pp. 103–111.

[35] O. Desjardins and J. Capecelatro, *Large-scale Eulerian-Lagrangian simulations of turbulent particle-laden riser flows*, Bulletin of the American Physical Society, 56 (2011), p. 106.

[36] O. Desjardins and P. Pepiot, *Analysis of dense particulate flow dynamics using a euler-lagrange approach*, Bulletin of the American Physical Society, 54 (2009), p. 106.

[37] B. Després and C. Mazeran, *Lagrangian gas dynamics in two-dimensions and Lagrangian systems*, Arch. Ration. Mech. Anal., 178 (2005), pp. 327–372.

[38] H. Dette and W. J. Studden, *The theory of canonical moments with applications in statistics, probability, and analysis*, Wiley Series in Probability and Statistics: Applied Probability and Statistics, John Wiley & Sons Inc., New York, 1997. A Wiley-Interscience Publication.

[39] F. Doisneau, *Eulerian modeling and simulation of polydisperse moderately dense coalescing spray flows with nanometrictoinertial droplets:application to Solid Rocket Motors*, PhD thesis, Ecole Centrale de Paris, 2013.

[40] F. Doisneau, F. Laurent, A. Murrone, J. Dupays, and M. Massot, *Eulerian multi-fluid models for the simulation of dynamics and coalescence of particles in solid propellant combustion*, J. Comput. Phys., 234 (2013), pp. 230–262.

[41] F. Doisneau, A. Sibra, J. Dupays, A. Murrone, F. Laurent, and M. Massot, *An efficient and accurate numerical strategy for two-way coupling in unsteady polydisperse moderately dense sprays: application to Solid Rocket Motor instabilities*, Journal of Propulsion and Power, (2013), pp. 1–39. In Press, Available on HAL, `http://hal.archives-ouvertes.fr/hal-00745991`.

[42] F. Doisneau, O. Thomine, F. Laurent, A. Vié, and M. Massot, *Eulerian modeling and simulation of small scale trajectory crossing and coalescence for moderate-stokes-number spray flows*, in Volume du Summer Program 2012, publication du Center for Turbulence Research, Stanford University, 2012, pp. 365–374.

[43] J. Donea, A. Huerta, J. P. Ponthot, and A. Rodríguez-Ferran, *Arbitrary Lagragian-Eulerian methods*, in Encyclopedia of Computational Mechanics, E. Stein, R. de Borst, and T. Hughes, eds., vol. 1, John Wiley & Sons, 2004, ch. 14, pp. 413–437.

[44] M. Duarte, Z. Bonaventura, M. Massot, A. Bourdon, S. Descombes, and T. Dumont, *A new numerical strategy with space-time adaptivity and error control for multi-scale streamer discharge simulations*, J. Comput. Phys., 231 (2012), pp. 1002–1019.

[45] G. Dufour, *Modélisation multi-fluide eulérienne pour les écoulements diphasiques à inclusions dispersées*, PhD thesis, Université Paul Sabatier Toulouse III, 2005.

[46] J. K. Dukowicz, *A Particle-Fluid Numerical Model for Liquid Sprays*, Journal of Computational Physics, 35 (1980), pp. 229–253.

[47] ——, *A particle-fluid numerical model for liquid sprays*, J. Comput. Phys., 35 (1980), pp. 229–253.

[48] A. Dulbecco, *Modeling of diesel HCCI combustion and its impact on pollutant emissions applied to global engine system simulation*, PhD thesis, University of Toulouse, 2009.

[49] C. Dumouchel, *On the experimental investigation on primary atomization of liquid streams*, Experiments in Fluids, 45 (2008), pp. 371–422.

[50] P. A. Durbin, *Separated Flow Computations with the k-ε-v^2 Model*, AIAA, 33 (1995), pp. 659–664.

[51] B. Duret, *Simulation numérique directe des écoulements liquide-gaz avec évaporation : application à l'atomisation*, PhD thesis, Institut National des Sciences Appliquées (INSA) Rouen, 2013.

[52] S. Elghobashi and G. C. Truesdell, *Direct numerical simulation of particle dispersion in a decaying isotropic turbulence*, J. Fluid Mech., 242 (1992), pp. 655–700.

[53] O. Emre, R. O. Fox, M. Massot, S. de Chaisemartin, S. Jay, and F. Laurent, *Towards eulerian modeling of a polydisperse evaporating spray under realistic internal-combustion-engine conditions*, Flow, Turbulence and Combustion, 93 (2014), pp. 689–722.

[54] O. Emre, D. Kah, S. Jay, Q.-H. Tran, A. Velghe, S. de Chaisemartin, R. Fox, F. Laurent, and M. M., *Eulerian moment methods for automotive sprays*, Accepted for a publication in Atomization and Sprays, (2014), pp. 1–44.

[55] O. Emre, F. Laurent, S. de Chaisemartin, S. Jay, and M. Massot, *Numerical analysis of a two-way coupled Eulerian high order moment method for the simulation of polydisperse evaporating sprays*, Submitted, (2014), pp. 1–28. available on HAL.

[56] G. Faeth, *Evaporation and combustion of spray*, Progress in Energy and Combustion Science, 9 (1983), pp. 1–76.

[57] C. Farhat, P. Guezaine, and C. Grandmont, *The discrete geometric conservation law and the nonlinear stability of ALE schemes for the solution of flow problems on moving grids*, J. Comput. Phys., 174 (2001), pp. 669–694.

[58] V. Ferrand, R. Bazile, J. Borée, and G. Charnay, *Gas droplet turbulent velocity correlations and two-phase interaction in an axisymmetric jet laden with partly responsive droplets*, Int. J. Multiphase Flow, 29 (2003), pp. 195–217.

[59] P. Fevrier, O. Simonin, and K. D. Squires, *Partitioning of particle velocities in gas-solid turbulent flows into a continuous field and a spatially uncorrelated random distribution: theoretical formalism and numerical study*, Journal of Fluid Mechanics, 533 (2005), pp. 1–46.

[60] R. O. Fox, *Computational Models for Turbulent Reacting Flows*, UK:Cambridge University Press, Cambridge, 2003.

[61] ——, *Fundamental of polydisperse multiphase flows*, in Computational Models for Turbulent Multiphase Reacting Flows, D. L. Marchisio and R. O. Fox, eds., vol. 492 of CISM Courses and Lectures, Springer, Vienna, 2007, pp. 79–123.

[62] R. O. Fox, *Introduction and fundamentals of modeling approaches for polydisperse multiphase flows*, in Multiphase Reacting Flows: Modelling and Simulation, D. L. Marchisio and R. O. Fox, eds., vol. 492 of CISM International Centre for Mechanical Sciences, Springer Vienna, 2007, pp. 1–40.

[63] ——, *Large-Eddy-Simulation tools for multiphase flows*, Annual Review of Fluid Mechanics, 44 (2012), pp. 47–76.

[64] R. O. Fox, *On multiphase turbulence models for collisional fluid-particle flows*, J. Fluid Mech., (2014). In press.

[65] R. O. Fox, F. Laurent, and M. Massot, *Numerical simulation of spray coalescence in an Eulerian framework: direct quadrature method of moments and multi-fluid method*, J. Comput. Phys., 227 (2008), pp. 3058–3088.

[66] L. Fréret, S. De Chaisemartin, J. Reveillon, F. Laurent, and M. Massot, *Eulerian models and three-dimensional numerical simulation of polydisperse sprays*, in Proceedings of the International Conference on Multiphase Flows, Tampa, Florida, 2010, pp. 1–12. http://hal.archives-ouvertes.fr/hal-00498207/en/.

[67] L. Fréret, C. Lacour, S. de Chaisemartin, S. Ducruix, D. Durox, F. Laurent, and M. Massot, *Pulsated free jets with polydisperse spray injection : Experiments and numerical simulations*, in Proceedings of the Combustion Institute, vol. 32, 2009, pp. 2215–2222.

[68] L. Fréret, O. Thomine, J. Reveillon, S. de Chaisemartin, F. Laurent, and M. Massot, *On the role of preferential segregation in flame dynamics in polydisperse evaporating sprays*, in Proceedings of the Summer Program 2010, Center for Turbulence Research, Stanford University, 2011, pp. 383–392.

[69] L. Fréret, O. Thomine, S., F. Laurent, J. Reveillon, and M. Massot, *Direct numerical simualtion of polydisperse evaporating sprays in 3d jet configuration using euler-eulerand euler-lagrange formalisms*, in Volume du Summer Program 2012, publication du Center for Turbulence Research, Stanford University, 2012, pp. 345–354.

[70] D. Fuster, A. Bagu, T. Boeck, L. L. Moyne, A. Leboissetier, S. Popinet, P. Ray, R. Scardovelli, and S. Zaleski, *Simulation of primary atomization with an octree adaptive mesh refinement and VOF method*, International Journal of Multiphase Flow, 35 (2009), pp. 550 – 565.

[71] M. Garcia, *Développement et validation du formalisme Euler-Lagrange dans un solveur parallle non-structur pour la simulation aux grandes chelles*, PhD thesis, Institut National Polytechnique de Toulouse, 2009.

[72] G. A. E. Godsave, *Studies of the combustion of drops in a fuel spray: the burning of single drops of fuel*, in Proceedings of the 4th Symp. (International) on Combustion, The Comb. Institute, Baltimore, 1953, pp. 818–830.

[73] J. Greenberg, I. Silverman, and Y. Tambour, *On the origin of spray sectional conservation equations*, Combustion and Flame, 93 (1993), pp. 90–96.

[74] C. Habchi, *Modélisation tridimensionnelle de l'injection et de la préparation du mélange gaz/carburant dans les moteurs à combustion interne*, Mémoire de HDR, 2006.

[75] E. Hairer and G. Wanner, *Solving Ordinary Differential Equations. II: Stiff and Differential-Algebraic Problems*, vol. 2 of Springer Series In Computational Mathematics, Springer, Berlin, 1996.

[76] M. Herrmann, *A balanced force refined level set grid method for two-phase flows on unstructured flow solver grids*, Journal of Computational Physics, 227 (2008), pp. 2674 – 2706.

[77] J. B. Heywood, *Internal Combustion Engine Fundamentals*, McGraw-Hill series in mechanical engineering, 1988.

[78] C. W. Hirt, A. A. Amsden, and J. L. Cook, *An arbitrary Lagrangian-Eulerian computing method for all flow speeds*, J. Comput. Phys., 14 (1974), pp. 227–253.

[79] A. Huerta and W. Liu, *Viscous flow structure interaction*, J. Pressure Vessel Technol., 110 (1988), pp. 15–21.

[80] K. Hyland, S. McKee, and M. Reeks, *Derivation of a PDF kinetic equation for the transport of particles in turbulent flows*, J. Phys. A, 32 (1999), pp. 6169–6190.

[81] J. J. Hylkema, *Modélisation cinétique et simulation numérique d'un brouillard dense de gouttelettes. Application aux propulseurs à poudre*, PhD thesis, Ecole Nationale Supérieure de l'Aéronautique et de l'Espace, 1999.

[82] M. Ishii, *Thermo-Fluid dynamic theory of two-phase flow*, Eyrolles, 1975.

[83] D. Kah, *Taking into account polydispersity for the modeling of liquid fuel injection in internal combustion engines*, PhD thesis, Ecole Centrale Paris, `http://tel.archives-ouvertes.fr/tel-00618786`, 2010.

[84] D. Kah, O. Emre, Q. H. Tran, S. de Chaisemartin, S. Jay, F. Laurent, and M. Massot, *High order moment method for polydisperse evaporating spray with mesh movement: application to internal combustion engines*, Submitted, (2014).

[85] D. Kah, F. Laurent, L. Fréret, S. de Chaisemartin, R. Fox, J. Reveillon, and M. Massot, *Eulerian quadrature-based moment models for polydisperse evaporating sprays*, Flow Turbul. Combust., 85 (2010), pp. 649–676. Special Issue Dedicated to Stephen B. Pope.

[86] D. Kah, F. Laurent, M. Massot, and S. Jay, *Modeling of polydisperse sprays using a high order size moment method for the numerical simulation of advection and evaporation*, in Proceedings of the 11th ICLASS, International Conference on Liquid Atomization and Spray Systems Vail, Colorado, 2009.

[87] D. Kah, F. Laurent, M. Massot, and S. Jay, *A high order moment method simulating evaporation and advection of a polydisperse liquid spray*, J. Comput. Phys., 231 (2012), pp. 394–422.

[88] R. J. Kee, F. M. Rupley, and J. A. Miller, *Chemkin-ii: A fortran chemical kinetics package for the analysis of gas-phase chemical kinetics*, tech. rep., 1989.

[89] S. Kokh and F. Lagoutière, *An anti-diffusive numerical scheme for the simulation of interfaces between compressible fluids by means of a five-equation model*, J. Comput. Phys., 229 (2010), pp. 2773–2809.

[90] F.-A. Lafossas, O. Colin, F. L. Berr, and P. Menegazzi, *Application of a new 1D combustion model to gasoline transient engine operation*, SAE paper, 2005-01-2107 (2005).

[91] O. Laget, B. Reveille, C. Habchi, , L. Martinez, K. Truffin, and C. Angelberger, *Les Calculations of a Four Cylinder Engine*, SAE Technical Paper, (2011).

[92] F. Laurent, *Modélisation mathématique et numérique de la combustion de brouillards de gouttes polydispersés*, PhD thesis, Université Claude Bernard, Lyon 1, 2002.

[93] ——, *Numerical analysis of Eulerian multi-fluid models in the context of kinetic formulations for dilute evaporating sprays*, M2AN Math. Model. Numer. Anal., 40 (2006), pp. 431–468.

[94] F. Laurent and M. Massot, *Multi-fluid modeling of laminar polydispersed spray flames: origin, assumptions and comparison of the sectional and sampling methods*, Combust. Theor. Model., 5 (2001), pp. 537–572.

[95] F. Laurent, M. Massot, and P. Villedieu, *Eulerian multi-fluid modeling for the numerical simulation of coalescence in polydisperse dense liquid sprays*, J. Comput. Phys., 194 (2004), pp. 505–543.

[96] F. Laurent, A. Sibra, and F. Doisneau, *Two-size moment eulerian multi-fluid model for polydisperse sprays: a flexible and efficient computational approach, in preparation*, (2014).

[97] F. Laurent, A. Vié, C. Chalons, R. Fox, and M. Massot, *A hierarchy of Eulerian models for trajectory crossing in particle-laden turbulent flows over a wide range of Stokes numbers*, in Annual Research Brief of the Center for Turbulence Research, Center for Turbulence Research, Stanford University, 2012, pp. 193–204.

[98] V. Le Chenadec, *A stable and conservative framework for detailed numerical simulation of primary atomization*, PhD thesis, Stanford University, 2012.

[99] S. Le Martelot, *Contribution la simulation numérique directe de l'ébullition*, PhD thesis, Aix Marseille Université, 2013.

[100] ——, *Simulation numérique directe de la crise d'ébullition dans les systèmes spatiaux*, PhD thesis, Ecole Polytech Marseille, 2013.

[101] R. Lebas, T. Menard, P. Beau, A. Berlemont, and F. Demoulin, *Numerical simulation of primary break-up and atomization: DNS and modelling study*, International Journal of Multiphase Flow, 35 (2009), pp. 247 – 260.

[102] R. J. Leveque, *Finite volume methods for hyperbolic problems*, Cambridge Texts in Applied Mathematics, Cambridge University Press, Cambridge, 2002.

[103] R. L. Libo, *Kinetic Theory: Classical, Quantum, and Relativistic Descriptions*, vol. 2 of Prentice-Hall Advanced Reference Series, London, 1998.

[104] B. Mandumpala Devassy, *Atomization modeling of liquid jets using an Eulerian-Eulerian model and a Surface Density Approach*, PhD thesis, Aix Marseille Université, 2013.

[105] B. Mandumpala Devassy, C. Habchi, and E. Daniel, *A new atomization model for high speed liquid jets using a turbulent, compressible, two-phase flow model and a surface density approach*, in Proceedings of the 25th ILASS, European Conference on Liquid Atomization and Spray Systems, Chania, Greece, 2013, pp. 1–8.

[106] D. L. Marchisio and R. O. Fox, *Solution of population balance equations using the direct quadrature method of moments*, J. Aerosol Sci., 36 (2005), pp. 43–73.

[107] C. Marle, *On macroscopic equations governing multiphase flow with diffusion and chemical reactions in porous media*, International Journal of Engineering Science, 20 (1982), pp. 643 – 662.

[108] L. Martinez, A. Benkenida, and B. Cuenot, *A model for the injection boundary conditions in the context of 3d simulation of diesel spray: Methodology and validation*, Fuel, 89 (2010), pp. 219 – 228.

[109] L. Martinez, A. Vié, S. Jay, A. Benkenida, and B. Cuenot, *Large Eddy Simulation of Fuel sprays using the Eulerian Mesoscopic Approach. Validations in realistic engine conditions*, in in ICLASS, 2009.

[110] F. Mashayek, *Direct numerical simulations of evaporating droplet dispersion in forced low Mach number turbulence*, International Journal of Heat and Mass Transfer, 41 (1998), pp. 2601–2617.

[111] F. Mashayek, F. Jaberi, R. Miller, and P. Givi, *Dispersion and polydispersity of droplets in stationary isotropic turbulence*, International Journal of Multiphase Flow, 23 (1997), pp. 337–355.

[112] E. Masi, *Theoretical and numerical study of the modeling of unsteady nonisothermal particle-laden turbulent flows by an Eulerian-Eulerian approach*, PhD thesis, Institut National Polytechnique de Toulouse, 2010.

[113] E. Masi and O. Simonin, *An algebraic-closure-based moment method for unsteady eulerian modeling of non-isothermal particle-laden turbulent flows in very dilute regime and high stokes number*, in 7th Int. Symposium on Turbulence, Heat and Mass Transfer, Palermo, IT, 2012.

[114] E. Masi, O. Simonin, and B. Bédat, *The mesoscopic eulerian approach for evaporating droplets interacting with turbulent flows*, Flow, Turbulence and Combustion, 86 (2011), pp. 563–583.

[115] E. Masi, O. Simonin, E. Riber, P. Sierra, and L. Gicquel, *Development of an algebraic-closure-based moment method for unsteady Eulerian simulations of particle-laden turbulent flows in very dilute regime*, International Journal of Multiphase Flow, 58 (2014), pp. 257 – 278.

[116] M. Massot, *Eulerian multi-fluid models for polydisperse evaporating sprays*, in Computational Models for Turbulent Multiphase Reacting Flows, D. L. Marchisio and R. O. Fox, eds., vol. 492 of CISM Courses and Lectures, Springer, Vienna, 2007, pp. 79–123.

[117] M. Massot, S. de Chaisemartin, L. Fréret, D. Kah, and F. Laurent, *Eulerian multi-fluid models : modeling and numerical methods*, in "Modeling and computations of nanoparticles in fluid flows", Lecture Notes of the von Karman Institute, NATO RTO-EN-AVT 169, 2009, pp. 1–86. Available on HAL : http://hal.archives-ouvertes.fr/hal-00423031/en/.

[118] M. Massot, R. Knikker, C. Péra, and J. Réveillon, *Lagrangian/Eulerian analysis of the dispersion of evaporating droplets in a non-homogeneous turbulent flow*, in In Proceedings of ICMF'04, 2004.

[119] M. Massot, F. Laurent, S. de Chaisemartin, L. Fréret, and D. Kah, *Eulerian multi-fluid models: modeling and numerical methods*, in Modelling and Computation of Nanoparticles in Fluid Flows, Lectures Notes of the von Karman Institute, NATO RTO-EN-AVT-169, 2009, pp. 1–86. `http://www.cso.nato.int/`.

[120] M. Massot, F. Laurent, D. Kah, and S. de Chaisemartin, *A robust moment method for evaluation of the disappearance rate of evaporating sprays*, SIAM J. Appl. Math., 70 (2010), pp. 3203–3234.

[121] B. Maury, A. Roudneff-Chupin, and F. Santambrogio, *A macroscopic crowd motion model of gradient flow type*, Mathematical Models and Methods in Applied Sciences, 20 (2010), pp. 1787–1821.

[122] G. Mauviot, A. Albrecht, and T. Poinsot, *A new 0D approach for Diesel combustion modeling coupling probability density function with complex chemistry*, SAE paper, 2006-01-3332 (2006).

[123] R. McGraw, *Description of aerosol dynamics by the quadrature method of moments*, Aerosol Science and Technology, 27 (1997), pp. 255–265.

[124] ——, *Numerical advection of correlated tracers: preserving particle size/composition moment sequences during transport of aerosol mixtures*, J. Phys.: Conf. Ser., 78 (2007), p. 5p.

[125] L. R. Mead and N. Papanicolaou, *Maximum entropy in the problem of moments*, J. Math. Phys., 25 (1984), pp. 2404–2417.

[126] T. Ménard, S. Tanguy, and A. Berlemont, *Coupling level set/VOF/ghost fluid methods: Validation and application to 3d simulation of the primary break-up of a liquid jet*, International Journal of Multiphase Flow, 33 (2007), pp. 510 – 524.

[127] R. Miller and J. Bellan, *Direct numerical simulation of a confined three-dimensional gas mixing layer with one evaporating hydrocarbon-droplet-laden stream*, Journal of Fluid Mechanics, 384 (1999), pp. 293–338.

[128] R. S. Miller and J. Bellan, *Direct numerical simulation and subgrid analysis of a transitional droplet laden mixing layer*, Phys. Fluid, 12 (2000), pp. 650–671.

[129] M. Moreau, O. Simonin, and B. Bédat, *Development of gas-particle euler-euler les approach: A priori analysis of particle sub-grid models in homogeneous isotropic turbulence*, Flow, Turbulence and Combustion, 84 (2010), pp. 295–324.

[130] J. B. Mossa, *Extension polydisperse pour la description euler-euler des écoulements diphasiques réactifs - TH/CFD/05/74*, PhD thesis, Institut National Polytechnique de Toulouse, 2005.

[131] A. Murrone and P. Villedieu, *Numerical modeling of dispersed two-phase flows*, tech. rep., Aerospace Lab 2, 2011.

[132] R. Nigmatulin, *Spatial averaging in the mechanics of heterogeneous and dispersed systems*, International Journal of Multiphase Flow, 5 (1979), pp. 353 – 385.

[133] P. J. O'Rourke, *Collective drop effects on vaporizing liquid sprays*, PhD thesis, Princeton University, 1981.

[134] A. Ozel, P. Fede, and O. Simonin, *Development of filtered Euler-Euler two-phase model for circulating fluidised bed: High resolution simulation, formulation and a priori analyses*, International Journal of Multiphase Flow, 55 (2013), pp. 43 – 63.

[135] M. Pai and S. Subramaniam, *Two-way coupled stochastic model for dispersion of inertial particles in turbulence*, Journal of Fluid Mechanics, 700 (2012), pp. 29–62.

[136] R. V. R. Pandyz and F. Mashayek, *Non-isothermal dispersed phase of particles in turbulent flow*, Journal of Fluid Mechanics, 475 (2003), pp. 205–245.

[137] S. V. Patankar, *Numerical Heat Transfer and Fluid Flow*, Hemisphere Publishing Corporation, Washington D. C., 1980.

[138] C. Pera, S. Chevillard, and J. Reveillon, *Effects of residual burnt gas heterogeneity on early flame propagation and on cyclic variability in spark-ignited engines*, Combustion and Flame, 160 (2013), pp. 1020 – 1032.

[139] B. Perthame, *Kinetic formulation of conservation laws*, vol. 21 of Oxford Lecture Series in Mathematics and its Applications, Oxford University Press, Oxford, 2002.

[140] T. Poinsot and D. Veynante, *Theoretical and numerical combustion*, R.T. Edwards, 2nd edition, 2005.

[141] S. B. Pope, *Turbulent Flows*, UK: Cambridge University Press, Cambridge, 2000.

[142] S. B. Pope, *Self-conditioned fields for large-eddy simulations of turbulent flows*, Journal of Fluid Mechanics, 652 (2010), pp. 139–169.

[143] N. Pottier, *Physique statistique hors d'équilibre - Processus irréversibles linéaires*, EDP Sciences, 2007.

[144] W. H. Press, S. A. Teukolsky, W. T. Vetterling, and B. P. Flannery, *Numerical Recipes in Fortran 77*, Cambridge Texts in Applied Mathematics, Cambridge University Press, Cambridge, 1992.

[145] N. P. Rayapati, M. V. Panchagnula, J. Peddieson, J. Short, and S. Smith, *Eulerian multiphase population balance model of atomizing, swirling flows*, International Journal of Spray and Combustion Dynamics, 3, pp. 111–135.

[146] M. W. Reeks, *On a kinetic equation for the transport of particles in turbulent flows*, Physics of Fluids A: Fluid Dynamics (1989-1993), 3 (1991), pp. 446–456.

[147] J. Reveillon, *DNS of spray combustion, dispersion evaporation and combustion*, in Computational Models for Turbulent Multiphase Reacting Flows, D. L. Marchisio and R. O. Fox, eds., vol. 492 of CISM Courses and Lectures, Springer, Vienna, 2007, p. 229.

[148] J. Reveillon, N. Bray, and L. Vervisch, *DNS study of spray vaporization and turbulent micro-mixing*, in 36th Aerospace Sciences Meeting and Exhibit, Reno NV, 1998.

[149] J. Reveillon and F.-X. Demoulin, *Effects of the preferential segregation of droplets on evaporation and turbulent mixing*, J. Fluid Mech, 583 (2007), pp. 273–302.

[150] J. Reveillon, M.Massot, and C. Pera, *Analysis and modeling of the dispersion of vaporizing polydispersed sprays in trubulent flows*, in Proceedings of the 2002 CTR Summer Program, Stanford, CA, 2002, Center for Turbulence Research, pp. 393–404.

[151] J. Reveillon and L. Vervisch, *Analysis of weakly turbulent diluted-spray flames and spray combustion regimes*, J. Fluid Mech., 537 (2005), pp. 317–347.

[152] E. Riber, M. Garcia, V. Moureau, H. Pitsch, O. Simonin, and T. Poinsot, *Evaluation of numerical strategies for les of two-phase reacting flows*, in Proceedings of the Summer Program 2006, Center for Turbulence Research, Stanford University, 2006.

[153] E. Riber, V. Moureau, M. Garcìa, T. Poinsot, and O. Simonin, *Evaluation of numerical strategies for large eddy simulation of particulate two-phase recirculating flows*, Journal of Computational Physics, 228 (2009), pp. 539–564.

[154] J. Riley and G. Paterson, *Diffusion experiments with numerically integrated isotropic turbulence*, Physics of Fluids, 17 (1974), pp. 292–297.

[155] P. Rosin and E. Rammler, *Laws governing the fineness of powdered coal*, J. Inst. Fuel, (1933), pp. 29–36.

[156] M. Ruger, S. Hohmann, M. Sommerfeld, and G. Kohnen, *Euler/Lagrange calculations of turbulent sprays: the effect of droplet collisions and coalescence*, Atomization and Sprays, 10 (2000), pp. 47–81.

[157] R. Saurel and R. Abgrall, *A multiphase Godunov method for compressible multifluid and multiphase flows*, Journal of Computational Physics, 150 (1999), pp. 425 – 467.

[158] R. Saurel and O. L. Metayer, *A multiphase model for compressible flows with interfaces, shocks, detonation waves and cavitation*, J. Fluid Mech., 431 (2000), pp. 239–271.

[159] R. Scardovelli and S. Zaleski, *Direct Numerical Simulation of free-surface and interfacial flow*, Annual Review of Fluid Mechanics, 31 (1999), pp. 567–603.

[160] L. Schiller and A. Nauman, *A drag coefficient correlation*, VDI Zeitung, 77 (1935), pp. 318–320.

[161] B. Shotorban and S. Balachandar, *A Eulerian model for large-eddy simulation of concentration of particles with small Stokes numbers*, Phys. Fluids, 19 (2007), p. 118107.

[162] P. Sierra, *Modeling the dispersion and evaporation of sprays in aeronautical combustion chambers*, PhD thesis, INP Toulouse, 2012.

[163] I. Silverman, J. B. Greenberg, and Y. Tambour, *Asymptotic analysis of a premixed polydisperse spray flame*, SIAM J. Appl. Math., 51 (1991), pp. 1284 – 1303.

[164] W. A. Sirignano, *Fluid dynamics and transport of droplets and sprays*, Cambridge University Press, 1999.

[165] W. A. Sirignano, *Fluid Dynamics and Transport of Droplets and Sprays*, Cambridge University Press, Cambridge, 2010.

[166] R. So, L. Jin, and T. Gatski, *An explicit algebraic Reynolds stress and heat flux model for incompressible turbulence: Part I Non-isothermal flow*, Theoretical and Computational Fluid Dynamics, 17 (2004), pp. 351–376.

[167] D. B. Spalding, *The combustion of liquid fuels*, in Proceedings of the 4th Symp. (International) on Combustion, The Institute, Baltimore, 1953, pp. 847–864.

[168] K. D. Squires and J. K. Eaton, *Preferential concentration of particles by turbulence*, Physics of Fluids A: Fluid Dynamics (1989-1993), 3 (1991), pp. 1169–1178.

[169] G. Stokes, *Report on recent researches in hydrodynamics*, British Association Report, 1846.

[170] H. Struchtrup, *Macroscopic transport equations for rarefied gas flows*, Springer, 2005.

[171] S. Subramaniam, *Statistical representation of a spray as a point process*, Physics of Fluids, 12 (2000), p. 2413.

[172] S. Subramaniam, *Statistical modeling of sprays using the droplet distribution function*, Physics of Fluids, 13 (2001), p. 624.

[173] A. Tagliani, *Hausdorff moment problem and maximum entropy: A unified approach*, Applied Mathematics and Computation, 105 (1999), pp. 291 – 305.

[174] Y. Tambour, *A sectional model for evaporation and combustion of sprays of liquid fuel*, Isr. J. Technol., 18 (1980), pp. 47 – 56.

[175] C. M. Tchen, *Mean value and correlation problems connected with the motion of small particles suspended in a turbulent fluid*, PhD thesis, University of Delft, The Hague, 1947.

[176] S. Tenneti, R. Garg, C. Hrenya, R. O. Fox, and S. Subramaniam, *Direct numerical simulation of gas-solid suspensions at moderate reynolds number: Quantifying the coupling between hydrodynamic forces and particle velocity fluctuations*, Powder Technology, 203 (2010), pp. 57 – 69.

[177] O. Thomine, *Développement de méthodes multi-échelles pour la simulation numérique des écoulements réactifs diphasiques*, PhD thesis, Université de Rouen, 2011.

[178] J. Tillou, J.-B. Michel, C. Angelberger, and D. Veynante, *Assessing LES models based on tabulated chemistry for the simulation of diesel spray combustion*, Combustion and Flame, 161 (2014), pp. 525 – 540.

[179] E. F. Toro, *Riemann solvers and numerical methods for fluid dynamics*, Springer, 2009.

[180] D. J. Torres and M. F. Trujillo, *KIVA-IV: An unstructured ALE code for compressible gas flow with sprays*, J. Comput. Phys., 219 (2006), pp. 943–975.

[181] E. Tory, R. Buger, F. Concha, and M. Bustos, *Sedimentation and Thickening: Phenomenological Foundation and Mathematical Theory*, Springer, 1999.

[182] B. Truchot, *Développement et validation d'un modèle eulérien en vue de la simulation des jets de carburants dans les moteurs à combustion interne*, PhD thesis, Institut National Polytechnique de Toulouse, 2005.

[183] A. Vallet, A. A. Burluka, and R. Borghi, *Development of a Eulerian model for the atomization of a liquid jet*, Atomization and Sprays, 11 (2001).

[184] M. Vasenin, R. K. Narimanov, A. Glazunov, N. E. Kuvshinov, and V. A. Ivanov, *Two-phase flows in the nozzles of solid rocket motors*, Journal of Propulsion and Power, 11 (1995), pp. 583–592.

[185] O. Vermorel, S. Richard, O. Colin, C. Angelberger, A. Benkenida, and D. Veynante, *Multi-cycle les simulations of flow and combustion in a pfi si 4-valve production engine*, SAE Technical Paper, (2007), pp. 01–0151.

[186] C. Vessiller, *Contribution à l'étude des brouillards denses et dilués par la simulation numérique Euler/Euler et Euler/Lagrange*, PhD thesis, Ecole Centrale Paris and IFP Energies nouvelles, 2007.

[187] A. Vié, F. Doisneau, and M. Massot, *On the Anisotropic Gaussian velocity closure for inertial- particle laden flows.* Submitted, available on HAL, `http://hal.archives-ouvertes.fr/hal-00912319`, Dec. 2013.

[188] A. Vié, S. Jay, B. Cuenot, and M. Massot, *Accounting for polydispersion in the Eulerian Large Eddy Simulation of the two-phase flow in an aeronautical-type burner*, Flow, Turbulence and Combustion, 90 (2013), pp. 545–581.

[189] A. Vié, F. Laurent, and M. Massot, *Size-velocity correlations in high order moment methods for polydisperse evaporating sprays: modeling and numerical issues*, J. Comput. Phys., 237 (2013), pp. 277–310.

[190] A. Vié, E. Masi, O. Simonin, and M. Massot, *On the direct numerical simulation of moderate-Stokes-number turbulent particulate flows using Algebraic-Closure-Based and Kinetic-Based Moment Methods*, in Proceedings of the Summer Program 2012, Center for Turbulence Research, Stanford University, 2012, pp. 355–364.

[191] V. Vikas, Z. J. Wang, A. Passalacqua, and R. O. Fox, *Realizable high-order finite-volume schemes for quadrature-based moment methods*, J. Comput. Phys., 230 (2011), pp. 5328–5352.

[192] C. Villani, *A review of mathematical topics in collisional kinetic theory*, S. Friedlander and D. Serre Eds., 2002. Handbook of Fluid Mechanics.

[193] F. A. Williams, *Spray combustion and atomization*, Phys. Fluids, 1 (1958), pp. 541–545.

[194] ——, *Combustion Theory (Combustion Science and Engineering Series)*, ed F A Williams (Reading, MA: Addison-Wesley), 1985.

[195] D. L. Wright, *Numerical advection of moments of the particle size distribution in Eulerian models*, J. Aerosol Sci., 38 (2007), pp. 352–369.

[196] D. L. Wright, R. McGraw, and D. E. Rosner, *Bivariate extension of the quadrature method of moments for modeling simultaneous coagulation and sintering of particle populations*, J. Colloid Interface Sci., 236 (2001), pp. 242–251.

[197] Y. Xu and S. Subramaniam, *Effect of particle clusters on carrier flow turbulence: A direct numerical simulation study*, Flow, Turbulence and Combustion, 85 (2010), pp. 735–761.

[198] C. Yuan and R. Fox, *Conditional quadrature method of moments for kinetic equations*, Journal of Computational Physics, 230 (2011), pp. 8216 – 8246.

[199] C. Yuan, F. Laurent, and R. O. Fox, *An extended quadrature method of moments for population balance equations*, J. Aerosol Sci., 51 (2012), pp. 1–23.

[200] L. I. Zaichik, V. M. Alipchenkov, and E. G. Sinaiski, *Particles in Turbulent Flows*, Wiley-VCH, Weinheim, Germany, 2008.

[201] L. I. Zaichik, O. Simonin, and V. M. Alipchenkov, *An eulerian approach for large eddy simulation of particle transport in turbulent flows*, Journal of Turbulence, 10:4 (2009).

[202] P. Zeng, S. Sarholz, C. Iwainsky, B. Binninger, N. Peters, and M. Herrmann, *Simulation of primary breakup for diesel spray with phase transition*, in Recent Advances in Parallel Virtual Machine and Message Passing Interface, M. Ropo, J. Westerholm, and J. Dongarra, eds., vol. 5759 of Lecture Notes in Computer Science, Springer Berlin Heidelberg, 2009, pp. 313–320.

[203] H. Zhu, Z. Zhou, R. Yang, and A. Yu, *Discrete particle simulation of particulate systems: Theoretical developments*, Chemical Engineering Science, 62 (2007), pp. 3378 – 3396.

[204] M. Zolver, D. Klahr, J. Bohbot, O. Laget, and A. Torres, *Reactive CFD in engines with a new unstructured parallel solver*, Oil & Gas Science and Technology, 58 (2003), pp. 33–46.

Appendices

Appendix A

A.1 Specific aspects of time-space discretization

We report here some mandatory technicalities at the fully discrete level of the ALE splitting strategy sketched out in §3.3.3. A significant part of these stems from the use of staggered grids, which is imposed to us by the IFP-C3D environment.

A.1.1 Phase A in the one-way coupling framework

The equations to be solved are

$$\begin{aligned}
\partial_t(m_0) &= - K\tilde{n}(\boldsymbol{m},0), && \text{(A.1a)}\\
\partial_t(m_1) &= - Km_0, && \text{(A.1b)}\\
&\vdots \quad \vdots &&\\
\partial_t(m_N) &= -NKm_{N-1}, && \text{(A.1c)}\\
\partial_t(m_1\boldsymbol{u_d}) &= \underbrace{- Km_0\boldsymbol{u_d}}_{\mathrm{A}_1} + \underbrace{\tfrac{18\pi}{\rho_d}\mu_g m_0(\boldsymbol{u_g}-\boldsymbol{u_d})}_{\mathrm{A}_0}, && \text{(A.1d)}
\end{aligned}$$

for the spray, and

$$\partial_t(\rho_g) = \partial_t(\rho_g\boldsymbol{u_g}) = \partial_t(\rho_g E_g) = 0 \qquad \text{(A.2)}$$

for the gas. The simplicity of this system suggests a further splitting into a drag step A_0 and an evaporation step A_1. Since A_1 can be done using the Massot et al. [120], let us see how to solve A_0. The A_0 equations are

$$\begin{aligned}
\partial_t(m_0) &= 0, && \text{(A.3a)}\\
\partial_t(m_1) &= 0, && \text{(A.3b)}\\
&\vdots \quad \vdots &&\\
\partial_t(m_N) &= 0, && \text{(A.3c)}\\
\partial_t(m_1\boldsymbol{u_d}) &= \tfrac{18\pi}{\rho_d}\mu_g m_0(\boldsymbol{u_g}-\boldsymbol{u_d}) && \text{(A.3d)}
\end{aligned}$$

for the spray, and (A.2) for the gas. From the first $N+1$ equations of (A.3), we have $\boldsymbol{m}(t) = \boldsymbol{m}^n$. From (A.2), we have $\mu_g(t) = \mu_g^n$. The spray momentum equation (A.3d) becomes

$$\partial_t\boldsymbol{u_d} = \alpha^n(\boldsymbol{u_g}-\boldsymbol{u_d}), \qquad \alpha^n = \frac{18\pi}{\rho_d}\frac{\mu_g^n m_0^n}{m_1^n}, \qquad \text{(A.4)}$$

the solution of which is

$$\boldsymbol{u_d}(t) = \exp(-\alpha^n(t-t^n))\boldsymbol{u_d^n} + (1-\exp(-\alpha^n(t-t^n)))\boldsymbol{u_g^n}. \qquad \text{(A.5)}$$

Space discretization over a staggered grid is taken into account in a way similar to §3.3.1. Leaving the 3-D extension to readers, we write down the details for a 1-D mesh

using the same notations as in §3.3.1. By integrating of (A.3d) over the dual cell $[x_i, x_{i+1}[$ and by invoking approximations in the same vein as (3.51), we end up with

$$\partial_t \boldsymbol{u}_{\boldsymbol{d}i+1/2} = \alpha^n_{i+1/2}(\boldsymbol{u}_{\boldsymbol{g}i+1/2} - \boldsymbol{u}_{\boldsymbol{d}i+1/2}), \qquad \alpha^n_{i+1/2} = \frac{18\pi}{\rho_d}\frac{\Delta x_i \mu^n_{g,i} m^n_{0,i} + \Delta x_{i+1}\mu^n_{g,i+1} m^n_{0,i+1}}{\Delta x_i m^n_{1,i} + \Delta x_{i+1} m^n_{1,i+1}}, \tag{A.6}$$

The solution of this equation is

$$\boldsymbol{u}^{\mathrm{A}_0}_{\boldsymbol{d}i+1/2} = \exp(-\alpha^n_{i+1/2}\Delta t)\boldsymbol{u}^n_{\boldsymbol{d}i+1/2} + (1 - \exp(-\alpha^n_{i+1/2}\Delta t))\boldsymbol{u}^n_{\boldsymbol{g}i+1/2}. \tag{A.7}$$

A.1.2 Phase B

To alleviate notations without loss of generality, let us examine the one-dimensional case. The 1-D version of system (3.60) reads

$$\partial_t(J_d) \qquad - J_d\partial_x(u_d) = 0, \tag{A.8a}$$
$$\partial_t(J_d\boldsymbol{m}) \qquad\qquad = 0, \tag{A.8b}$$
$$\partial_t(J_d m_1 u_d) \qquad\qquad = 0. \tag{A.8c}$$

The mass balances (A.8b) are discretized on primal cells as

$$\Delta x^B_i \boldsymbol{m}^B_i = \Delta x^A_i \boldsymbol{m}^A_i. \tag{A.9}$$

The momentum balance (A.8c) is discretized on dual cells as

$$\tfrac{1}{2}(\Delta x^B_i m^B_{1,i} + \Delta x^B_{i+1} m^B_{1,i+1}) u^B_{d\,i+1/2} = \tfrac{1}{2}(\Delta x^A_i m^A_{1,i} + \Delta x^A_{i+1} m^A_{1,i+1}) u^A_{d\,i+1/2}. \tag{A.10}$$

Inserting (A.9) into (A.10) and gives

$$u^B_{d\,i+1/2} = u^A_{d\,i+1/2} \tag{A.11}$$

after simplification. The vertices are displaced by

$$x^B_{i+1/2} = x^A_{i+1/2} + u^B_{d\,i+1/2}\Delta t, \tag{A.12a}$$

from which it follows that

$$\Delta x^B_i = \Delta x^A_i + (u^B_{d\,i+1/2} - u^B_{d\,i-1/2})\Delta t = \Delta x^n_i + (u^A_{d\,i+1/2} - u^A_{d\,i-1/2})\Delta t. \tag{A.12b}$$

This enables us to retrieve $\boldsymbol{m}^B_i$ from (A.9). A condition on Δt is obviously needed to ensure $\Delta x^B_i > 0$. We impose the sufficient CFL-like condition

$$\frac{\Delta t}{\Delta x^A_i}\max\{|u^A_{d\,i-1/2}|, |u^A_{d\,i+1/2}|\} < \frac{1}{2}. \tag{A.13}$$

A.1.3 Phase C

We apply dimensional splitting to system (3.65), which produces a sequence of 1-D systems of the form

$$\begin{aligned}
&\partial_t(J_d) &&+ J_d\partial_x(u_d - w) &&= 0 && \text{(A.14a)}\\
&\partial_t(J_d\boldsymbol{m}) &&+ J_d\partial_x(\boldsymbol{m}(u_d - w)) &&= 0, && \text{(A.14b)}\\
&\partial_t(J_d m_1 \boldsymbol{u_d}) &&+ J_d\partial_x(m_1\boldsymbol{u_d}(u_d - w)) &&= 0, . && \text{(A.14c)}
\end{aligned}$$

Consider just one of the above 1-D system. Then, the vertices are displaced by

$$x_{i+1/2}^{n+1} = x_{i+1/2}^B - (u_{d\,i+1/2}^B - w_{i+1/2}^n)\Delta t = x_{i+1/2}^n + w_{i+1/2}^n\Delta t, \tag{A.15a}$$

from which it follows that

$$\begin{aligned}
\Delta x_i^{n+1} &= \Delta x_i^B - (u_{d\,i+1/2}^B - u_{d\,i-1/2}^B)\Delta t + (w_{i+1/2}^n - w_{i-1/2}^n)\Delta t\\
&= \Delta x_i^n + (w_{i+1/2}^n - w_{i-1/2}^n)\Delta t.
\end{aligned} \tag{A.15b}$$

The mass balances (A.14b) are discretized on primal cells by the explicit scheme

$$\Delta x_i^{n+1}\boldsymbol{m}_i^{n+1} = \Delta x_i^B\boldsymbol{m}_i^B - \Delta t(\boldsymbol{Q}_{i+1/2}^B - \boldsymbol{Q}_{i-1/2}^B), \tag{A.16}$$

for some numerical fluxes $\boldsymbol{Q}^B$, required to be homogeneous to $\boldsymbol{m}(u_d - w)$. Inspired by the approach of Kah et al. [87] for the slightly different system $\partial_t(\boldsymbol{m}) + \partial_x(\boldsymbol{m}u_d) = 0$, we consider

$$\boldsymbol{Q}_{i+1/2}^B = \begin{cases} \dfrac{1}{\Delta t}\displaystyle\int_{x_{i+1/2}^B - (u_{d\,i+1/2}^B - w_{i+1/2}^n)\Delta t}^{x_{i+1/2}^B} \hat{\boldsymbol{m}}_i^B(x)\,\mathrm{d}x & \text{if } u_{d\,i+1/2}^B - w_{i+1/2}^n > 0,\\ \dfrac{1}{\Delta t}\displaystyle\int_{x_{i+1/2}^B}^{x_{i+1/2}^B - (u_{d\,i+1/2}^B - w_{i+1/2}^n)\Delta t} \hat{\boldsymbol{m}}_{i+1}^B(x)\,\mathrm{d}x & \text{if } u_{d\,i+1/2}^B - w_{i+1/2}^n < 0, \end{cases} \tag{A.17}$$

for some reconstructions $\hat{\boldsymbol{m}}_i^B(.)$ of $\hat{\boldsymbol{m}}^B$ over the cells $i \in \mathbb{Z}$. Formula (A.17) is clearly consistent with the basic first-order upwind flux

$$\boldsymbol{Q}_{i+1/2}^B = \boldsymbol{m}_i^B(u_d^B - w^n)_{i+1/2}^+ + \boldsymbol{m}_{i+1}^B(u_d^B - w^n)_{i+1/2}^- \tag{A.18}$$

when $\hat{\boldsymbol{m}}_i^B(x) = \boldsymbol{m}_i^B$ is constant over cell i. To enhance accuracy for the transport of moments, let $\boldsymbol{p} = (p_1, \ldots, p_N)$ be the canonical moments introduced in §3.2.4. We set

$$\hat{\boldsymbol{m}}_i^B(x) = \boldsymbol{M}(\hat{m}_{0,i}^B(x);\, \hat{\boldsymbol{p}}_i^B(x)), \tag{A.19}$$

where the function

$$\boldsymbol{M}(m_0;\, \boldsymbol{p}) = m_0 \begin{pmatrix} 1\\ p_1\\ p_1((1-p_1)p_2 + p_1)\\ p_1((1-p_1)p_2(1-p_2)p_3 + (p_1 + p_2(1-p_1))^2)\\ \cdots \end{pmatrix} \tag{A.20}$$

returns $\boldsymbol{m} = (m_0, m_1, \ldots, m_N)$ as a function of $(m_0;\, p_1, \ldots, p_N)$, and

$$\begin{aligned} \hat{m}^B_{0,i}(x) &= m^B_{0,i} + Dm_{0,i}(x - x^B_i), && \text{(A.21a)} \\ \hat{p}^B_{1,i}(x) &= \overline{p}^B_{1,i} + Dp_{1,i}(x - x^B_i), && \text{(A.21b)} \\ &\vdots \qquad\quad \vdots \\ \hat{p}^B_{N,i}(x) &= \overline{p}^B_{N,i} + Dp_{N,i}(x - x^B_i), && \text{(A.21c)} \end{aligned}$$

are the piecewise affine reconstructions. These reconstructions involve some limited slopes $Dp_{k,i}$ and some *modified averages* $\overline{p}_{k,i}$, which are linearly related to the slopes by

$$\overline{p}_{k,i} = a_{k,i} + b_{k,i} Dp_{k,i} \tag{A.22}$$

in order to preserve the mean values of the moments $(m_1, \ldots, m_N)$. The calculation of the coefficients a_{2j}, a_{3j} and b_{2j}, b_{3j}, presented in [87], is completed using Maple[1], and implemented in the Fortran code. Notwithstanding some heaviness, their algebraic expressions do not entail sensible extra CPU cost.

The slopes for the canonical moments are determined using limiters in order to comply with the maximum principle

$$r_{k,i} \le p_k(x) \le R_{k,i}, \qquad \text{for all } \; x \in [x_{i-1/2}, x_{i+1/2}[\,, \tag{A.23}$$

where $r_{k,i} = \min\{p^B_{k,i-1}, p^B_{k,i}, p^B_{k,i+1}\}$ and $R_{k,i} = \max\{p^B_{k,i-1}, p^B_{k,i}, p^B_{k,i+1}\}$. By linearity, condition (A.23) is equivalent to

$$r_{k,i} \le a_{k,i} + b_{k,i} Dp_{k,i} \pm \tfrac{1}{2}\Delta x^B_i Dp_{k,i} \le R_{k,i}. \tag{A.24}$$

Solving for the slope, we get

$$\min\left\{ \frac{r_{k,i} - a_{k,i}}{b_{k,i} + \frac{1}{2}\Delta x^B_i}, \frac{a_{k,i} - R_{k,i}}{\frac{1}{2}\Delta x^B_i - b_{k,i}} \right\} \le Dp_{k,i} \le \min\left\{ \frac{R_{k,i} - a_{k,i}}{b_{k,i} + \frac{1}{2}\Delta x^B_i}, \frac{a_{k,i} - r_{k,i}}{\frac{1}{2}\Delta x^B_i - b_{k,i}} \right\}. \tag{A.25}$$

In practice, we opt for the limiter

$$Dp_{k,i} = \frac{1}{2}(\operatorname{sgn}(p^B_{k,i+1} - p^B_{k,i}) + \operatorname{sgn}(p^B_{k,i} - p^B_{k,i-1})) \min\left\{ \frac{|p^B_{k,i+1} - a_{k,i}|}{\Delta x^B_i + 2b_{k,i}}, \frac{|a_{k,i} - p^B_{k,i+1}|}{\Delta x^B_i + 2b_{k,i}} \right\}, \tag{A.26}$$

which can be checked to satisfy (A.25). The same limiter is used for the slope on the droplet number m_0. In order to ensure the non-negativity of m_0, the additional condition $\Delta x^B_i Dm_{0,i} \le 2m^B_{0,i}$ is require. This ensures that the extremum of $\hat{m}_{0,i}(\cdot)$, which occurs at one of the cell bound, remains positive. Finally, it can be shown that a sufficient stability condition for this moment transport scheme is

$$\frac{\Delta t}{\Delta x^B_i} \max\{|u^B_{d\,i-1/2} - w^n_{i-1/2}|, |u^B_{d\,i+1/2} - w^n_{i+1/2}|\} < \frac{1}{2}. \tag{A.27}$$

[1]Maplesoft, a division of Waterloo Maple, 2007

The momentum balance (A.14c) is discretized over dual cells by the explicit scheme

$$\tfrac{1}{2}(\Delta x_i^{n+1} m_{1,i}^{n+1} + \Delta x_{i+1}^{n+1} m_{1,i+1}^{n+1}) \boldsymbol{u}_{\boldsymbol{d}i+1/2}^{n+1} = \tfrac{1}{2}(\Delta x_i^B m_{1,i}^B + \Delta x_{i+1}^B m_{1,i+1}^B) \boldsymbol{u}_{\boldsymbol{d}i+1/2}^B - \Delta t(\Xi_{i+1}^B - \Xi_i^B) \tag{A.28}$$

using the numerical flux

$$\Xi_i^B = \boldsymbol{u}_{\boldsymbol{d}i-1/2}^B \left(\frac{Q_{1,i-1/2}^B + Q_{1,i+1/2}^B}{2} \right)^+ + \boldsymbol{u}_{\boldsymbol{d}i+1/2}^B \left(\frac{Q_{1,i-1/2}^B + Q_{1,i+1/2}^B}{2} \right)^- \tag{A.29}$$

where $Q_{1,i+1/2}^B$ is the m_1-component of the flux $\boldsymbol{Q}_{i+1/2}^B$ defined in (A.17). This allows the maximum principle

$$\min\{\boldsymbol{u}_{\boldsymbol{d}i-1/2}^B, \boldsymbol{u}_{\boldsymbol{d}i+1/2}^B, \boldsymbol{u}_{\boldsymbol{d}i+3/2}\} \leq \boldsymbol{u}_{\boldsymbol{d}i+1/2}^{n+1} \leq \max\{\boldsymbol{u}_{\boldsymbol{d}i-1/2}^B, \boldsymbol{u}_{\boldsymbol{d}i+1/2}^B, \boldsymbol{u}_{\boldsymbol{d}i+3/2}^B\} \tag{A.30}$$

to hold componentwise on $\boldsymbol{u}_{\boldsymbol{d}}$, provided some (complicated) stability criterion is met. This scheme is first-order with respect to $\boldsymbol{u}_{\boldsymbol{d}}$, but we content ourselves with this accuracy for the velocity.

Appendix B

B.1 Reynolds and Phase averaging

B.1.1 Reynolds average

The RA of a product can be decomposed:

$$\begin{aligned}\langle AB\rangle &= \langle (A' + \langle A\rangle)(B' + \langle B\rangle)\rangle \\ &= \langle A'B' + A' \langle B\rangle + B' \langle A\rangle + \langle A\rangle \langle B\rangle\rangle \\ &= \langle A'B'\rangle + \langle A'\rangle \langle B\rangle + \langle B'\rangle \langle A\rangle + \langle A\rangle \langle B\rangle \\ &= \langle A'B'\rangle + \langle A\rangle \langle B\rangle \end{aligned} \tag{B.1}$$

and

$$\begin{aligned}\langle ABC\rangle &= \langle (A'B' + A' \langle B\rangle + B' \langle A\rangle + \langle A\rangle \langle B\rangle)(C' + \langle C\rangle)\rangle \\ &= \langle A'B'C' + A'C' \langle B\rangle + B'C' \langle A\rangle + C' \langle A\rangle \langle B\rangle + A'B' \langle C\rangle + A' \langle B\rangle \langle C\rangle\rangle \\ &\quad + \langle B' \langle A\rangle \langle C\rangle + \langle A\rangle \langle B\rangle \langle C\rangle\rangle \\ &= \langle A'B'C'\rangle + \langle A'C'\rangle \langle B\rangle + \langle B'C'\rangle \langle A\rangle + \langle C'\rangle \langle A\rangle \langle B\rangle + \langle A'B'\rangle \langle C\rangle + \langle A'\rangle \langle B\rangle \langle C\rangle \\ &\quad + \langle B'\rangle \langle A\rangle \langle C\rangle + \langle A\rangle \langle B\rangle \langle C\rangle \\ &= \langle A\rangle \langle B\rangle \langle C\rangle + \langle A\rangle \langle B'C'\rangle + \langle B\rangle \langle A'C'\rangle + \langle C\rangle \langle A'B'\rangle + \langle A'B'C'\rangle \end{aligned} \tag{B.2}$$

B.1.2 Phase average

In the context of dilute disperse flows where the gas phase is modeled through compressible Navier-Stokes equation and polydisperse droplets by a moment method, both the gas density ρ_g and the spray density concentration denoted by the moment $m_{3/2}$ play an important role for the averaging procedure. Therefore, the relation between RA and the PA of an arbitrary variable A for

- the gas phase is

$$\langle \rho_g A\rangle = \langle \rho_g\rangle \langle A\rangle_g \,, \tag{B.3}$$

- the polydispersed phase is

$$\langle m_1 A\rangle = \langle m_1\rangle \langle A\rangle_d \,. \tag{B.4}$$

A useful identity relating the PA of the quantity A to its covariances with respect to the gas density and the moment m_1 can be also derived. Adding Eq. (B.3) to (B.4), one can obtain the following relation:

$$\langle A\rangle_d = \langle A\rangle_g + \frac{\big\langle \big(\rho_g + m_1\big) A\big\rangle - \langle \rho_g + m_1\rangle \langle A\rangle_g}{\langle m_1\rangle} \tag{B.5}$$

multiplying by $\langle \rho_g\rangle$ both the numerator and the denominator of the second term at the right-hand side in Eq. (B.5) and using the relation, one can easily obtain the following expression:

$$\langle A\rangle_d = \langle A\rangle_g + \frac{\langle m_1' A'\rangle}{\langle m_1\rangle} - \frac{\big\langle \rho_g' A'\big\rangle}{\langle \rho_g\rangle} \tag{B.6}$$

Deriving Reynolds averaged moment equations requires a density-weighted statistics of terms $\langle m_k A\rangle$ where m_k is the moment of order k with k is different from 3/2. This accounts for leading the following operation:

$$\langle m_k A\rangle = \frac{\langle m_1\rangle \langle m_k A\rangle}{\langle m_1\rangle} = \frac{\langle m_1\rangle \left[\, \langle A\rangle \langle m_k\rangle + \langle A' m_k'\rangle \,\right]}{\langle m_1\rangle} = \frac{\langle m_1 A\rangle - \langle m_1' A'\rangle}{\langle m_1\rangle} \langle m_k\rangle + \langle m_k' A'\rangle \tag{B.7}$$

therefore,

$$\langle m_k A\rangle = \langle m_k\rangle \langle A\rangle_d - \frac{\langle m_k\rangle}{\langle m_1\rangle} \langle m_1' A'\rangle + \langle m_k' A'\rangle \tag{B.8}$$

An other difficulty encountered during the derivation phase of RA equations is observed when the RA of a variable $\langle A\rangle$ is obtained. The latter need to be defined in function of a density-weighted statistics. This can be done either with respect to the gas phase,

$$\langle A\rangle = \langle A\rangle_g - \frac{\langle \rho_g' A'\rangle}{\langle \rho_g\rangle} \tag{B.9}$$

or the spray phase,

$$\langle A\rangle = \langle A\rangle_d - \frac{\langle m_1' A'\rangle}{\langle m_1\rangle}. \tag{B.10}$$

B.2 Full RA equations

The aim of this part is to give further details in the derivation of full coupled RA two-phase flow equations. Some source terms contain third-order correlations, which need to be carefully explicated for modeling issues. Let us then focus on each RA equation in the reminder.

B.2.1 RA moment equations

$$\partial_t \langle m_0\rangle + \nabla_{\boldsymbol{x}} \cdot \left(\langle m_0\rangle \langle \boldsymbol{u_d}\rangle_d - \frac{\langle m_0\rangle}{\langle m_1\rangle} \langle m_1' \boldsymbol{u_d}'\rangle + \langle m_0' \boldsymbol{u_d}'\rangle \right) = R_S \langle n(t,\boldsymbol{x},0)\rangle \,, \tag{B.11a}$$

$$\partial_t \langle m_1\rangle + \nabla_{\boldsymbol{x}} \cdot \left(\langle m_1\rangle \langle \boldsymbol{u_d}\rangle_d \right) = \langle \mathcal{M}\rangle \,, \tag{B.11b}$$

$$\partial_t \langle m_2\rangle + \nabla_{\boldsymbol{x}} \cdot \left(\langle m_2\rangle \langle \boldsymbol{u_d}\rangle_d - \frac{\langle m_2\rangle}{\langle m_1\rangle} \langle m_1' \boldsymbol{u_d}'\rangle + \langle m_2' \boldsymbol{u_d}'\rangle \right) = -2R_S \langle m_1\rangle \,, \tag{B.11c}$$

$$\partial_t \langle m_3\rangle + \nabla_{\boldsymbol{x}} \cdot \left(\langle m_3\rangle \langle \boldsymbol{u_d}\rangle_d - \frac{\langle m_3\rangle}{\langle m_1\rangle} \langle m_1' \boldsymbol{u_d}'\rangle + \langle m_3' \boldsymbol{u_d}'\rangle \right) = -3R_S \langle m_2\rangle \,. \tag{B.11d}$$

B.2.2 RA spray momentum equation

Taking the RA of (6.9e) yields

$$\partial_t \langle m_1\rangle \langle \boldsymbol{u_d}\rangle_d + \nabla_{\boldsymbol{x}} \cdot \left[\langle m_1\rangle \left(\langle \boldsymbol{u_d}\rangle_d^2 + \langle \boldsymbol{u_d}'' \boldsymbol{u_d}''\rangle_d + \langle P_d\rangle_d \right) \right] = \langle \boldsymbol{\mathcal{A}}\rangle + \langle \mathcal{M} \boldsymbol{u_d}\rangle \tag{B.12}$$

The source term at the right hand side of Eq. (B.12) still needs to be developed. Through the formulas (B.8) and (B.2) given in B.1, the mean source term due to drag force can be developed as

$$\begin{aligned}\langle \boldsymbol{\mathcal{A}} \rangle =& \left(\langle m_0 \rangle \left\langle \frac{1}{\tau_d^*} \right\rangle + \left\langle m_0' (\frac{1}{\tau_d^*})' \right\rangle \right) \left(\langle \boldsymbol{u_g} \rangle_g - \langle \boldsymbol{u_d} \rangle_d + \frac{\langle m_1' \boldsymbol{u_d}' \rangle}{\langle m_1 \rangle} - \frac{\left\langle \rho_g' \boldsymbol{u_g}' \right\rangle}{\langle \rho_g \rangle} \right) \\ &+ \langle m_0 \rangle \left(\left\langle \boldsymbol{u_g}' (\frac{1}{\tau_d^*})' \right\rangle - \left\langle \boldsymbol{u_d}' (\frac{1}{\tau_d^*})' \right\rangle \right) + \left\langle m_0' \boldsymbol{u_g}' (\frac{1}{\tau_d^*})' \right\rangle - \left\langle m_0' \boldsymbol{u_d}' (\frac{1}{\tau_d^*})' \right\rangle \\ &+ \left\langle \frac{1}{\tau_d^*} \right\rangle \left(\langle m_0' \boldsymbol{u_g}' \rangle - \langle m_0' \boldsymbol{u_d}' \rangle \right), \end{aligned} \tag{B.13}$$

whereas the mean momentum exchange created by the evaporating spray is given through the expression

$$\langle \mathcal{M} \boldsymbol{u_d} \rangle = - R_S \left(\langle m_0 \rangle \langle \boldsymbol{u_d} \rangle_d - \frac{\langle m_0 \rangle \langle m_1' \boldsymbol{u_d}' \rangle}{\langle m_1 \rangle} + \langle m_0' \boldsymbol{u_d}' \rangle \right). \tag{B.14}$$

B.2.3 RA granular temperature equation

The RA of the granular temperature equation (6.39) is given as

$$\begin{aligned}\partial_t \langle m_1 \rangle \langle \Theta \rangle_d + \nabla_{\boldsymbol{x}} \cdot \left[\langle m_1 \rangle \left(\langle \Theta \rangle_d \langle \boldsymbol{u_d} \rangle_d + \langle \Theta'' \boldsymbol{u_d}'' \rangle_d \right) \right] =& - \langle m_1 \rangle \langle P_d \rangle_d : \nabla_{\boldsymbol{x}} \langle \boldsymbol{u_d} \rangle_d \\ &- \langle m_1 \rangle \langle P_d : \nabla_{\boldsymbol{x}} \boldsymbol{u_d}'' \rangle_d + S^{\Theta}. \end{aligned} \tag{B.15}$$

with the source term given by the following averaged quantities:

$$S^{\Theta} = \langle \mathcal{U} + \mathcal{M} \Theta \rangle \tag{B.16}$$

$$\langle \mathcal{U} \rangle = -2 \left[\left\langle \frac{1}{\tau_d^*} \right\rangle \langle m_0 \Theta \rangle + \left\langle \left(\frac{1}{\tau_d^*} \right)' (\Theta m_0)' \right\rangle \right] \tag{B.17}$$

and

$$\langle \mathcal{M} \Theta \rangle = -R_S \left[\langle m_0 \rangle \langle \Theta \rangle_d - \frac{\langle m_0 \rangle}{\langle m_1 \rangle} \langle m_1' \Theta' \rangle + \langle m_0' \Theta \rangle \right], \tag{B.18}$$

B.2.4 RA total granular energy equation

The RA of the total granular equation given in (6.9f) yields the following relation:

$$\begin{aligned}&\partial_t \langle m_1 \rangle \langle E \rangle_d + \nabla_{\boldsymbol{x}} \cdot \left[\langle m_1 \rangle \left(\langle E \rangle_d \langle \boldsymbol{u_d} \rangle_d + \langle E \boldsymbol{u_d}'' \rangle_d + \langle \boldsymbol{u_d} \rangle_d \cdot \langle P_d \rangle_d \right) \right] = \\ &- \nabla_{\boldsymbol{x}} \cdot \left(\langle m_1 \rangle \langle P_d \cdot \boldsymbol{u_d}'' \rangle_d \right) + \left\langle S^E \right\rangle, \end{aligned} \tag{B.19}$$

with

$$\left\langle S^E \right\rangle = \langle \mathcal{E} + \mathcal{M} E \rangle . \tag{B.20}$$

B.2.5 RA spray phase mean kinetic energy

Multiplying Eq. (6.25) by the mean spray velocity $\langle \boldsymbol{u_d} \rangle_d$ gives rise to the following mean kinetic energy equation after some manupulations:

$$\partial_t \langle m_1 \rangle K + \nabla_{\boldsymbol{x}} \cdot \left[\langle m_1 \rangle \left(K \langle \boldsymbol{u_d} \rangle_d + \langle \boldsymbol{u_d} \rangle_d \cdot \left[\langle P_d \rangle_d + \langle \boldsymbol{u_d}'' \boldsymbol{u_d}'' \rangle_d \right] \right) \right] =$$
$$\langle m_1 \rangle \left(\langle P_d \rangle_d + \langle \boldsymbol{u_d}'' \boldsymbol{u_d}'' \rangle_d \right) : \nabla_{\boldsymbol{x}} \langle \boldsymbol{u_d} \rangle_d + \mathfrak{S}_d^K \tag{B.21}$$

with $\mathfrak{S}_d^K$ the source term given as

$$\mathfrak{S}_d^K = \left(\langle \boldsymbol{\mathcal{A}} \rangle + \langle \mathcal{M} \boldsymbol{u_d} \rangle \right) \langle \boldsymbol{u_d} \rangle_d + \langle \mathcal{M} \rangle \left(K - \langle \boldsymbol{u_d} \rangle_d^2 \right) \tag{B.22}$$

B.2.6 RA gas mass equation

Applying the RA on Eq. (6.13a) accounts for the following expression:

$$\partial_t \langle \rho_g \rangle + \nabla_{\boldsymbol{x}} \cdot \langle \rho_g \rangle \langle \boldsymbol{u_g} \rangle_g = \langle \mathcal{M}_g \rangle \tag{B.23}$$

B.2.7 PA gas phase momentum equation

The PA gas-phase momentum equation is found from (6.13b):

$$\partial_t \langle \rho_g \rangle \langle \boldsymbol{u_g} \rangle_g + \nabla_{\boldsymbol{x}} \cdot \left[\langle \rho_g \rangle \left(\langle \boldsymbol{u_g} \rangle_g^2 + \langle \boldsymbol{u_g}''' \boldsymbol{u_g}''' \rangle_g \right) + \langle P_g \rangle \right] = \nabla_{\boldsymbol{x}} \cdot \langle \rho_g \rangle \langle \tau \rangle_g + \langle \mathfrak{S}^{\rho \boldsymbol{u}} \rangle \tag{B.24}$$

with

$$\langle \mathfrak{S}^{\rho \boldsymbol{u}} \rangle = \langle \mathcal{M}_g \boldsymbol{u_d} \rangle + \langle \boldsymbol{\mathcal{A}}_g \rangle \tag{B.25}$$

The source term accounting for both the evaporation and the drag is expressed as:

$$\begin{aligned} \langle \boldsymbol{\mathcal{A}}_g \rangle = &- \left(\langle m_{1/2} \rangle \left\langle \frac{1}{\tau_d^*} \right\rangle + \left\langle m'_{1/2} (\frac{1}{\tau_d^*})' \right\rangle \right) \left(\langle \boldsymbol{u_g} \rangle_g - \langle \boldsymbol{u_d} \rangle_d + \frac{\left\langle m'_{3/2} \boldsymbol{u_d}' \right\rangle}{\langle m_{3/2} \rangle} - \frac{\langle \rho'_g \boldsymbol{u_g}' \rangle}{\langle \rho_g \rangle} \right) \\ &- \left\langle \frac{1}{\tau_d^*} \right\rangle \left(\langle m'_{1/2} \boldsymbol{u_g}' \rangle - \langle m'_{1/2} \boldsymbol{u_d}' \rangle \right) - \langle m_{1/2} \rangle \left(\left\langle \boldsymbol{u_g}' (\frac{1}{\tau_d^*})' \right\rangle - \left\langle \boldsymbol{u_d}' (\frac{1}{\tau_d^*})' \right\rangle \right) \\ &- \left\langle m'_{1/2} \boldsymbol{u_g}' (\frac{1}{\tau_d^*})' \right\rangle + \left\langle m'_{1/2} \boldsymbol{u_d}' (\frac{1}{\tau_d^*})' \right\rangle \end{aligned} \tag{B.26}$$

and

$$\langle \mathcal{M}_g \boldsymbol{u_d} \rangle = R_S \left(\langle m_{1/2} \rangle \langle \boldsymbol{u_d} \rangle_d - \frac{\langle m_{1/2} \rangle \left\langle m'_{3/2} \boldsymbol{u_d}' \right\rangle}{\langle m_{3/2} \rangle} + \langle m'_{1/2} \boldsymbol{u_d}' \rangle \right) \tag{B.27}$$

B.2.8 RA gas phase internal energy equation

Taking the RA of Eq. (6.17) accounts for the expression

$$\begin{aligned}\partial_t \langle\rho_g\rangle \langle e_g\rangle_g + \nabla_{\boldsymbol{x}} \cdot \langle\rho_g\rangle \left[\langle e_g\rangle_g \langle \boldsymbol{u_g}\rangle_g + \langle e_g''' \boldsymbol{u_g}'''\rangle_g \right] &= - \langle P_g\rangle : \nabla_{\boldsymbol{x}} \left(\langle \boldsymbol{u_g}\rangle_g - \frac{\langle \rho_g' \boldsymbol{u_g}'\rangle}{\langle\rho_g\rangle} \right) \\ &- \langle P_g' : \nabla_{\boldsymbol{x}} \boldsymbol{u_g}'\rangle + \langle\rho_g\rangle \left[\langle\tau\rangle_g : \nabla_{\boldsymbol{x}} \langle \boldsymbol{u_g}\rangle_g + \langle \tau''' : \nabla_{\boldsymbol{x}} \boldsymbol{u_g}'''\rangle_g \right] \\ &- \nabla_{\boldsymbol{x}} \cdot \langle \mathbf{q}\rangle + \mathfrak{S}^{\rho e}\end{aligned} \tag{B.28}$$

with

$$\mathfrak{S}^{\rho e} = -2 \left\langle \frac{1}{\tau_d^*} \right\rangle \langle m_{1/2}\Theta_g\rangle - \frac{3}{2} R_d \langle m_{1/2}\Theta_g\rangle \tag{B.29}$$

and

$$\langle m_{1/2}\Theta_g\rangle = \langle m_{1/2} \boldsymbol{u_g} \cdot \boldsymbol{u_d}\rangle - \langle m_{1/2}\Theta\rangle - \frac{1}{2} \left(\langle m_{1/2} \boldsymbol{u_d} \cdot \boldsymbol{u_d}\rangle + \langle m_{1/2} \boldsymbol{u_g} \cdot \boldsymbol{u_g}\rangle \right) \tag{B.30}$$

Let us give explicit forms for third order correlations;

$$\begin{aligned}\langle m_{1/2} \boldsymbol{u_g} \cdot \boldsymbol{u_d}\rangle &= \langle m_{1/2}\rangle \langle \boldsymbol{u_g} \cdot \boldsymbol{u_d}\rangle + \langle m_{1/2}' (\boldsymbol{u_g} \cdot \boldsymbol{u_d})'\rangle \\ &= \langle m_{1/2}\rangle \left(\langle \boldsymbol{u_g} \cdot \boldsymbol{u_d}\rangle_d - \frac{\langle m_{3/2}' (\boldsymbol{u_g} \cdot \boldsymbol{u_d})'\rangle}{\langle m_{3/2}\rangle} \right) + \langle m_{1/2}' (\boldsymbol{u_g} \cdot \boldsymbol{u_d})'\rangle \\ &= \langle m_{1/2}\rangle \left(\langle \boldsymbol{u_g}\rangle_d \cdot \langle \boldsymbol{u_d}\rangle_d + \langle \boldsymbol{u_g}''' \cdot \boldsymbol{u_d}''\rangle_d \right) \\ &= \langle m_{1/2}\rangle \left[\left(\langle \boldsymbol{u_g}\rangle_g + \frac{\langle \alpha_d' \boldsymbol{u_g}'\rangle}{\langle 1-\alpha_d\rangle \langle\alpha_d\rangle} \right) \cdot \langle \boldsymbol{u_d}\rangle_d + \langle \boldsymbol{u_g}''' \cdot \boldsymbol{u_d}''\rangle_d \right]\end{aligned} \tag{B.31}$$

$$\begin{aligned}\langle m_{1/2} \boldsymbol{u_d} \cdot \boldsymbol{u_d}\rangle &= \langle m_{1/2}\rangle \langle \boldsymbol{u_d} \cdot \boldsymbol{u_d}\rangle + \langle m_{1/2}' (\boldsymbol{u_d} \cdot \boldsymbol{u_d})'\rangle \\ &= \langle m_{1/2}\rangle \left(\langle \boldsymbol{u_d} \cdot \boldsymbol{u_d}\rangle_d - \frac{\langle m_{3/2}' (\boldsymbol{u_d} \cdot \boldsymbol{u_d})'\rangle}{\langle m_{3/2}\rangle} \right) + \langle m_{1/2}' (\boldsymbol{u_d} \cdot \boldsymbol{u_d})'\rangle \\ &= \langle m_{1/2}\rangle \left(\langle \boldsymbol{u_d}\rangle_d \cdot \langle \boldsymbol{u_d}\rangle_d + \langle \boldsymbol{u_d}'' \cdot \boldsymbol{u_d}''\rangle_d \right)\end{aligned} \tag{B.32}$$

$$\begin{aligned}\langle m_{1/2} \boldsymbol{u_g} \cdot \boldsymbol{u_g}\rangle &= \langle m_{1/2}\rangle \langle \boldsymbol{u_g} \cdot \boldsymbol{u_g}\rangle + \langle m_{1/2}' (\boldsymbol{u_g} \cdot \boldsymbol{u_g})'\rangle \\ &= \langle m_{1/2}\rangle \left(\langle \boldsymbol{u_g} \cdot \boldsymbol{u_g}\rangle_d - \frac{\langle m_{3/2}' (\boldsymbol{u_g} \cdot \boldsymbol{u_g})'\rangle}{\langle m_{3/2}\rangle} \right) + \langle m_{1/2}' (\boldsymbol{u_g} \cdot \boldsymbol{u_g})'\rangle \\ &= \langle m_{1/2}\rangle \left(\langle \boldsymbol{u_g}\rangle_g \cdot \langle \boldsymbol{u_g}\rangle_g + \langle \boldsymbol{u_g}''' \cdot \boldsymbol{u_g}'''\rangle_g + \frac{\langle \alpha_d' (\boldsymbol{u_g} \cdot \boldsymbol{u_g})'\rangle}{\langle 1-\alpha_d\rangle \langle\alpha_d\rangle} \right)\end{aligned} \tag{B.33}$$

The third order term in the final structure of (B.34) can be still simplified by the following way:

$$\begin{aligned}\left\langle \alpha_d' \left(\boldsymbol{u_g} \cdot \boldsymbol{u_g}\right)' \right\rangle =& \left\langle \alpha_d' \left(\left\langle \boldsymbol{u_g} \right\rangle_g + \boldsymbol{u_g}''' \right) \cdot \left(\left\langle \boldsymbol{u_g} \right\rangle_g + \boldsymbol{u_g}''' \right) \right\rangle \\ =& 2 \left\langle \alpha_d' \boldsymbol{u_g}''' \right\rangle \cdot \left\langle \boldsymbol{u_g} \right\rangle_g + \left\langle \alpha_d' \boldsymbol{u_g}''' \cdot \boldsymbol{u_g}''' \right\rangle \end{aligned} \tag{B.34}$$

$$\begin{aligned}\left\langle m_{1/2} \Theta_g \right\rangle =& \left\langle \boldsymbol{u_g} \right\rangle_g \cdot \left\langle \boldsymbol{u_d} \right\rangle_d + \left\langle \boldsymbol{u_g}''' \cdot \boldsymbol{u_d}'' \right\rangle_d - k_d - k_g - \left\langle \Theta \right\rangle_d - \left(K + K_g\right) \\ &+ \frac{\left\langle \alpha_d' \boldsymbol{u_g}''' \right\rangle}{\left\langle 1 - \alpha_d \right\rangle \left\langle \alpha_d \right\rangle} \left(\left\langle \boldsymbol{u_d} \right\rangle_d - \left\langle \boldsymbol{u_g} \right\rangle_g \right) - \frac{1}{2} \frac{\left\langle \alpha_d' \boldsymbol{u_g}''' \cdot \boldsymbol{u_g}''' \right\rangle}{\left\langle 1 - \alpha_d \right\rangle \left\langle \alpha_d \right\rangle} \end{aligned} \tag{B.35}$$

B.2.9 RA gas phase mean kinetic energy equation

The gas-phase mean kinetic energy is known from the PA gas-phase velocity. It can be deduced by multiplying the PA gas-phase momentum equation by $\left\langle \boldsymbol{u_g} \right\rangle_g$ which leads to the following expression:

$$\begin{aligned}&\partial_t \left\langle \rho_g \right\rangle K_g + \nabla_{\boldsymbol{x}} \cdot \left[\left\langle \rho_g \right\rangle K_g \left\langle \boldsymbol{u_g} \right\rangle_g + \left\langle \boldsymbol{u_g} \right\rangle_g \left(\left\langle \rho_g \right\rangle \left\langle \boldsymbol{u_g}''' \boldsymbol{u_g}''' \right\rangle_g + \left\langle P_g \right\rangle \right) \right] = \\ &\left(\left\langle \rho_g \right\rangle \left\langle \boldsymbol{u_g}''' \boldsymbol{u_g}''' \right\rangle_g + \left\langle P_g \right\rangle \right) : \nabla_{\boldsymbol{x}} \left\langle \boldsymbol{u_g} \right\rangle_g + \left\langle \boldsymbol{u_g} \right\rangle_g \nabla_{\boldsymbol{x}} \left(\left\langle \rho_g \right\rangle \left\langle \tau \right\rangle_g \right) + S_g^K \end{aligned} \tag{B.36}$$

with the source term

$$S_g^K = \left\langle \boldsymbol{\mathcal{A}}_g \right\rangle \left\langle \boldsymbol{u_g} \right\rangle_g + \left\langle \mathcal{M}_g \right\rangle \left(K_g - \left\langle \boldsymbol{u_g} \right\rangle_g^2 \right) + \left\langle \mathcal{M}_g \boldsymbol{u_d} \right\rangle \left\langle \boldsymbol{u_g} \right\rangle_g \tag{B.37}$$